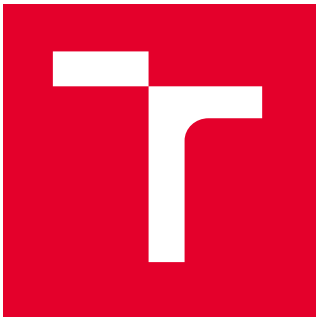

BRNO UNIVERSITY OF TECHNOLOGY

VYSOKÉ UČENÍ TECHNICKÉ V BRNĚ

FACULTY OF CHEMISTRY

FAKULTA CHEMICKÁ

INSTITUTE OF MATERIALS SCIENCE

ÚSTAV CHEMIE MATERIÁLŮ

STUDYING THE PROPERTIES OF MOLECULAR PHOTOACTIVE MATERIALS VIA THE METHODS OF COMPUTATIONAL CHEMISTRY

STUDIUM VLASTNOSTÍ MOLEKULÁRNÍCH FOTOAKTIVNÍCH MATERIÁLŮ METODAMI VÝPOČETNÍ CHEMIE

DOCTORAL THESIS

DIZERTAČNÍ PRÁCE

AUTHOR — **Ing. Jan Truksa**

AUTOR PRÁCE

SUPERVISOR — **doc. Ing. Ota Salyk, CSc.**

ŠKOLITEL

BRNO 2022

BRNO UNIVERSITY OF TECHNOLOGY
FACULTY OF CHEMISTRY

Assignment Doctoral Thesis

Department:	Institute of Materials Science	Academic year: 2022/23
Student:	**Ing. Jan Truksa**	
Study programme:	Chemistry, Technology and Properties of Materials	
Study field:	Chemistry, Technology and Properties of Materials	
Head of thesis:	**doc. Ing. Ota Salyk, CSc.**	

Title of Doctoral Thesis:

Studying the properties of molecular photoactive materials via the methods of computational chemistry

Doctoral Thesis:

1) Prepare a literature search focused on the modeling of molecules using the electron density functional method.
2) Describe the possibilities of predicting the spectroscopic and electrical properties of molecular materials using the aforementioned methods.
3) Describe the possibilities of extending the predictions of these properties for small molecules and oligomers to polymer chains.
4) Use the knowledge gained in the study of structures based on flavine and polythiophene, which can be used for applications in optoelectronics. Focus on the geometric structure, visible light absorption, and energy of the highest filled and lowest unfilled orbitals.
5) Discuss the obtained data and compare with experimental results either based on your own measurements or from the literature. Evaluate whether it is possible to recommend substances for future synthesis based on the data obtained.

Deadline for Doctoral Thesis delivery: 11.9.2022:

Ing. Jan Truksa student	doc. Ing. Ota Salyk, CSc. Head of thesis	doc. Ing. František Šoukal, Ph.D. Head of department

In Brno dated 1.9.2021

prof. Ing. Martin Weiter, Ph.D.
Dean

ABSTRACT

In this work, the principles of theoretical density functional theory are briefly discussed first, together with the method of searching for lowest-energy structures of molecules and predicting the spectroscopic and electronic properties. Afterwards, the results of the theoretical analysis of the geometry and electronic structure of two types of molecules is presented, combined with experimental results. First, the alloxazine and lumazine, considered together as flavins, and their derivatives represent molecular materials, while adamantyl substituted polythiophenes represent polymer materials.

With respect to the flavins, different basis sets, together with the B3LYP functional, were used to find the best possible fit to experimental absorption spectra. Here, the B3LYP/6-31+G** and B3LYP/aug-cc-PVDZ methods proved to have the best correlation, with correlation coefficients 0.95 and 0.96, respectively, while the def2SVP set reached 0.94. In this context, the B3LYP/6-31+G** method seems to be the most cost-efficient. By measuring the absorption spectra of selected flavins in a mixture of dimethylsulfoxide (DMSO) and water, the spectra of flavin isomers – the alloxazine and isoalloxazine form were gained. The response of these molecules to changes in the concentration of DMSO and water will be the object of further study.

For the polythiophenes, the electronic and optical properties were theoretically investigated using model octamers, while the conformations of the adamantylated side chains were considered using trimer molecules, due to a high computational complexity. Here, the methyladamantyl thiophene was found to have a more rigid structure compared to the ethyladamantyl substituted chain, which was later confirmed *via* crystallographic analysis and atomic force microscopy scans. Crystal structures were confirmed to be present, with lattice parameters comparable to poly(3-hexylthiophene) (**P3HT**). Inspired by this research, different polymer backbones based on polythiophene were considered for future synthesis. The main recommendation here is to lower the amount of side substituents, so that only one in two or one in three thiophenes bear an adamantylated side chain.

Overall, the molecules presented here are interesting candidates for future use in optoelectronics, and the theoretical predictions generally agree with experimental results, although the comparison with experiment is not always trivial, *e.g.*, in the case of the polythiophene side chains.

KEYWORDS

Computational Chemistry, Optoelectronic Materials, Spectroscopy, Visible Light Absorption, Density Functional Theory, Alloxazine, Lumazine, Polythiophene

ABSTRAKT

V této práci jsou nejprve rychle nastíněny principy teorie funkcionálu elektronové hustoty (DFT), spolu s praktickými metodami hledání nejníže energeticky postavených struktur organických molekul a predikování jejich spektroskopických a elektronických vlastností. Poté jsou prezentovány výsledky teoretické analýzy geometrie a elektronové struktury dvou druhů molekul v kombinaci s experimentálními výsledky. Nejprve jsou diskutovány alloxazin, lumazin a jejich deriváty, souhrnně nazývané flaviny, které reprezentují molekulární materiály. Naproti tomu, struktury na bázi polythiofenu reprezentují polymerní materiály.

V případě flavinů byla nejprve nalezena nejlepší možná korelace teoretických absorpčních spekter s experimentálními na základě výpočtů se třemi různými bázovými soustavami v kombinaci s funkcionálem B3LYP. Dobrá shoda byla nalezena pomocí metod B3LYP/6-31+G** a B3LYP/aug-cc-PVDZ, které dosáhly korelačních koeficientů 0.95 a 0.96. Naproti tomu soustava def2SVP dosáhla pouze 0.94. V tomto kontextu se tak metoda B3LYP/6-31+G** jeví jako nejefektivnější vzhledem k náročnosti na výpočetní kapacitu. Měřením absorpčních spekter vybraných flavinů ve směsi dimethylsulfoxidu (DMSO) a vody byla získána spektra jednotlivých izomerů – alloxazinové a isoalloxazinové formy. Reakce těchto molekul na změny koncentrace DMSO a vody bude předmětem dalšího studia.

U polythiofenů byly studovány optické a elektrické vlastnosti na modelových oktamerech, zatímco geometrie a konformace adamantylovaných substitutentů byly z důvodu vysoké výpočetní náročnosti modelovány na trimerových molekulách. Bylo zjištěno, že thiofenový řetězec s postranními methyladamantylovými skupinami vykazuje vyšši rigiditu než řetězec substituovaný ethyladamantylem, což bylo později potvrzeno krystalografickou analýzou a skenováním povrchu pomocí mikroskopie atomárních sil. Byly nalezeny krystalické struktury s parametry srovnatelnými s poly(3-hexylthiofenem) (**P3HT**). Na základě tohoto výzkumu byly navržený nové páteřní řetězce pro možnou syntézu, jako hlavní doporučení se zde jeví snížení počtu substituentů, aby adamantylový postranní řetězec byl přítomen pouze na každém druhém či třetím thiofenu.

Zde prezentované molekuly jsou zajímavými kandidáty pro využití v optoelektronice, a teoretické predikce dosahují dobrou shodu s experimentem, přestože jejich srovnání není vždy triviální, jako je tomu například u postranních řetězců polythiofenu.

KLÍČOVÁ SLOVA

Výpočetní chemie, Optoelektronické materiály, Spektroskopie, Absorpce viditelného světla, Teorie funkcionálu elektronové hustoty, Alloxazin, Lumazin, Polythiofen

TRUKSA, Jan. *Studium vlastností molekulárních fotoaktivních materiálů metodami výpočetní chemie* [online]. Brno, 2022 [cit. 2022-09-08]. Dostupné z: https://www.vutbr.cz/studenti/zav-prace/detail/146841. Dizertační práce. Vysoké učení technické v Brně, Fakulta chemická, Ústav chemie materiálů. Vedoucí práce Ota Salyk

DECLARATION

I declare that the dissertation thesis has been worked out by myself and that all the quotations from the used literary sources are accurate and complete. The content of the diploma/bachelor thesis is the property of the Faculty of Chemistry of Brno University of Technology and all commercial uses are allowed only if approved by both the supervisor and the dean of the Faculty of Chemistry, BUT.

.....

student's signature

ACKNOWLEDGMENT

I would like to thank the head of my thesis, doc. Ing. Ota Salyk, CSc., and my great mentors doc. Ing. Jozef Krajčovič, Ph.D., and prof. Ing. Vladimír Lukeš, DrSc., for advice and patience during the making of my thesis. Further thanks should be extended to Mgr. Jan Richtár, Ph.D., Ing. Matouš Kratochvíl, Ph.D., Ing. Ján Jančík, and Ing. Lucia Ivanová, for synthesizing the investigated molecules, and help with their characterization.

CONTENTS

1 INTRODUCTION

The field of computational chemistry has gained a great deal of interest during the past decade. Its enormous utility is based on the fact that it enables chemists to study structures that are unstable or dangerous, such as transitional states or highly toxic molecules. Furthermore, even before a new molecule is synthesized, its properties can be theoretically predicted. This possibility allows for great savings of time and money for synthetic chemists, who can gain an idea which potential molecules are worth synthesising. As such, the computational chemist may serve as a "navigator" in the synthetic effort, helping his colleagues to reach their goals at a lower cost than they would without his assistance.

First, a short overview of computational methods which are currently in use will be given, with a special focus on the density functional theory (DFT) computations. Then, the practical use of DFT in the prediction of molecular properties will be discussed in more detail. The properties of interest include molecular geometry, spectroscopic properties, and aromaticity.

Since this work is aimed at novel molecules with interesting spectroscopic properties, special attention will be paid to the prediction of different types of spectra. The most relevant type to this work is the Ultraviolet and Visible Spectrum (UV/VIS), both in the sense of absorption and emission. When discussing the spectroscopic behaviour of molecules, the effect of the solvent or solid-state interactions must be also mentioned, especially when connected to UV/VIS spectroscopy.

This work is further focused on two types of molecules – the flavins, alloxazine, lumazine and their derivatives, and polythiophenes with different side substituents. Interestingly, alloxazine and lumazine are rarely mentioned in conjunction in the literature, which motivates a detailed side-by-side study of these molecules, with the hope of creating a unified theoretical basis for their behaviour and modification These molecules have remarkable spectroscopic abilities, such as the tunability of their spectrum by the modification of the parent molecule, or by the addition on electron-donating or electron-accepting groups [1].

The polythiophenes will be theoretically investigated in terms of model octamers and trimers, due to the large computational complexity involved, especially when the large adamantylated side chains are considered. Finally, some candidates for future synthesis will be discussed, based on their geometry and electronic structure. Different uses of these materials include optoelectronics such as Organic Light Emitting Diodes (OLEDs), or photocatalysis.

2 THEORETICAL BACKGROUND

At present, the methods for predicting molecular structure and properties can be divided into five categories, the simplest of which is Molecular Mechanics. In this method, the molecule is considered to be a collection of balls held together by springs, which represent atoms and bonds. If there is available data on the properties of these springs, such as their equilibrium lengths and angles between them, and the energy needed to stretch and bend them, it is possible to calculate the energy of a given molecule. Or, taking the opposite approach, to calculate the optimal geometry of a molecule by varying the geometry until an energy minimum is found [2].

In Semiempirical calculations, based on Schrödinger's equation, a library of parameters, obtained by fitting previously calculated geometries to experimental results, is used to approximate the solution. On the other hand, in *ab initio* methods, Schrödinger's equation is solved with the least possible number of approximations, and experimental parameters are generally not used. The result of such a calculation is the energy and wavefunction of a molecule, from which the electron distribution can be deduced. In the Density Functional Theory method, unlike the previous two, the electron distribution is calculated directly. This method has gained great popularity since the 1980s and will be discussed in more detail below [2]. The DFT represents a reasonable compromise between the precision and speed, as it offers accuracy comparable to *ab initio* at a much higher speed. Since it was generalized to treat time-dependent phenomena, the time-dependent density functional theory (TDDFT) is useful for predicting molecular excitations and energy emissions.

Finally, the Molecular Dynamics (MD) method is used to study the behaviour of molecules in an external forcefield. This is done by the integration of Newtonian equations of motion. The Monte Carlo (MC) method is comparable in scope but based on random perturbations of the molecular or atomic ensemble, without an explicit time dependence. For instance, it is possible to study the geometry change of an enzyme molecule as it binds onto a substrate, or the interaction of water molecules with a solute [2,3].

2.1 Density Functional Theory

In 1964 and 1965, Kohn, Hohenberg and Sham [4, 5] proposed a method to replace the electron wavefunction with the electron density function ρ (m^{-3}):

$$\psi\left(\mathbf{r}_1, \mathbf{r_2}, \dots, \mathbf{r}_{N_{\mathrm{el}}}, \sigma_1, \sigma_2, \dots, \sigma_{N_{\mathrm{el}}}\right) \rightarrow \rho(x, y, z), \tag{1}$$

Where ψ is the wave function, $\mathbf{r}_i$ is the position vector, N_{el} is the number of electrons, and σ is the spin of an electron. A great advantage of this approach is, that ρ is a real function of three variables, and it corresponds to an observable quantity.

The first Hohenberg-Kohn theorem states, that all properties of a molecule in the ground state are determined by the ground-state density function ρ_0. Effectively, any ground state property of a molecule is a functional of ρ_0. A functional is any rule that assigns a number to some

function. According to the first Hohenberg-Kohn theorem, the ground-state energy, among other quantities, is a functional $\mathscr{E}_0$ of ρ_0:

$$E_0 = \mathcal{E}[\rho_0]. \tag{2}$$

Unfortunately, the theorem does not state how to find the exact functional $\mathscr{E}$. However, an approximate energy E_0 can be obtained by using an approximate functional. Since there are many different approximations, and the correct functional for a certain use is not *a priori* known, it is necessary to choose functionals based on previous experience. For example, a Lee-Yang-Parr functional would be used for calculating spectroscopic properties such as excitation and emission spectra, and a Minnesota functional would be used to calculate thermodynamic variables, such as reaction enthalpies. One consequence of this theorem is, that if an exact functional $\mathscr{E}$ were to be found, the DFT method would give accurate results in a fraction of the time needed for *ab initio* calculations [2, 6, 7, 8].

The second Hohenberg-Kohn theorem states, that any density function ρ other than ρ_0, commonly referred to as a trial function, will give an energy higher than the true E_0. The electronic energy from the trial function ρ_t is the energy of electrons moving in the potential field of the nuclei V. This electronic energy is denoted as E_v, its functional as $\mathscr{E}_v$, and the theorem is formulated:

$$E_\mathrm{v} = \mathcal{E}_\mathrm{v}[\rho_t] \geq \mathcal{E}_0[\rho_0] = E_0. \tag{3}$$

The electron density must satisfy two conditions: first, the sum of electrons in all infinitesimal volumes must be equal to the total number of electrons in the molecule. Second, the electron density must be nonnegative everywhere in the system. Thus, if coordinates are replaced by position vectors:

$$\int \rho(\mathbf{r}) d\mathbf{r} = N_\mathrm{el}, \mathbf{r} = (x, y, z), \tag{4}$$

$$\rho(\mathbf{r}) \geq 0 \; for \; all \; \mathbf{r}. \tag{5}$$

Of course, the equality $E_v = E_0$ holds only in case the electron density function used is the true density ρ_0. It should be further noted, that both theorems hold for exact functionals. When using approximate functionals, the resulting energy can be lower than E_0 [2]. For the proof of both theorems, the reader is referred to Levine's textbook on quantum chemistry [9].

Based on the theorems mentioned above, the Kohn-Sham approach for calculating molecular properties was developed. To deal with the fact that the true ρ_0 and $\mathscr{E}_0$ are unknown, this approach relies on two ideas: first, to divide E_0 into a portion which can be calculated without using the functional, and a relatively small term which contains the functional. This way, an error in the functional has the lowest possible influence on the energy. The second idea is to use an initial guess for ρ, which is then iteratively refined.

Concerning the first idea, a fictional noninteracting reference system is defined. In this system, the electrons do not interact, and the ground-state electron density is supposed to equal the true distribution ρ_0. The deviations from the behaviour of a real system are treated together with the approximate functional. If the electronic energy is written as a sum of functionals, the energy can be expressed as:

$$E_0 = \langle T_\mathrm{e}[\rho_0]\rangle + \langle V_{\mathrm{nu-el}}[\rho_0]\rangle + \langle V_{\mathrm{el-el}}[\rho_0]\rangle. \quad (6)$$

The $V_{\mathrm{nu-el}}$ term is simply a classical potential energy expression. The kinetic energy term is given as a sum of the kinetic energy of the reference system and a correction ΔT_e. Similarly, the $V_{\mathrm{el-el}}$ term is defined as a sum of the coulombic repulsion and a correction $\Delta V_{\mathrm{el-el}}$ for real behaviour:

$$E_0 = \langle T_\mathrm{e}[\rho_0]\rangle_\mathrm{ref} + \Delta\langle T_\mathrm{e}[\rho_0]\rangle + \int \rho_0(\mathbf{r})\, V(\mathbf{r})\mathrm{d}\mathbf{r} + \frac{1}{2}\iint \frac{\rho_0(\mathbf{r_A})\rho_0(\mathbf{r_B})}{\mathbf{r_{AB}}} d\mathbf{r}_1 d\mathbf{r}_2 + \Delta\langle V_{\mathrm{el-el}}[\rho_0]\rangle \quad (42)$$

where $\mathbf{r}_{\mathrm{AB}}$ is the vector between electrons A and B. The exchange-correlation functional is defined as the sum of the two corrections:

$$E_\mathrm{XC} = \Delta\langle T_\mathrm{e}[\rho_0]\rangle + \Delta\langle V_{\mathrm{el-el}}[\rho_0]\rangle. \quad (7)$$

To make the calculations mathematically tractable, Kohn and Sham have introduced a fictional reference system, in which n noninteracting electrons experience a potential field $V_\mathrm{s}(\boldsymbol{r})$, which is chosen to make the ground-state electron probability density $\rho_\mathrm{s}(\boldsymbol{r})$ of the reference system equal to the true density ρ_0.

The Hamiltonian of the reference system is then the sum of single-electron operators $\hat{h}^{KS}$:

$$\hat{H}_s = \sum_{i=1}^{n} \hat{h}_i^{KS} = \sum_{i=1}^{n} \left[-\frac{1}{2}\Delta_i + V_s(\boldsymbol{r})\right], \quad (8)$$

with the Kohn-Sham equation for a single orbital:

$$\hat{h}\psi_\mathrm{i}^\mathrm{KS} = \varepsilon_\mathrm{i}^\mathrm{KS}\psi_\mathrm{i}^\mathrm{KS}. \quad (9)$$

The ground state is expressed in terms of Kohn-Sham (KS) spinorbitals ψ^KS [9]. The spatial parts of these orbitals can be expanded into basis functions (see **Section 2.4**), and for the probability density:

$$\rho_\mathrm{r} = \sum_{\mathrm{i}=1}^{N_\mathrm{el}} \left|\psi_\mathrm{i}^\mathrm{KS}\right|^2. \quad (10)$$

Furthermore, the exchange-correlation potential v_XC is defined as the derivative:

$$v_\mathrm{XC}(\mathbf{r}) = \frac{dE[\rho(\mathbf{r})]}{d\rho(\mathbf{r})}. \quad (11)$$

The energy E_0 can then be found from the E_{XC}, and the KS orbitals, since KS orbitals satisfy:

$$\left(-\frac{1}{2}\Delta_{el} - \sum_{nuclei}\frac{Z_{nu}}{r_{el-nu}} + \int \frac{\rho(\mathbf{r}_{el_2})}{\mathrm{r}_{el_1-el_2}} d\mathbf{r}_{el_2} + v_{XC}\right)\psi_i^{KS} = \varepsilon_i^{KS}\psi_i^{KS}. \quad (12)$$

It should be noted that KS orbitals arise from a fictional reference system, and there is, in fact, no molecular wave function involved in the DFT method, so KS orbitals do not have physical significance, outside of making the above calculations possible. They do, however, resemble actual *ab initio* molecular orbitals. From here, the energy is typically determined by an iterative process. First, a one-electron KS equation is solved for electron number one, where the repulsion term consists of this electron and an electrostatic field of all other electrons in the system. This gives a function $\psi_1^{KS}(1)$, which is expected to be closer to the real one. This process is then repeated for all other electrons in the system until $\psi_1^{KS}(N_{el})$ is reached. The whole cycle is repeated until it reaches a Ψ_k^{KS}, or an energy E_k produced from it, that is essentially the same as that of the previous cycle Ψ_{k-1}^{KS}. Then the field of cycle k is said to be self-consistent with the field of k − 1 and the calculation is finished. This approach is therefore called the Self Consistent Field (SCF) procedure, first proposed by Hartree [2].

The E_{XC} functional can further be split into the exchange-energy and correlation-energy parts:

$$E_{XC} = E_x + E_C \quad (13)$$

In practice, the E_X part is determined according to one of several approximations shown in **Tab. 1**, and E_C, being much smaller in absolute value, is set as the difference between E_{XC} and E_X. While basis sets remain a part of DFT, they play a smaller role than in *ab initio* [9, 10].

Furthermore, different functionals may be range-separated, which means the electron-electron repulsion operator is separated into a long- and short-range part, to mitigate the tendency to overestimate electron delocalization. Another possibility is dispersion correction, which adds additional terms to describe van-der-Waals type interactions. Double-hybrid methods explicitly account for dispersion via the Møler-Plesset (MP2) correction term, but it may be combined with other empirical parameters [9,10]. An overview of the functionals is given in **Tab. 1**.

Tab. 1 *The five general types of correlation-exchange functionals*

Approximation	Meaning
Local Density (LDA)	The density is treated as a slowly varying function in a field of uniform electron gas, together with a continuous and homogeneous positive charge. The E_{XC} and v_{XC} are functions of ρ strictly at a given point $\boldsymbol{r}$.
Local Spin-Density (LSDA)	A correction of the LDA for molecules near dissociation and open-shell states. Electrons that would be assigned the same spatial KS orbital and opposite spin in the LDA have different spatial orbitals. The density $\rho_\alpha(\boldsymbol{r})$ of spin-α and $\rho_\beta(\boldsymbol{r})$ of spin-β electrons are dealt with separately.
Generalized Gradient (GGA)	A correction of the LSDA for greater variation of the density ρ with position. E_{XC} and v_{XC} are functions of ρ at $\boldsymbol{r}$, and in its infinitesimal neighbourhood, the E_{XC}^{GGA} functional also involves the gradients of $\rho_\alpha(\boldsymbol{r})$ and $\rho_\beta(\boldsymbol{r})$.
Meta Generalized Gradient (Meta-GGA)	An additional improvement of GGA, that accounts for the second derivatives of $\rho_{\alpha,\beta}$, or the Kohn-Sham kinetic energy density: $\tau_\alpha = \frac{1}{2}\sum_i \left\lvert \nabla \psi_{i\alpha}^{KS} \right\rvert^2$ (14) which is a sum across all occupied orbitals.
Hybrid	A widely used type of functional, a weighted sum of exchange energy found from the KS orbitals (see chapter 2.2), and GGA or Meta-GGA functionals.
Double-Hybrid	This method first solves for the KS orbitals using a hybrid functional and then calculates an *ab initio* MP2 correction term using the computed KS orbitals and energies.

2.2 Time-Dependent Density Functional Theory

In order to treat the behaviour of quantum mechanical systems outside of the ground state or other equilibrium states, the time-dependent DFT (TDDFT) was developed [9, 11]. In this theory, the time-dependent Hamiltonian is used:

$$\hat{H}(t) = \hat{T} + \hat{V}(t) + \hat{V}_{part} \tag{15}$$

where $\hat{V}_{\mathrm{part}}$ is the potential energy of particles in the system, and $\hat{V}(t)$ is a time-dependent external scalar potential field. The evolution of the system is then evaluated by solving the time-dependent Schrödinger equation. Formally, the solution can be expressed in terms of an evolution operator. Often, perturbation theory is used, where $\hat{H}(t)$ is considered to be the sum of a Hamiltonian $\hat{H}_0$ at the time t_0, and a TD finite perturbation $\hat{H}_1(t)$ at $t \geq t_0$. From this, properties of a time-dependent many-body system can be found. The full derivation is beyond the scope of this work but is described in the textbook by C. Ullrich [11].

Runge and Gross [12] have shown, that there is a one-to-one correspondence between the density operator of an N-electron system and the time-dependent potential, *i.e.*, there is a unique

electron density for each scalar, Taylor-expandable potential $V(t)$ and *vice versa*. Furthermore, all observable quantities are functionals of the electron density. Thus, formally, any desired quantity in a time-dependent system may be gained *via* TDDFT. Of course, practical problems of DFT do still apply. However, the constraints imposed on V by Runge and Gross make it impossible to treat phenomena described by vectors, like electromagnetic waves and magnetic fields, although a generalized formalism for vector fields was later developed [11, 13].

The possibility of replacing ρ_0 with some reference system was treated by van Leeuwen [14, 15]. Then, it is possible to solve the time-dependent Kohn-Sham equation:

$$\left[-\frac{1}{2}\Delta_i + V_s(\boldsymbol{r},t)\right]\psi_{\mathrm{i}}^{\mathrm{KS}}(\boldsymbol{r},t) = \mathrm{i}\frac{\partial\psi_{\mathrm{i}}^{\mathrm{KS}}(\boldsymbol{r},t)}{\partial t} \tag{16}$$

where the orbitals at time t_0, $\psi_{\mathrm{i}}^{\mathrm{KS}}(\mathbf{r}, t_0)$, are found from a self-consistent solution of the static KS equation (9). The occupied initial orbitals are then propagated by the TD-KS equation. Furthermore, a TD exchange-correlation potential must of course be approximated, with the condition that it must match the static v_{XC} at time t_0. Since self-consistency in TDDFT must be achieved over time as well as space, the SCF procedure is considerably more difficult. For the numerical solution, the predictor-corrector scheme may be used [11].

The approximation of $v_{\mathrm{XC}}(t)$ is further complicated by initial state dependence – for a multi-electron system, it is possible to arrive at the same ρ ($\mathbf{r}$, t) propagating from different initial states, and thus the potential is not uniquely defined, as shown by Maitra and Burke [16, 17]. Thus, it is not always adequate to simply use an XC potential from classical DFT, *i.e.*, the adiabatic approximation.

Often, the full solution of the density time-dependence is not necessary or practical, *e.g.*, in systems that do not heavily deviate from an equilibrium state. This is the case for electronic excitations of organic molecules, where the incident light applies a relatively small perturbation to the whole system. The small differences between the states can be calculated using linear response theory. Where the XC potential expression is linearized, referred to as the TD-XC kernel. The system may also be Fourier-transformed into the frequency domain, producing the frequency-dependent kernel. While nonlinear response theory exists, it is beyond the scope of this work [11]. Some possible approximations are given in **Tab. 2**.

***Tab. 2**. Some examples of exchange-correlation approximations of the XC kernel. Since the hierarchy is less orderly than in standard DFT, it is not practical to list every possible approach toward constructing an XC kernel. Other possible functionals, such as the tensor approach in TDCDFT, are disqualified by the focus on linear response theory.*

Approximation	Meaning
Random Phase (RPA)	The kernel is set to zero, dynamic effects are ignored.
Adiabatic	The frequency-dependent kernel is replaced with a static limit, derived from static XC approximations, such as LDA, GGA *etc.*, see Table 1.
TD Optimized Effective Potential (TDOEP)	The XC potential is expressed as a functional of KS orbitals, *via* an integral equation. Possible to find an approximate [18] or exact [11] form.

The TDDFT method provides electronic spectra that are in good agreement with experiment, especially when close to the Frontier Molecular Orbitals FMOs, as long as the ground state XC potential is correct. On the other hand, it can fail in the case of triplet states on open-shell molecules or very large π-conjugated systems [11, 19]. Furthermore, if charge transfer between two spatially separated regions is involved, TDDFT results may be expected to be around 2 eV lower than the true excitation energies. A reasonable solution to this is the use of range-separated hybrid functionals, and non-adiabatic approximations [11]. Finally, Maitra [20] and Botti [21] have shown, that it is possible to extend the TDDFT formalism to periodic systems such as crystal lattices, an important note for the application in material science.

2.3 Solvent Models

The interactions of analyte and solvent pose a great problem in predicting geometries or spectroscopic properties since the solvent molecules stabilize slightly different confirmations of the ground and excited states of the analyte than those found in the gas phase. Therefore, using geometries stabilized in the gas phase (GP) often does not give an accurate fit to experimental data gained in solution. Usually, a shift in both the absorption band and the emission band is introduced by the presence and different polarity of the solvent. This is called the solvatochromic shift. Furthermore, due to constant fluctuations of the solvent molecules, the experimental band are broadened. To mitigate these effects, a correction for solvent polarizability, acidity and basicity can be used. More ambitious approaches, such as a continuum model or a molecular dynamics model have also been proposed [22, 23].

In explicit-solvent calculations, the investigated molecule is surrounded by solvent molecules. Various orientations of the solvent are then computed, and average properties are taken from the individual results. On the other hand, in continuum-solvent models, the solvent is modelled as a continuous dielectric, around a cavity that contains the solute molecule. Their interaction is then treated by an additional potential energy term in the Hamiltonian – the solvent molecules create an electric field in the region near the solute molecule, which is denoted the reaction field. Thus, methods where the molecular charge distribution is allowed to shift according to the influence of the solvent, are called Self-Consistent Reaction Field (SCRF) methods [9].

Early SCRF methods modelled the molecular cavity as a sphere or ellipsoid [24]. However, Miertuš, Scrocco and Tomasi [25] have proposed to create a more complex cavity by surrounding each nucleus with a sphere with a radius of 1.2 times the van der Waals radius of that atom. A van der Waals (vdW) radius is experimentally determined from distances between nonbonded atoms in molecular crystals [26] and serves as an approximation of the atomic radius. Kammeyer and Whitman [27] have determined that using the Hartree-Fock (HF) method, a sphere containing 98 % of the electron probability density is in good agreement with experimental vdW radii. This method is called the polarizable-continuum model (PCM).

Since the cavity in PCM has such a complex shape, the solvent-solute interaction energy term must be determined numerically. Electrostatics shows that an apparent surface charge distribution may be defined on the surface of the molecular cavity, which produces an electrostatic potential equal to that of the dielectric continuum. In practice, this is achieved by dividing the surface into *i* regions and placing an apparent charge Q_i into each one. The values of Q_i and the potential gradient in the solvent continuum are then determined iteratively, from an initial guess that is based on the electron density of the solute molecule in a vacuum. The converged values of charge are then used to find an initial interaction potential for the Hamiltonian, which then gives an improved electron density in the solute molecule and a new cycle is started until the entire system has converged [9].

A possible variation of this model is to use the contour surfaces of the constant electron probability density of the solute molecule instead of vdW radii. This is the isodensity PCM model, proposed by Foresman [28]. As a direct consequence of this approach, the size of the cavity changes with each iteration. A further refinement is the self-consistent isodensity PCM method, that allows geometry optimization and frequency analysis to be carried out on the solvated systems [9, 28]. The PCM model was further generalized by Cancès *et. al.* [29] to include anisotropic solvents, such as liquid crystals. This is the integral equation formulation PCM.

2.4 Atomic Basis Set Selection

To describe the wavefunction of an entire molecule, the concept of the Molecular Orbital (MO) was introduced. This approximation of the molecular wavefunction ψ as a linear combination of atomic orbitals (LCAO) was formalized by Mulliken [2, 10]. Here, the MO is gained from a weighted sum of the respective atomic orbitals. Since the AOs cannot be exactly represented, except for single electron atoms and molecules such as H, H_2^+, He^+, approximations must be used. Thus, each AO is in turn expressed in terms of simple functions, denoted as basis functions. These form a basis set. The individual basis functions are typically located on the atoms of a molecule. In theory, the molecular wavefunction can be approximated to any desired degree of accuracy, if suitable basis functions are used, and if the basis set has a large enough size. Note that an exact analytic description of the molecular wavefunction would typically require the basis set to be of infinite size [2, 9].

Roothnan has formalised this approach by expressing each AO of a multi-electron atom as a linear combination of a complete set of functions – the basis set:

$$\begin{matrix} 1s = \sum_i b_i \chi_i \\ 2s = \sum_i c_i \chi_i \end{matrix} \tag{17}$$

where χ_i are the basis functions, and b_i, c_i are coefficients to be found by the SCF approach. Multiple basis functions can be located on a single nucleus, and there is no upper limit on how many these functions may be used to represent the system. Typically, there is a basis function for each orbital used to describe the atom. For instance, carbon and hydrogen atoms will have the smallest basis sets:

$$\begin{matrix} \psi(C\ 1s), \psi(C\ 2s), \psi(C\ 2p_x), \psi\big(C\ 2p_y\big), \psi(C\ 2p_z) \\ \psi(H\ 1s) \end{matrix}.$$

In that case, a CH_4 molecule will have nine MOs, able to hold eighteen electrons, while only five orbitals will be filled. The rest will be unoccupied, denoted as virtual orbitals. Furthermore, an energy level ε is assigned to each component wavefunction, which corresponds to the energy of a single MO [2, 9, 10].

The first commonly used basis set was the Slater-type Orbital (STO), which has the normalised form:

$$\begin{matrix} \chi = \frac{\left(\frac{2\zeta}{a_0}\right)^{n+0.5}}{\sqrt{(2n)!}} r^{n-1} e^{-\frac{\zeta r}{a_0}} Y_l^m(\theta, \phi) \\ \zeta = \frac{Z-s}{n} \end{matrix} \tag{18}$$

where n is the principal quantum number, and s is the shielding constant. Due to the computational complexity involved in the STO description, the Slater orbital is commonly replaced by a linear combination of Gaussian functions. So, an orbital around some atom A could be expressed in terms of the following functions:

$$g = N x_A^{\mathrm{i}} y_A^{\mathrm{j}} z_A^{\mathrm{k}} e^{-\alpha r_A^2} \tag{19}$$

where N is a normalisation constant, i, j, k are nonnegative integers, α is a positive orbital exponent, and r_A is the distance to nucleus A. Alternatively, Gaussian orbitals can be given in a spherical form. Note that a single Gaussian gives a poor representation of the wavefunction around a nucleus, therefore several are used. This still improves performance over STOs [2,9].

The following table (**Tab. 3**) gives a brief explanation of commonly used keywords, that denote certain types of basis sets, and are valid for both STOs, and Gaussian-type function (GTF) orbitals. It is worth remembering, that an STO is a single function, while one GTF is a linear combination of several functions.

Tab. 3 *Frequently occurring types of basis sets*

Keyword	Meaning
Minimal	One orbital for every inner shell and valence shell of each atom, as in equation (30).
Extended	Any set larger than a minimal one, *i.e.*, more than one orbital for every shell of each atom.
Multiple-zeta	Each STO/GTF of a minimal set is replaced by multiple functions – by two functions for a double-zeta, three functions for a triple-zeta etc.; note that more than triple-zeta sets are not typically used, since accuracy improvements do not make up for the increased complexity.
Split-valence	Multiple basis functions are used for each AO in the valence shell, while a minimal number of functions is used for inner-shell AOs. This type is further subdivided into double-zeta and triple-zeta valence sets, according to the number of functions used for each orbital.
Polarised	There are additional functions, which represent orbitals with a higher quantum number l than the maximum of the ground-state valence shell, *e.g.*, adding p-orbital functions to a hydrogen atom or d-orbitals to carbon. In equation (33), $i + j + k = l$. Polarisation allows for greater variability in the AO shape.
Diffuse	A basis set with additional functions, that have very small orbital exponents, typically 0.01 to 0.1. This is done to model anions, lone electron pairs or hydrogen-bonded molecules, that have a significant electron density at a large distance from the nuclei.

The selection of an appropriate basis set is a matter of balance between the accuracy and efficiency of the computation. Since the computational complexity scales rapidly (with the 4^{th} power) with the number of individual basis functions, the set should be as small as possible. Therefore, a basis set is typically chosen to reflect the nature of the problem, such as using a diffuse basis set for ionized molecules. For DFT computations, triple-zeta polarized basis sets typically reduce the basis-related error to a few kJ mol^{-1} [10].

The most often used basis sets at currently include the Pople 6-31G double zeta and 6-311 triple zeta sets [30, 31], with polarization and diffuse functions added as required. The Pople sets are perhaps the most widely used, and a large amount of literature has been written on their performance, giving a good idea of the possibilities of certain functional/basis sets combinations, and contributing to the overall popularity [10]. Further, there are the Alhrichs type sets, e.g., the double zeta polarized def2SVP [32], often offering greater flexibility and computational efficiency than the Pople sets [10]. Finally, the correlation-consistent basis sets, such as cc-PVDZ, developed by Dunning et. al. [33], are aimed at reproducing the correlation energy of valence electrons. Placing the basis functions on the atomic nuclei efficient, but it does introduce a basis set superposition error – since electron density around one nucleus can be described by the functions belonging to another nucleus, the strength of the bond between them can be overestimated, and the molecular energy artificially lower, especially in the case of van der Waals interactions. This can be dealt with by drastically increasing the size of the basis set, or the so-called CounterPoise correction [10].

2.5 Prediction of Organic Molecular Structures

Once a desired functional/basis set combination has been selected, a set of orbitals that minimize the molecular energy is found by the iterative SCF procedure.

A proton is around 1836 times heavier than an electron. Therefore, each nucleus is several orders of magnitude heavier than an electron, and much slower moving. Born and Oppenheimer [2, 34] have proposed to split the wavefunction into parts describing the state of nuclei and electrons, denoted ψ_{n} and ψ_{el}, respectively. The function ψ_{el} is expected to be the solution of the Schrödinger equation in a system with stationary nuclei:

$$\left(\hat{T}_{\mathrm{el}} + \hat{V}_{\mathrm{nu-el}} + \hat{V}_{\mathrm{el-el}}\right)\psi_{\mathrm{el}} = E_{\mathrm{el}} \cdot \psi_{\mathrm{el}}. \tag{20}$$

After accounting for the mutual repulsion of nuclei, which is not a part of the electronic Hamiltonian (14), the result is a molecular energy E_{PES}, parametrically dependent on the configuration of nuclei in the system. This relationship between the energy of a molecule and its geometry is called the Potential Energy Surface (PES). The PES may be used to find transition states and equilibrium geometries. Graphically, the PES can be represented for two- or three-atom molecules as the function of bond lengths and bond angles. For larger molecules, more than three orthogonal axes would be required for a complete visualisation, and therefore the PES cannot be represented in a 3D space [1, 3]. Instead, a slice of the graph at certain points of interest. Some examples of the PES for ethane (C_2H_6) are shown in **Fig. 1**. In **Fig. 1a**, the dihedral angle (see inset of **Fig. 1b**) and the C–H bond lengths are expected to be constant at 60 ° and 1.114 Å, respectively. In **Fig. 1b**, all bond lengths are expected to be constant (1.519 Å for C–C), and the dihedral angle is varied.

Although the PES is often not explicitly shown in scientific papers, it is an essential concept in computational chemistry. Points on the PES curves in **Fig. 1**. correspond to single configurations of the molecule. The points with the lowest energy represent stable configurations. Mathematically, the surface can be defined as a function of generalized coordinates q_1, q_2 …, q_{n}:

$$E = f(q_1, q_2, \ldots, q_{\mathrm{n}}), \tag{21}$$

where q_1, q_2, …, q_{n} correspond to the individual bond lengths and angles. If the bond length R corresponds to q_1, and the dihedral angle to q_2, then the minimum in Fig. 1a corresponds to the equilibrium value of q_1 and is described by the equation $\mathrm{d}E / \mathrm{d}q_1 = 0$. Similarly, the minimum in **Fig. 1b** is the equilibrium of q_2, described by $\mathrm{d}E / \mathrm{d}q_2 = 0$. Generally, stationary points, which describe either stable structures or transition structures, are defined as points on the geometry, where:

$$\frac{\partial E}{\partial q_1} = \frac{\partial E}{\partial q_2} = \cdots = \frac{\partial E}{\partial q_{\mathrm{n}}} = 0. \tag{22}$$

Stationary points, corresponding to stable molecules are energy minima, transition structures are saddle points. The lowest-energy pathway between two energy minima is called a reaction coordinate. A saddle point is a maximum with respect to the reaction coordinate, but it is a minimum with respect to other directions on the PES [2, 34].

It should be noted, that even at the absolute zero temperature, *i.e.*, 0 K, the molecule still vibrates. Therefore, the molecule still has some energy at 0 K. This is called the Zero Point Energy (ZPE). For accurate computations, the ZPE should be added to the electronic and nuclear repulsion energies of the computed molecules. However, the ZPEs of reactants and products are usually very similar and tend to cancel out when calculating reaction energy [9].

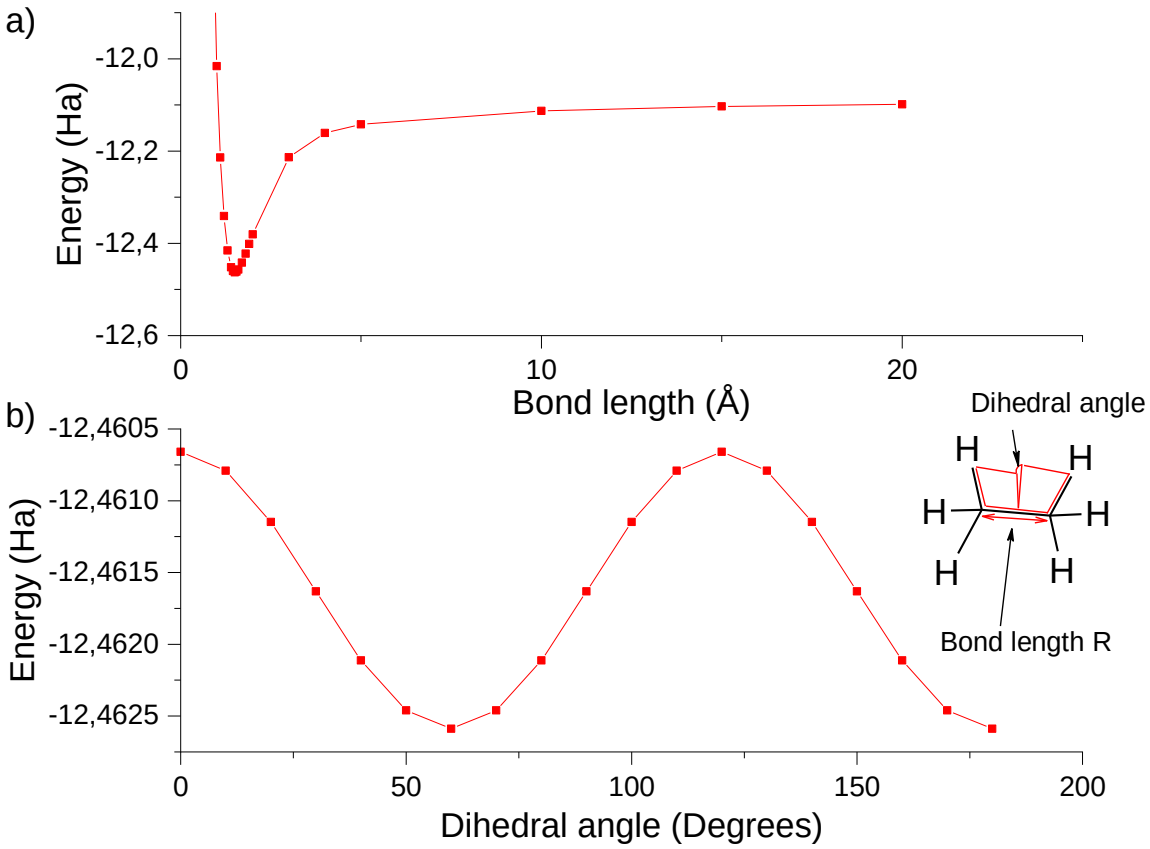

Fig. 1. *Slices of the PES for ethylene; a) Effect of the C–C bond length change on the potential energy of the molecule; b) Effect of the dihedral angle on the energy; inset: illustration of the dihedral angle and bond length on the molecule*

Predicting the structure of single molecules is a matter of constructing the PES and searching for local and global minima, by the methods described in chapter 2.1. Extensive literature already exists on the topic of the performance of different methods and possible errors [2, 10]. The process is generally known as geometry optimization and utilizes an algorithm that systematically alters the specified molecule until an energy minimum is found.

An issue with this approach is, that the geometry found by the algorithm might not be a global energetic minimum. Ethane can exist in two conformations with respect to the dihedral angle – staggered and eclipsed. The staggered conformation, at angles of 60 °, 180 ° and 300 ° degrees is the global minimum, and the most stable (see **Fig. 1**). The molecule can still exist in the eclipsed conformation, and if the input geometry specified by the user has a dihedral angle of around 120 °, *i.e.*, it is closer to the eclipsed conformation, that one may be marked as optimal, despite being only a local energy minimum on the PES. Of course, it is actually a maximum with respect to the dihedral angle variation, but a local minimum for the C–C and C–H bond lengths. This situation is illustrated in **Fig. 2**. Therefore, it is necessary to be careful while setting the input geometry and checking the output [2, 9, 10].

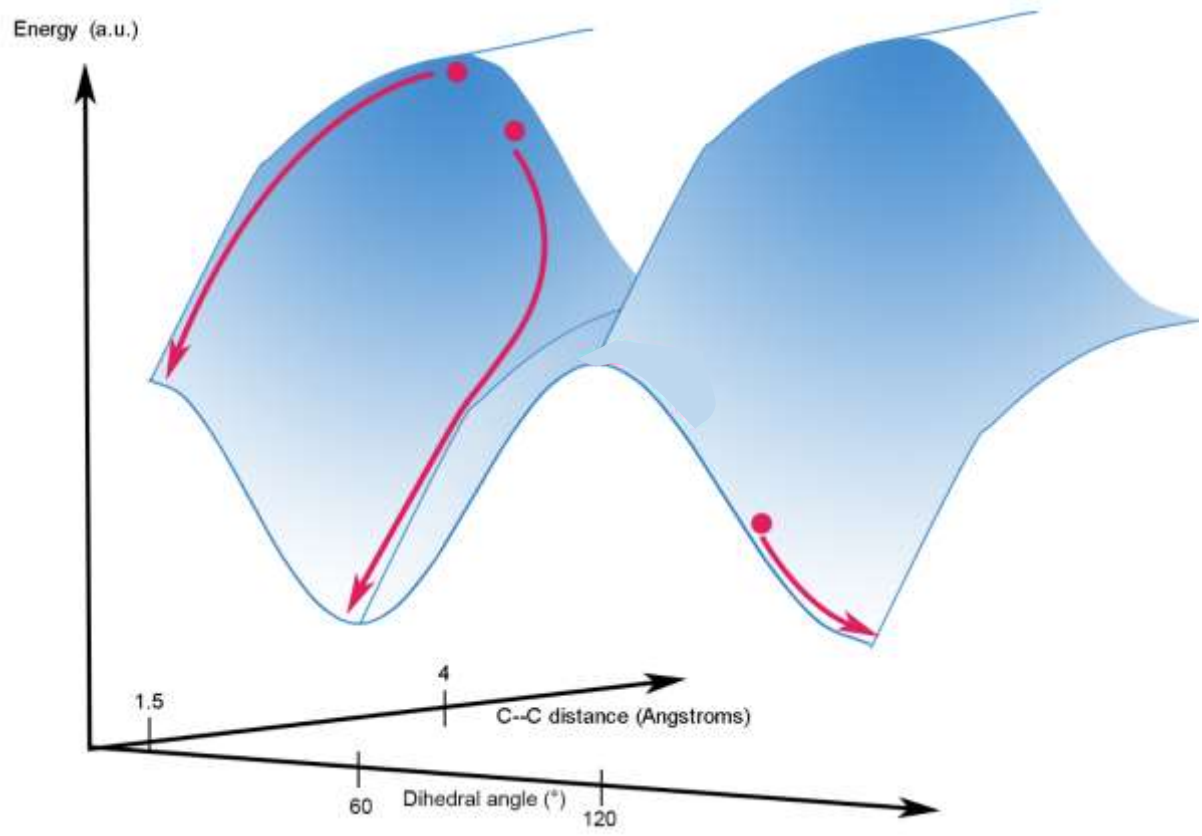

***Fig. 2**. A part of the PES of ethane, dependent on the dihedral angle and C—C bond length. The energy axis is in arbitrary units (a.u.), not to be confused with atomic units, and not to scale, since energy changes with bond length are an order of magnitude larger than with the dihedral angle. The darker areas denote higher energy. The dots and arrows denote possible input configurations by the user, and which stationary point will be assigned to them as an optimal geometry by the algorithm.*

Modern algorithms typically utilize the second derivative in addition to equation (22) since it allows the user to identify minima reliably [35]. Some sort of approximation of the PES is typically also used, which may be a simple parabola in the case of a diatomic molecule or a considerably more complicated function for a multi-dimensional PES. Geometry optimization algorithms are still a subject of research [2, 10, 36]. On the other hand, Pawłowski et. al. [37]

have proposed to replace the iterative refinement process by fitting geometries to experimental microwave spectra.

To lend some rigour to the qualitative description given above, let us mention, that the general optimization is done iteratively, according to the matrix equation:

$$\mathbf{q}_{\mathrm{O}} = \mathbf{q}_{\mathrm{i}} - \mathbf{H}^{-1}\mathbf{g}_{\mathrm{i}} \tag{23}$$

where $\mathbf{q}_{\mathrm{O}}$ is the vector of optimized molecular coordinates, $\mathbf{q}_{\mathrm{i}}$ is the vector of initial molecular coordinates, **H** is the Hessian, which is a matrix of second-order derivatives of E with respect to molecular coordinates, and $\mathbf{g}_{\mathrm{i}}$, the gradient matrix *i.e.,* a vector of first-order derivatives of E w.r.t. the molecular coordinates.

Since there is a possibility that the algorithm will terminate at other points than the energy minimum, some way of checking whether the result is a minimum or a saddle point is clearly needed. This is done by calculating the normal mode vibrations, *i.e.,* the stretching and bending of chemical bonds where all atoms move in phase with the same frequency, which are the subject of infrared (IR) spectroscopy. Considering two bound atoms A and B, the normal mode wavenumber ν (cm^{-1}), used for the sake of convention, is given by:

$$\nu = \frac{1}{2\pi c_{\mathrm{l}}}\left(\frac{k}{\mu}\right)^{\frac{1}{2}}, \mu = \frac{m_{\mathrm{A}} m_{\mathrm{B}}}{m_{\mathrm{A}} + m_{\mathrm{B}}}, \tag{24}$$

where c_{l} is the velocity of light ($c_{\mathrm{l}} \approx 3 \cdot 10^{8}$ m s^{-1}), k is the vibrational force constant, and μ is the reduced mass [2, 22]. The normal mode vibrations' directions and force constants can be quite easily gained by the diagonalization of the Hessian. It should be noted, that the Hessian used in the geometry calculation is not accurate enough, and a new Hessian must be constructed for the frequency analysis. The calculated frequencies make sense only at a stationary point, and only if the same method is used to both optimize geometry and find the frequencies, *e.g.,* the same functional and basis set. Then, the nature of a stationary point is simple to determine:

For a stable geometry on the PES, all the force constants k are positive. This means that for every vibration of the molecule, there is always a restoring force, which brings it to the equilibrium, *i.e.,* the molecule undergoes periodic vibrations. On the other hand, a transition geometry has a negative force constant for one of the vibrations, and therefore an imaginary frequency. The physical interpretation of this fact is, that there is one vibration, for which there is no restoring force – this movement of the atoms leads to a more stable arrangement, and it is not periodic. This rearrangement corresponds to movement along the reaction coordinate [2, 10]. Of course, the actual output geometry should also be visually checked. As was aptly remarked by Lewars [2]: "It should look right."

To predict the macromolecular structure of molecules such as peptides, DNA or polymers, molecular mechanics and semiempirical methods are typically used, as *ab initio* and DFT methods require too much time and computational power at this scale [2, 3].

Furthermore, subjects such as enzyme-substrate bonding or crystalline structure are a subject of great interest. These can be treated by DFT methods, provided that the scale is not too large, *e.g.*, only the immediate binding site of a protein or a single crystallographic cell is considered. There exists copious literature about biomolecule binding, such as the work of Fox et. al. [24]. In the case of crystal structure, there is an emerging field of crystallographic computing, which includes topics such as the treatment of X-Ray spectra, analysis of electron density, and of course the calculations of intermolecular forces with *ab initio* and DFT techniques. Such a procedure generally consists of calculating candidate structures with their cohesive energies. For a further introduction to this field, the reader is referred to the work of Gavezzotti [38].

Aromaticity is a key concept when describing cyclic organic compounds, especially heterocycles. Aromatic compounds are cycles with a conjugated system of π bonds, and 4N + 2 π electrons, where N is a natural number. They are characterized by the ability to sustain a diamagnetic ring current, and many unique substitution reactions. The first measure of aromaticity was the resonance energy. For instance, benzene has a theoretical hydrogenation enthalpy of around 360 kJ mol^{-1}, *i.e.*, three times the value for cyclohexene. However, the experimental value is only 210 kJ mol^{-1}. The difference between these two values is called the resonance energy. Many other ways of experimentally determining aromaticity have been developed. For a critical overview, the reader is referred to the work of Katritzky et. al. [39].

A frequently used theory-based measure of aromaticity is the Harmonic Oscillator Model of Heterocyclic Electron Delocalization (HOMHED) index. This is a geometry-based index, where the geometry of some cyclic molecule is compared to a standard. The standard should be a fully symmetrical aromatic molecule, such as benzene. Of course, in the case of heterocyclic rings, the standard molecule must be carefully selected to be as similar as possible to the composition of the analysed molecule. To determine the HOMHED index, first, a normalization constant α (Å^{-2}) is determined:

$$\alpha = 2\left\{\left(R_{\mathrm{opt}} - R_{\mathrm{sin}}\right)^2 + \left(R_{\mathrm{opt}} - R_{\mathrm{doub}}\right)^2\right\}^{-1}, \tag{28}$$

where R_{opt} is the bond length in a symmetrical aromatic molecule, R_{sin} is the length of a reference single bond and R_{doub} is the length of a reference double bond. This constant is calculated for every type of bond present in the molecule, *e.g.* C–C, C–N, C–S, C–O etc. Next, the HOMHED index is determined as the sum:

$$HOMHED = 1 - \frac{1}{m}\left\{\alpha_{\mathrm{CC}} \sum\left(R_{\mathrm{opt}}^{\mathrm{CC}} - R_{\mathrm{i}}^{\mathrm{CC}}\right)^2 + \alpha_{\mathrm{CX}} \sum\left(R_{\mathrm{opt}}^{\mathrm{CX}} - R_{\mathrm{i}}^{\mathrm{CX}}\right)^2 + \cdots\right\}, \tag{29}$$

i.e., the difference of the bond length of the analysed molecule *R*i from the optimal bond length of that type. The sum is repeated for all types of bonds in the molecule, and *m* is the total number of bonds [40]. By convention, the highest HOMHED value of 1 is assigned to benzene, as the ideal aromatic molecule.

The reference data can be obtained from single molecules, such as N–$(CH_3)_3$, or from the average bond length of many molecules. Similarly, it is possible to use both a theoretical equilibrium bond length or an experimental value, obtained, for example, from X-ray diffraction. In the case of heterocyclic molecules, the constant α_{CX} is typically larger than α_{CC}. This means that a change in a hetero-bond length will have a greater impact on the HOMHED value than a C–C bond change. In general, a higher aromaticity value is assigned to six-membered rings, than five-membered ones. Heterocycles with nitrogen have HOMHED values closest to benzene, followed by sulphur and oxygenated heterocycles have the smallest values. In the range of 1.0–0.5, the molecule is considered aromatic, while for 0.5–0.0, it is nonaromatic, and if the HOMHED has a negative value, it is antiaromatic. Antiaromatic rings are generally unstable [39]. Of course, this index describes only one aspect of aromaticity – geometry, which is arguably the simplest to understand. Other measures of aromaticity include the magnetic properties of aromatics rings, described by the NICS indices [41, 42]. An older study by Katritzky et. al. [39] suggests, that magnetic-field-based measures are better to predict the aromaticity of five-membered rings, while geometry-based measures, including bond orders, work better on six-membered rings. The authors also remarked that at least three factors are needed to fully describe aromaticity in heterocyclic compounds, due to the differences in the electronic structure of the heteroatom and carbon, and at least two in all-carbon rings.

2.6 Optical and Electrical Properties Prediction

During spectroscopic experiments, time-dependent waves of electromagnetic radiation are shined on a system in a stationary state to see, if the system will transition into a different stationary state. Unfortunately, this requires a treatment using the time-dependent Schrödinger equation. The time-dependent changes can be expressed using perturbation theory. In short, two special cases may be described:

$$\begin{aligned} &\text{absorption:} && E_m - E_n = \mathrm{h}\nu \\ &\text{emission:} && E_n - E_m = \mathrm{h}\nu \end{aligned} \tag{30}$$

That is, if the frequency of incident radiation is equal to the energy difference of the states, divided by h, the radiation will be absorbed by the system, and a transition will occur. On the other hand, if the system is in a higher energetic state, an emission of radiation with frequency ν can occur [3, 8]. The most used techniques, to be discussed in the following paragraphs, are Infra-Red (IR), UV and visible light (UV/VIS) spectroscopy. Nuclear Magnetic Resonance spectroscopy is beyond the scope of this work. An in-depth discussion of the methods may be found in Atkins' textbook [23].

As was already discussed, the vibrational frequencies which correspond to the IR spectrum are calculated as a part of the geometry optimization procedure. It should be noted that a spectrum gained by computation cannot be expected to perfectly match an experimental spectrum. This is generally true for any spectroscopic method, and is the result of interactions between different molecules, between molecules and solvents, and other problems, specific to each type of

spectrum, such as interactions between normal mode vibrations in the case of IR. The values often need to be shifted or multiplied by a constant to match the experiment [2, 22].

Deviations from experimental value are mostly caused by the interactions of the analysed molecule and solvent (*e.g.*, dimethyl sulfoxide − DMSO). To deal with this, either the dielectric properties of a bulk solvent may be studied in a so-called continuum model, or several molecules of the solvent may be explicitly added to the analysed molecule during computation – this is the specific solute-solvent interaction model.

Another technique of great interest is spectroscopy in the ultraviolet and visible light range (UV/VIS). The electromagnetic radiation in this range has enough energy to change the electronic distribution of molecules. Here, the singlet ground state of the molecule is typically denoted as S_0. When absorbing radiation with the wavelength λ (nm), an electron is excited into a singlet excited state S_n. From here, the electron will eventually relax back to S_0, with the possibility of an intersystem crossing between S_n and a triplet state T_n. During relaxation, the molecule will lose energy either by collision with surrounding molecules or by an energy emission. If this emission falls into the visible light range, it is called fluorescence (from S_n), or phosphorescence (from T_n). Possible transitions are illustrated in **Fig. 3** Note, that not all organic molecules can absorb VIS radiation. Typically, there must be a conjugated system of π bonds [23]. Furthermore, there is an individual PES associated with each singlet and triplet excited state. From a quantum mechanical point of view, intersystem crossings into T_n states, and internal conversions happen at intersections of the S_n excited state PES with the T_n PES and the S_0 ground state PES, respectively. **Figure 3** further shows an illustration of the different potential surfaces. Due to the complex shape of the PES, the intersections usually take the form of a multi-dimensional cone and are therefore known as conical intersections [43].

Understanding the physics of electronic excitation and the ability to predict excitation and emission spectra is of great value in the research of any photoinduced processes. Extensive documentation on UV/VIS spectra calculation by *ab initio*, DFT and semiempirical methods is available. While the reliable prediction of electronic excited states is still an unsolved problem, great success has been made by the development of TDDFT since the Kohn-Sham orbital energy differences have been found to be an excellent approximation for excitation energies, and as shown by Runge and Gross [12], the TD wavefunction can be determined, up to an arbitrary phase factor, by the initial wavefunction ψ_0, and charge density ρ ($\boldsymbol{r}$, t). Excitation energies can be determined as shown by Casida [44] and simplified by Tamm and Dancoff [45]. As an additional refinement, if not always necessary, Ghosh and Dara [46] have expanded the TDDFT method to treat magnetic field effects.

With this technique, it is possible to calculate properties such as excited-state equilibrium geometries, and dipole moments, using first-order perturbation theory [43]. On the other hand, the TDDFT is known to fail in the case of large conjugated π-systems, such as fused aromatic compounds, charge transfer or multiple-electron excitations [22]. The inaccuracy of predicting charge transfer excitation can be mitigated by using range-separated hybrid functionals [43].

When a fluorescence spectrum is to be predicted, the same TDDFT method can be used, and the excited state of the molecule is used as input, instead of the ground state. It is also possible to treat more complicated photochemical processes than simple fluorescence, as described for example in a review by Casida [47].

Finally, once the energy of a light emission has been computationally determined, the lifetime τ (ns) of the spontaneous emission can be approximated by:

$$\tau = \frac{c^3}{2E_{fl}^2 f} \tag{31}$$

Where c is the speed of light in atomic units, E_{fl} is the fluorescence energy in electronvolts (eV), and f is the computed oscillator strength [48].

Furthermore, optical properties are closely related to charge transport in the molecular structures. For example, the i-th ionization potential (IP) – the energy needed to remove an electron from the i-th MO into the vacuum can be approximated as the negative energy of that Hartree-Fock orbital according to the Koopmans' theorem, i.e.:

$$IP = -\varepsilon_i = E(\mathrm{X}^+) - E(\mathrm{X}), \tag{32}$$

Where $E(\mathrm{X}^+)$ is the electronic energy of a cation of some molecule X, and $E(\mathrm{X})$ is the neutral-form energy of that molecule. Similarly, the electron affinity (EA) – the energy released when a free electron is attracted into an unoccupied orbital is roughly equal to the energy of the given orbital, LUMO or higher. These are referred to as the vertical IP and EA, respectively [48]. While the values of vertical IP typically have a fairly good experimental agreement with for ionizations from the HOMO, vertical EAs provide only a rough approximation [48]. For a more accurate look, the adiabatic energies should be considered, where the ion form of the molecule is stabilized first including the ZPE correction, and the IP or EA is calculated [49]:

$$\begin{aligned} IP &= E^{opt}(X^+) - E^{opt}(X) \\ EA &= E^{opt}(X) - E^{opt}(X^-) \end{aligned}. \tag{33}$$

Using modern *ab initio* methods, the ionization potentials can be determined with a precision on the order of 0.009 eV, unfortunately, this is restricted to small molecules such as H_2O due to the theoretical complexity and basis set size (up to octuple zeta) involved [50].

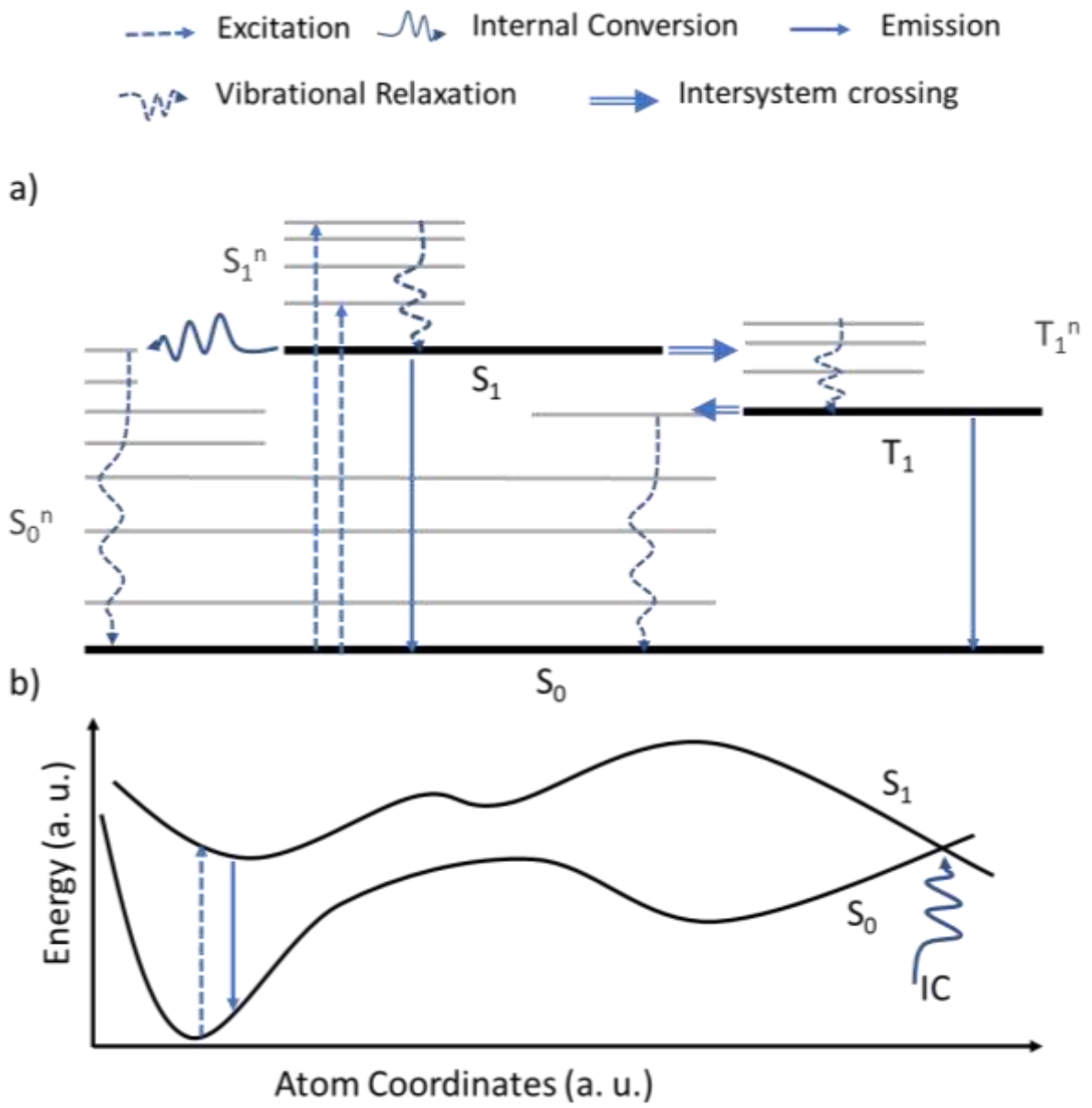

Fig. 3*. a) Simplified Jablonski diagram, illustrating electron excitations and relaxation. Vibrational energy levels are denoted by the superscript n; b) A schematic illustration of the excitation, emission, and internal conversion processes on the molecular PES. Internal conversion is denoted by IC, as opposed to intersystem crossing (ISC)*

Further, the FMO energy levels are important for the operation of devices such as solar cells, transistors, or OLEDs. Generally, at the junction of the organic material and some inorganic electrode, the alignment of HOMO, LUMO and the Fermi energy level of the electrode E_F decides the nature of the charge transport. If the E_F of the electrode is lower than the HOMO of the organic, electrons contained in the organic material will tend to transport into the electrode, until the charges are equalized. Similarly, if the electrode E_F is higher than the organic LUMO, electrons will tend to transport from the electrode into the organic. If the E_F lies between HOMO and LUMO, no spontaneous charge transfer is expected to happen, although it can be stimulated

by adding an external bias to the electrode. For a detailed review of the nature of organic/inorganic interfaces, the reader is referred to the exhaustive review by Otero [51].

In solar cells and OLEDs, an interface between a p-semiconducting material and n-semiconducting material has a similar importance. Here the LUMO orbital of the n-semiconductor must be aligned higher than the HOMO of the p-semiconductor, so that the electron and hole from external electrodes can recombine to produce a light emission in an OLED, or that the exciton created by the light absorption of a solar cell can be split, and the electron and hole can be transported into the circuit by the respective conducting materials [48].

As a curiosity, Pearson [52] has defined the electronegativity of the molecule – the ability to attract electrons to itself – as the average of the HOMO and LUMO energies, and chemical hardness as one-half of the difference IP – EA. These quantities can be used e.g., in the prediction of reactivity in double bond containing monomers [53]. Further, some correlations between the physical hardness of a material and the chemical hardness of the constituent molecules have been mentioned in the literature [54], ultimately unsuccessful due to varying conditions of measurements in impact tests.

Thus, FMO energy levels are important from the thermodynamic point of view, while the rate of transfer can be described with the reorganisation energy E_R, given by the Marcus theory, see e.g., the work of Bredas et. al. [55] or Purushotham et. al [56]. Here, the intramolecular reorganisation energy is given by:

$$E_R = E^0\left(X^{+/-}\right) - E^0(X) + E^{+/-}(X) - E^{+/-}\left(X^{+/-}\right), \tag{34}$$

where $E^0(X^{+/-})$ is the energy of the ionized form of X in the neutral state geometry, $E^{+/-}(X)$ is the energy of the neutral form of X in the ionized state geometry etc. An illustration of the E_R in relation to the PESs of the neutral molecules and ions is shown in **Fig. 4**.

It is important to study the changes in structure since charge transport in organic molecules and polymers is connected to distortions in the geometry. Indeed, the electric charge is transported by carriers delocalized across multiple conjugated π-bonds, referred to as polarons or bipolarons for single and double charges, respectively [48, 57]. For further reference, see the book of Blythe and Bloor [58]. As shown above, reorganisation energy is effectively the measure of structural changes in a molecule when receiving an electric charge. Thus, normally, the lower the E_R, the faster the charge transport. There is also an outer component to this energy, due to the polarization of the surrounding medium. It is on the same order of magnitude as internal E_R and depends on the charge and geometry of the molecules in question, see [55].

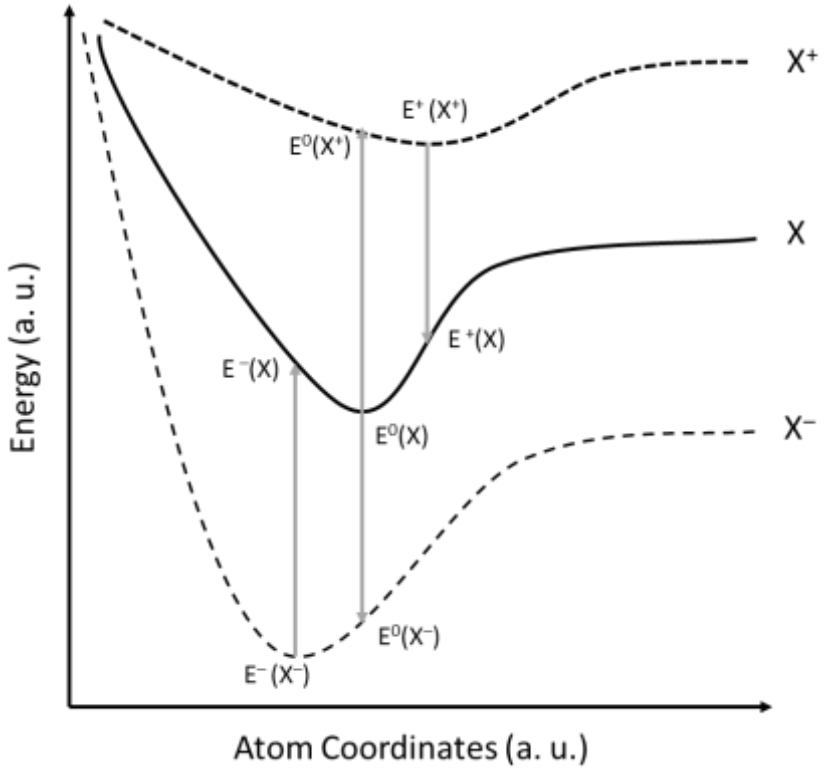

Fig. 4 *The PESs of a neutral state, anion, and cation of some molecule X. The points that are used for the calculation of E_R have been marked [55, 56]. Note that The E_R is essentially a sum of the vertical ionization and de-ionization potentials.*

2.7 Extrapolation to Solids

Since it is generally not possible to model polymer chains of realistic length *via* DFT, the results must be somehow extrapolated, or used indirectly, possibly to fine-tune the monomer equilibrium geometries and the force field response in a molecular dynamics simulation. Quite often, a DFT-stabilized monomer is represented by a single sphere, and the MD computation is carried out on the spheres, instead of individual atoms. This approach is referred to as coarse-graining (CG) [59] and will be briefly mentioned in connection to some polythiophene studies.

The other option is to extrapolate results towards some limit, where the behaviour of the modelled oligomeric chain will match that of the polymer. The studied property, usually the HOMO/LUMO gap, or excitation energy, is taken as a function of the reciprocal of the number of monomers in the polymer backbone $1/N_m$, or the number of conjugated double bonds in the backbone $1/N_b$ [60]. The latter approach allows for comparing chains with different-sized monomers, e.g., polythiophenes (PTs) and fused polythiophenes. Clearly, as the oligomer grows, both $1/N_m$ and $1/N_b$ will approach zero. Therefore, if the relationship of the HOMO/LUMO gap with one of the reciprocals can be fitted with an appropriate function, the value as the reciprocal approaches zero will correspond to the polymer HOMO/LUMO gap or other desired quantity.

The simplest possible fit is, of course, a linear function. However, the linear fit often fails to predict the behaviour of polymers, especially in the case of polythiophenes, where the relation of excitation energy to polymer length saturates for long oligomers [61]. In the case of the HOMO/LUMO gap, a two-parameter model described by Kuhn [62] has proven quite efficient, as demonstrated e.g. by Wykes [63] and Gierschner [61]:

$$E_{Nb} = E_1\sqrt{1 - D_k\cos\left(\frac{\pi}{N_b+1}\right)}, \tag{51}$$

where E_{Nb} is the electronic excitation energy of a chain with N_b double bonds, E_1 is the energy of a single double bond, and D_k is a relative force constant, measuring the coupling of single and double bonds. As Wykes and co-workers [63] have found, in the case of PT, E_1 = 7.7 eV, D_k = 0.89. Further, the effective conjugation length (ECL) is defined as the length of an oligomer chain with the absorption wavelength within 1 nm of the infinitely long polymer [64]. On the other hand, Gierschner et. al. [61] have defined the maximum conductive chain length N_{MCC} as the intersection of the linear fit of excitation energies vs. $1/N_b$ and the horizontal line drawn from the polymer limit in the E vs $1/N_b$ plot. That is, as the number of C=C bonds in the backbone, at which a linear fit will reach the excitation energy of the polymer limit. This measure is less dependent on the nature of the polymer backbone and substitutions, making it easier to draw comparisons. A typical value of N_{MCC} is around 20 [61].

3 RESEARCH RELATED TO THE STUDIED MATERIALS

Optoelectronics is a quickly growing field, featuring such devices as light-emitting diodes and solar cells. There are many reasons to be interested in optoelectronics, especially considering present-day energetics concerns. To meet the goals of replacing non-renewable energy sources, new and cheaper functional materials will need to be developed, which should be less of a burden on the environment than the continued operation of conventional power plants. Such materials need to be developed with care for the manufacture, subsequent device fabrication and waste disposal.

To ensure easy and cheap handling, it is possible to develop materials that can be applied from solution, by techniques such as spin coating. The material should ideally form structures that need no additional treatment like heating or drying, although that is difficult to ensure. In this regard, materials soluble in water and other cheap non-toxic solvents such as ethanol should have high importance. Further, for the correct function of optoelectronic materials, their spectroscopic properties and conductivity are the key properties. It can be especially advantageous to absorb visible light in the 500–600 nm wavelength range since sunlight has the highest spectral irradiance here [65].

Finally, taking inspiration from nature can aid the design of new molecules, which can then be created to be bio-degradable or inert and thus eliminate any environmental risks. Such molecules could also find use in biology and medicine, serving as markers and biosensors.

In this work, two distinct types of molecules will be studied, based on the relevant research projects. First, the bioactive Flavin (Alloxazine) family of molecules, which are comparatively simple to incorporate into bio-systems, and efficiently absorb visible light, making them prime candidates for use in such fields as bio-imaging or catalysis. Then, polythiophene-type molecules will be considered. These polymers have gained great attention in the past for their electric conductivity. Here, several types of novel substitutions are introduced, such as adamantylated side chains.

3.1 Alloxazine Chemistry

Alloxazines, commonly also known as flavins, are naturally-occurring derivatives of the tri-cyclic benzo[g]pteridine-2,4-dione, which is itself based on the parent molecule lumazine (see **Fig. 4**), although lumazine itself typically is not considered to be a part of this family, instead being classified as a pteridine derivative [66, 67]. At the present time, 5-deazaalloxazines are also included in the flavin definition, however, these compounds are closer in behaviour to nicotinamides than flavin analogues [67].

To avoid further confusion, a unified naming convention shall be adopted in this work, with names assigned to the molecules shown in appropriate figures, along with any trivial names. The names used in this work shall be printed in a bold typeface.

Alloxazine-type molecules have long been known as efficient chromophores [68, 69], especially due to the tremendous amount of work done by the group of Sikorski et. al. [69, 70]. Presently, these molecules are considered for use in bioorganic sensing and optoelectronics. Their application in this field is advantageous, because of the great tunability of their spectroscopic properties, and the ability to be incorporated into DNA [1, 71, 72, 73]. As shown in **Fig. 4**, one of the possible synthetic pathways utilizes the molecule alloxan [74], which is likely the origin of the name Alloxazine. Lumazine is a part of the metabolic pathways of flavins, such as the biosynthesis of riboflavin [75]. Due to the structural similarity, the possibilities for the application of lumazine are almost the same as for **AL**, although no direct comparative study has been performed to the author's knowledge.

Furthermore, these molecules undergo isomerisation, which amounts to the transfer of a proton from N(1) to N(10), see **Fig. 4** [76]. This leads to a noticeable red shift of about 50-100 nm [73] in the absorption and fluorescence spectrum. In an aqueous environment, the concentration of the isomers depends on pH – at pH = 4, pure **AL** is present. At pH = 10, the solution is expected to have around 9 % of **iAL** [74]. The isomerisation mechanism is well documented for protic solvents, where the group of Mal [76] has brought an adequate explanation. In aprotic solvents, this process is not expected to happen [76], though absorption peaks, which could correspond to **iAL**, have been found in the dimethyl sulfoxide (DMSO) solvent [74]. Whether the **iAL** form could be present due to trace amounts of water in the DMSO, or if there is a different, aprotic, isomerisation mechanism is still up to discussion, although a water-facilitated mechanism is generally considered in the literature [77, 78].

In the case of lumazine, the same basic isomerization is reported as in alloxazine, although the red shift is often ascribed to an N(1) or N(3) deprotonated form, present in neutral and basic solutions [79, 80, 81], while there is expected to be a minority population of the **iLum** form [82]. Interestingly, studies of **AL** are focused on the N(1)–N(10) tautomers, while studies of **Lum** mostly consider ion forms. Recently, Wörner et. al. [83] have explored the structure of 6,7,8-trimethyl**Lum** under illumination, and have confirmed the presence of an ionic form, while no such study supports the photo-induced deprotonation of **AL**.

The isoAlloxazine form exhibits significantly larger fluorescence quantum yields, and longer lifetimes [76]. Penzkofer et. al. [84] have proposed a water-assisted tautomerization mechanism. Prukala et. al. [85] have systematically studied the pH dependence of lumichrome (**Lch**) (see **Fig. 5**). This was achieved by blocking certain N atoms by methyl groups. These substitutions, illustrated in **Fig. 5**, are designed to disable the tautomerization, thus making it possible to measure the spectra of individual isomers regardless of conditions in the solution. Indeed, the **1-MeLch** spectra in all pH environments are much more similar than **Lch** spectra, especially in an alkaline environment, where the **iLch** form would exist.

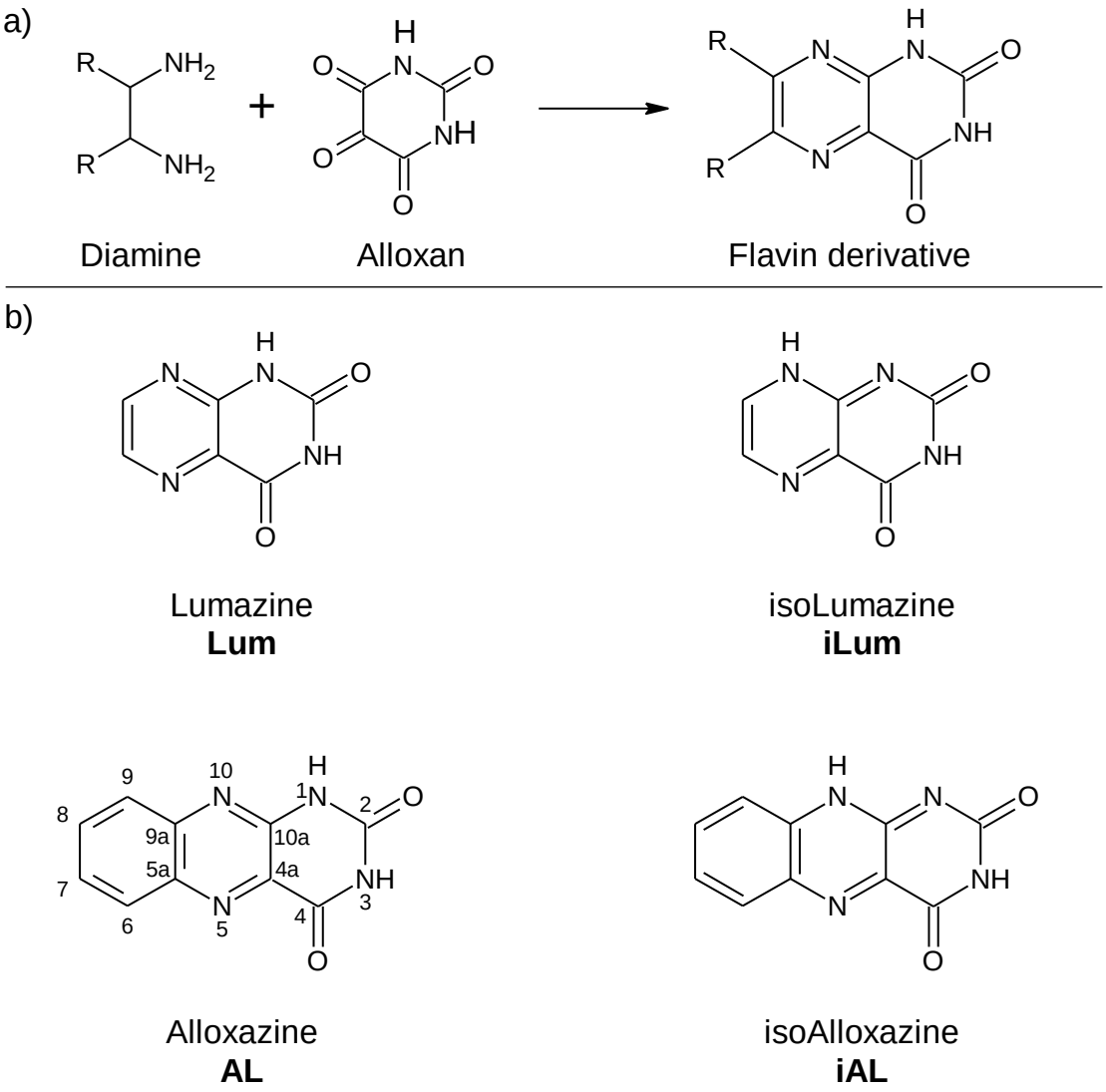

Fig. 4 *a) The synthetic pathway utilizing the alloxan molecule, where R stands for an arbitrary organic moiety; b) The basic structures of lumazine and alloxazine, and their isomers.*

It, therefore, comes as no surprise, that the use of Flavins as fluorescent dyes has been proposed, *e.g.*, by Navarro et. al. [86], who have prepared a rather unusual class of molecules, i.e. two Lum cores, fused together via an ether bridge at the C(6) atoms. The fluorescence spectra of these molecules showed a remarkable linear dependence on the pH level.

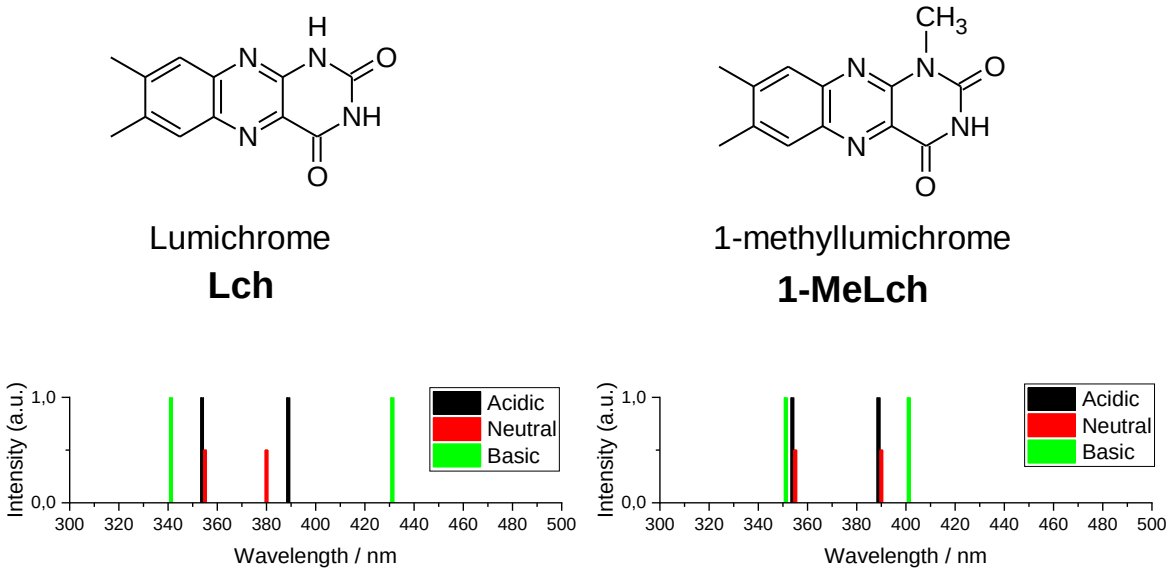

Fig. 5 *The structures of lumichrome and 1-methyllumichrome; essentially alloxazine with two methyl (CH_3) substituents. A sketch of the spectra, measured in [85], is under the molecules, with the visible pH dependence. The neutral-pH absorption peaks have been lowered for greater visibility in the highly overlapping spectrum and should not be interpreted as having a lower intensity than the acidic-pH peaks.*

Logically, this isomerization behaviour is generally only observable in protic solvents, where there is a stable H^+ concentration to be described with pH. However, Richtar et. al. [74] have observed some **iAL** peaks in the aprotic DMSO solvent, as mentioned earlier. Choudhury et. al. [87] have pointed out a red shift in solvents that consist of acetonitrile (ACN) and water, and dimethylformamide and water mixtures, the absorption spectrum consistently shifts into higher wavelengths, and an isoalloxazinic peak appears in the emission spectrum. They have theorized, that this behaviour could be used to monitor the local solvent concentration in the space around the Flavin molecule, similarly to how Gharat et. al. [88] have used changes in emission behaviour of carbon dots to elucidate their structure. Indeed, since then, the role of the pteridine moiety in tyrosine-kinase inhibitance has been successfully described by Khattab et. al. [89], using fluorescence spectroscopy in an ACN–H_2O mixture of varying concentration.

Furthermore, flavins take part in many biochemical redox reactions, where they serve as electron-transfer mediators and cofactors in flavoproteins and nucleotides [67, 90]. The redox mechanism of a simple **iAL** molecule is shown in **Fig. 6**. Due to this well-documented redox behaviour, flavin-type molecules have been considered for use in energy storage. In this regard, some early work has been done by Lee et. al. [91, 92], who proposed the use of riboflavin (see **Fig. 6**) in a reaction pathway analogous to the natural process in mitochondria, with Li^+ ions used for charge exchange with a Li counter electrode. The reversible riboflavin/Li redox system exhibited an energy density of around 106 mAh g^{-1}. Furthermore, they have found out, that the stability of the system may be enhanced by substituting methyl groups into positions C(7) and C(8), and that the redox potential may be elevated by the addition of Cl atoms into these

positions. The DFT calculations carried out by Lee and co-workers have indicated the insertion of Li between the N(1) or N(5) and adjacent oxygen atoms.

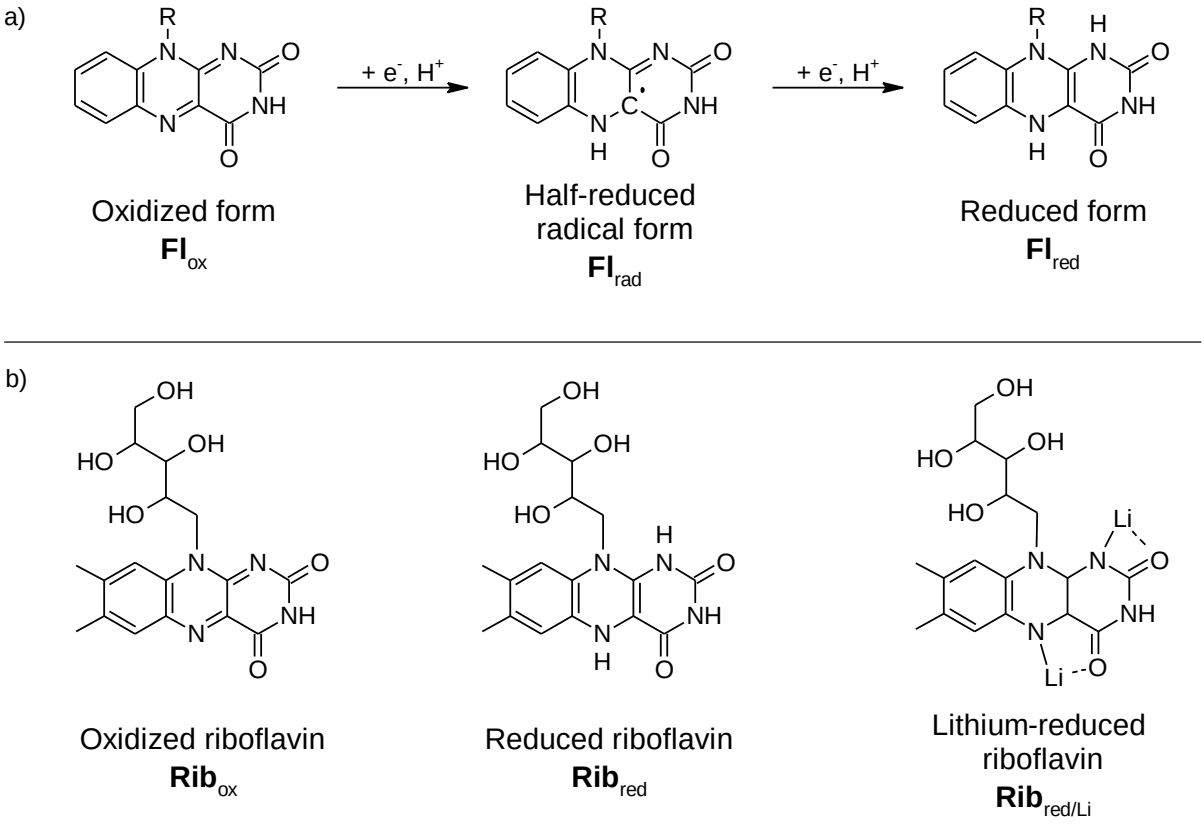

Fig 6 *a) The natural flavin reduction pathway, occurring e.g., in mitochondria; b) The riboflavin molecule in its oxidized, reduced and Li-reduced state, as proposed by Lee et. al.[60]*

Recently, the possible role of Flavins in medical fluorescence imaging has been highlighted by Golczak [93], who has used the **AL** molecule with an additional fused benzene ring for an in vitro study of human red blood cells with fluorescence lifetime imaging microscopy. The use of substituted Flavins as photosensitizers may also have a biological significance in the context of photoantimicrobial therapy, where *e.g.*, riboflavin has been proven to be able to convert oxygen from the triplet state into singlet, which then kills bacteria due to its strong oxidative properties [94]. However, even non-biological oxidations can be considered, e.g. the preparation of sulfoxides from sulphides via an Alloxazine molecule, amidated at the N(3) position, as shown by Guo et. al. [95]. In the past, attempts to fabricate transistors have been made [96], but without much feedback from the scientific community. Lumazine and pterin derivatives have been extensively studied as photosensitisers with a similar potential use for **AL** derivatives [97, 98, 99]. Since they bind to cell membranes more easily, they are naturally more attractive for photoantimicrobial therapy [97]. In general, lumazines have been the object of intensive research and use in pharmacology [100].

Catalysis and photocatalysis, already briefly mentioned before, is one of the most promising fields for Flavins. In this context, much work has been done by the group of Professor Cibulka [101]. This body of work includes the use of flavinium salts (see **Fig. 7**) for the oxidative splitting of cyclobutadiene molecules. Due to the positive charge on the salt, it is strong to work in the ground state, without electronic excitation. Thus, they are commonly used for oxygenation reactions [95, 102, 103]. Another possibility is the use of riboflavin, with an acetylated ribityl chain to form amides from aldehydes and secondary amines [104].

Flavinium salt Bridged flavinium salt

Fig. 7 *The structure of flavinium salts*

Electrochemically, the reduction of alloxazines is accompanied by the formation of an anion on the C(4)=O oxygen, and further a protonation of N(5) and N(10) [105]. As found by Mondal *et. al.* [106], the protonated forms of **AL** exhibit a blue shift of around 100 nm, while the radical forms show no shift in the electronic spectra for the radical form in **Fig. 6**, and a red shift for the double-protonated radical form. However, since studies do not agree on the exact positions of unpaired electrons in radical ion forms, possibility for comparison is limited. A reversible hydroxylation of the C(4a) position was also observed [67]. According to an electrochemical study of lumazine [107], reversible oxygenation is possible in the C(6) position in neutral and basic solutions, preceded by a protonation of the N(5) and N(8) positions, thus completely removing the aromaticity of the molecule.

From the computational point of view, some groundwork was laid by Salzmann and Sikorska [108, 109, 110]. They have investigated the electronic excited states both in a vacuum and in an implicit and explicit water solvent. They have found, that to fully account for the solvatochromism of the two absorption peaks of **AL** and **Lch**, a combination of implicit and explicit models is needed, requiring 4-6 H_2O molecules to fully account for solvation in water.

Kabir et. al. [111] have expanded upon the work of Salzmann, by systematically studying hydrogen bonding on the flavin moiety. In their extensive study, they have created a surface consisting of spheres with a radius of 3.4 Å on each atom. Then, they systematically placed water molecules on this surface and carried out over 100 optimizations with different configurations. Their work resulted in dividing the molecule into a hydrophilic part, consisting of the heterocyclic rings, and a hydrophobic part, consisting of the benzene ring. There are predicted to be around twice as many water molecules located around the hydrophilic part, versus the hydrophobic part. However, both the studies of Kabir and Salzmann [111, 108] focus

only on the parent **AL** and the extremely simple derivative **Lch**, without even considering the isomerization. This leaves them open to the question, how does their model account for other derivatives, and whether such complexity is truly needed. Indeed, in the case of IR spectra in [111], it is not possible to state that the implicit-explicit combination fits the experiment better than the implicit model alone. Similarly, the experiments with ACN in [108], with predictions carried out only using implicit solvent, are in comparable agreement with the complex six-molecule water solvation.

Chang et. al [112] carried out an extensive computational study of the singlet and triplet excited states, with the aim of explaining the much weaker fluorescence quantum yield of **AL** as opposed to **iAL**. Indeed, the rate constant of nonradiative decay is predicted to be at least an order of magnitude higher than the fluorescence rate constant [113]. They have used a large quantum mechanics/molecular mechanics (QM/MM) model containing hundreds of water molecules. This study resulted in the description of the intersystem crossing mechanism, either directly from the singlet excited state $^1\pi\pi^*$ into $^3\pi\pi^*$, or by a relaxation from $^1\pi\pi^*$ to $^1n\pi^*$, and a crossing after that. Finally, an ISC is possible from $^1\pi\pi^*$ to $^3n\pi^*$, followed by relaxation to $^3\pi\pi^*$. The band structure of **iAL** is similar to its isomer, albeit with lower rates of radiationless relaxation, which results in a higher fluorescence quantum yield [114, 115, 116].

By investigating Alloxazine-water complexes, Mal et. al. [117] have concluded, that the tautomerization is linked to the motion of the assisting H_2O molecule, and to a large extent driven by the solvation dynamics of water. Therefore, it can be expected to occur on the time scale of 100 fs. Furthermore, they found that the majority of the proton transfers occurs in the excited state, due to a significantly lower energetic barrier, which was already observed by Penzkofer [118] as phototautomerism. Their theory is further supported by the fact that when acetic acid (AcOH) is added to the water, thus altering the local solvent structure, and forming **Fl**-AcOH complexes, the tautomerism slows down by several orders of magnitude [117]. And the behaviour in different pH levels is caused by specific H-bonding interactions, rather than the acidity of the N(1) hydrogen. This observation could lead to a general description of Flavin isomerization, independent of the solvent.

Guo et. al. [113] have recently published a detailed study of flavins methylated and acetylated in positions N(1) and N(3), which were expected to increase the rate of intersystem crossing into triplet states, important for the generation of singlet oxygen in photosensitization. They have concluded, that nonradiative decay is preferred to phosphorescent as well as fluorescent emission. This is due to the coupling of normal mode vibrations of the **AL** moiety with various substituent functional groups. However, the population of molecules in the T_1 triplet state can be increased by perturbing the **AL** framework e.g. by substituting an acetyl or methyl group to the N(1) position, which also decreases the reorganisation energy associated with the excitation. On the other hand, the same substitution in the N(3) position has the opposite effect, strengthening the vibrational coupling, substantially increasing the reorganisation energy and benefiting nonradiative decay.

North et. al. [119] have concerned themselves with simple asymmetrical substitutions in the C(7) and C(8) positions, i.e., using different substituents on C(7) and C(8) in every molecule. They have predicted that electron-donating substituents, such as $–CH_3$, lead to a more even distribution of the HOMO orbital and a substantial bend along the imaginary axis formed by N(5) and N(10), which correlates with their Mulliken atomic charges. Electron-withdrawing substituents, e.g., –CN have the exact opposite effect, resulting in a planar molecule and frontier MOs localized on individual atoms. Furthermore, electrochemical processes are predicted to be thermodynamically favoured in the latter group, having a higher negative Gibbs energy than derivatives with electron-donating substituents, since the molecular bend straightens during redox reactions, which presents an additional energy barrier.

Afaneh et. al. [82] have performed an extensive study of the lumazine structure in neutral conditions. They have considered many possible isomers, including protonated oxygens. By ordering them in terms of relative energy, they have found that the **Lum** form as shown in fig. 4 is the lowest, followed by **iLum**, around 8 kJ mol^{-1} higher. Forms with protons on the C(2)=O and C(4)=O oxygen atoms are around 40 kJ mol^{-1} higher. It follows that a majority presence of **Lum** can be expected in pH-neutral water or aprotic solvents, along with a smaller population of **iLum** or an anion in water. In acidic environments, the **Lum** form is expected exclusively, with an addition of N(1) and N(3) deprotonated anions in alkaline solutions [82, 79].

Some recently published ways of modifying the **AL** molecule are shown in **Tab. 6**. It is a general overview, since the problems mentioned above, such as the use of different solvents and characterisation techniques, make direct comparison difficult. Furthermore, no detailed studies exist on *e.g.*, the influence of the alkyl substituent length on the molecule's properties. Furthermore, some modifications have very little experimental description, such as the substitution of phenyl to N(10) [120]

***Table 6**. A non-exhaustive overview of strategies for alloxazine modification found in the literature; the results of the modifications are given as compared to the parent molecule.*

Modification		Result	Reference
Extended π-conjugation by fusing aromatic rings to C(7)–C(8) bond		Red shift in electronic spectra, enlarging the hydrophobic part of the molecule, increased thermal stability	[74, 93]
Alkyl chain substitution:	On N(1)	Increased rate of ISC, increased light emission	[113, 121, 120, 122, 109]
	On N(3)	Increased rate of nonradiative decay	
	On N(1), N(3)	Increased solubility in nonpolar solvents	
	On N(10)	Considerable red shift (around 100 nm) in electronic spectra, increased fluorescence intensity and quantum yield, loss of pH dependence in electronic spectra	
Ethyladamantyl substitution on N(1) and N(3)		Increased thermal stability, a slight decrease in molar absorption coefficient, a slight increase in fluorescence intensity	[121]
Electron donating groups on C(7) and C(8)		A slight red shift of electronic spectra, increased redox potential	[74, 119]
Electron withdrawing groups on C(7) and C(8)		A slight blue shift of electronic spectra for strong groups such as –F, decreased redox potentials	[74, 119, 123]
Sulfonation on C(2)		Considerable red shift (around 100 nm), substantially increased rate of ISC and triplet quantum yield	[122]
Heterocyclic substitution to C(7) and C(8)		Blue shift in absorption spectra, the HOMO orbital is delocalized largely on the substituent	[74]
Substituting N(5) with carbon (deazaalloxazine)		Blue shift in electronic spectra, longer excited state lifetimes	[124, 125]

A wealth of information exists on the structural modifications of lumazine, unfortunately often focused on purely biological descriptors such as antibacterial activity [126], which makes a comparison with the photophysics of **AL** modification impossible. Due to the similarity of the two molecules, it could be assumed that most modification strategies can be carried over from alloxazine, however, computational chemistry could provide at least a limited insight here. For example, substituents in the C(6) and C(7) positions of **Lum** should have a stronger effect on the electronic structure, since they are not shielded from the heterocyclic moiety by an additional benzene ring as is the case in C(7) and C(8) substituted **AL**. Indeed, the strong electron-withdrawing group –CN has a much larger effect on **Lum**, than other such groups have on **AL**, leading to a substantial red shift in spectra and increased acidity of the N(1) proton [127]. Furthermore, the C(2)–NH_2 substituted lumazine, denoted pterin, is often researched for use in medicine [128]. On the other hand, a hypothetical C(2)–NH_2 substituted alloxazine is not discussed at all. Due to the relative ease of formation of the –OH groups on C(2) and C(4) in **Lum**, it is possible to bind alkyl chains to these oxygens, forming a type of derivative that is not present in alloxazine chemistry [129]. The result is a lipophilic compound with the same electronic transitions and photosensitisation capabilities as **Lum**.

3.2 Polythiophene Chemistry

Polythiophene-based materials are used in the fabrication of devices such as OLEDs, Organic Field Effect Transistors (OFETs), Organic Photovoltaic Cells (OPVs) or sensors since they are efficient semiconductors with well-known optical properties. Their main advantages lie in the low production cost and synthetic flexibility. Indeed, by modifying the molecule, it is possible to tune the solubility, structure, and electrochemical properties, as will be shown below [130]. A basic structure of polythiophene (**PT**) is shown in **Fig. 9**. Furthermore, the sulphur atom on a thiophene ring contributes to the molecular aromaticity and allows the formation of intermolecular S–S and S–O weak bonds, due to the lone pair electrons in 3s and 3p orbitals [130, 131]. Recently, Palamà et. al. [132] have used this bonding ability for the self-assembly of electroactive microfibers. Obviously, **PT** has the capacity to create organised solid-state structures even without any modifications, which makes it a prime candidate for use in optoelectronics. Finally, the quinoid resonance structure (**see Fig. 9**) of thiophene oligomers and polymers features higher rigidity and lower band gap, although it is higher in energy.

In general, it is possible to modify this molecule by elongating the main chain, inserting a different building block such as benzene into the main chain, adding a substituent on the S atom, or substituting in positions C(3) or C(4). The simplest way to obtain a new derivative is to introduce a substituent to a 2–7 membered oligothiophene chain. These studies not only provide potential new materials [133, 134] but also serve to give insight into the nature of **PT**s since oligomers are easier to treat mathematically [130].

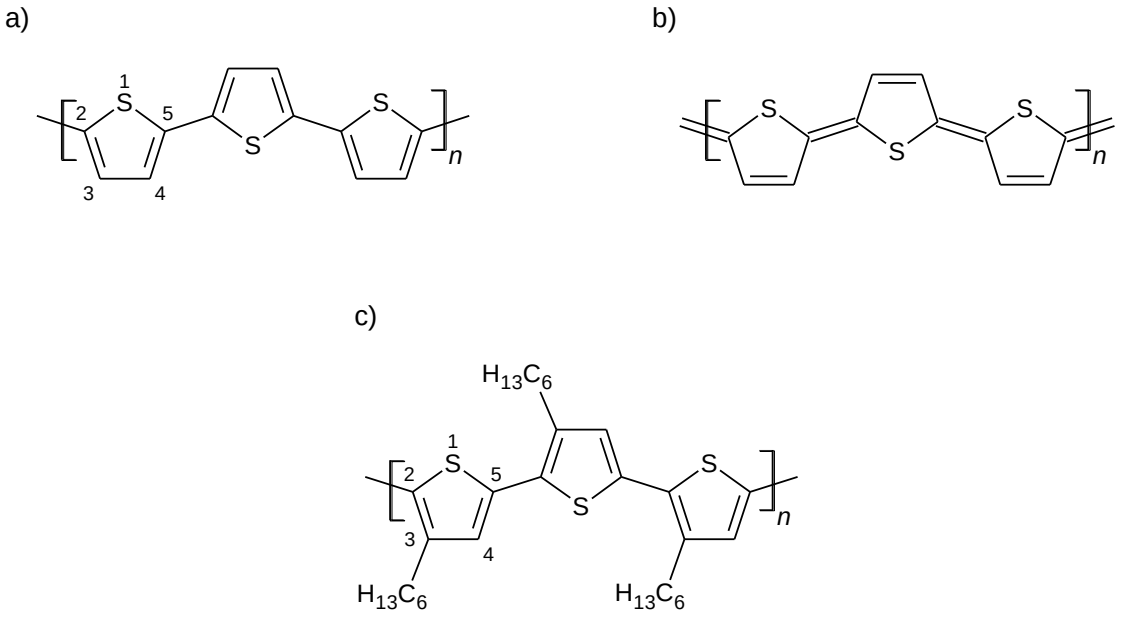

Fig. 9 *The structure of polythiophene: a) The aromatic form and the numbering of the thiophene moiety; b) The quinoid form; c) Poly(3-hexylthiophene), the most common substituted* ***PT***

Unsubstituted oligothiophenes typically have a comparatively low charge carrier mobility, below 0.1 $cm^2 V^{-1} s^{-1}$. This can be raised substantially by ending the chain with alkyl groups in the C(2) and C(5) positions on the ends of the oligomer chain. Fluoride-substituted benzene was found to have a similar effect. In this way, the mobility rises to 0.6 $cm^2 V^{-1} s^{-1}$ [135, 136]. The thiophene dimer absorbs visible light around 300 nm and has an emission band around 360 nm. The addition of thiophene units to the chain causes a red shift due to higher conjugation, and a substantially larger fluorescence quantum yield. Once over 25 thiophene units are present in the chain, the absorption and emission wavelengths stabilize at 450 nm and 650 nm, respectively.

Unsubstituted thiophenes linked in the C(2) and C(5) positions are p-type semiconductors, and together with the aforementioned photophysical properties and tendency to form intermolecular structures, are often used in optoelectronics. On the other hand, less literature exists on n-type semiconductive **PT**s, which will nevertheless be important in the future to manufacture components like bipolar transistors and donor layers of OPV cells [130, 137].

When designing materials for use in optoelectronics, the frontier molecular orbital energies and the charge carrier mobility are of prime importance. They can be readily modified by either substituting an electron-withdrawing group into the C(3), and C(4) positions, or by inserting it into the main chain. The former approach was applied *e.g.*, by Hou et. al. [138] by introducing carboxyl groups into the C(3) position. The latter approach usually involves copolymerization with strong electron-donating building blocks, typically fused thiophenes such as thienothiophene and naphtodithiophene [139, 140]. The addition of various pyrrolopyrroles (**PP**s) is also popular. This promotes the formation of rigid quinoid structures and extended π-conjugation [130, 140]. The interactions between donor and acceptor moieties can be further controlled by introducing spacers, as shown by McCulloch et. al. [141]. They have inserted selenophene and tellurophene units into the main chain, where the larger chalcogen atoms reduce the aromaticity and the band gap. Furthermore, the larger atoms facilitate the formation of polymer aggregates and thus increase the field-effect mobility up to 1.6 $cm^2 V^{-1} s^{-1}$ [141].

While the addition of large, fused building blocks has wonderful effects on the electrical properties of **PT**, it typically leads to reduced solubility and thus creates a processability problem. This is typically mitigated by substituting alkyl side chains in the C(3) and C(4) positions [130, 142]. Furthermore, alkyl side chains with heteroatoms (generally O and S) can be further used to fine-tune the absorption properties [143]. The side chains have a further influence on the intermolecular packing and thermal stability of the materials [142, 144], thus opening side-chain engineering as a distinct branch of study in conductive polymers (CPs). For example, it has been known for some time that decreasing the number of thiophene units that have a side chain increases oxidative stability, at the cost of charge carrier mobility [145].

While the systematic studies of the side chain influence on thermal stability started relatively recently, Cao et. al. [144] have explored the effect of different linear and branching alkyls and have found that by placing the branching point closer to the backbone, both melting point and

glass transition temperature are increased as a result of tighter molecular packing in the side-chain direction. For an illustration of substituted **PT** packing, see **Fig. 10**. At the same time, Schaffrinna et. al. [146] have investigated the optical properties of substituted **PT**s, and have managed to create a significant blue shift of around 100 nm, both in solution and in a thin film, by substituting acetic acid in the C(3) position. This material also exhibited good adhesion to the polar surfaces due to packing in the edge-on direction (**see Fig. 10**).

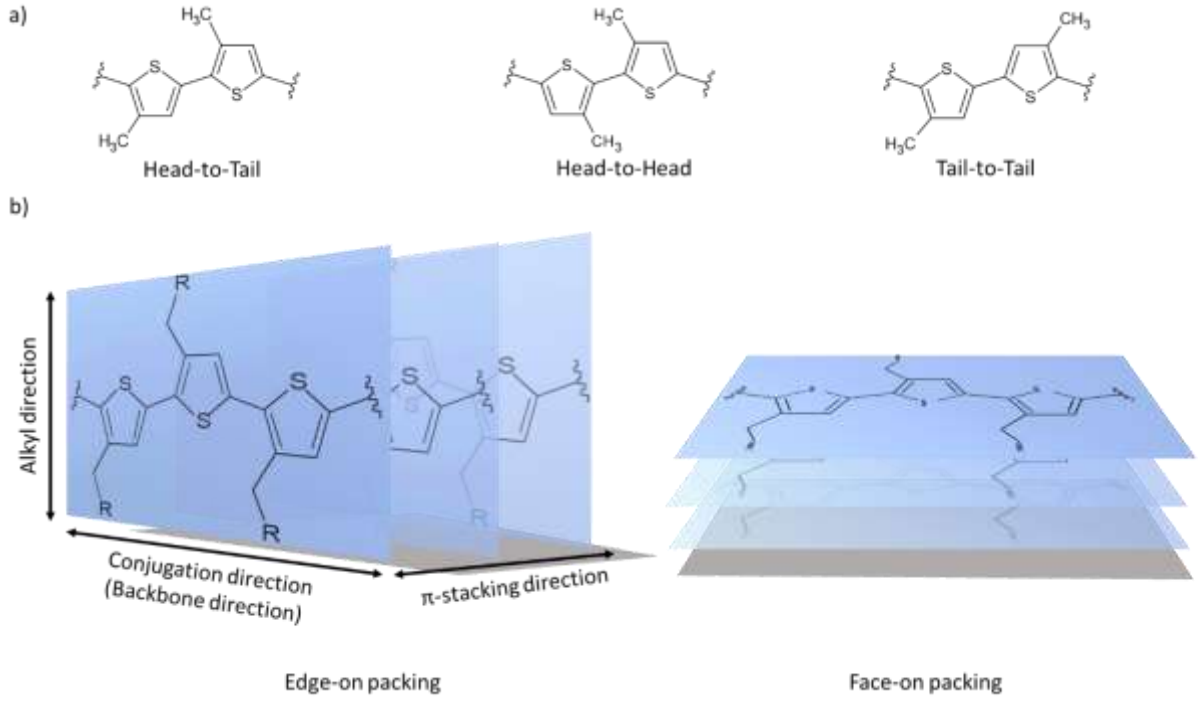

Fig. 10 *a) Possible regioregularities of substituted polythiophenes; b) An illustration of the possible packing of side-chain substituted polythiophenes in relation to the substrate (grey surface) [145]*

Perhaps the most used molecule of the polythiophene class is the hexyl-substituted poly(3-hexylthiophene), denoted **P3HT**. It reaches charge carrier mobilities of around 0.2 $cm^2 V^{-1} s^{-1}$ when in the edge-on orientation and head-to-tail regioregularity (see **Fig. 10**). On the other hand, other the head-to-head and tail-to-tail arrangements cause torsion in the structure, thus lowering the overall conjugation and charge mobility. The absorption and emission bands of **P3HT** are located around 450 nm and 550 nm, respectively, while in solution. Deposition into thin film leads to a red shift of around 50 nm in absorption, and 200 nm in emission. While this polymer is usually applied by spin coating, Blasi et. al. [147] have recently used inkjet printing to prepare an electrolyte-gated OFET, where the material exhibited more efficient π–π stacking. Since printing can be used for depositing large areas of the polymer, this technique could prove important in the manufacture of OPVs. On the other hand, Kleinschmidt et. al. [148] have criticised the widespread use of **P3HT**, and the fact it is considered a model polymer. They have argued that it is too dissimilar from the donor-acceptor polymers since it has a higher crystallinity with efficient π-stacking, which requires frequent folding of the polymer backbone,

impossible in polymers based on e.g., on fused heterocycles as discussed above. Therefore, according to them, **P3HT** is used mainly due to its wide availability and long tradition. Still, any new conductive material will have to perform at least comparably to modern-day staples such as **P3HT** or poly(3,4-ethylene dioxythiophene) (**PEDOT**), to be considered for commercial use. Thus, drawing at least some comparisons to these polymers seems inevitable.

Since the favourable conductive properties of **P3HT** stem largely from its packing [148], another viable strategy could be to further improve the crystallinity and π-stacking of **PT**s *via* side chain engineering, which was briefly discussed above. Some groundwork has been laid by Nguyen et. al. [149], who have synthesized poly(3-alkylthiophenes) (**P3AT**s) with butyl, hexyl, and octyl side chains, with well-defined molecular weights (MWs). Subsequent analysis has revealed that larger alkyl chains lead to higher crystallinity, and optimal performance in OPV cells, which was likely caused by the higher degree of crystallinity. On the other hand, the side chains proved to have only a small influence on the position of optical absorption and emission bands, whereas the length of the main chain, characterised by MW, had a much greater influence. This is hardly surprising, since the spectroscopic properties are mainly a function of FMO energy levels, which are not influenced by alkyl substitution very much, and side chains with some heteroatoms would need to be used. These results were later expanded to dodecyl side chains by Park et. al. [150], who have, at the same time, also prepared a lower-regioregularity dodecyl-substituted **PT**, which exhibits remarkable capabilities for self-assembly, and manages to form liquid crystals.

Finally, Lin et. al. [151] have introduced alkylthio side chains. As expected, a heteroatom close to the thiophene moiety has a significant influence on FMO energies, causing a red shift of the spectra by 70–100 nm. Furthermore, noncovalent S–S and S–π interactions promote ordered molecular packing. In this regard, the material substituted with the linear hexylthio chain exhibited the highest charge carrier mobility, since the regular packing is inhibited with branched side chains due to sterical effects. On the other hand, the branched alkylthio substitution allows a higher degree of regioregularity to be attained with respect to linear chains, i.e., 99 % vs. 85 %, respectively.

While current research focuses on different linear and branched molecules, there is a lack of studies performed with a large, three-dimensional substituent, such as adamantane. This molecule is stable, biocompatible, and readily self-organizes into crystals [152]. In the past, this substituent has been used to enhance the crystallinity and hole mobility of molecular materials such as **PP**s, without compromising their spectroscopic properties and fluorescence quantum yields. In fact, adamantyl substitution was found to induce crystallization in long, needle-like structures, that are around 1 μm long [153]. Thus, it represents unexplored opportunities in side-chain engineering.

In n-type organic semiconductors, thiophene units usually only appear as oligomer spacers with a length of 1–3 units between large nitrogen-containing moieties such as naphthalene diimide [154], since an efficient n-type semiconductor requires a large overlap of individual LUMO

orbitals, not typically observed in thiophene chains [155]. On the other hand, it has been shown that an n-semiconducting oligothiophene can be prepared by capping the end positions with a fluorinated alkyl chain [156]. This represents some hope, that inserting fluorinated building blocks into the polymer backbone, or as side substituents, n-semiconducting **PT**s will be achieved relatively easily.

In the field of computational chemistry, much work has been done regarding organic electronics, see *e.g.*, the recent study by Barboza [157]. However, due to the focus on substituted **PT** in the publication, polymers containing fused building blocks are considered to be beyond the scope of this work and will not be discussed. Due to inherent problems with computing geometries of polymer chains as discussed in chapter 2.7, *ab initio* and DFT calculations have to be limited to oligomer structures, while more complicated studies are sometimes carried out using molecular dynamics, *e.g.*, Moreno et. al. [158]. In this study, the effect of branched alkyl substituents on the molecular packing was studied by MD methods. This study has visually shown the difference between linear and branched substituents, especially the large extent of disorders in the alkyl chain direction.

While DFT methods are not yet able to give precise insight into polymer molecular packing, some information, especially about the intramolecular effects can be extracted from computations carried out on oligomers. Already in 2004, Marcon et. al. [159] used *ab initio* intramolecular torsional potential and charge distribution of 6–membered oligomers (sexithiophenes) to obtain a better fit of the molecular mechanics force field. By using these more advanced parameters, they managed to obtain a theoretical crystal structure of sexithiophene and fluorinated sexithiophene that were in good agreement with the experiment. For further reference, **Fig. 11** shows the dihedral angles considered in further studies, and an illustrative sketch of the typical potential profiles, where $(\mathbf{T})_2$ denotes the thiophene dimer, $(\mathbf{3HT})_2$ denotes the 3-hexylthiophene dimer etc.

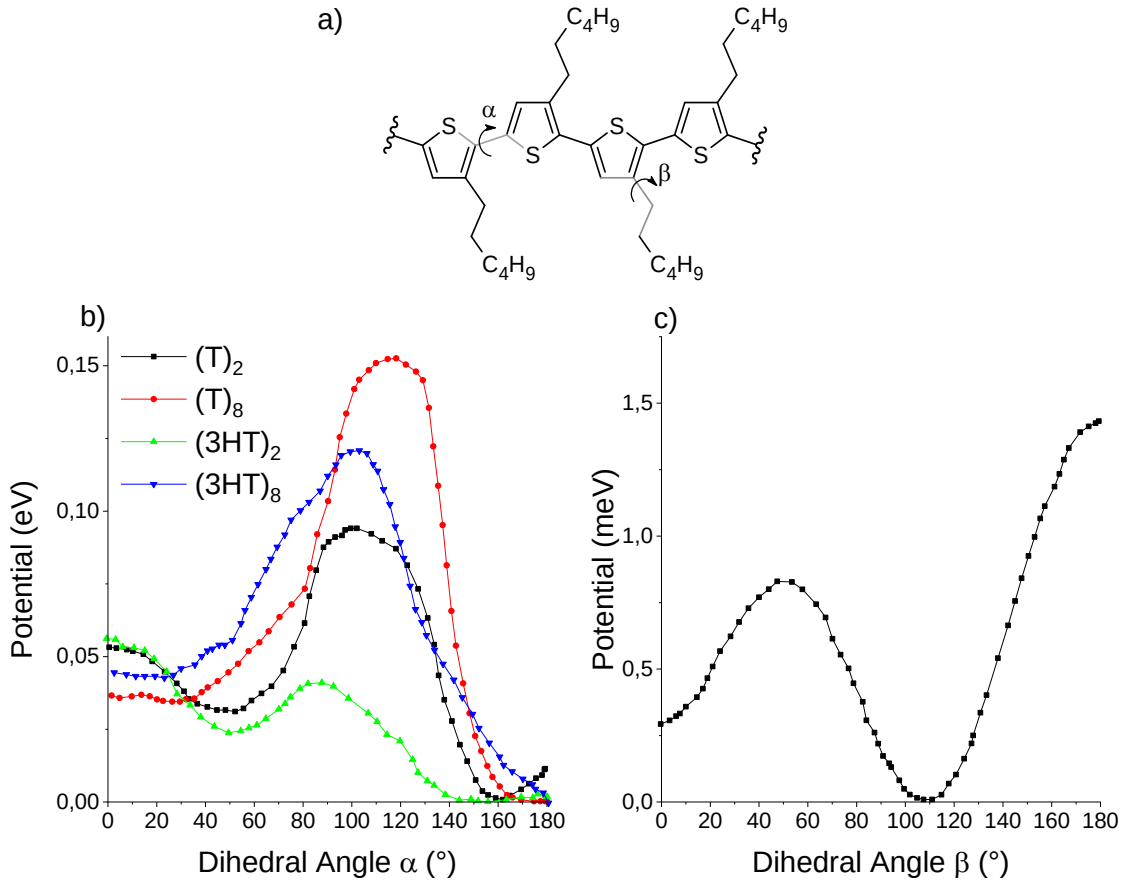

Fig. 11 *a) The dihedral angles of interest on a* ***P3HT*** *chain; b) A sketch of the α-angle potential energy profile for* ***PT*** *and* ***P3HT*** *dimer and octamer [160, 161, 162]; c) A sketch of the β-angle potential profile for* ***P3HT*** *[158]. Note that the dihedral potential of the thiophene octamer* ***(T)₈*** *appears significantly larger than the hexyl-substituted* ***(3HT)₈*** *octamer, which is suspicious and likely caused by the overestimation of the Pople basis set mentioned by Wildman [161]. Literature however agrees on the potential maxima and minima of the given dihedrals.*

After this first systematic computational study of oligothiophenes, Darling et. al. [160] addressed the question of the polymer limit – how many thiophene units are needed for a DFT model to be accurate for a polymer chain, especially when the side chains are treated explicitly. While the alkyl side chains do not participate in forming FMOs, and thus do not directly contribute to light absorption, they are extremely important for crystal packing and therefore the conductivity of **P3HT**, and it is difficult to imagine a successful model of side-substituted **PT**s that does not explicitly treat them. Furthermore, the side substituents affect the dihedral angles between thiophene units, thus contributing to the conjugation in the backbone. The study of Darling was especially focused on dihedrals and has determined, that 8–10 thiophene units provide a good approximation for the **PT** chain, while there are only negligible differences between the torsional potential profiles of 10- and 14-unit **P3AT** chains. Some problems with this study are, that only ethyl side chains were used instead of hexyl to simplify the computations and that no other factor than torsional potential was considered. The results were however later confirmed by Huang [163], who has shown the difference in torsional potential between the 2- and 14- unit oligomers. Indeed, the global minimum of torsional potential is

around 150 ° for dimer thiophene, and 180 ° for an octamer and higher. This behaviour is attributed to the increasing electron dislocation in longer chains, which makes deviations from a planar conformation less energetically favourable. They have further evaluated the probability distribution of dihedral angles in the thiophene chain via atomistic MD simulations of **P3HT** dodecamers, which was found to heavily favour planar distribution, although the notation used in the study makes the interpretation difficult. It was, however, the first study to feature simulations of a significant **3HT** chain together with fullerene molecules, used as n-type semiconductors in some solar cells [164].

DuBay et. al. [165] have highlighted the importance of choosing the correct method for geometry optimizations since thiophene dimers adopt a planar structure in the 3-21G* basis set and a torsionally distorted structure in larger basis sets. They have further argued that the planar structures observed in crystallographic studies are products of the crystal packing and should not be expected in isolated chains that are considered in *ab initio* and DFT studies, regardless of the chain length. Indeed, some small local minima were found by Darling [160] around the 130 ° and 160 ° angles in the 10–14-unit oligomers, that Huang et. al. have not reproduced in their calculations on **P3HT**. Thus, the planar structure, shown e.g., by Scherer et. al. [166] in their CG MD simulations can be ascribed to the presence of hexyl chains and improved molecular packing, although direct comparison with DFT results is difficult due to the coarse-graining. Bhatta et. al. [167] have expanded the torsional potential studies by showing the correlation between the α-angle rotated chain and the HOMO/LUMO gap in a study carried out on **P3HT** and a fused thiophene polymer. They have shown that the gap grows by 2 eV in energy when the dihedral angle is 90 ° for **P3HT**, while it grows by around 1 eV for the fused polymer, thus demonstrating the importance of good chain conjugation in unfused polythiophenes, and the influence of the rigid monomer units.

Wildman et. al. [161] have performed a large comparison of dihedral potentials in different basis sets at the CAM-B3LYP level of theory. They have found, that the Pople sets from 3-21G, employed in [160] to 6-31+G** significantly overestimate the torsional barrier at 90 °, and the cc-pVTZ basis was found to be generally more accurate. Otherwise, the general shape of the curve agrees with Darling et. al. [160]. Unfortunately, Wildman's study did not involve any substitutions to the thiophene core.

Recently, Barboza et. al. [157] performed a systematic DFT study of the influence of different simple side chains in the C(4) position, such as fluoride, methyl, or amino groups. Unfortunately, the 6-31G basis set was used, which was previously shown to be inaccurate. They have further tested both the commonly used B3LYP functional, and the M06HF. Out of these two, B3LYP proved to be more accurate. The asymmetry introduced by adding one substituent per thiophene unit has some interesting predicted effects, for example, the addition of an –OH group gives electrophilic properties to the thiophenes at the opposite end of the chain. While substituting a phenyl into C(4) shifts the reactivity away from the S atom in thiophene to the substituent, which could have a positive effect on the stability of the polymer backbone, and a potential use in sensorics, since it would considerably broaden the spectrum of

detectable analytes. Generally, all the substituents were found to lower the band gap, but ones containing heteroatoms have an order-of-magnitude larger effect. While electron-withdrawing or accepting groups like –CN or $–NH_2$ lower the energy levels of FMOs, the band gap stays almost the same, unless a heteroatom is directly bound to the thiophene core, which represents an interesting development in side-chain engineering.

In another recent study, Sirohi et. al. [168] attempted to model the charge transport in a **PT**-based OFET device *via* DFT. They have also considered similar side substitution to Barboza [157] and observed generally the same results on the FMO levels. Most interestingly, their study predicts, that the p-type semiconductivity of **PT** could be shifted to n-type simply by a change of conformation in the polymer channel, and a change in gate bias. There could be some theoretical support for this since electron transport can be helped by delocalizing the LUMO orbital, as mentioned above. However, Sirohi and others have only considered charge transport in a hexamer molecule, decidedly not reaching the polymer limit. Further, only charge transport in the direction of the backbone is considered, and since the experimental charge transport is observed to be anisotropic (see [145]), the accuracy of this study is questionable, although the previous MD study by Lan [169] has found the predicted charge transfer mobility along the backbone to be three orders of magnitude larger than mobility in the π-stacking direction, theoretically supporting the setup used by Sirohi. On the other hand, Lan has also pointed out the high dependence of interchain mobility on the dihedral angle α, showing that manipulating the backbone from an ideal conjugation is a thing to be avoided. While the authors have gained convincingly looking current-voltage characteristics of the molecular transistor, a viable DFT treatment of real-life transistors will likely not be available in the near future.

4 AIMS OF THE THESIS

Apart from giving an overview of the DFT method and its practical use, this work mainly aims to investigate the properties of the two types of molecules mentioned above, especially to see whether they could find some use in the field of optoelectronics.

Concerning the flavin class of molecules, the first aim of the research is to develop a consistent model of their spectroscopic behaviour based on existing experimental data from our own research (see below in chapter 4.2), and from literature. This model could then be used to predict the behaviour of possible synthesized molecules, and to pick the most suitable candidates for a given application in optoelectronics, for instance, information such as the FMO energies and the HOMO/LUMO gap can be used to determine possible candidates for OPVs or other areas like photocatalysis.

Further, it should be possible to find some insight into the molecular structure, *e.g.*, by investigating the geometrical distortion caused by different substituents, that could be useful for further synthesis.

Since the topics of **AL** and **Lum** chemistry are so rarely mentioned together, it is a further goal to determine, whether a coherent model could be prepared for both of these classes simultaneously. On the other hand, deazaflavins have been shown as too different in reactivity (see the beginning of chapter 3.1, or ref. [67] for details), and it is doubtful that they fit the same chemical space, i.e. that a model made for alloxazine would fully fit them. Furthermore, there is significantly less data on the photophysics of deazaflavins in the literature, essentially all of it being done by the group of Sikorski [124, 125], and no samples were available for this work, since the synthetic route is different [170].

In the case of the thiophene derivatives, the main aim was to theoretically investigate the influence of the novel adamantyl side substituents on the properties of **PT**, especially with regards to the possible conformations of the side chains with respect to the backbone and sterical effects, which could provide some insight on the possibility of intermolecular packing in the side chain direction. As before, the FMO energy levels and spectroscopic properties will be important.

5 METHODS OF RESEARCH

With the general aims of this work established, a closer description of the computational and experimental procedures will now be provided.

5.1 Calculation

In the case of DFT studies of flavins, the three-parameter hybrid B3LYP functional [171, 172] is typically used in photophysical studies with reasonable accuracy, e.g., in the work of Bracker et. al. [123], predicting the excitation and emission energies of fluorinated **AL** within 0.08 eV, or Daidone's study [173] on the solvatochromism of riboflavin. The B3LYP functional also has one of the lowest mean absolute errors with respect to excitation energy compared to other TDDFT computations [11, 22]. It is outdone by the *ab initio* Complete Active Space [174] or Coupled Cluster [175] methods, and in some cases by the DFT hybrid functional PBE0 [176]. It should be noted that CAS methods are time intensive and highly nuanced [177], and therefore not practical for common use in an experiment-focused branch like organic chemistry, where reasonably accurate and fast results that may need a small correction are more valuable than perfect results that require weeks for every molecule. This argument can also be applied to the other ab initio methods, while the other competitor, PBE0, is not accurate in the case of dipole moments and slightly less accurate for bond lengths than B3LYP [11], which therefore remains the most reasonable choice of functional.

The question of basis sets is considerably more open. Most works use the family defined by Pople, especially the 6-31G* [178] basis set, typically adding polarization functions due to the presence of many heteroatoms, see e.g., the work of Climent et. al. [115], Daidone [173] or the group of Sikorski [179, 93]. In some cases, for the **Lum** and **AL** molecules, the larger 6-311+G** [180] triple-split valence set with added diffusion and polarization functions has been used by Afaneh [82] and Mal [117]. The combination B3LYP/6-31G* performs reasonably well and can be expected to predict excitation energies within 0.4 eV of the experiment, as seen in the recent work by Golczak [93].

On the other hand, Bracker [123] has recently achieved much more accurate results with the B3LYP/TZVP method, using the triple-zeta valence polarized basis of Aldrichs et. al. [181], while Merz [43] and Afaneh [182] have achieved great accuracy predicting the excitation energies, individual FMO energies, and complexation free energies for thienyl**Lum**-heavy metal complexes in the case of Afaneh using the correlation-consistent cc-PVTZ set by Dunning and coworkers [183].

However, the studies mentioned above are focused on a very narrow selection of molecules, sometimes only considering the parent molecules, or a single specific derivative, such as the fluorinated **AL** in [123], or the fused benzene derivative in [93]. No comprehensive study on the accuracy of different basis sets is known to the author of this work. Therefore, it seems reasonable to perform computations using the B3LYP functional and the basis sets mentioned

above and compare their results from a wider range of molecules both from literature and from the author's experiments to create a meaningful model. Thus, the basis sets 6-31+G** will be used as a compromise between the most common 6-31G* and the larger 6-311+G**. Further, the aug-cc-PVDZ [183] set, augmented with a diffuse function will be used instead of the larger cc-PVTZ, and the def2SVP [184] instead of the larger Ahlrichs basis. The move to smaller basis sets was made, since the reported studies typically focus on small molecules, such as simple **AL** and derivatives of **Lum**, while this work considers larger molecules with multiple fused benzene rings and heterocyclic substituents while computing spectra in solution via the PCM models. Thus, for ease of computation, smaller basis sets were selected where possible, with the hope that the accuracy will not be significantly harmed by the transition from triple- to double-split valence sets. Tight optimisation criteria were set for the computation, with a large DFT integration grid.

For future reference, the molecules considered in the flavin-focused part of the study are shown in **Fig. 12**, where the molecules drawn in bold black lines have been previously prepared and characterised – and so they can be compared to experimental results. The molecules drawn in thin grey lines are not available for synthesis at this time. Further, the A, B, and C notation for the individual rings of the **AL** and **Lum** moieties is introduced, useful for describing structural changes caused by different substituents by the HOMHED index.

Finally, the Coulomb-attenuated CAM-B3LYP [185] functional was tested, in order to see if the results improved with long-range correction. It was however found early on that it significantly overestimates the energy levels, and so standard B3LYP was used for most of the study. The final combinations of functionals and basis sets for this part of the study are summarized in **Tab. 7** below.

Since some molecules, *e.g.*, **ThLum** (see **Fig. 12**), involve substituents that can freely rotate the lowest energy conformation of the substituent w.r.t the **AL** or **Lum** moiety will first need to be found via a scan of potential energies across the possible rotations. Since the experiments were carried out in DMSO, the computations will be carried out by first stabilizing the gas phase geometry, and then using the PCM model [186] for minor alterations.

Once the optimal geometries with the lowest electronic energy both in the GP and in implicit DMSO were gained, the vertical singlet transition energies and oscillator strengths between the initial and final electronic states were computed by the TDDFT method using the B3LYP functional. Further, excited state geometries and deexcitation energies were found by the same method. Due to the fact, that TDDFT calculations of excited state geometries of organic heterocycles including flavins can lead to saddle points at the potential energy surface [108], the true minima on the potential energy surface were confirmed by an inspection of the frequencies for all geometry stabilizations.

The substituted molecules in this part were chosen based on the previous investigations – electron-withdrawing groups have a larger influence on the optical properties of the flavin than alkyls or electron donors. The structural changes of the investigated substituents can be described by the HOMHED indices, benzene, pyrazine, and pyrimidine were used as standards for the rings A, B and C respectively (see **Fig. 12**), to try and take the positions of the heteroatoms into account.

Note, that due to the computational complexity of the aug-cc-PVDZ basis, the excited molecular geometry and absorption and emission spectra of the very large, conjugated molecules **PhePh**, **PhePh2** and **PyrPh** were not computed at this time.

Table 7 *A summary of the functional/basis combinations used for the flavin study*

Functionals used	Basis sets used
B3LYP	6-31+G**
	aug-cc-PVDZ
	def2SVP
CAM-B3LYP	6-31+G**

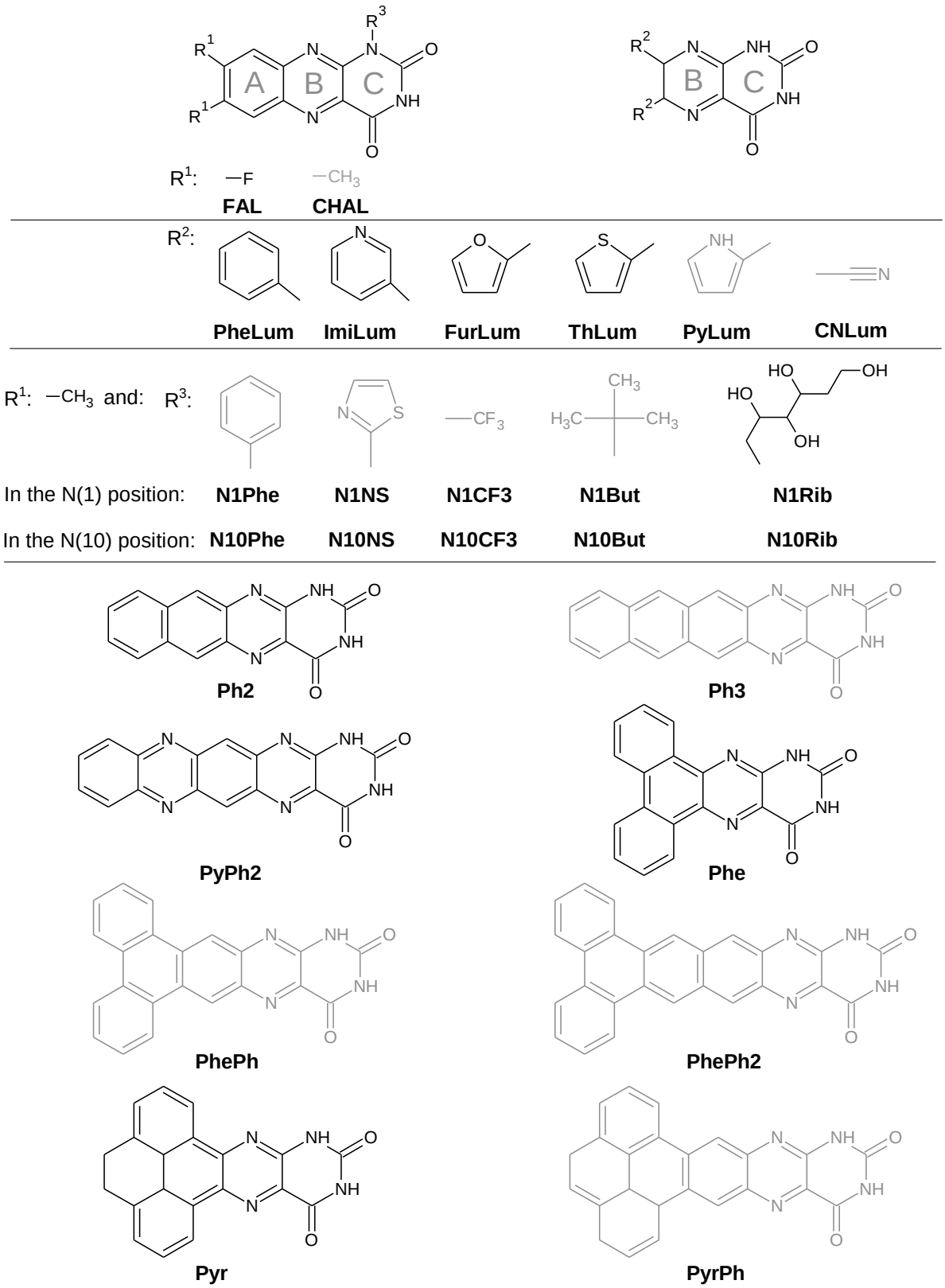

Fig. 12 *The **AL** and **Lum** derivatives considered in this work. The molecules where relevant experimental data is available are printed in black, ones that are purely theoretical are grey. The A, B, C ring notation of alloxazine and lumazine is also shown. While the **CHAL** molecule is widely used, spectroscopic data in DMSO is not available at this time. Isoalloxazine forms are not pictured but are included in the study.*

For the computations on **PT** and its derivatives, the large study by McCormick [187], which involved numerous fused derivatives as well as differently substituted thiophenes, has shown that B3LYP functional performs very well for poly(3-alkylthiophenes) **P3ATs** while predicting HOMO energies, while LUMO energies are overestimated by around 0.5–1 eV, leading to a total overestimation of the band gap by around 1 eV. For other types of derivatives, the performance of this functional wildly varies, and it cannot be recommended except for careful case-by-case consideration. The same can be said for CAM-B3LYP, which overestimates all energies by more than one eV. Unfortunately, the authors did not investigate what the influence of the 6-311G* basis set on the results could be. This is especially problematic since the Pople sets have since been shown to systematically overestimate the results of **PT** calculations by Wildman et. al. [161].

Indeed, Barboza et. al. [157] have shown the B3LYP to be superior to another alternative, the M06HF hybrid of Truhlar and Zhao [188], which has been proposed by Oliveira et. al. [189]. While the vertical excitation energies gained from the M06HF functional have a qualitatively similar trend at the polymer limit as experimental results, M06HF overestimates excitation energies more than B3LYP and was abandoned even by the group of Oliveira [190].

On the other hand, the computations in this part of the thesis are aimed at long chains, and molecules with bulky substituents, that often exceed one hundred heavy atoms (i.e., heavier than hydrogen). Therefore, the complexity of the computation should be a primary concern, and the reasonably-well performing and often used B3LYP seems a feasible choice, with the caveat that the theoretical band gaps may need adjustment. It does seem rational, however, that a different basis set should be used instead of the Pople bases. Körzdörfer and coworkers [191] have favoured the cc-PVTZ basis set for large π-conjugated systems, which has however been shown to dramatically underestimate the FMO energy levels of **PT** oligomers, even in conjunction with B3LYP, and would give accurate results only with *ab initio* methods or very specific long-range functionals.

The combination of an extensive basis set and a computationally intensive model does not bode well for the large system considered here. However, in the past, the older Ahlrich DZP set [181] was used to model optoelectronic properties of conjugated polymers by Wilbraham et. al. [192]. Thus, the updated def2SVP basis seems a reasonable compromise between the accuracy of a triple-zeta def2TZVP set and computational simplicity, to obtain qualitatively reliable results, that can be fit to the experimental measurements, as recommended by its authors [32]. It was also successfully used to investigate crystal structures of conjugated polymers by Yao et. al. [193]. To sum up, computations on the polythiophene chains were performed using the B3LYP/def2SVP method. For the sake of simplicity, calculations were performed in the gas phase. As before, the optimisation process was performed by tight optimisation criteria and a large DFT integration grid. True minima on potential energy surface were confirmed for small model molecules through vibrational analysis by no imaginary frequencies check. Using the described method, the minimum-energy geometries were found for model octamers and trimers of the molecules in question, which are shown in **Fig. 13**.

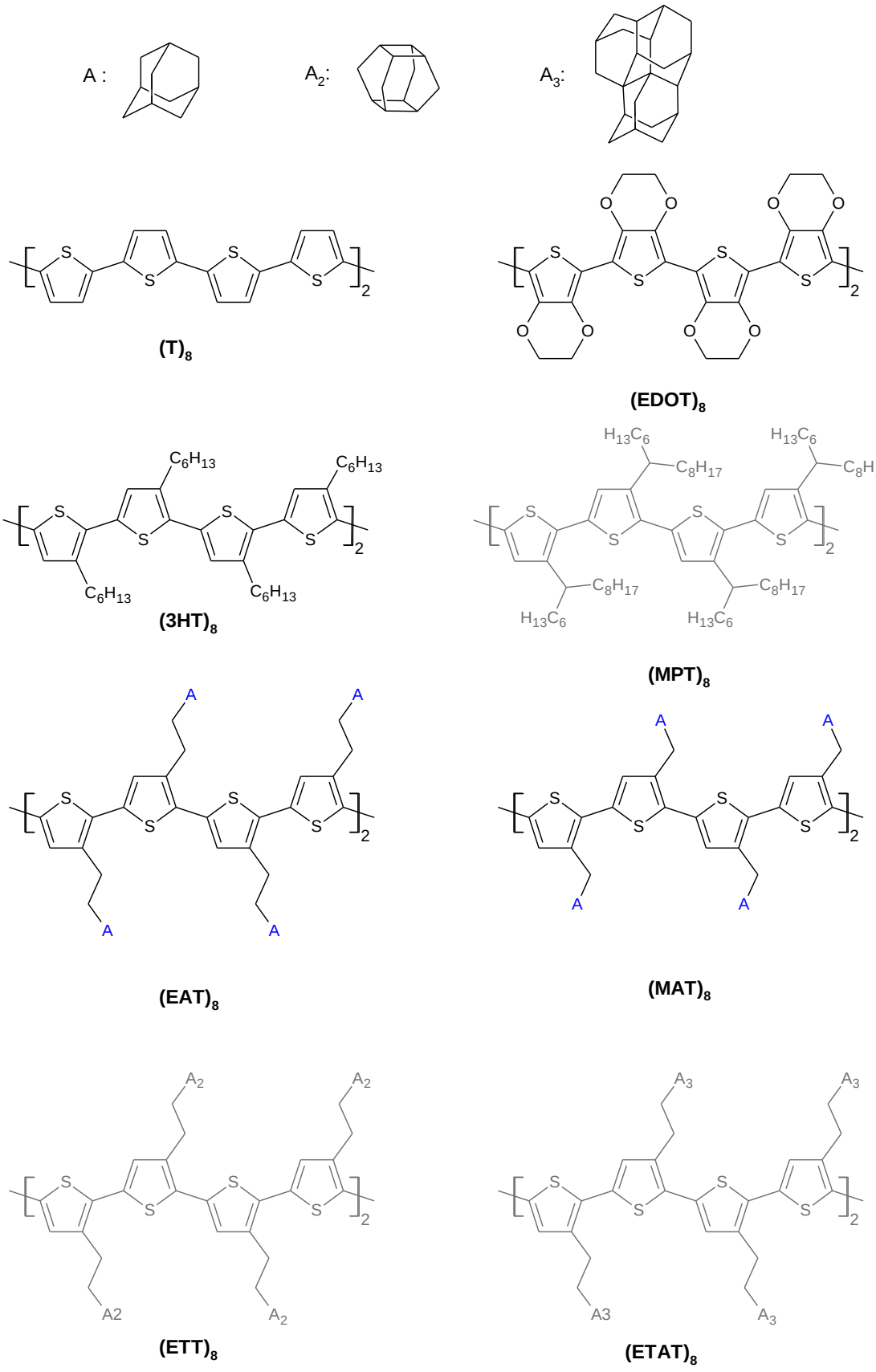

Fig. 13 *The structures considered in the study of adamantylated thiophenes [JT3]. The trimers are not pictured.*

Two all-*trans* arrangements were considered for all molecules since previous studies have shown that *cis* conformations are not energetically preferred in unsubstituted and alkyl-substituted **PT**s due to sterical repulsion between side chains [162]. One of the two considered orientations was the *syn*-conformer, with positive values for all α dihedral angles, which gives it a spiral shape. The second was the *anti*-conformer, with alternating positive and negative values of the α dihedral.

The octamers in question are (**T**)$_8$ to have a theoretical baseline for other results; (**3HT**)$_8$ and the ethylene dioxythiophene octamer (**EDOT**)$_8$ to gain a comparison to the main competitors for any thiophene-based polymer; 3-methyladamantyl thiophene (**MAT**)$_8$ and 3-ethyladamantyl thiophene (**EAT**)$_8$ which represent the novel adamantyl-substituted **PT**s; 3-ethyltetraasterane thiophene (**ETT**)$_8$ as a possible alternative to adamantyl substitution with a bulky molecule of similar size; 3-ethyltriamantane thiophene (**ETAT**)$_8$ which represents a theoretical limit of an extremely large three-dimensional substituent; and 3-methyl-9-pentadecane thiophene (**MPT**)$_8$, that shows the effect of incorporating the pentadecane chain, commonly used in organic electronics [194]. Once the lowest-energy geometries were found, the vertical transition energies and oscillator strengths between the initial and final electronic states were computed by the TDDFT method.

The trimer calculations were focused on finding the potential energy profile of rotation around the dihedral β angle, this was performed by a scan across the whole range of rotation, with a 20° step and a finer 5° step scan at the energy maxima. A relaxed PES scan was done, i.e., the lowest-energy geometry was found for every alteration of the dihedral. This part of the study was performed only for the (**3HT**)$_3$, (**MAT**)$_3$ and (**EAT**)$_3$ trimers, since the relaxed PES scan is very resource and time intensive, and it did not seem to make sense to perform it for the other substituted molecules that only exist in theory.

5.2 Experimental

The absorption spectra were measured using a Specord 50 Plus UV-Vis spectrophotometer (Analytik Jena, Jena, Germany). Emission measurements were done using a Horiba Fluorolog (Horiba Jobin Yvon, Kyoto, Japan). The concentration of all samples was 1 10^{-5} mol l^{-1}. The baseline for the spectra was determined by measuring the absorption of the solvent, either pure DMSO (purchased from Honeywell Research Chemicals, 99.9 % purity, maximum 0.02 % water content [195]) or the appropriate DMSO-H_2O mixture. A Hellma QS quartz cuvette with an optical path of 1 cm was used for the optical measurements. All experiments were performed at room temperature, while deionized water with the conductivity of 0.06 μS cm^{-1} (prepared in-house at the Faculty of Chemistry) was used to dilute the samples when needed.

First, the molecules had to be solvated in pure DMSO and diluted by the water where applicable, since **AL** and its derivatives are not soluble in H_2O. While **Lum** is water-soluble, it was better

to maintain the same practice for all molecules. The final relative concentrations of DMSO were 100 and 50 molar percentage (mol. %), respectively.

The molecules studied by this method were **Lum**, **AL**, **FAL**, and **ImiLum**. The **Lum** molecule was supplied by the BDL Czech Republic at > 99.0 % purity, and other measured samples were prepared according to the work of Richtar et al [74], and generously donated by dr. Richtar.

Further, the molecules **Ph2**, **PyPh2**, **Phe** and **Pyr** were measured in DMSO only, at the same concentration and room temperature. Other measurements, such as the heterocycle-substituted lumazines were taken from literature or the previous work of this group, such as [74]. The DMSO used in this part contained a larger fraction of water (purchased from Penta Chemicals, maximum 0.3 % water content [196]), and the samples can therefore be expected to contain significant populations of both isomers.

Atomic Force Microscopy (AFM) was performed on thin layer samples of **P3HT**, and the newly prepared **PEAT** and **PMAT**. The AFM scans were done using a Burker NanoWizard microscope in the noncontact mode using the TESPA V2 cantilever. After the measurement, an automatically determined baseline was subtracted from all scanned lines to account for the internal vibrations of the cantilever. The samples for measurement were prepared by spin coating a thin layer of the polymer in question onto an Indium Tin Oxide (ITO)/glass substrate at 3000 revolutions per minute (rpm) for 60 seconds with a 30 s pre-spin at 1500 rpm. The solutions for spin coating were prepared by dissolving the polymer in question in chloroform (**$CHCl_3$**) in a 10 mg ml^{-1} concentration.

5.3 Software

To carry out the computations described above, the Gaussian 16 [197] program package was used, allowing for the simple use of a plethora of functionals and basis sets, with the corresponding corrections, e.g., range correction or empirical dispersion. The absorption spectra recording was done via the ASpectUV [198] program, provided by the manufacturer of the spectrometer. Similarly, the fluorescence measurements were recorded and processed using the FluorEssence [199] software. The computations were carried out with the use of the Metacentrum VO [200] infrastructure.

For the visualisations of molecular geometries, molecular orbitals and dipole moments, the Avogadro [201] and Molekel [202] freeware program packages were used, while crystallographic information was visualised with the Mercury [203] software. For processing the computational results and measured data, the MS Excel and Origin 2019 proprietary packages were used.

6 RESULTS AND DISCUSSION

In this part of the work, the results of the investigation into the different functional/basis combinations for alloxazines and lumazines will be presented, followed by the results of the explicit water solvation modelling. Selected theoretical singlet transition energies and oscillator strengths of both absorptions and emissions for the performed calculations are shown in **Tables 1S**–**6S** of the supplementary document. Afterwards, the structural parameters of the new adamantyl-substituted **PT**s will be discussed, and finally, the predicted properties of the novel adamantylated building blocks.

6.1 Flavins structure and spectroscopy

First, the lowest-energy conformations of the heterocycle-substituted lumazines and the N(1) and N(10) substituted lumichromes (**CHAL**) were found. In **Tab. 8**, the dihedral angles γ_1, γ_2, and δ of these conformations are given, as shown in **Fig. 14**. The angles γ_1, and γ_2 are always taken from the C atom opposite to the heteroatom, in order to take the asymmetry of heterocyclics into account. Thus, when both γ_1 and γ_2 have a positive or negative value, the molecule is arranged symmetrically, while if they do not have the same sign, the molecule is asymmetrical. The two arrangements are illustrated in **Fig. 14**. Further, the dihedral angle τ between the C(5)–C(6)–C(7)–C(8) atoms of the lumazine B ring is shown in **Tab. 8**. Molecules which have the heterocyclic substituents close to a planar arrangement, *i.e.*, 0 or 180 °, cause a large change of this dihedral, distorting the ring.

Further, the isomerisation introduces asymmetry into many of the **Lum** derivatives, as one of the heterocycles interacts with the N(10) hydrogen, and the other possibly increases the angle γ_2, in order to compensate for the distortion of the central moiety. This effect is the most pronounced in the Imidazole-substituted **ImiLum**, and in the oxygenated **FurLum**, where the asymmetry does not occur, but the shift of γ_2 is significant at – 20 °. On the other hand, the hypothetical **PyLum** derivative is the closest to a planar structure, but at the cost of a very large strain on the central rings. Since phenyl has no heteroatoms and no possibility to interact with the N(10) hydrogen, apart from slight repulsion, the **PheLum** structure remains the same.

Finally, the substituents in the N(1) and N(10) positions of CH have a dihedral δ dependent on their structure, with But and CF3 preferring a non-eclipsed conformation, and the planar phenyl and thiazole prefer a 90 °angle. The ribityl chain in N(1) interacts with the C(2)=O group, which leads to a large change in the dihedral versus the typically encountered riboflavin – **N10Rib** in this study. Further, with large substituents such as But and CF3, a bending of the isoalloxazine moiety is observed, as previously shown by North [119]. It seems that a pyramid-shaped substituent directly bound to N(10) is required to induce this effect since it is not present in **N10Rib**, **N10Phe** or **N10NS**, but it was observed for methyl in the N(10) position by North. Interestingly, the bend observed by North was not observed in the corresponding **N10CH$_3$** molecule in this study, possibly due to the difference in method, or the inclusion of the solvent model.

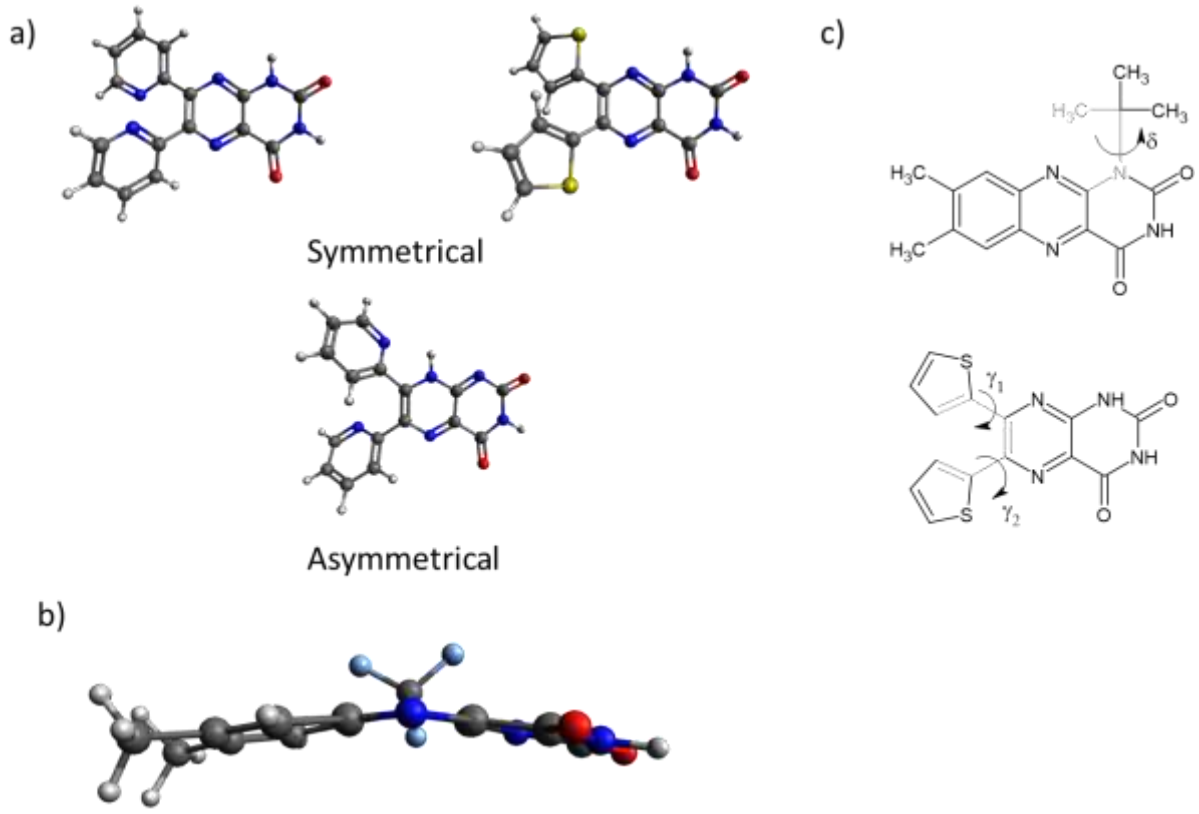

Fig. 14 *a) The symmetrical / asymmetrical arrangement of the lumazines, where yellow atoms are sulfur, blue atoms are nitrogen, and red atoms are oxygen; b) The structural bend of the B ring, observed with butyl and CF_3 substitutions into the N(10) position; c) A description of the respective angles.*

Tab. 8 *The dihedral angles of the lowest-energy configurations in the heterocycle-substituted* ***Lum*** *and the N(1) and N(10) substituted* ***CHAL****. Due to the negligible differences across basis sets, only def2SVP values are given.*

Molecule	γ_1 (°)	γ_2 (°)	τ (°)	Molecule	δ
PheLum	-149.089	-140.049	8.524	**N1But**	38.831
iPheLum	-135.309	-140.95	5.115	**N10But**	-123.206
ImiLum	145.013	149.624	-8.409	**N1CF$_3$**	60.001
iImiLum	28.396	-157.221	7.618	**N10CF$_3$**	79.495
PyLum	24.997	15.212	26.961	**N1NS**	100.008
iPyLum	14.725	13.822	24.977	**N10NS**	97.083
FurLum	-23.457	156.349	-9.174	**N1Phe**	82.198
iFurLum	-22.05	176.174	-6.438	**N10Phe**	89.502
ThLum	-24.741	-35.007	-10.899	**N1Rib**	63.192
iThLum	48.24	26.096	4.746	**N10Rib**	-75.045

The native **AL** molecule shows a high degree of aromaticity, with the HOMED index being 0.94, 0.93 and 0.83 for rings A, B and C, respectively. The isomerisation brings about a decrease in aromaticity, with **iAL** having the values 0.98, 0.87 and 0.68 in the three rings, obviously caused by the double bond shifting from ring B to ring C. Binding substituents in the N(1) or N(10) position decreases the aromaticity of the C and B ring respectively, due to deforming the rings, especially in the case of large three-dimensional substituents like CF_3 [JT2]. Interestingly, as more benzenes are fused to the A ring, the aromaticity also generally decreases, showing that the A ring geometry deviates from benzene [JT1].

The measured absorption and emission spectra are collected in **Figs. 15**, **16**. To keep the text simple, and because spectra are mostly reported that way in the literature, electronic spectra are discussed in terms of wavelength. The relevant values of energy are, however, shown in the figures and tables, and collected in the supplementary material. The results from the basis sets 6-31+G**, CAM-B3LYP/6-31+G**, def2SVP and aug-cc-PVDZ are given in tables **1S**, **2S**, **3S** and **4S**, respectively for absorption, and **5S** and **6S** for emissions. In **Figs. 15** and **16**, the spectra are arranged together with the predictions of the relevant basis sets, and CAM-B3LYP stands for the CAM-B3LYP / 6-31+G** method. To make the figures legible, two plots are given for each molecule, with the actual theoretical transitions summarized below in a table. To identify the transitions, numbers are placed next to the relevant bands, thus *e.g.*, the solid black band around 425 nm in the first alloxazine spectrum marked with a one, refers to the $S_0 \rightarrow S_1$ transition of **iAL** in the 6-31+G** basis. While the figures take up a lot of space, this seems to be the best way of presenting the results.

Since **AL**, **Lum**, **FAL**, and **ImiLum** were measured in the presence of water as well as pure DMSO, there is a possibility to find the alloxo- and isoalloxo-form peaks exactly. Indeed, the **AL** spectra seem to match those of Sikorska et. al. [110] for the isoalloxazine and alloxazine forms of **CHAL**. Since the methyl groups in the C(7) and C(8) positions are not expected to influence the absorption properties, the same should be applicable to **AL** and its derivatives. Therefore, **Fig. 15** shows spectra of the four aforementioned molecules in pure DMSO and in the presence of water, where the **AL** structure has notable peaks at 378 and 325 nm, which can be assigned to the $S_0 \rightarrow S_1$ ($373\ nm_{6\text{-}31+G^{**}}$), and $S_0 \rightarrow S_3$ ($325\ nm_{6\text{-}31+G^{**}}$) theoretical transitions, respectively. The **iAL** form in pure DMSO has notable peaks at 457 nm and a very large peak at 280 nm. These are slightly more problematic to match, since the computations generally underestimate the higher-λ peak, and overestimate the lower-λ one, e.g., $418\ nm_{6\text{-}31+G^{**}}$ and $299\ nm_{6\text{-}31+G^{**}}$, respectively. Although the UV-absorptive 280 nm peak is not of prime importance to optoelectronics, and it is not discussed as often as the visible-light absorptions. The coupled cluster basis set was found to have the smallest underestimation, predicting the isoalloxazine $S_0 \rightarrow S_1$ transition at $436\ nm_{aug\text{-}cc\text{-}PVDZ}$.

With regards to fluorescence, there is an **iAL** peak reported at 513 nm, well-matched by the $S_1 \rightarrow S_0$ transition ($513\ nm_{aug\text{-}cc\text{-}PVDZ}$), while the 426 nm peak, seen in the presence of water, is matched by the **AL** $S_1 \rightarrow S_0$ transition ($453\ nm_{aug\text{-}cc\text{-}PVDZ}$). The same considerations apply to all of the four molecules, therefore, for the sake of brevity, the relevant theoretical absorption

bands are shown in **Fig. 15**, and the precise energies and wavelengths are summarized in the tables given below the individual spectra.

Further, the effect of attaching a simple electron-withdrawing group is seen in **Fig. 15**. On the other hand, in the **FAL** spectrum, no such shifts in absorption or emission wavelength are seen, only the $S_2 \rightarrow S_0$ transition of **FAL** has a lowered intensity w.r.t. the **AL** spectrum. This is likely caused by the fact that the additional benzene ring of **AL** shields the rest of the moiety against the effect of the electron-withdrawing group.

The situation with the other molecules measured for this study – **Ph2**, **PyPh2**, **Phe**, **Pyr** – is more complicated. Their spectra are expected to contain the absorptions of both forms, and the theoretical absorption bands are often close together. The **Ph2** and **PyPh2** spectra contain very broad bands at 451 nm and 520 nm, respectively. It would be possible to match the $S_0 \rightarrow S_1$ excitations (516 $nm_{6\text{-}31+G^{**}}$ and 571 $nm_{6\text{-}31+G^{**}}$). They have oscillator strengths below 0.05, which corresponds to the low absorbance of the bands. On the other hand, significant oscillator strengths are predicted for the $S_0 \rightarrow S_3$ transitions – 372 $nm_{6\text{-}31+G^{**}}$ for **Ph2**, and 416 $nm_{6\text{-}31+G^{**}}$ for **PyPh2**. These in turn correspond to the vibronically resolved band of **Ph2** at 387 nm, and **PyPh2** at 435 nm. Finally, the predicted 409 $nm_{6\text{-}31+G^{**}}$ transition of the **iPh2** form, and the **iPyPh2** transition, predicted at 445 $nm_{6\text{-}31+G^{**}}$ likely contribute to these bands. As before, detailed spectra of the molecules are shown in **Fig. 16**, with the relevant values tabulated.

Comparing the results for **AL** and **Lum** in **Fig. 15** and the results for the larger fused derivatives in **Fig. 16**, the effect of the conjugation is visible. The 380 nm peak of **iLum** is shifted to around 450 nm after adding a benzene ring to form **AL**, and the shoulder of the 325 nm Lum peak, which occurs at around 375 nm grows into a high-absorbance band, that overshadows the 325 nm peak. This is accurately predicted by the used methods, since the predicted $S_0 \rightarrow S_2$ transition that is responsible for this band in **Lum** shifts into $S_0 \rightarrow S_1$ and $S_0 \rightarrow S_3$ transitions, which fit the spectrum well. A similar shift is seen in the $S_1 \rightarrow S_0$ transitions, although the methods predict the position of the **Lum** emission band quite poorly. As more rings are added, the transitions of the alloxazine and isoalloxazine form seem to move closer together and merge into a single absorption band in **Ph2** and **PyPh2**, where this change is surely caused by the presence of additional nitrogen atoms. The 2D structure of **Phe** retains the distinct iso and alloxazine transitions, although substantially red shifted. Finally, the $S_1 \rightarrow S_0$ transition of alloxazine appears to be shifted to 450 nm in **Pyr**, while the $S_1 \rightarrow S_0$ iso alloxazine transition is negligible in the measured spectrum. The addition of fused rings is also followed by the broadening of the absorption band at 280–300 nm in **iAL**, and participation of alloxazine-form peaks therein.

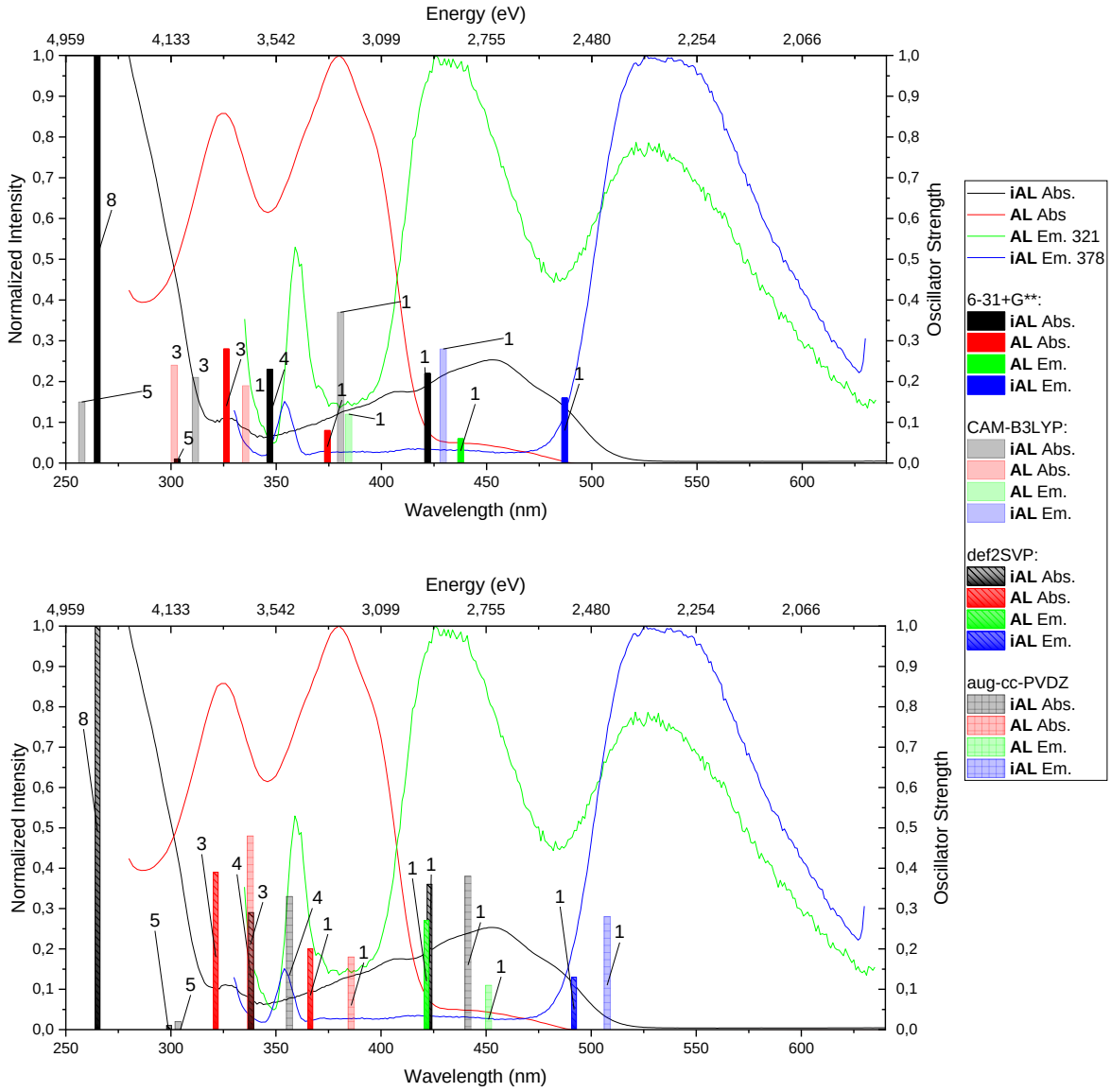

Experimental Wavelength (nm), Energy (eV)	6-31+G** Wavelength (nm), energy (eV)	CAM-B3LYP Wavelength (nm), energy (eV)	def2SVP Wavelength (nm), energy (eV)	aug-cc-PVDZ Wavelength (nm), energy (eV)
457 (2.713)	418_i (2.966) 0 → 1	376_i (3.297) 0 → 1	419_i (2.959) 0 → 1	436_i (2.844) 0 → 1
325 (3.815)	343_i (3.615) 0 → 4	307_i (4.039) 0 → 3	334_i (3.712) 0 → 4	351_i (3.532) 0 → 4
280 (4.428)	261_i (4.750) 0 → 8	253_i (4.901) 0 → 5	261_i (4.750) 0 → 8	298_i (4.161) 0 → 8
378 (3.280)	373 (3.324) 0 → 1	334 (3.712) 0 → 1	365 (3.397) 0 → 1	384 (3.229) 0 → 1
325 (3.815)	325 (3.815) 0 → 3	300 (4.133) 0 → 3	320 (3.874) 0 → 3	336 (3.690) 0 → 3
$520\ (2.384)_{Em}$	491_i (2.583) 1 → 0	434_i (2.857) 1 → 0	496_i (2.500) 1 → 0	513_i (2.417) 1 → 0
$426\ (2.910)_{Em}$	439 (2.525) 1 → 0	386 (3.212) 1 → 0	423 (2.931) 1 → 0	453 (2.737) 1 → 0

Fig. 15 *The measured absorption and emission spectra of* ***AL***, ***Lum***, ***FAL***, *and* ***ImiLum*** *the corresponding theoretical transitions with oscillator strengths given on the y-axis on the right. The numbers above transitions denote the target state for absorptions, and the initial state for emissions, so a 1 is an $S_0 \rightarrow S_1$ or $S_1 \rightarrow S_0$ transition, respectively. Exact positions of the experimental and theoretical peaks are given alongside the spectra. Furthermore, energy levels in the table are indicated by numbers (0 → 1 is the $S_0 \rightarrow S_1$ transition etc.) and theoretical transitions belonging to the iso form are marked by the subscript i. Emission is denoted by the subscript Em in the first column.*

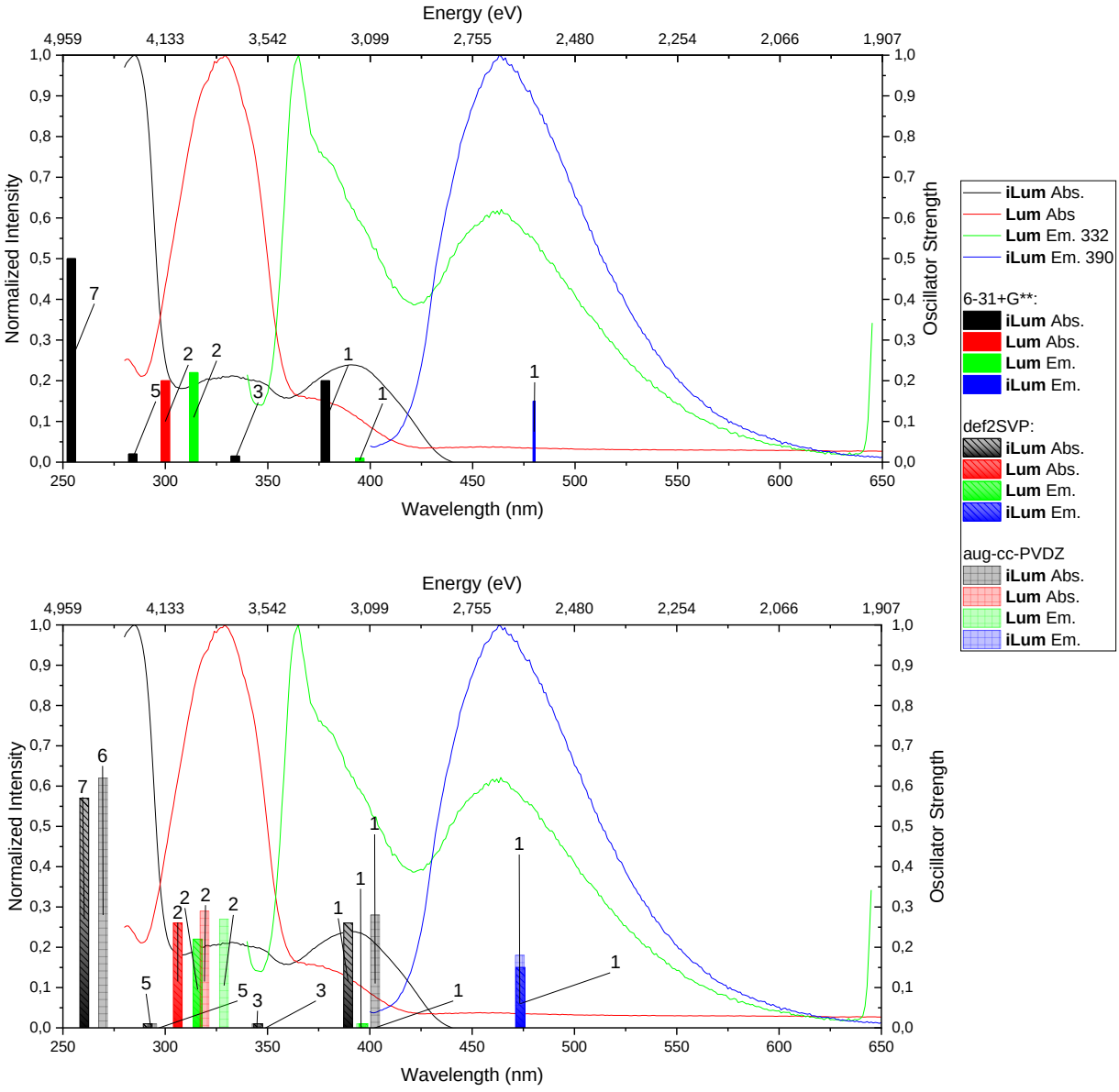

Experimental wavelength (nm), Energy (eV)	6-31+G** Wavelength (nm), energy (eV)	def2SVP Wavelength (nm), energy (eV)	aug-cc-PVDZ Wavelength (nm), energy (eV)
390 (3.179)	374_i (3.315) 0 → 1	383_i (3.237) 0 → 1	396_i (3.131) 0 → 1
332 (3.734)	330_i (3.757) 0 → 3	339_i (3.657) 0 → 3	338_i (3.668) 0 → 3
328 (3.780)	304 (4.078) 0 → 2	304 (4.078) 0 → 2	317 (3.911) 0 → 2
287 (4.320)	280_i (4.428) 0 → 5	285_i (4.350) 0 → 7	287_i (4.320) 0 → 6
$467\ (2.655)_{Em}$	480_i (2.583) 1 → 0	480_i (2.583) 1 → 0	480_i (2.583) 1 → 0
$377\ (3.289)_{Em}$	318 (3.899) 2 → 0	318 (3.899) 2 → 0	331 (3.746) 2 → 0

Fig. 15 (cont.) *The measured absorption and emission spectra of* ***AL***, ***Lum***, ***FAL***, ***CNLum***, *and* ***ImiLum*** *the corresponding theoretical transitions with oscillator strengths given on the y-axis on the right. The numbers above transitions denote the target state for absorptions, and the initial state for emissions, so a 1 is an $S_0 \rightarrow S_1$ or $S_1 \rightarrow S_0$ transition, respectively. Exact positions of the experimental and theoretical peaks are given alongside the spectra. Furthermore, energy levels in the table are indicated by numbers (0 → 1 is the $S_0 \rightarrow S_1$ transition etc.) and theoretical transitions belonging to the iso form are marked by the subscript i. Emission is denoted by the subscript Em in the first column.*

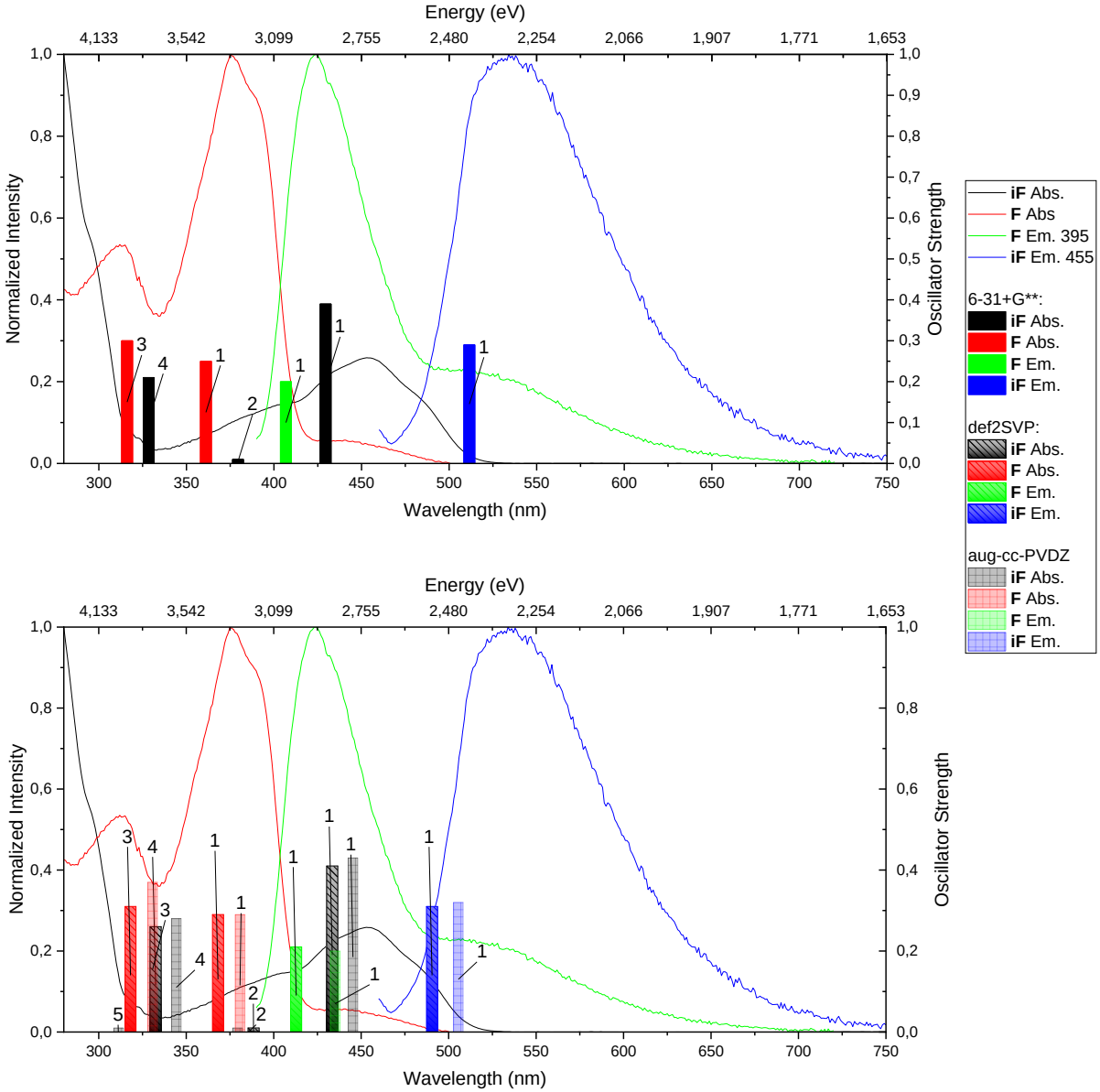

Experimental wavelength (nm), Energy (eV)	6-31+G** Wavelength (nm), energy (eV)	def2SVP Wavelength (nm), energy (eV)	aug-cc-PVDZ Wavelength (nm), energy (eV)
445 (2.786)	420_i (2.952) 0 → 1	424_i (2.924) 0 → 1	437_i (2.837) 0 → 1
395 (3.139)	370_i (3.351) 0 → 2	379_i (3.271) 0 → 2	371_i (3.342) 0 → 2
300 (4.133)	319_i (3.887) 0 → 4	323_i (3.839) 0 → 4	336_i (3.690) 0 → 4
376 (3.297)	358 (3.463) 0 → 1	365 (3.397) 0 → 1	378 (3.280) 0 → 1
317 (3.911)	313 (3.961) 0 → 3	315 (3.936) 0 → 3	328 (3.780) 0 → 3
$530\ (2.339)_{Em}$	521_i (2.380) 1 → 0	500_i (2.480) 1 → 0	514_i (2.412) 1 → 0
$427\ (2.904)_{Em}$	410 (2.904) 1 → 0	416 (2.980) 1 → 0	438 (2.831) 1 → 0

Fig. 15 (cont.) *The measured absorption and emission spectra of* ***AL***, ***Lum***, ***FAL***, ***CNLum***, *and* ***ImiLum*** *the corresponding theoretical transitions with oscillator strengths given on the y-axis on the right. The numbers above transitions denote the target state for absorptions, and the initial state for emissions, so a 1 is an $S_0 \rightarrow S_1$ or $S_1 \rightarrow S_0$ transition, respectively. Exact positions of the experimental and theoretical peaks are given alongside the spectra. Furthermore, energy levels in the table are indicated by numbers (0 → 1 is the $S_0 \rightarrow S_1$ transition etc.) and theoretical transitions belonging to the iso form are marked by the subscript i. Emission is denoted by the subscript Em in the first column.*

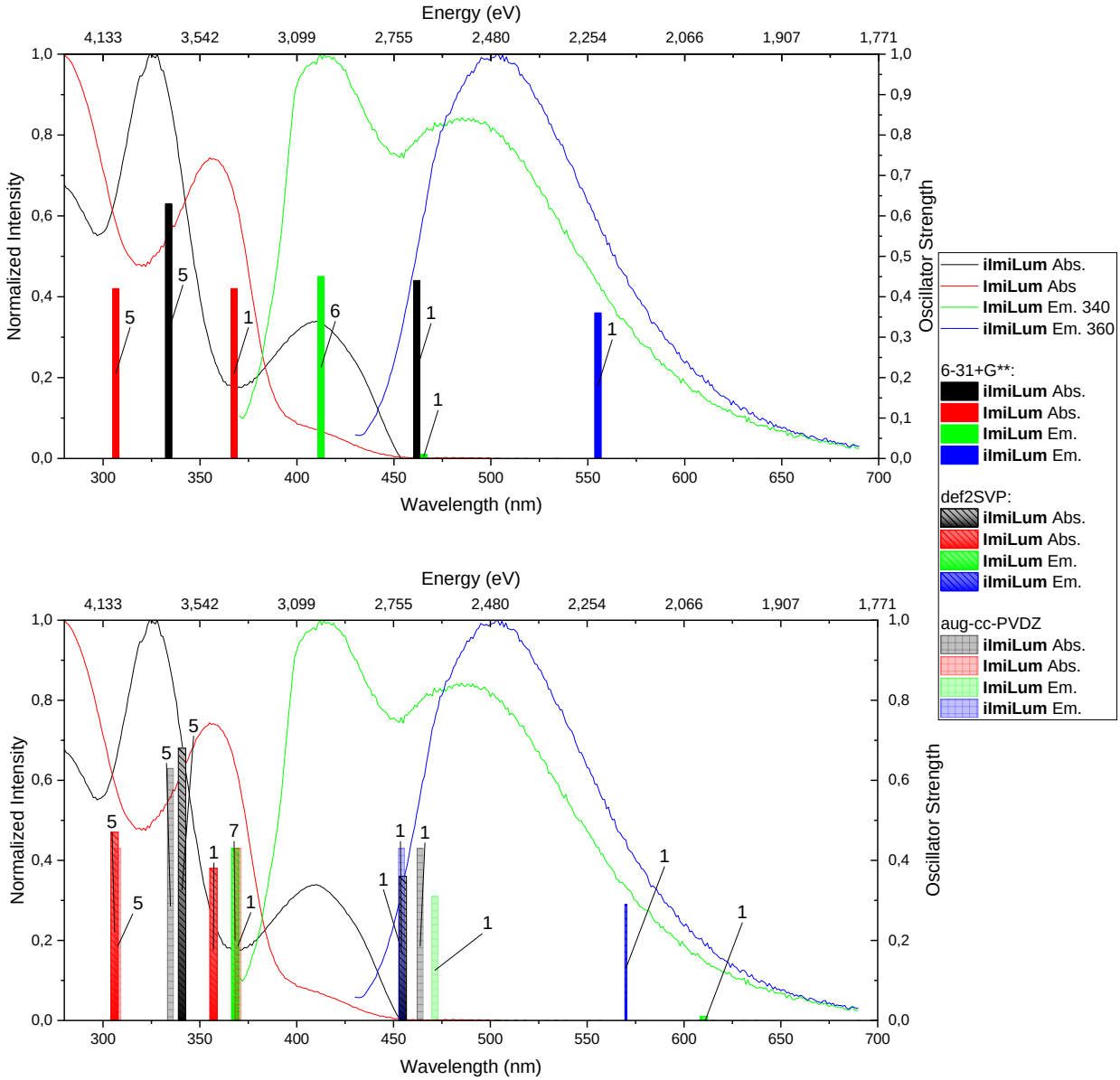

Experimental wavelength (nm), Energy (eV)	6-31+G** Wavelength (nm), energy (eV)	def2SVP Wavelength (nm), energy (eV)	aug-cc-PVDZ Wavelength (nm), energy (eV)
425 (2.917)	457_i (2.713) 0 → 1	451_i (2.749) 0 → 1	459_i (2.701) 0 → 1
320 (3.874)	329_i (3.769) 0 → 5	337_i (3.679) 0 → 5	330_i (3.757) 0 → 5
357 (3.473)	366 (3.388) 0 → 1	357 (3.473) 0 → 1	368 (3.369) 0 → 1
280 (4.133)	305 (4.065) 0 → 5	308 (4.025) 0 → 5	306 (4.052) 0 → 5
$500\ (2.480)_{Em}$	560_i (2.214) 1 → 0	570_i (2.175) 1 → 0	459 (2.701) 1 → 0
$410\ (3.024)_{Em}$	414 (2.995) 6 → 0	372 (3.333) 7 → 0	473 (2.621) 7 → 0

Fig. 15 (cont.) *The measured absorption and emission spectra of* ***AL***, ***Lum***, ***FAL***, *and* ***ImiLum*** *the corresponding theoretical transitions with oscillator strengths given on the y-axis on the right. The numbers above transitions denote the target state for absorptions, and the initial state for emissions, so a 1 is an $S_0 \rightarrow S_1$ or $S_1 \rightarrow S_0$ transition, respectively. Exact positions of the experimental and theoretical peaks are given alongside the spectra. Furthermore, energy levels are indicated by numbers ($0 \rightarrow 1$ is the $S_0 \rightarrow S_1$ transition etc.) and theoretical transitions belonging to the iso form are marked by the subscript i. Emission is denoted by the subscript Em in the first column.*

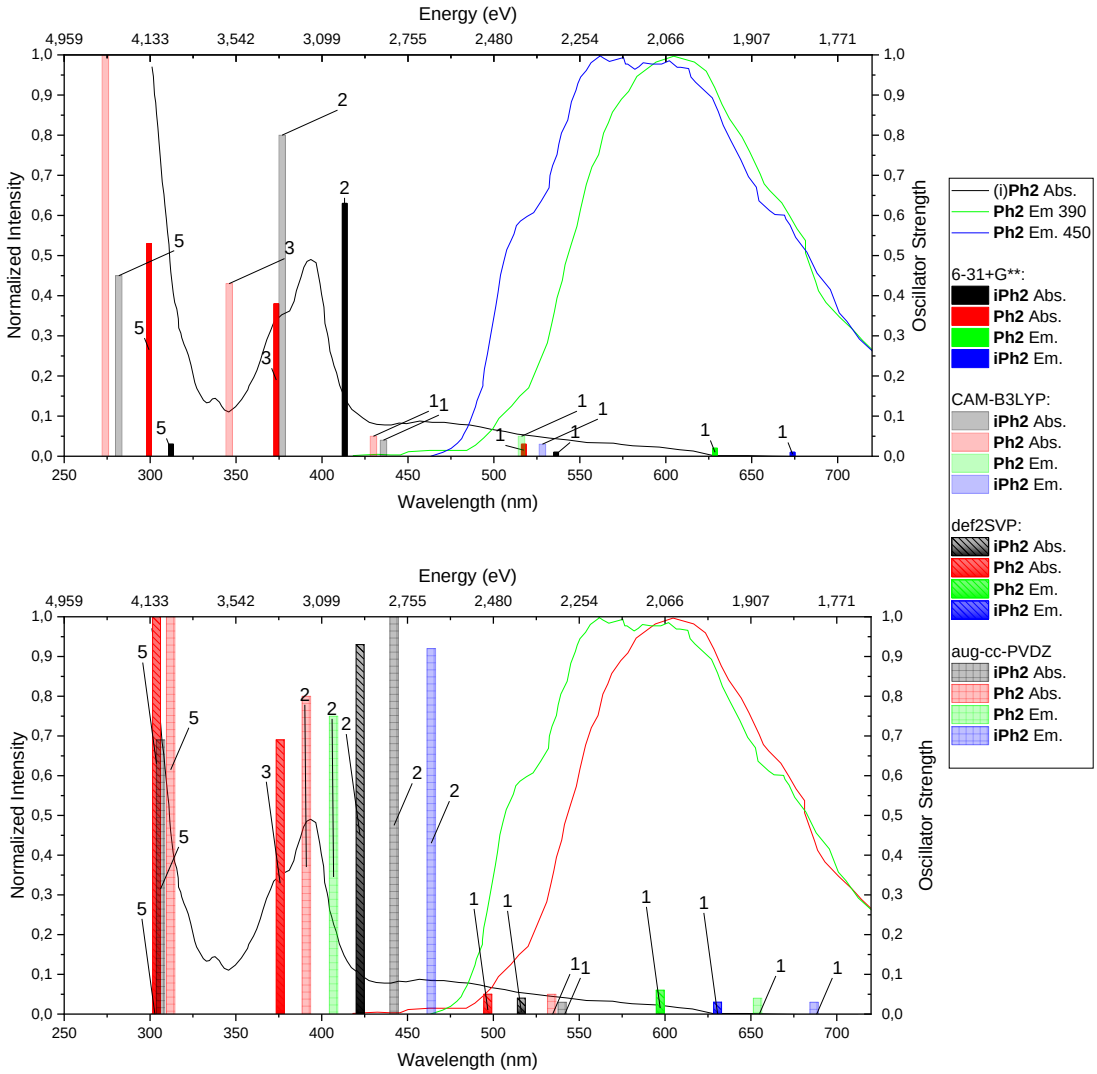

Experimental Wavelength (nm), Energy (eV)	6-31+G** Wavelength (nm), energy (eV)	CAM-B3LYP Wavelength (nm), energy (eV)	def2SVP Wavelength (nm), energy (eV)	aug-cc-PVDZ Wavelength (nm), energy (eV)
	532_i (2.331) 0 → 1	430_i (2.883) 0 → 1	508_i (2.441) 0 → 1	531_i (2.335) 0 → 1
516 (2.403)	516 (2.403) 0 → 1	371_i (3.342) 0 → 2	414_i (2.995) 0 → 2	433_i (2.863) 0 → 2
387 (3.204)	409_i (3.031) 0 → 2	428 (2.897) 0 → 1	494 (2.510) 0 → 1	531 (2.335) 0 → 1
280 (4.427)	372 (3.333) 0 → 3	344 (3.604) 0 → 3	373 (3.324) 0 → 3	388 (3.195) 0 → 3
	298 (4.161) 0 → 5	272 (4.558) 0 → 5	301 (4.119) 0 → 5	309 (4.012) 0 → 5
575 (2.156)$_{Em}$	678_i (1.829) 1 → 0	534_i (2.321) 1 → 0	639_i (1.940) 1 → 0	696_i (1.779) 1 → 0
	630 (1.968) 1 → 0	518i (2.393) 1 → 0	600 (2.066) 1 → 0	657 (1.886) 1 → 0

Fig. 16 *The measured absorption and emission spectra of* ***Ph2***, ***PyPh2***, ***Phe*** *and* ***Pyr***, *the corresponding theoretical transitions with oscillator strengths given on the y-axis on the right. The numbers above transitions denote the target state for absorptions, and the initial state for emissions, so a 1 is an $S_0 \rightarrow S_1$ or $S_1 \rightarrow S_0$ transition, respectively. Exact positions of the experimental and theoretical peaks are given alongside the spectra. Furthermore, energy levels are indicated by numbers ($0 \rightarrow 1$ is the $S_0 \rightarrow S_1$ transition etc.) and theoretical transitions belonging to the iso form are marked by the subscript i. Emission is denoted by the subscript Em in the first column.*

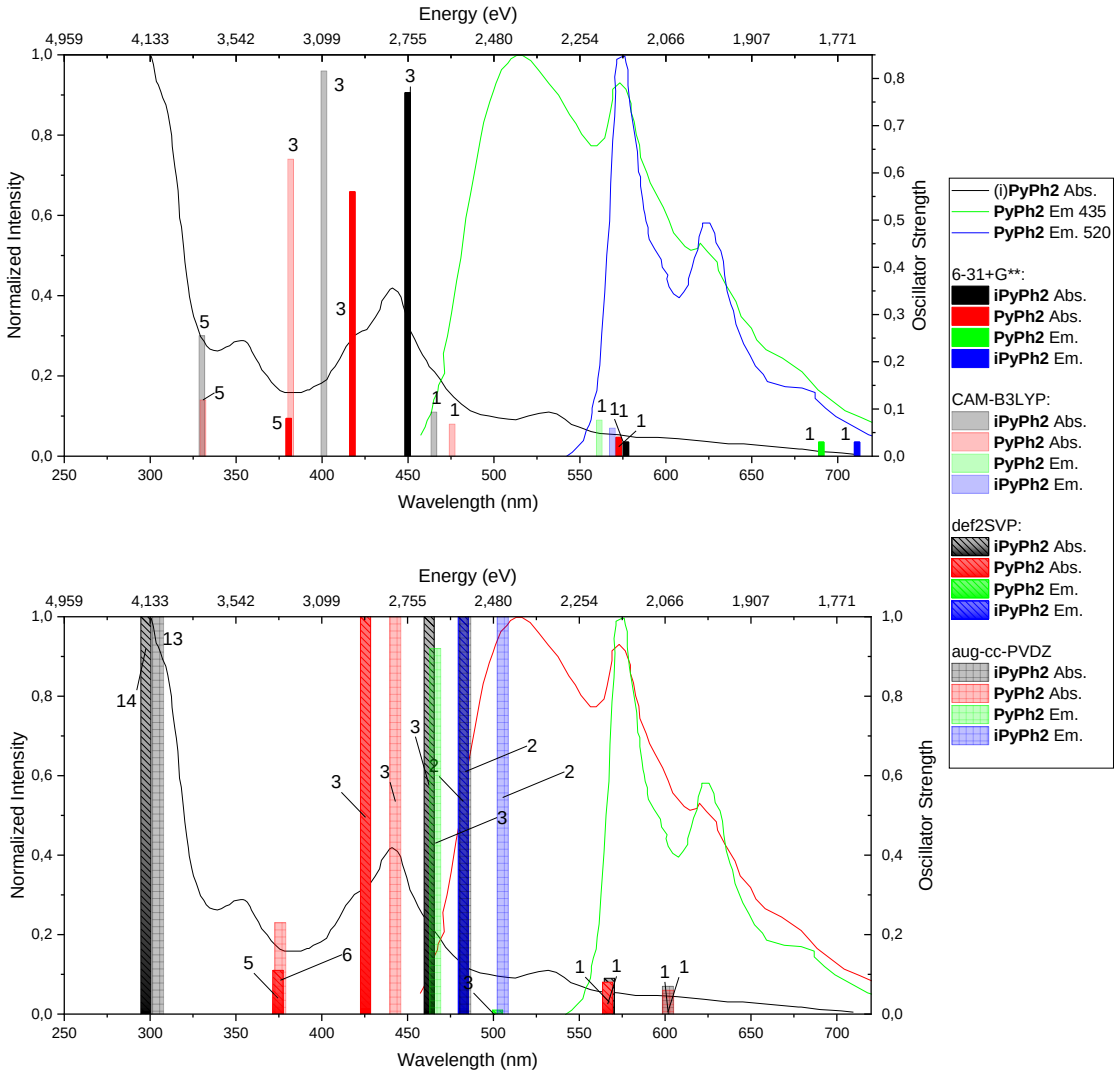

Experimental Wavelength (nm), Energy (eV)	6-31+G** Wavelength (nm), energy (eV)	CAM-B3LYP Wavelength (nm), energy (eV)	def2SVP Wavelength (nm), energy (eV)	aug-cc-PVDZ Wavelength (nm), energy (eV)
575 (2.156)	572_i (2.168) 0 → 1	460_i (2.695) 0 → 1	557_i (2.226) 0 → 1	590i (2.101) 0 → 1
435 (2.850)	445_i (2.786) 0 → 3	396_i (3.131) 0 → 3	452_i (2.743) 0 → 3	472i (2.627) 0 → 2
300 (4.133)	–	325_i (3.815) 0 → 5	287_i (4.320) 0 → 14	293_i (4.232) 0 → 13
416 (2.980)	416 (2.980) 0 → 3	380 (3.263) 0 → 3	422 (2.938) 0 → 3	439 (2.824) 0 → 3
356 (3.483)	379 (3.271) 0 → 5	329 (3.769) 0 → 5	371 (3.342) 0 → 5	372 (3.333) 0 → 6
$550\ (2.254)_{Em}$	716_i (2.313) 1 → 0	574_i (2.161) 1 → 0	493_i (2.515) 3 → 0	517_i (2.397) 1 → 0
$500\ (2.480)_{Em}$	692 (1.732) 1 → 0	563 (2.202) 1 → 0	506 (2.450) 2 → 0	470 (2.512) 1 → 0

Fig. 16 (cont.) *The measured absorption and emission spectra of* ***Ph2***, ***PyPh2***, ***Phe*** *and* ***Pyr***, *the corresponding theoretical transitions with oscillator strengths given on the y-axis on the right. The numbers above transitions denote the target state for absorptions, and the initial state for emissions, so a 1 is an $S_0 \rightarrow S_1$ or $S_1 \rightarrow S_0$ transition, respectively. Exact positions of the experimental and theoretical peaks are given alongside the spectra. Furthermore, energy levels are indicated by numbers ($0 \rightarrow 1$ is the $S_0 \rightarrow S_1$ transition etc.) and theoretical transitions belonging to the iso form are marked by the subscript i. Emission is denoted by the subscript Em in the first column.*

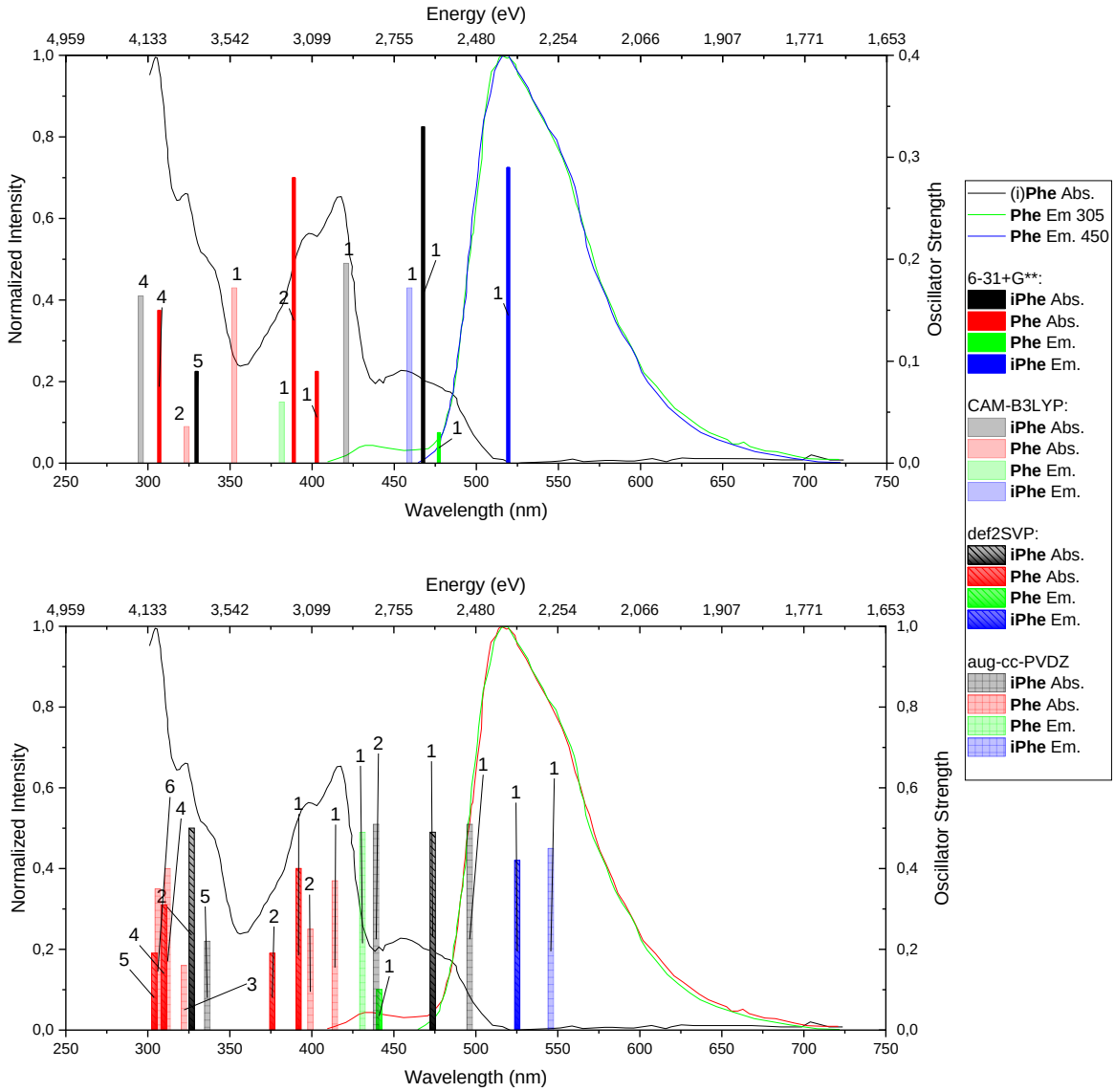

Experimental Wavelength (nm), Energy (eV)	6-31+G** Wavelength (nm), energy (eV)	CAM-B3LYP Wavelength (nm), energy (eV)	def2SVP Wavelength (nm), energy (eV)	aug-cc-PVDZ Wavelength (nm), energy (eV)
450 (2.755)	465_i (2.666) 0 → 1	416_i (2.980) 0 → 1	468_i (2.649) 0 → 1	433_i (2.863) 0 → 1
320 (3.874)	327_i (3.792) 0 → 5	291_i (4.261) 0 → 4	321_i (3.862) 0 → 1	330_i (3.757) 0 → 1
410 (3.024)	402 (3.084) 0 → 1	–	390 (3.179) 0 → 1	412 (3.009) 0 → 1
395 (3.139)	388 (3.195) 0 → 2	351 (3.532) 0 → 1	374 (3.315) 0 → 1	397 (3.123) 0 → 1
300 (4.133)	306 (4.052) 0 → 4	322 (3.850) 0 → 2	308 (4.025) 0 → 1	310 (3.999) 0 → 1
$500\ (2.480)_{Em}$	522_i (1.792) 1 → 0	464_i (3.239) 1 → 0	531_i (2.335) 1 → 0	552_i (2.242) 1 → 0
$420\ (2.952)_{Em}$	478 (2.375) 1 → 0	383 (2.673) 1 → 0	443 (2.799) 1 → 0	433 (2.858) 1 → 0

Fig. 16 (cont.) *The measured absorption and emission spectra of* ***Ph2***, ***PyPh2***, ***Phe*** *and* ***Pyr***, *the corresponding theoretical transitions with oscillator strengths given on the y-axis on the right. The numbers above transitions denote the target state for absorptions, and the initial state for emissions, so a 1 is an $S_0 \rightarrow S_1$ or $S_1 \rightarrow S_0$ transition, respectively. Exact positions of the experimental and theoretical peaks are given alongside the spectra. Furthermore, energy levels are indicated by numbers ($0 \rightarrow 1$ is the $S_0 \rightarrow S_1$ transition etc.) and theoretical transitions belonging to the iso form are marked by the subscript i. Emission is denoted by the subscript Em in the first column.*

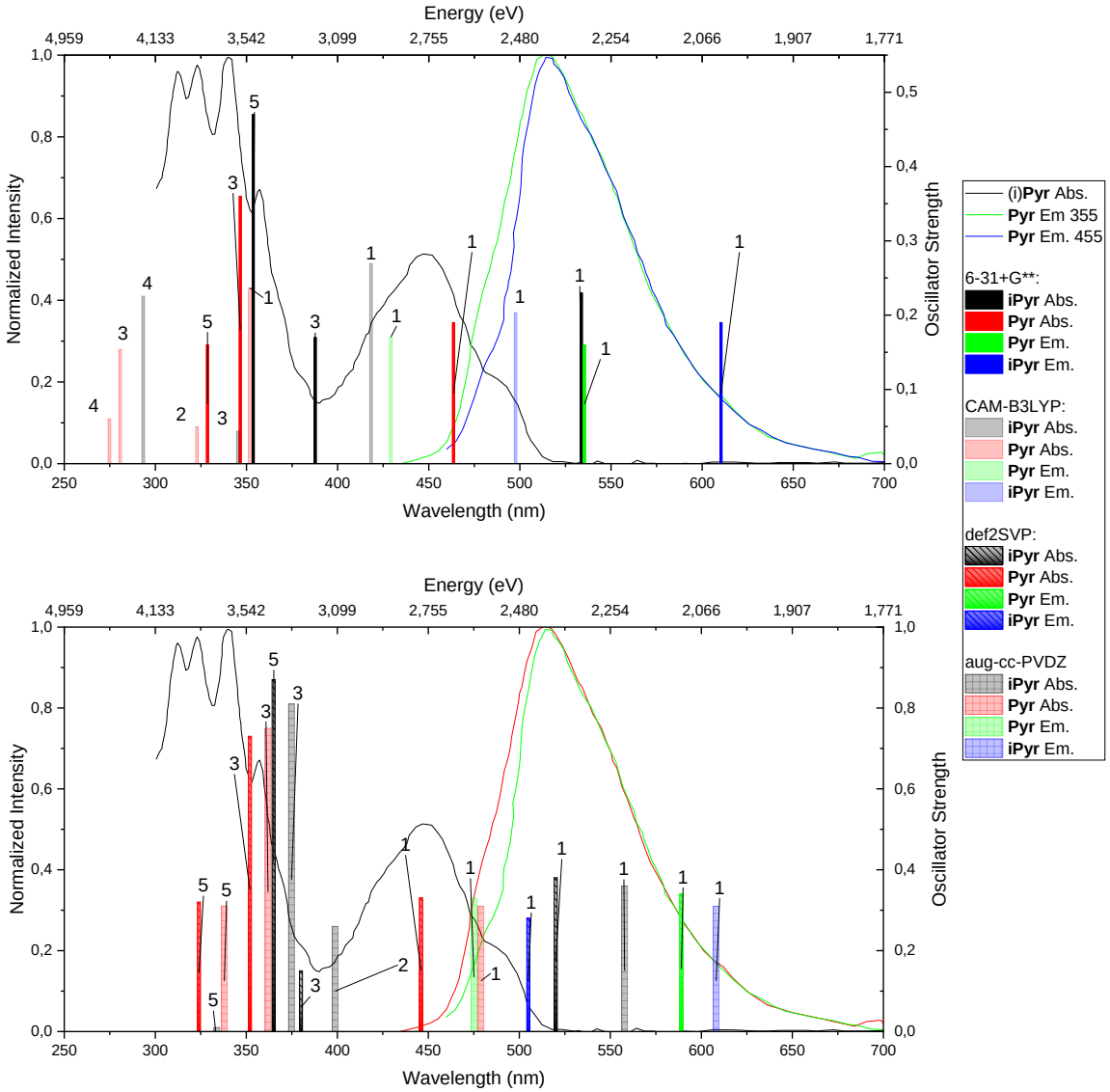

Experimental Wavelength (nm), Energy (eV)	6-31+G** Wavelength (nm), energy (eV)	CAM-B3LYP Wavelength (nm), energy (eV)	def2SVP Wavelength (nm), energy (eV)	aug-cc-PVDZ Wavelength (nm), energy (eV)
486 (2.551)	532_i (2.331) 0 → 1	416_i (2.980) 0 → 1	517_i (2.398) 0 → 1	552_i (2.246) 0 → 1
370 (3.351)	386_i (3.212) 0 → 3	343_i (3.615) 0 → 2	377_i (3.289) 0 → 3	369_i (3.360) 0 → 3
350 (3.542)	352_i (3.522) 0 → 5	291_i (4.261) 0 → 4	362_i (3.425) 0 → 5	328_i (3.780) 0 → 5
455 (2.725)	463 (2.678) 0 → 1	351 (3.532) 0 → 1	445 (2.786) 0 → 1	477 (2.599) 0 → 1
340 (3.647)	346 (3.583) 0 → 3	322 (3.850) 0 → 2	351 (3.532) 0 → 3	360 (3.444) 0 → 3
330 (3.757)	328 (3.780) 0 → 5	280 (4.428) 0 → 4	323 (3.839) 0 → 5	336 (3.690) 0 → 5
$510\ (2.431)_{Em}$	612_i (2.026) 1 → 0	500_i (2.481) 1 → 0	590_i (2.101) 1 → 0	614_i (2.016) 1 → 0
$510\ (2.431)_{Em}$	536 (2.313) 1 → 0	430 (2.883) 1 → 0	508 (2.441) 1 → 0	477 (2.598) 1 → 0

Fig. 16 (cont.) *The measured absorption and emission spectra of **Ph2**, **PyPh2**, **Phe** and **Pyr**, the corresponding theoretical transitions with oscillator strengths given on the y-axis on the right. The numbers above transitions denote the target state for absorptions, and the initial state for emissions, so a 1 is an $S_0 \rightarrow S_1$ or $S_1 \rightarrow S_0$ transition, respectively. Exact positions of the experimental and theoretical peaks are given alongside the spectra. Furthermore, energy levels are indicated by numbers ($0 \rightarrow 1$ is the $S_0 \rightarrow S_1$ transition etc.) and theoretical transitions belonging to the iso form are marked by the subscript i. Emission is denoted by the subscript Em in the first column.*

The absorption spectra for the heterocycle-substituted lumazines were measured by Richtar et. al. [74] and are used as reference. While the authors have provided exact wavelengths of absorption and emission global maxima, they have not done so for other bands. Especially in the case of emission, the bands are very broad, and it is difficult to exactly assign a theoretical transition. In lieu of originally measured spectra, **Tab. 9** shows the positions of absorption and emission bands of **PheLum**, **FurLum**, and **ThLum**, and the transitions assigned to the relevant basis sets. The absorption bands of riboflavin (**N10Rib**) measured by Daidone [173] are also included. Unfortunately, Daidone et. al. have not published an emission spectrum of riboflavin.

Due to the broad fluorescence bands, and the fact that the method in this work was optimized for ground-state molecules and absorption predictions, the predicted emissions do not correlate satisfactorily with the experiment. However, as shown in **Figs. 15** and **16** and in **Tab. 9**, there is at least a qualitative agreement, especially for the aug-cc-PVDZ basis set, and when considering the several hundred nanometres thick absorption bands measured in ref. [74]. Interestingly, while the calculations typically underestimate the **iAL** and **iLum** absorptions as seen above, the opposite is true in the case of heterocyclic substitution, where the $S_0 \rightarrow S_1$ transitions of **iPheLum** and **iThLum** are notable outliers, being overestimated by around 35 nm by both the aug-cc-PVDZ and 6-31+G** sets and placed theoretically outside of the very broad measured absorption bands, which could be caused by the presence of other conformations than the absolute energetic minimum. On the other hand, in the **ThLum** spectrum in [74], there is a small shoulder at around 525 nm, which could correspond to this **iThLum** transition. Then, the major peak at 470 nm would be caused by the $S_0 \rightarrow S_1$ transition of **ThLum**, and the fit becomes much better. On the other hand, the original authors have shown the absorption of **ThLum** to end around 460 nm, which is not enough to disqualify its transition from taking part in the spectrum. Furthermore, the band assigned to **iThLum** itself is broad, and the actual position of the peak could be up to debate. Therefore, it is tempting to assign the theoretical transitions as described above, but not possible in good conscience. Thus, for the purpose of this work, the **iThLum** peak was located between 450–500 nm and is likely a superposition of the $S_0 \rightarrow S_1$ excitations of both isomers.

A similar problem applies to the **PheLum** derivative, which has a more resolved spectrum, and the transitions at 460 $nm_{6\text{-}31+G^{**}}$ and 462 $nm_{aug\text{-}cc\text{-}PVDZ}$ are overestimated without ambiguity. This overestimation seems to be caused by the diffuse functions overestimating the conjugation in the molecules, since it is not as large in the def2SVP values, and the transition at 446 nm could actually be accepted as a part of the **iPheLum** band. Otherwise, the theoretical predictions are within 30 nm of experimental values, which is an acceptable outcome concerning the SCRF model.

Tab. 9 *The absorption and emission bands of* ***PheLum****,* ***FurLum****, and* ***ThLum*** *as found by Richtar et al. [74], and* ***N10Rib*** *from the work of Daidone [173]. The relevant energy values are given in parentheses. Furthermore, energy levels are indicated by numbers (0 → 1 is the $S_1 \rightarrow S_0$ transition etc.) and theoretical transitions belonging to the iso form are marked by the subscript i;*) it is unclear from visual inspection of the spectrum where the absorption band actually lies, although the authors have placed it originally at 477 nm, it seems to be closer to 500 nm, see also discussion above.*

Molecule	Absorption wavelength (nm), energy (eV)	6-31+G** Absorption wavelength (nm), energy (eV)	def2SVP Absorption wavelength (nm), energy (eV)	aug-cc-PVDZ Absorption wavelength (nm), energy (eV)
PheLum	425 (2.917)	460_i (2.695) 0 → 1	446_i (2.780) 0 → 1	462_i (2.684) 0 → 1
	363 (3.416)	386 (3.212) 0 → 1	371 (3.342) 0 → 1	386 (3.212) 0 → 1
	310 (3.999)	312_i (3.974) 0 → 4	321_i (3.862) 0 → 5	310_i (3.999) 0 → 8
	290 (4.275)	307 (4.038) 0 → 5	293 (4.231) 0 → 5	283 (4.381) 0 → 8
FurLum	495 (2.505)	523_i (2.371) 0 → 1	517_i (2.398) 0 → 1	522_i (2.375) 0 → 1
	419 (2.959)	437 (2.837) 0 → 1	420 (2.952) 0 → 1	438 (2.831) 0 → 1
	358 (3.542)	350 (3.542) 0 → 4	347 (3.573) 0 → 2	357 (3.791) 0 → 1
	320 (3.874)	325_i (3.815) 0 → 4	350_i (3.542) 0 → 4	327_i (3.594) 0 → 1
	280 (4.428)	284 (4.365) 0 → 6	287 (4.320) 0 → 5	289 (4.290) 0 → 1
ThLum	*500 (2.480)	537_i (2.309) 0 → 1	513_i (2.417) 0 → 1	538_i (2.304) 0 → 1
	430 (2.917)	451 (2.749) 0 → 1	430 (2.883) 0 → 1	454 (2.731) 0 → 1
	393 (3.155)	373_i (3.324) 0 → 3	368_i (3.369) 0 → 2	375 (3.306) 0 → 2
	320 (3.874)	326_i (3.369) 0 → 3	337_i (3.679) 0 → 5	322_i (3.850) 0 → 5
	300 (4.133)	302 (4.105) 0 → 5	314 (3.948) 0 → 5	303 (4.092) 0 → 6
N10Rib	440 (2.818)	Not evaluated due to convergence problems	426 (2.910) 0 → 1	440 (2.818) 0 → 1
	350 (3.542)		360 (3.444) 0 → 3	353 (3.512) 0 → 3
Molecule	Emission wavelength (nm), Energy (eV)	6-31+G** Emission wavelength (nm), energy (eV)	def2SVP Emission wavelength (nm), energy (eV)	Aug-cc-PVDZ Emission wavelength (nm), energy (eV)
PheLum	500 (2.480)	557_i (2.226) 1 → 0	554_i (2.238) 1 → 0	488_i (2.541) 1 → 0
	430 (2.883)	472 (2.627) 1 → 0	470 (2.638) 1 → 0	462 (2.684) 1 → 0
FurLum	515 (2.407)	643_i (1.928) 1 → 0	614_i (2.019) 1 → 0	647_i (1.916) 1 → 0
	450 (2.755)	533 (2.326) 1 → 0	499 (2.485) 1 → 0	536 (2.313) 1 → 0
ThLum	525 (2.362)	562_i (2.206) 1 → 0	544_i (3.031) 1 → 0	566_i (2.190) 1 → 0
	475 (2.610)	419 (2.959) 2 → 0	409 (1.893) 2 → 0	424 (2.924) 2 → 0

Next, statistically significant fits of the experimental and predicted values have been by the procedure described above. The CAM-B3LYP functional proved to have the worst fit, with a systematic underestimation of the excitation energies. Therefore, this functional was abandoned early on. **Figure 17** shows the linear regressions of the fits described above, for the best performing basis sets – 6-31+G** and aug-cc-PVDZ – in terms of the wavelengths and energies. The fits of the two other methods are summarized in **Tab. 10**. In these fits, the theoretical values are used as the independent variable on the *x*-axis, while experimental values are the dependent variable, plotted on the *y*-axis. Thus, if the slope is larger than one, the

experimental values are generally larger than the predictions, and the model tends to underestimate, and vice versa when the slope is less than one. Further, there is a slight discrepancy between the energy and wavelength fits, as seen in **Fig. 17** this is likely caused by the computational errors introduced by converting the experimental wavelength data into energy values. Therefore, the wavelength data are believed to be a better fit, since they are only burdened by the measurement error of the spectrometer. Apart from that, it is difficult to compare the fits of wavelength and energy due to the nonlinear relationship between the two quantities.

Previously [JT1], a significant correlation with the alloxazine forms of **AL**, **Ph2 PyPh2**, **Pyr** and **Phe** was found, with a correlation coefficient of 0.97 with the 6-31+G** basis set. In the present work, the isoalloxazine forms were included, together with the lumazine-type molecules, in order to see if the same model can be applied to both types of molecules. Generally, the fit is slightly worsened by adding the **Lum**-type molecules, especially their iso forms, due to the inconsistency in underestimating **iAL** peaks, while overestimating substituted **iLum** peaks. On the other hand, the correlation coefficients stay around 0.95 and while the exclusion of isoalloxazine form aids the fit slightly, it does not have a significant effect. For comparison, the fits without isoalloxazine values are included in the tables in **Fig. 17** and **Tab. 10**.

As seen below, the 6-31+G** and aug-cc-PVDZ basis sets have a comparable correlation coefficient, with the def2SVP set being slightly worse. On the other hand, the def2SVP fit line is the closest to $y = x$, meaning the values are accurate, but lack precision, and have a larger spread than the other methods. At the same time, the aug-cc-PVDZ basis set has the greatest overestimation, which may be caused by overestimating the degree of π-conjugation, thus calculating the orbital gaps too low. There are also notable outliers from this basis set, which are the **iPh2** $S_0 \rightarrow S_2$ transition, the **iPyr** $S_0 \rightarrow S_1$ transition, and the **iF** $S_0 \rightarrow S_4$ transition. It is therefore no surprise, that when the iso-forms are excluded, the aug-cc-PVDZ fit is the best.

There are also visible aggregates in **Fig. 17**, especially around the y = 300 nm and y = 280 nm lines. This is caused by reading values from experimental spectra, where the absorption band at 280–300 nm is often not clearly resolved, and multiple molecules get this wavelength assigned due to experimental imprecision. Therefore, deleting the iso-forms from the dataset automatically improves all fits, since these ambiguities are at least in part removed. The electron-withdrawing substituted **FAL** molecule is overestimated respectively in the $S_0 \rightarrow S_4$ transition by all basis sets. Similarly, the **Ph2** $S_0 \rightarrow S_5$ transition is consistently overestimated. Finally, the cluster seen around the y = 450 nm line is the product of underestimating the $S_0 \rightarrow S_1$ transition of isoalloxazine isomers, as already mentioned earlier.

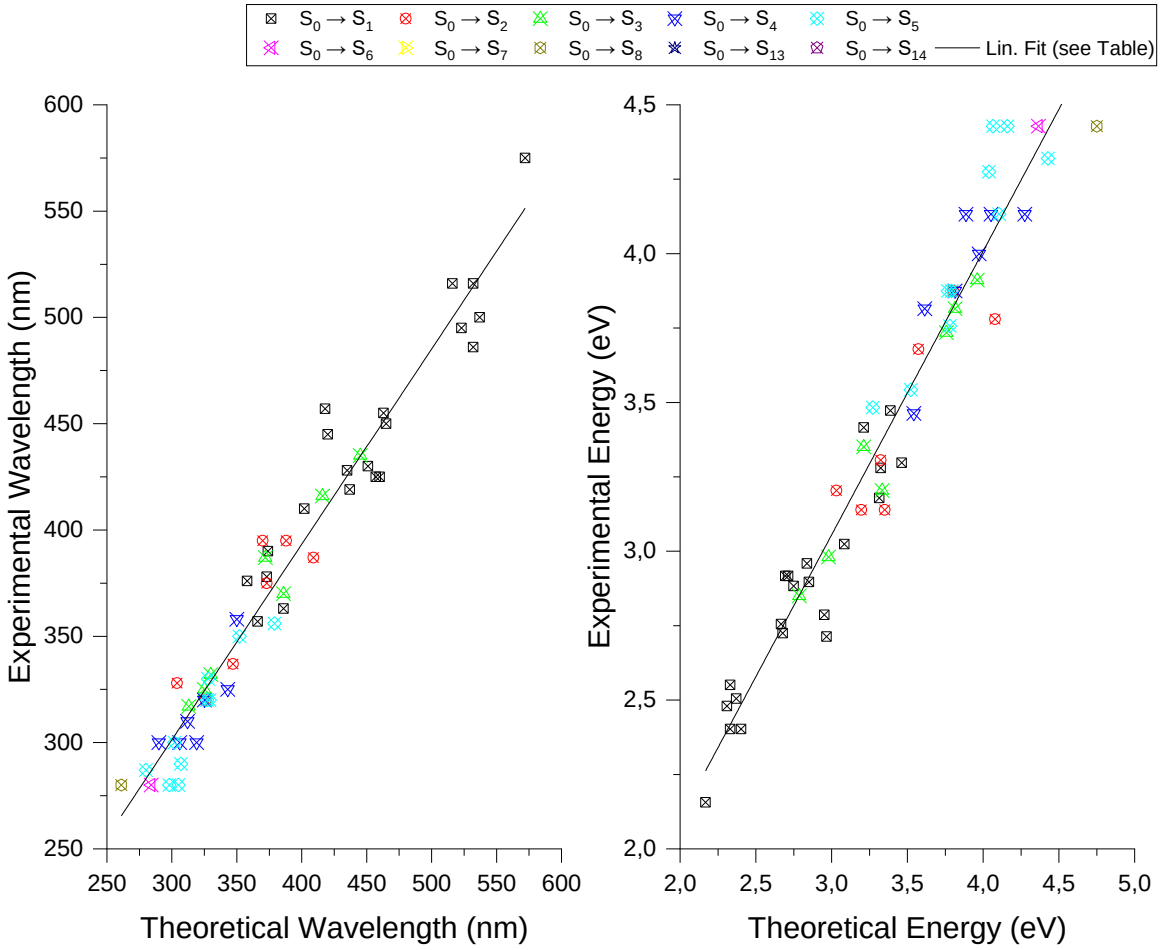

Basis set	6-31+G**	6-31+G** No iso forms
Linear Fit (Wavelength, nm)	$\lambda_{exp} = 0{,}919 \cdot \lambda_{teor} + 25{,}638$	$\lambda_{exp} = 0{,}970 \cdot \lambda_{teor} + 8{,}704$
R	0,951	0,953
Linear Fit (Energy, eV)	$E_{exp} = 0{,}953 \cdot E_{teor} + 0{,}195$	$E_{exp} = 0{,}987 \cdot E_{teor} + 0{,}067$
R	0,944	0,936

Fig. 17 *The obtained linear dependences for the 6-31+G**, def2SVP, and aug-cc-PVDZ computations, in terms of both wavelength on the left and energy on the right. Information about the fit is given in the tables.*

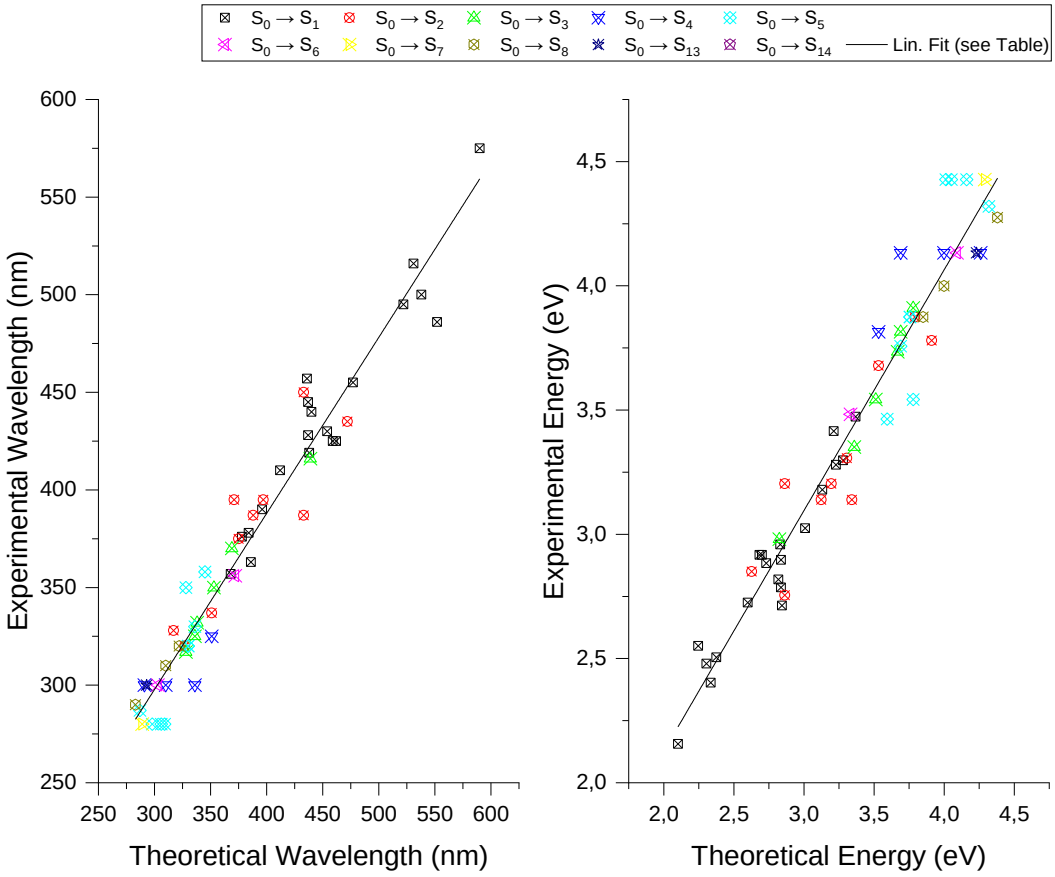

Basis set	aug-cc-PVDZ	aug-cc-PVDZ No iso forms
Linear Fit (Wavelength, nm)	$\lambda_{exp} = 0{,}902 \cdot \lambda_{teor} + 27{,}253$	$\lambda_{exp} = 0{,}920 \cdot \lambda_{teor} + 20{,}526$
R	0,951	0,970
Linear Fit (Energy eV)	$E_{exp} = 0{,}969 \cdot E_{teor} + 0{,}189$	$E_{exp} = 0{,}961 \cdot E_{teor} + 0{,}214$
R	0,944	0,952

Fig. 17 (cont.) *The obtained linear dependences for the 6-31+G**, def2SVP, and aug-cc-PVDZ computations, in terms of both wavelength on the left and energy on the right. Information about the fit is given in the tables.*

Tab. 10 *The summary of the linear fits of CAM-B3LYP/6-31+G** and B3LYP/def2SVP theoretical and experimental spectra.*

Basis set	CAM-B3LYP/6-31+G**	6-31+G** No iso forms
Linear Fit (Wavelength, nm)	$\lambda_{exp} = 1{,}366 \cdot \lambda_{teor} - 85{,}686$	$\lambda_{exp} = 0{,}970 \cdot \lambda_{teor} - 105{,}197$
R	0,876	0,825
Linear Fit (Energy, eV)	$E_{exp} = 1{,}032 \cdot E_{teor} - 0{,}460$	$E_{exp} = 1{,}110 \cdot E_{teor} - 0{,}759$
R	0,839	0,786
Basis set	def2SVP	def2SVP No iso forms
Linear Fit (Wavelength, nm)	$\lambda_{exp} = 0{,}990 \cdot \lambda_{teor} + 1{,}840$	$\lambda_{exp} = 1{,}079 \cdot \lambda_{teor} - 25{,}442$
R	0,948	0,954
Linear Fit (Energy, eV)	$E_{exp} = 0{,}991 \cdot E_{teor} + 0{,}051$	$E_{exp} = 1{,}054 \cdot E_{teor} - 0{,}204$
R	0,936	0,933

Some selected molecular orbitals are shown in **Fig. 18**, depicted as iso-surfaces of the value 0.025 au. Since no qualitative differences were found across the basis sets, only 6-31+G** orbitals are presented, so as not to complicate the text. First, the MOs of both isomers of alloxazine and lumazine are shown for reference. A visual comparison of these molecules also shows how the frontier orbitals delocalise across the larger conjugated system. This is continued with **Ph2**, and **Pyr**, clearly, the HOMO and LUMO delocalisation grows with the size of the conjugated system. Further, other orbitals participate in the strong electronic transitions and are shown as needed. This further illustrates the influence of modification on the electronic structure. Only alloxazine-form molecules are included since the differences between isomers are negligible. The iso-form orbitals are given in **Fig. 1S** of the supplementary material.

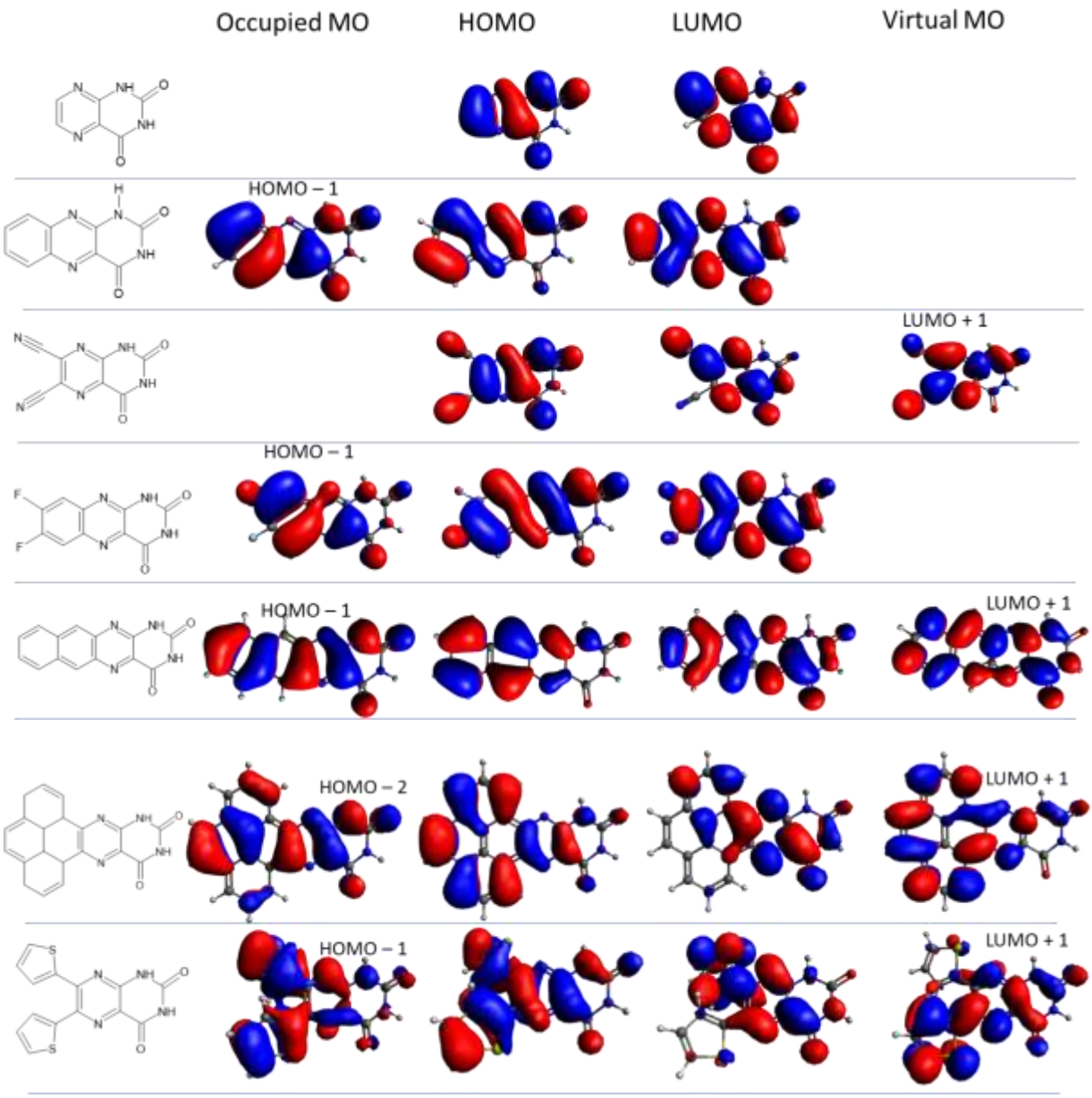

Fig. 18 *Selected molecular orbitals. Apart from HOMO and LUMO, other orbitals that take part in significant electronic transitions are shown. The relevant structures are included to assist in interpreting the figure.*

Finally, knowledge of the HOMO/LUMO gaps and energy levels can be useful for device engineering in optoelectronics, where the alignment of molecular energy levels across different materials plays a decisive role (see **Section 2.6**). Therefore, a brief overview of the energy levels is now presented, accompanied by an illustration in **Fig. 19**. The results of the two well-performing basis sets, 6-31+G** and aug-cc-PVDZ, have been selected for this part.

Generally, the isoalloxazine / isolumazine form has a smaller HOMO/LUMO gap, as predicted by Chang [112]. The large conjugated **Ph2**, **Ph3**, and **PhePh2** molecules appear to be exceptions to this rule, although there is no experimental confirmation currently. Indeed, the available measurements by Richtar [74] and Golczak [93] do not indicate this to be the case for **Ph2**.

Further, the strong electron-withdrawing group seems to have a profound effect on **Lum**, with the gaps of **CNLum** being around 0.4 eV lower than those of **Lum**. On the other hand, the energy levels of **FAL** remain essentially unchanged w.r.t. **AL**. Substituents in the N(1) or N(10) positions have very little effect on FMOs, except for $–CF_3$, which lowers the **iAL** gap by around 0.1 eV. The effect of these substituents would likely have been bigger if they contained a heteroatom bound directly to the N(1) or N(10) positions. However, with the current molecules, it seems that the N(1) or N(10) substitution can be freely used for controlling solvation or crystal packing properties, and the alloxazine or isoalloxazine properties will be retained.

As the conjugated system grows, the HOMO/LUMO gap predictably decreases, and in the extreme case of very large molecules such as **PhePh2**, it is lowered by around 1.5 eV w.r.t. the parent molecule **AL** or **iAL**. On the other hand, substituting heterocycles in the C(6) and C(7) positions of **Lum** consistently lowers the respective HOMO/LUMO gaps by around 1.5 eV. In this context, both enlarging the fused system, and substituting freely rotating rings seem to be valid design strategies for tuning the electronic structure of the molecules.

The 6-31+G** basis set consistently gives larger values than aug-cc-PVDZ, as seen in **Fig. 19**. Interestingly, both basis sets seem to be in complete agreement on the heterocycle-substituted lumazines. This could be caused by the fact that the **Lum** geometry is distorted by the substitution, thus cutting off the conjugation and not giving the aug-cc-PVDZ basis the chance to overestimate. Further, the two sets agree in the cases of very large fused molecules, such as **Pyr** or **PhePh**, suggesting that there is a limit of conjugated double bonds, where both sets reliably converge.

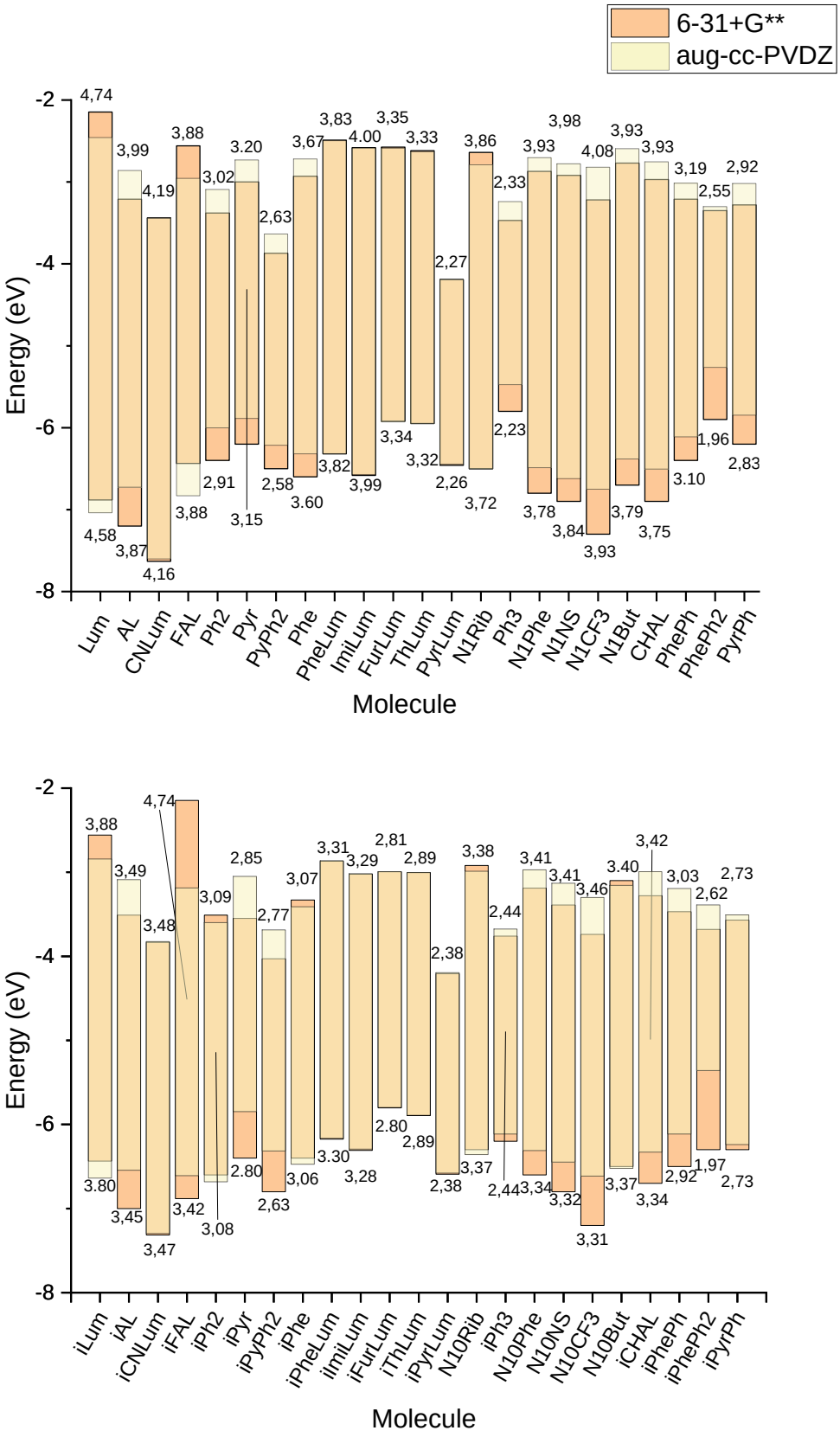

Fig. 19 *The HOMO and LUMO energy levels and associated gaps of the molecules in this study. Values gained from the aug-cc-PVDZ set are shown as semitransparent, values from the 6-31+G** set are in solid colours. HOMO/LUMO Gap values of 6-31+G** are on the top, values from aug-cc-PVDZ are on the bottom of the columns.*

6.2 Adamantylated Thiophene Building Blocks

As mentioned in **Section 5.1**, a study of model octamers in two ideal all-trans arrangements was performed. For the *syn*-conformers, this leads to a helical structure, while the anti-conformers take on a bow-like shape of the backbone, especially prominent in the adamantyl-substituted molecules, as shown in **Fig. 2S** – due to size, pictures of the entire molecules have been moved to the supplementary material. The exceptions in **Fig. 2S** are **(EDOT)$_8$** and **(PT)$_8$** octamers, which have a practically planar optimized conformation starting from both *syn*- and *anti*- orientations, although **(PT)$_8$** retains the *syn*/*anti* distinction, **(EDOT)$_8$** is completely planar. The optimised dihedral angles α in the middle of the chains, where they are likely to represent the conformations of real chains, are collected in **Tab. 11**, along with the relevant electronic energies, where -s stands for the *syn*-, and -a stands for the *anti*- conformer. The relevant values for all backbone dihedrals are shown in **Tab. 7S**.

Tab. 11 *The gas-phase B3LYP/def2SVP dihedral angles α (in degrees) between the aromatic rings (from left to right) for S_0 geometry, and the corresponding electronic energies. The anti- conformer is denoted by -a and the syn- conformer by the -s suffix.*

Molecule	α_4 (°)	α_5 (°)	α_6 (°)	Energy (Hartree)
(T)$_8$-s	173	173	171	– 4 413.207 986 **6**3
(T)$_8$-a	– 173	173	– 171	– 4 413.207 986 **3**4
(EDOT)$_8$	180	180	180	– 6 233.924 384 91
(3HT)$_8$-s	151	150	149	– 6 297.730 883 **7**8
(3HT)$_8$-a	– 151	150	– 149	– 6 297.730 883 **8**7
(MAT)$_8$-s	142	142	144	– 7 839.49**2** 286 47
(MAT)$_8$-a	– 149	143	– 153	– 7 839.49**5** 049 83
(EAT)$_8$-s	149	149	147	– 8 153.57**6** 862 44
(EAT)$_8$-a	– 148	152	– 144	– 8 153.57**8** 403 00
(MPT)$_8$-s	– 159	154	– 155	– 9 438.521 **2**06 83
(MPT)$_8$-a	137	138	138	– 9 438.521 **6**66 82
(ETT)$_8$-s	146	146	146	– 8 772.02**0** 396 10
(ETT)$_8$-a	– 151	152	– 149	– 8 772.02**1** 655 24
(ETAT)$_8$-s	148	146	147	– 11 865.334 **2**43 00
(ETAT)$_8$-a	– 144	158	– 146	– 11 865.334 **4**85 00

As seen above, the *anti*-conformation is slightly energetically preferred, even for extremely large substituents like in the **(ETAT)$_8$** molecule. Further, the differences in energy between the conformers increase with the size of the substituents, as they are of the same order of magnitude for **(PT)$_8$** and **(3HT)$_8$**, and three orders of magnitude larger for the bulky substituents.

Based on this investigation, it seems that a large, branched substituent, represented by **(MPT)$_8$**, creates a chaotic structure around the backbone, where we cannot consistently expect favourable packing. On the other hand, the addition of an extremely large 3D substituent, like in **(ETAT)$_8$**, causes a torsional strain in the whole structure due to steric repulsion between the individual substituents, evidenced by the large variation on the **(ETAT)$_8$-a** dihedral angles. Further, the methyladamantyl substitution has a similar effect, causing a strain on the backbone

due to the proximity of the bulky group, which may have a negative effect on the conjugation and therefore the optical and electronic properties.

With regards to experiment, the dihedral angles found for **(T)$_8$** and **(3HT)$_8$** seem overestimated, since the six-membered sexithiophene chain has a fully planar conformation according to crystallographic studies [204]. The same is the case for the 1,3,4,6-hexyl substituted sexithiophene [205], although the comparison with **(3HT)$_8$** is not exactly possible – the experimental sexithiophene is not substituted on all rings, which will surely increase the rotational freedom of the hexamer. Further, the gas-phase optimised length of the hexyl side chain was found to be 7.32 Å, while the X-Ray diffraction experiments give the value of 7.70 Å [206] for **P3HT**, which is probably the result of inter-chain interactions in the crystal, which lead to the planarization of the experimentally studied polymers and oligomers. Indeed, the overall comparison is complicated by the fact that there is no literature on the exact octamers that are considered in this study since the synthetic possibilities do not align with the computational polymer limit.

Next, the side-chain conformations were studied on trimer building blocks – the **(3HT)$_3$**, **(MAT)$_3$**, and **(EAT)$_3$**. The larger side chains were omitted in this part, since the relaxed-PES scans are computationally expensive, and there seems to be no need for such a detailed study of molecules that do not exist at this time. The potential energy profiles are shown in **Fig. 20**, together with the relevant dihedral angles.

For the model **(3HT)$_3$** chain, a global minimum was found at 280°. Further, two local minima at 20° and 100° were identified with an energy difference of 0.91 kJ mol^{-1}, allowing rotation in the range of 0° to 100° with respect to the thiophene ring, with a small torsion barrier at 60°. For model **(MAT)$_3$**, the torsional motion is more energetically restricted, with clear minima at 80° and 280 °, and barriers that are significantly higher than in the previous case. The **(EAT)$_3$** molecule, on the other hand, has similar possibilities for torsional motion as the **(3HT)$_3$**. There are notable local minima at 20° and 100°, with a difference of 1.40 kJ mol^{-1}, and a small torsional barrier at 40° for the *syn*- conformer, and 280° and 340° minima with a small barrier at 320° for the *anti*-conformer. Furthermore **Fig. 20 (d)** shows the torsional energy with respect to the ethyl bridge between thiophene and the adamantyl substituent, with a clear minimum at 180°. The potential curves are mirrored in the ethyladamantyl substituted molecules, likely because the side chains prefer a conformation, where both hydrogens on the ethyl C(22) and C(23) atoms (see **Fig. 20 (e)** are equidistant to the S(36) sulphur atom. This happens at 280° in the *syn*- conformer, and at 80° in the *anti*-conformer.

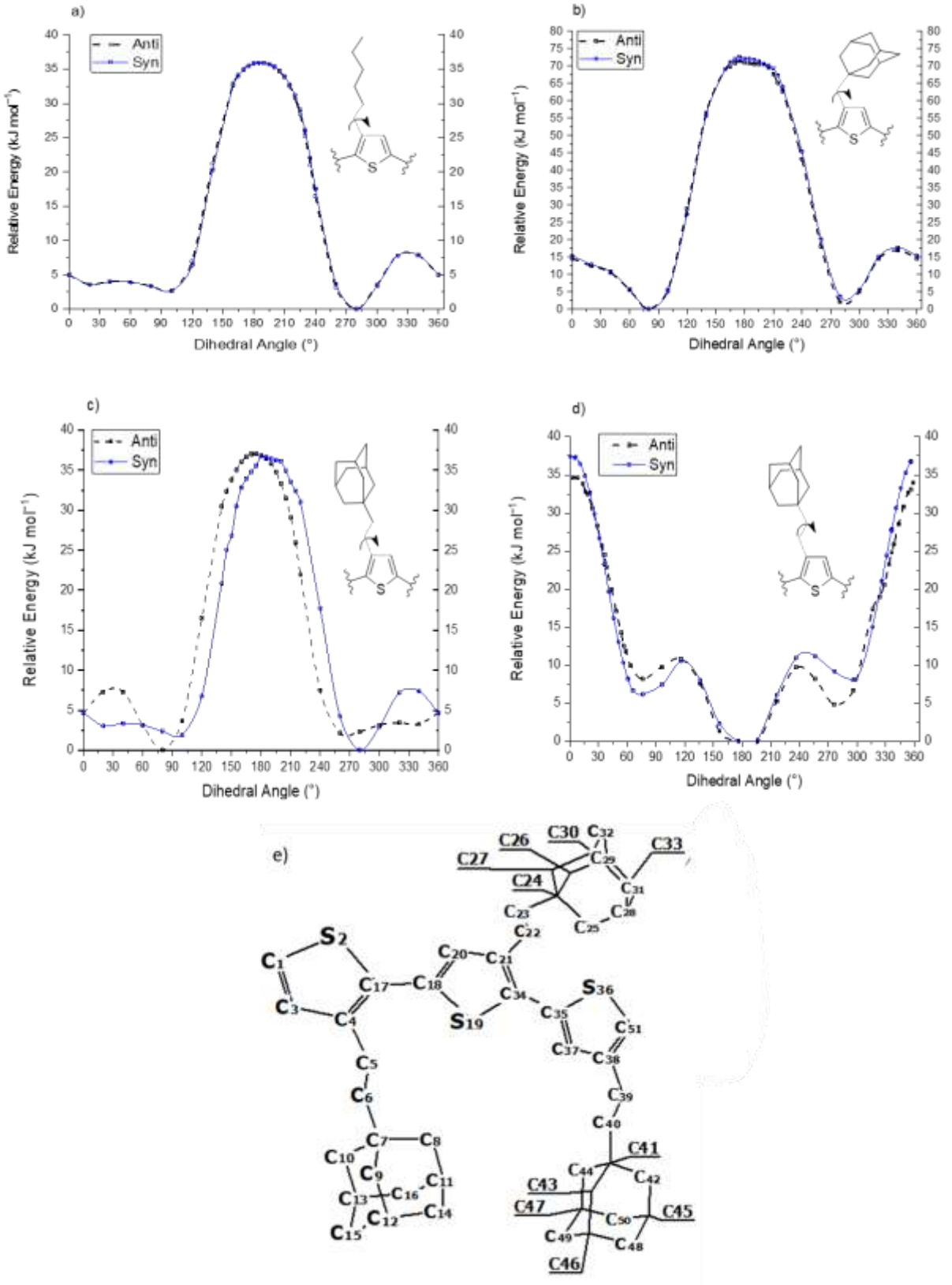

Fig. 20 *The change of relative B3LYP/def2svp energy of single substituent rotation with respect to the indicated torsional angle of the linkage between the thiophene plane and the substituent for model 3-hexylthiophene (a) and 3-methyladamantylthiophene (b) trimers.*

Therefore, it seems that the side chains of **MAT** are restricted in rotation, while the **EAT** chain possesses rigid ethyladamantyl groups with a 180 ° dihedral around the ethyl bridge, which relatively freely rotate with respect to the thiophene moiety. These results agree with previous molecular dynamics studies and crystal structures of **P3HT** [207]. Further, **Fig. 21** shows the minimal hydrogen-hydrogen atom distances between neighbouring substituents, which are dependent on the size. For **(EAT)$_8$**, this distance was found to be 3.03 Å, while for the larger **(ETAT)$_8$** and **(MPT)$_8$**, it was 2.76 Å and 2.68 Å. The **(ETT)$_8$** molecule is close to the previous ones, with 2.72 Å.

Therefore, the less bulky substituents on **EAT** and **MAT** are more likely to allow the interaction and insertion of a neighbouring side chain in a limited range of conformation. The **MAT** especially has very few stable conformations and steep energetic barriers and thus has the highest chance to create a highly organized structure in comparison to **3HT**. So, although it is not possible to predict the crystal structures exactly, it seems that the **PEAT** should have a slightly higher degree of crystallinity than **P3HT**, and **PMAT** should be significantly better. This arrangement could in turn support the semiconducting properties due to the enhanced packing.

Indeed, as found by the AFM scans shown in **Fig. 22**, the **P3HT** sample shows a noticeable large structure, that is significantly taller than the rest of the surface (around 9 nm high). According to the predictions, the **PEAT** sample shows clusters rising from the surface to around 28 nm, and 14 nm in the **PMAT** sample. These tall clusters could be impurities left behind from the synthesis, they do however grow with the size of the side substituent, so they may contain at least some polymer chains. Further, there are visible domains in all the samples that could be crystalline clusters. In **P3HT**, they are around 0.5 µm across and 0.1 µm thick and spaced far apart in a noisy matrix. In **PEAT**, the surface seems to have less noise, and the domains are around 0.5 µm in both directions, rising by a few nm from the matrix, which is rendered in dark orange. The **PMAT** sample contains a large number of domains that are around 0.5 µm in both directions, and they take up most of the surface. This gives further evidence of the increased degree of crystallinity of the adamantyl-substituted polymers. Finally, some grooves are found on the surfaces, depicted as black lines, which are likely a product of the thin layer preparation.

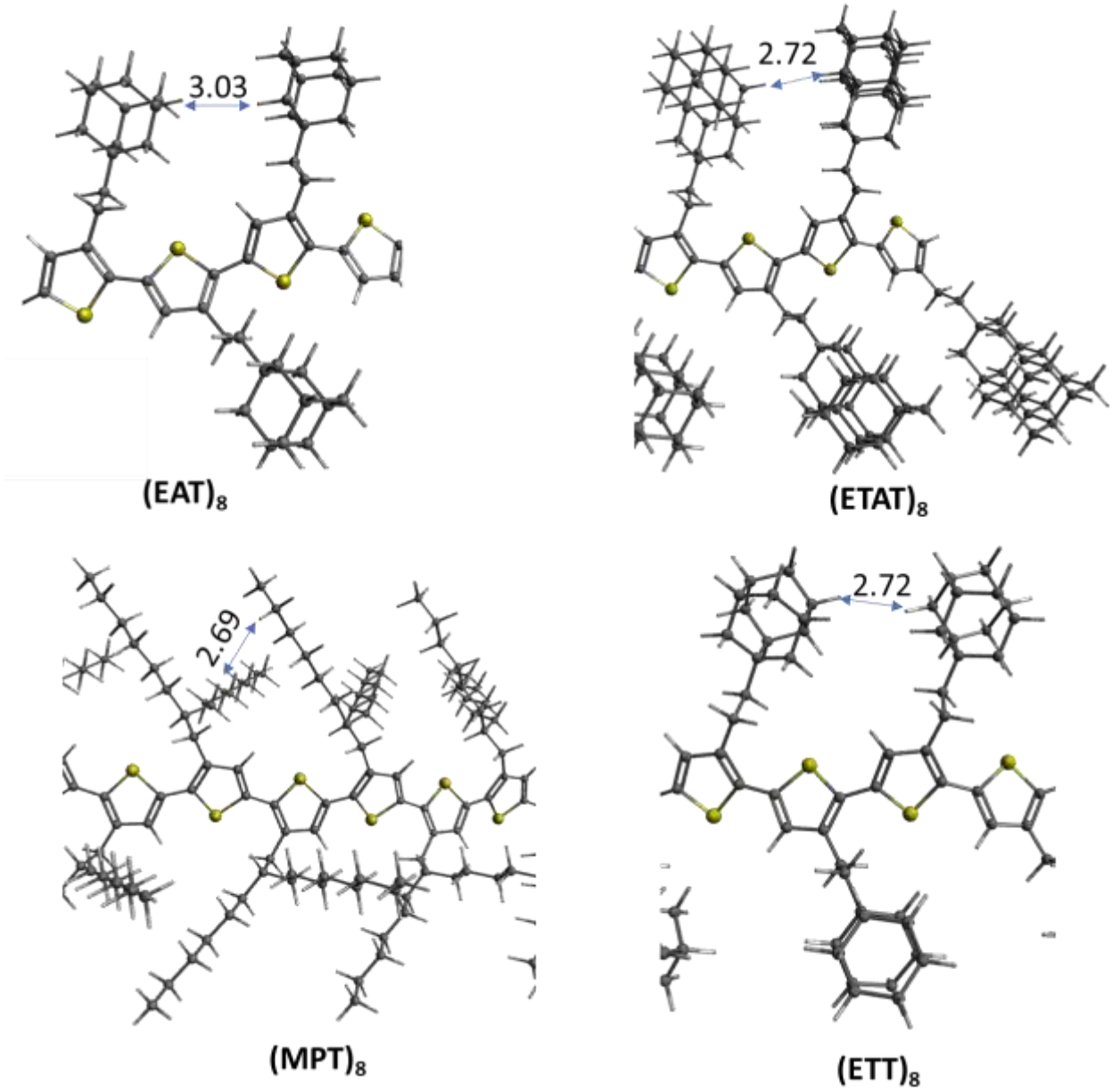

Fig. 21 *The distances between neighbouring substituents of a)* ***(EAT)$_8$****; (b)* ***(ETAT)$_8$****; (c)* ***(MPT)$_8$****,* ***(ETT)$_8$****. The relevant values are marked, and distances are in units of Å.*

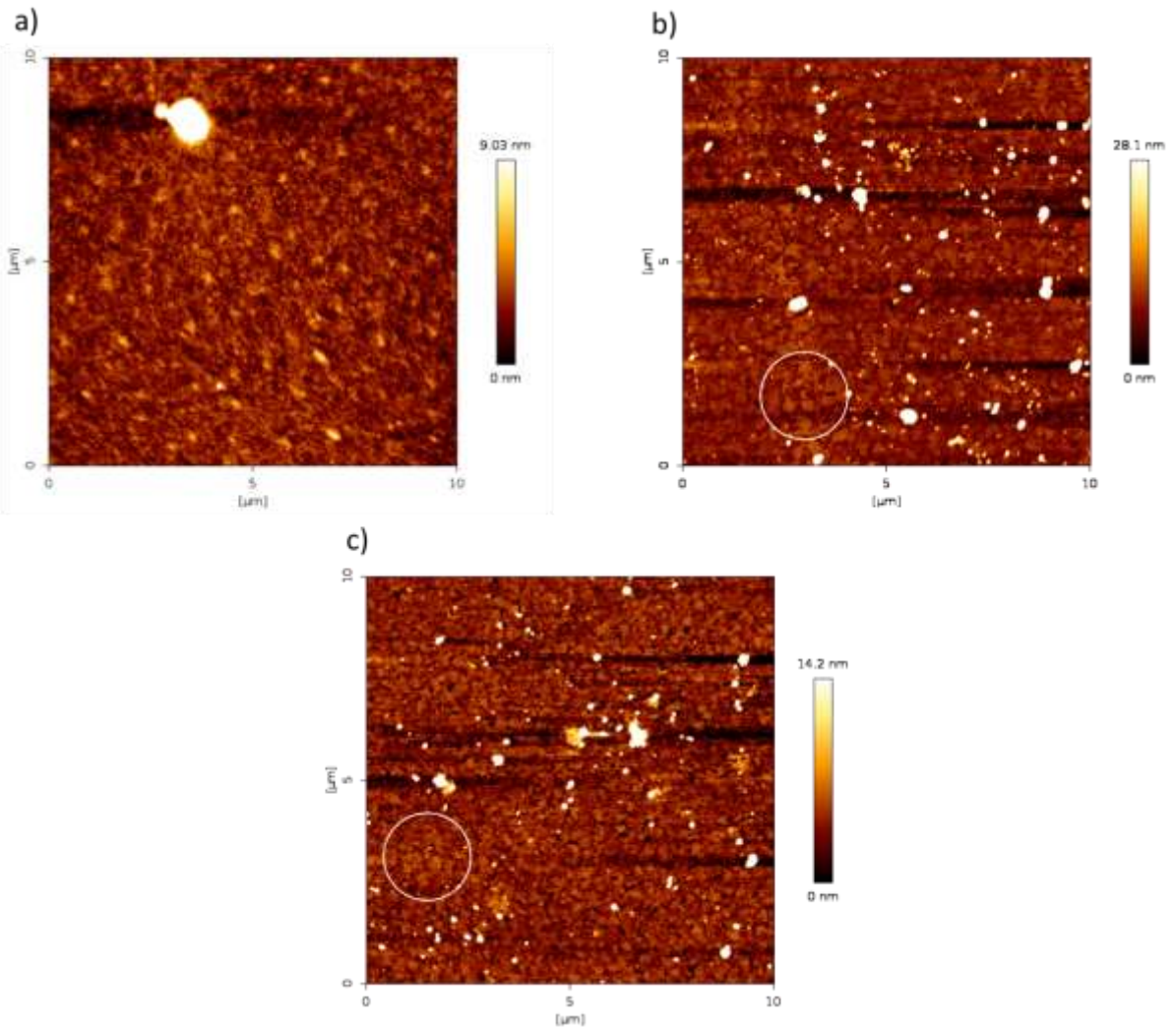

Fig. 22 *the AFM scans of (a)* ***P3HT****; (b)* ***PEAT****; (c)* ***PMAT****; the large clusters are rendered in white, the crystalline domains are circled*

Indeed, the Grazing Incidence Wide Angle X-Ray Scattering (GIWAXS) measurement, has revealed edge-on oriented intermolecular packing features with an intramolecular periodicity comparable to **P3HT**, and about double crystal stacking periodicity in the other directions. An orthorhombic lattice with the parameters a = 37 (or 42) Å, b = 3.7 Å, c = 4.1 Å was proposed. Overall, the **PMAT** sample was found to have the most ordered structure [JT3]. Next, the optical absorption and emission were investigated, along with the computed electronic transitions and orbital energies. In all cases, only one significant transition was found, the $S_0 \rightarrow S_1$, from the HOMO to the LUMO. A comparison of theoretical transitions with experimental results is shown in **Tab. 12**. Since the experiments were performed in chloroform solution and thin layer, the results are accordingly marked.

Table 12 *The theoretical $S_0 \rightarrow S_1$ transitions of the model octamers, compared with experimental absorption wavelengths where applicable; sol. denotes measurement in chloroform solution, layer denotes results from thin layer measurements.*

Molecule	Theoretical energy (eV)	Theoretical wavelength (nm)	Theoretical oscillator strength	Experimental wavelength (nm)
T-s	2.650	467	2.97	Not measured
T-a	2.650	467	2.97	
EDOT	2.437	508	3.17	Not measured
HT-s	3.050	406	2.61	450 sol.
HT-a	3.050	406	2.61	508 layer
MAT-s	3.025	409	2.48	390 sol.
MAT-a	3.215	385	2.36	387 layer
EAT-s	2.933	422	2.46	458 sol.
EAT-a	3.094	400	2.49	475 layer
MPT-s	2.723	455	2.54	Not measured
MPT-a	3.319	373	2.31	
ETT-s	2.908	426	2.48	Not measured
ETT-a	3.178	390	2.48	
ETAT-s	2.933	422	2.42	Not measured
ETAT-a	3.131	395	2.43	

As seen from **Tab. 12**, the theoretical absorptions of the new molecules are significantly dependent on the *syn*- and *anti*-conformations, unlike the previously synthesized counterparts. Further, it seems that the *syn*-conformer has a more favourable conjugation since the electronic excitations require lower energy. By comparison with the results, the **$(MAT)_8$** has the best agreement between theory and experiment, where the *anti*-conformer fits the measurements better both in solution and in thin layer. Indeed, it is unlikely that a crystal structure comparable to **P3HT** would contain the helical structures found in the *syn*-derivates. It should also be noted that there is essentially no change in the **PMAT** spectra in the solution and thin layer, likely because there is no change in conformation in the solid state as opposed to the solution, due to the structural rigidity of the methyladamantyl moiety.

On the other hand, the **$(3HT)_8$** and **$(EAT)_8$** have a comparable agreement with experimental values, as both are about 40 nm off. The **$(EAT)_8$-s** variant is closer to experimental data, although it is unlikely that such structures would be present, as discussed before. There is also a red shift of around 20 nm between solution and thin layer for **PEAT**, and a 50 nm shift for **P3HT**, which could be caused by the greater rigidity of ethyladamantyl compared to hexyl. The **PEAT** sample, however, has a longer effective conjugation compared to **PMAT**, evidenced by the higher absorption wavelength, which should give it better charge transfer properties. Indeed, space charge limited current spectroscopy measurements have shown **PEAT** to have an order of magnitude larger charge carrier mobility than **PMAT**. Interestingly, the HOMO and LUMO orbitals, pictured in **Fig. 23**, show no significant difference for **$(MAT)_8$** or **$(EAT)_8$**. The syn-conformers are pictured since they have the highest difference in absorption wavelengths and thus the conjugation difference should be the most prominent.

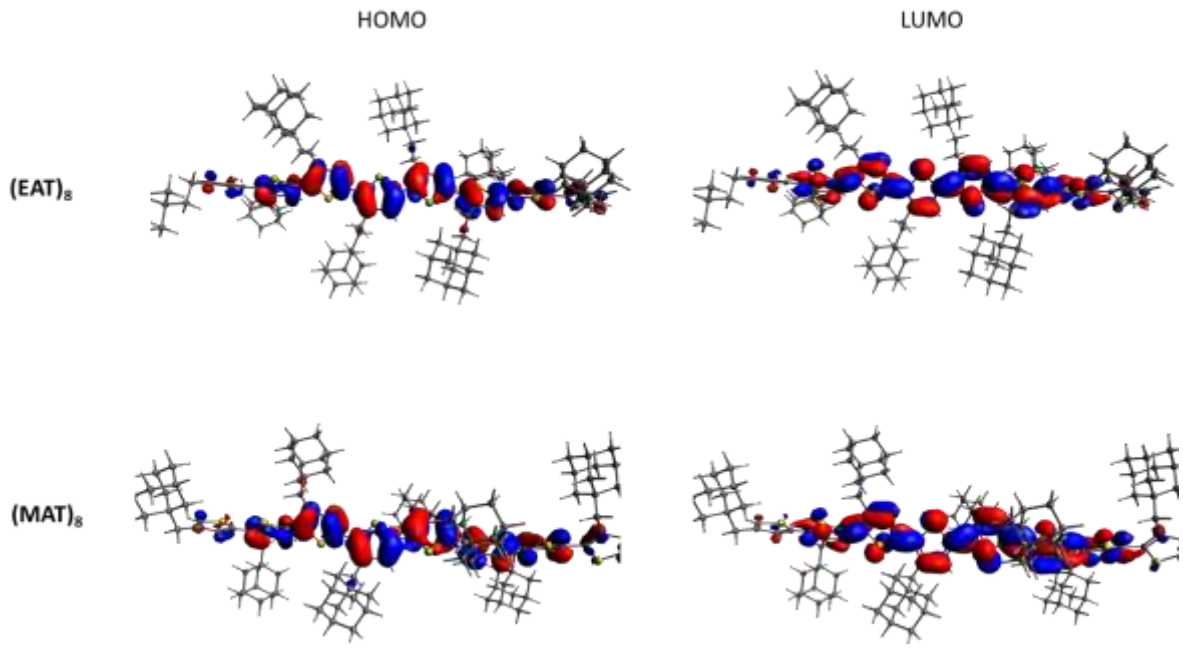

Fig. 23 *The detail of HOMO and LUMO orbitals on the polymer backbone of* ***(PMAT)$_8$-s*** *and* ***(PEAT)$_8$-s***

The purely theoretical molecules exhibit a red shift of around 30 nm across the *syn*- and *anti*-conformers for **(ETT)$_8$** and **(ETAT)$_8$**, and an 80 nm shift for **(MPT)$_8$**. The branched pentadecane substituent can actually take up more space and cause a larger strain on the backbone than bulky structures with a comparable number of atoms that are compactly bound together.

These findings illustrate the influence of the side chain geometry on optical properties. Next, the frontier molecular orbital energies are shown in **Fig. 24**. It comes as no surprise, that the *syn*- and *anti*-conformations have no influence on the energy levels of **(T)$_8$** and **(3HT)$_8$**, and that the HOMO/LUMO gap is lower for the *syn*-conformers of the other molecules, which is consistent with the electronic excitation predictions. Further, the HOMO level is consistently decreased by about 0.1 eV, while the LUMO level is increased by the same amount across *syn*- and *anti*-conformers, except for the branched **(MPT)$_8$** derivative, where the differences are about 0.3 eV.

Bhatta et. al. [60] have determined the polymer limit of the HOMO/LUMO gap to be around 2.50 eV for **P3HT**, while the model octamer values are 2.97 eV and 3.14 eV for **(3HT)$_8$-s** and **(3HT)$_8$-a** respectively, indicating that these oligomers do not fully reach the polymer limit, although larger molecules are not practical to compute. The situation is likely the same for **(EAT)$_8$** as the predicted absorption wavelength is considerably lower than the experimental value, indicating that the predicted excitation energy is larger than it truly is. Further, introducing the bulky substituents increases the gap, lowering HOMO by around 0.1 eV, and raising LUMO by the same amount. The values are slightly larger in **(MAT)$_8$**, documenting the larger influence of the adamantyl when it is bound closer to the backbone.

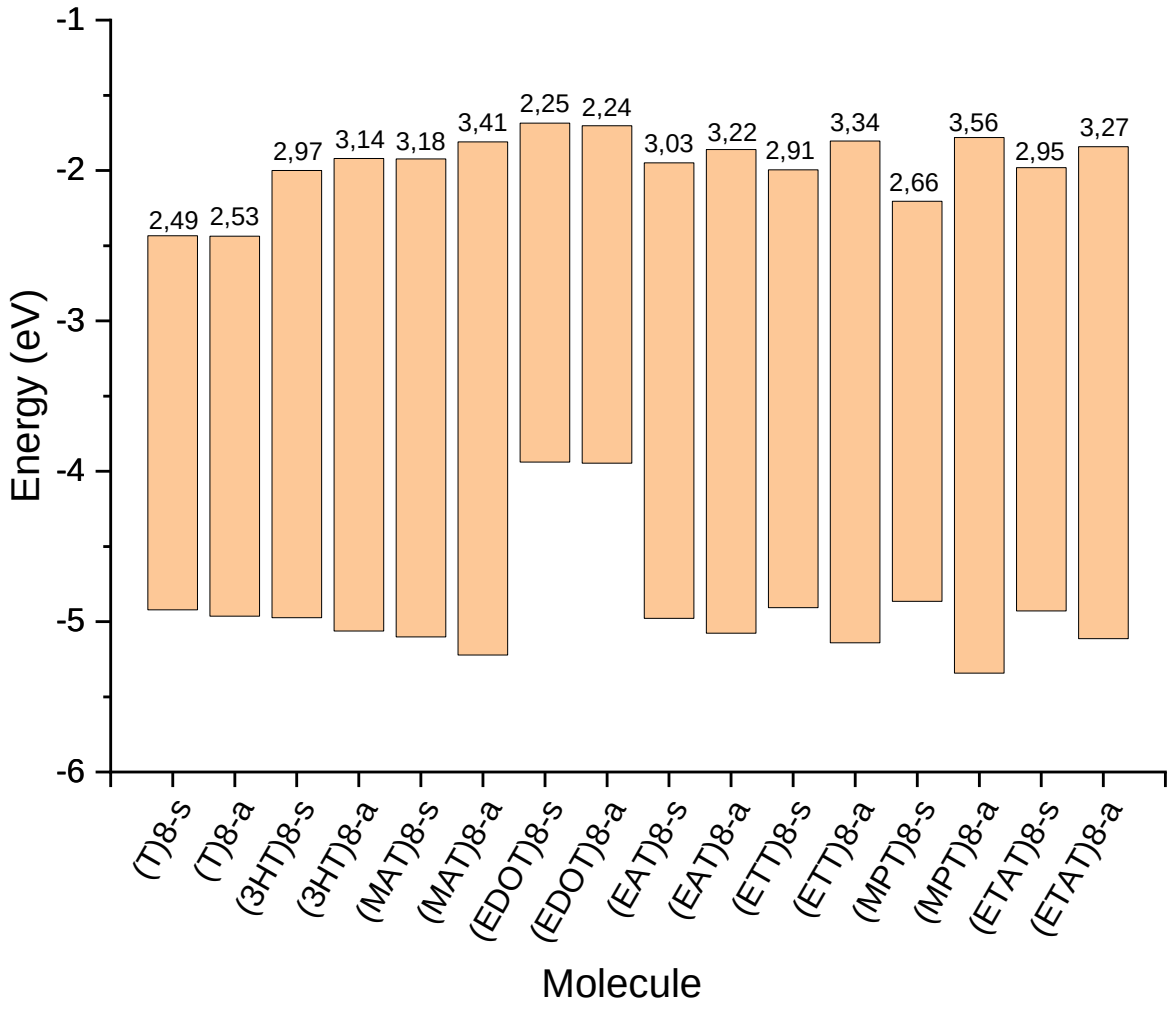

Fig. 24 *The theoretical frontier molecular orbital energies and the HOMO/LUMO gap values of the model octamers*

Finally, the novel polymers possess the thermal and chemical stability to produce long-lived devices and are processable in solvents convenient for upscaling and industrial production, such as chloroform [JT3]. The adamantane side chains have proved to provide a good amount of space for intermolecular interactions and the insertion of the side substituents of a neighbouring chain, showing a crystal structure comparable to **P3HT**. Thus, these materials could be serious competitors in the future.

7 CONCLUSION

In this work, the structures, and optoelectronic properties of alloxazine, lumazine and polythiophene type molecules were investigated. The properties were mainly electronic excitation and deexcitation wavelengths, along with frontier molecular orbital energy levels for alloxazine and lumazine, while the polythiophenes were considered in more detail with respect to structure.

First, the flavin molecules, are represented by alloxazine and lumazine derivatives. Several basis sets were tested in combination with the B3LYP functional to see which has the best fit to experimental electronic spectra. Interestingly, the def2SVP basis set was found to be accurate but not precise, being the closest to a 1:1 correlation, but with a larger spread of individual values. On the other hand, the 6-31+G** and aug-cc-PVDZ sets overestimate many transitions, but have a larger precision, leading to an overall better correlation. One common flaw of these computations is the inaccuracy concerning the isoalloxazine and isolumazine absorption peak that corresponds to the $S_0 \rightarrow S_1$ or HOMO → LUMO transition. Indeed, if these isomeric forms are excluded, the fit is significantly better. This discrepancy also represents room for improvement of the computational model. Here, a vibronic analysis according to the Franck-Condon method could be employed, since the experimentally visible transition may involve a different vibrational excited state. Nevertheless, the B3LYP/6-31+G** method represents a cost-effective and accurate way of computing electronic spectra, unless there are specific requirements like the inclusion of explicit solvent molecules, in which case more specialized basis sets may need to be used.

Briefly, the flavin structure was investigated. The modifications considered in this work were found to generally distort the rings in the alloxazine and lumazine moieties and lower their aromaticity. The geometry of lumazines substituted with freely rotating rings was found to be strongly dependent on the N(1) to N(8) isomerization, and a bend of the alloxazine moiety was found for N(10) substituted molecules as previously reported, although it seems to only occur with substituents that have a tetrahedral shape.

Despite the fact literature commonly does not include lumazine in the definition of flavins, there seems to be no reason, from the point of view presented here, not to consider them together, especially since deazaalloxazines are included, in spite of having a significantly different behaviour. A difference worth pointing out is the larger impact of electron-withdrawing substituents on the **Lum** molecule compared to **AL**. This is likely caused by the shielding of the substituent by the additional benzene ring of **AL**. From this point of view, the better synthetic strategy seems to be using electron-withdrawing or donating substituents to modify **Lum**, while fusing aromatic rings to **AL**, to tune the energy levels and absorption spectra. Synthesis of new derivatives according to the theoretical investigation is ongoing.

The novel polythiophene molecules were found to have optoelectronic properties similar to **P3HT**, with molecular packing that seems to agree with the shape of the computed *anti*-conformers of the model octamers in question. The analysis of side chain conformations has found the methyladamantyl substituted chains to have a more rigid structure, due to having fewer degrees of freedom than ethyladamantyl chains. With later AFM and crystallographic analysis, the **PMAT** sample was indeed found to have a higher degree of crystallinity than **PEAT**. Since the conductivity of polythiophenes stems mainly from molecular packing, it is interesting to note that the **PEAT** sample was found to have a larger charge carrier mobility than **PMAT**, although a theoretical explanation for this would likely require a molecular dynamics treatment. Unfortunately, as evidenced by the difference between experimental and theoretical absorption energies and comparison with literature, the model octamers are not enough to reach the polymer limit, although it is not practical to compute larger molecules.

In the future, the models could be improved by the use of molecular dynamics models, to better study the conformations and molecular packing of both flavins and polythiophenes in the solid state, bringing more accurate predictions and a better understanding of the charge transfer processes involved. Experimentally, more attention could be paid to the interactions of flavins with water and other solvents, especially in the case of such molecules as **CNLum** and **FAL**, where the interaction of the exposed electron-withdrawing groups with polar solvent molecules could have interesting effects. A publication focused on this topic is currently in preparation.

As far as polythiophenes are concerned, more attention could be paid to the modifications of the polymer backbone, and detailed studies of adiabatic ionization potentials, electron affinities and reorganization energies will have to be carried out to gain a truly deep understanding of the effects of both side substitution and backbone modification.

8 LIST OF SYMBOLS AND ABBREVIATIONS

DFT	Density Functional Theory
UV/VIS	Ultraviolet and Visible spectrum
OLED	Organic Light-Emitting Diode
TDDFT	Time-Dependent Density Functional Theory
MD	Molecular Dynamics
MC	Monte Carlo
ρ	Electron Density Function
Ψ	Electron Wavefunction
$\mathbf{r}_i$	position vector
N_{el}	Number of Electorns in a System
σ	Electron Spin
x, y, z	Cartesian Coordinates
$\mathscr{E}$	Functional of Energy
E	Energy
V	Potential Energy
T	Kinetic Energy
E_{XC}	Exchange-Correlation Functional
$\hat{H}$	Hamiltonian
$\hat{h}$	Single Electron Hamiltonian
ε	single-orbital energy
KS	Kohn-Sham
v_{XC}	Exchange-Correlation Potential
k	dummy variable
SCF	Self-Consistent Field
MP	Møler-Plesset
LDA	Local Density Approximation
LSDA	Local Spin-Density Approximation
ρ_α, ρ_β	Spin Density
GGA	Generalized Gradient Approximation
τ_α, τ_β	Kohn-Sham kinetic energy density
$\hat{V}$	Potential Energy Operator
$\hat{T}$	Kinetic Energy Operator
t	Time
TD	Time Dependent
XC	Exchange-Correlation

RPA	Random Phase Approximation
TDOEP	Time-Dependent Optimized Effective Potential
MO	Molecular orbital
FMO	Frontier Molecular Orbital
GP	Gas Phase
SCRF	Self-Consistent Reaction Field
vdW	van der Waals
HF	Hartree-Fock
PCM	Polarizable Continuum Model
Q	Electric Charge
LCAO	Linear Combination of Atomic Orbitals
AO	Atomic Orbital
STO	Slater-type Orbital
n	Principal Quantum Number
g	Gaussian basis function
N	Normalization Constant
i, j, k	nonnegative integers
GTF	Gaussian-type Function
l	Azimuthal Quantum Number
PES	Potential Energy Surface
q	Generalized Coordinate
ZPE	Zero Point Energy
a.u.	arbitrary units
H	Hessian
g_i	Gradient Matrix
IR	Infrared
v	wavenumber
c_l	velocity of light
k	vibrational force constant
m	Mass
μ	Reduced Mass
HOMHED	Harmonic Oscillator Model of Heterocyclic Electron Delocalization
R	Bond Length
DMSO	Dimethyl Sulfoxide
S_0	Singlet Ground State
S_n	Singlet Excited State

T_n	Triplet State
λ	wavelength
τ	fluorescence lifetime
f	oscillator strength
ISC	Intersystem Crossing
IP	Ionization Potential
X	An arbitrary molecule
EA	Electron Affinity
HOMO	Highest Occupied Molecular Orbital
LUMO	Lowest Unoccupied Molecular Orbital
CG	Coarse-Graining
N_m	number of monomers in the polymer backbone
N_b	number of conjugated double bonds in the backbone
NMCC	maximum conductive chain length
ECL	effective conjugation length
D_k	a relative force constant
AL	Alloxazine
Lum	Lumazine
Lch	Lumichrome
1-MeLch	1-methyl lumichrome
i	prefix indicating an isoAlloxazine/isolumazine form
ACN	Acetonitrile
Fl	Flavin
Rib	Riboflavin
ox	Oxidized
red	Reduced
QM/MM	Quantum Mechanics/Molecular Mechanics
AcOH	Acetic Acid
OFET	Organic Field Effect Transitor
OPV	Organic Photovoltaic Cell
PT	Polythiophene
CP	Conductive Polymer
PP	Pyrrolopyrrole
P3HT	Poly(3-hexylthiophene)
PEDOT	Poly(3,4-ethylenedioxythiophene)
MW	Molecular Weight

FMO	Frontier Molecular Orbital
T	Thiophene
3HT	3-hexylthiophene
α	dihedral angle between thiophene cores
β	dihedral angle between thiophene core and its substituent
B3LYP	Becke 3 parameter functional with Lee-Yang-Parr nonlocal correlation
CAM	Coulomb attenuating method
M06HF	Truhlar and Zhao hybrid functional
CAS	Complete Active Space
PBE0	Perdew, Burke, Erzerhof pure functional made into a hybrid by Adamo
6-31G	Pople double zeta valence basis set
6-311G	Pople triple zeta valence basis set
*	suffix denoting that polarized functions are added to a Pople set
+	symbol denoting that diffuse functions are added to a Pople set
TZVP	Triple-zeta Valence Polarized Ahlrichs basis set
cc-PVTZ	correlation-consistent triple-zeta polarized Dunning basis set
ThLum	6,7-thienyllumazine
aug	prefix denoting that diffuse functions are added to a Dunning basis set
PhePh	lumazine with pyrazine fused to the C(7) C(8) bond
PhePh2	alloxazine with triphenylene fused to the C(7) C(8) bond
PyrPh	alloxazine with pyrazine fused to the C(7) C(8) bond
FAL	7,8difluoroalloxazine
CHAL	7,8-dimethylalloxazine
PheLum	6,7-diphenyllumazine
ImiLum	6,7-diimidazolelumazine
FurLum	6,7-difuranlumazine
PyLum	6,7-dipyrrolelumazine
CNLum	6,7-dicyanolumazine
N1Phe	alloxazine with phenyl in the N(1) position
N10Phe	alloxazine with phenyl in the N(10) position
N1NS	alloxazine with thiazole in the N(1) position
N10NS	alloxazine with thiazole in the N(10) position
N1CF3	alloxazine with –CF3 in the N(1) position
N10CF3	alloxazine with –CF3 in the N(10) position
N1But	alloxazine with isobutyl in the N(1) position
N10But	alloxazine with isobutyl in the N(10) position

N1Rib	alloxazine with ribityl in the N(1) position
N10Rib	alloxazine with ribityl in the N(10) position
Ph2	alloxazine with benzene fused to the C(7) C(8) bond
Ph3	alloxazine with naphtalene fused to the C(7) C(8) bond
PyPh2	alloxazine with quinoxaline fused to the C(7) C(8) bond
Phe	lumazine with phenantrene fused to the C(6) C(7) bond
Pyr	lumazine with pyrazine fused to the C(6) C(7) bond
P3AT	Poly(3-alkylthiophene)
EDOT	3,4-ethylenedioxythiophene
MAT	3-methyladamantyl thiophene
EAT	3-ethyladamantyl thiophene
ETT	3-ethyltetraasterane thiophene
ETAT	3-ethyltriamantane thiophene
MPT	3-methyldodecapentane thiophene
AFM	Atomic Force Microscopy
ITO	Indium Tin Oxide
rpm	revolutions per minute
τ	dihedral angle between the C(5)–C(6)–C(7)–C(8) atoms of the **Lum** B ring
γ	dihedral angle between the lumazine B ring and the heterocyclic substituent
δ	dihedral angle between the alloxazine A or B ring and the substituent
λ	Wavelength
Em	Emission
-a	suffix indicating an *anti*-conformer of polythiophene
-s	suffix indicating a *syn*-conformer of polythiophene

9 LITERATURE

[1] RAJENDAR, Burki, Arivazhagan RAJENDRAN, Zhiqiang YE, Eriko KANAI, Yusuke SATO, Seiichi NISHIZAWA, Marek SIKORSKI and Norio TERAMAE. Effect of substituents of alloxazine derivatives on the selectivity and affinity for adenine in AP-site-containing DNA duplexes. Organic & Biomolecular Chemistry [online]. 2010, 8(21) [accessed on 2022-02-21]. ISSN 1477-0520. doi:10.1039/c0ob00057d

[2] LEWARS, Errol G. Computational Chemistry: Introduction to the Theory and Applications of Molecular and Quantum Mechanics. 2nd. Springer Netherlands, 2011. ISBN 978-90-481-3861-6.

[3] HAILE, J.M. Molecular Dynamics Simulation: Elementary Methods. New York: John Wiley, 1992. ISBN 0-471-81966-2.

[4] HOHENBERG, P. and W. KOHN. Inhomogeneous Electron Gas. Physical Review [online]. 1964, 136(3B), B864-B871 [accessed 2020-04-28]. DOI: 10.1103/PhysRev.136.B864. ISSN 0031-899X. Available from: https://link.aps.org/doi/10.1103/PhysRev.136.B864

[5] KOHN, W. and L. J. SHAM. Self-Consistent Equations Including Exchange and Correlation Effects. Physical Review [online]. 1965, 140(4A), A1133-A1138 [accessed. 2020-04-28]. DOI: 10.1103/PhysRev.140.A1133. ISSN 0031-899X. Available from: https://link.aps.org/doi/10.1103/PhysRev.140.A1133

[6] SOUSA, Sérgio Filipe, Pedro Alexandrino FERNANDES and Maria João RAMOS. General Performance of Density Functionals. The Journal of Physical Chemistry A [online]. 2007, 111(42), 10439-10452 [accessed 2020-04-28]. DOI: 10.1021/jp0734474. ISSN 1089-5639. Available from: https://pubs.acs.org/doi/10.1021/jp0734474

[7] ZHAO, Yan and Donald G. TRUHLAR. Applications and validations of the Minnesota density functionals. Chemical Physics Letters [online]. 2011, 502(1-3), 1-13 [accessed. 2020-04-28]. DOI: 10.1016/j.cplett.2010.11.060. ISSN 00092614. Available from: https://linkinghub.elsevier.com/retrieve/pii/S0009261410015411

[8] ZHAO, Yan and Donald G. TRUHLAR. Density Functionals with Broad Applicability in Chemistry. Accounts of Chemical Research [online]. 2008, 41(2), 157-167 [accessed 2020-04-28]. DOI: 10.1021/ar700111a. ISSN 0001-4842. Available from: https://pubs.acs.org/doi/10.1021/ar700111a

[9] LEVINE, Ira N. Quantum chemistry. 7th ed. Boston: Pearson, c2014. ISBN 978-0-321-80345-0.

[10] JENSEN, Frank. Introduction to computational chemistry. Third edition. Chichester: Wiley, 2017. ISBN 978-111-8825-990.

[11] ULLRICH, Carsten A. Time-dependent density-functional theory: concepts and applications. Oxford: Oxford University Press, 2012. Oxford graduate texts. ISBN 978-0-19-956302-9.

[12] RUNGE, Erich and E. K. U. GROSS. Density-Functional Theory for Time-Dependent Systems. Physical Review Letters [online]. 1984, 52(12), 997-1000 [accessed 2022-09-05]. ISSN 0031-9007. Available from: doi:10.1103/PhysRevLett.52.997

[13] TOKATLY, I. V. Time-dependent current density functional theory on a lattice. Physical Review B [online]. 2011, 83(3) [accessed. 2022-09-05]. ISSN 1098-0121. Available from: doi:10.1103/PhysRevB.83.035127

[14] VAN LEEUWEN, Robert. Mapping from Densities to Potentials in Time-Dependent Density-Functional Theory. Physical Review Letters [online]. 1999, 82(19), 3863-3866 [accessed 2022-09-05]. ISSN 0031-9007. Available from: doi:10.1103/PhysRevLett.82.3863

[15] VAN LEEUWEN, ROBERT. KEY CONCEPTS IN TIME-DEPENDENT DENSITY-FUNCTIONAL THEORY. International Journal of Modern Physics B [online]. 2012, 15(14), 1969-2023 [accessed 2022-09-05]. ISSN 0217-9792 Available from: doi:10.1142/S021797920100499X

[16] MAITRA, Neepa T. and Kieron BURKE. Demonstration of initial-state dependence in time-dependent density-functional theory. Physical Review A [online]. 2001, 63(4) [accessed 2022-09-05]. ISSN 1050-2947. Available from: doi:10.1103/PhysRevA.63.042501

[17] MAITRA, N.T. Initial-State Dependence and Memory. In: MARQUES, Miguel A.L., Carsten A. ULLRICH, Fernando NOGUEIRA, Angel RUBIO, Kieron BURKE and Eberhard K. U. GROSS, ed. Time-Dependent Density Functional Theory [online]. Berlin, Heidelberg: Springer Berlin Heidelberg, 2006,

2006, s. 61-74 [accessed 2022-09-05]. Lecture Notes in Physics. ISBN 978-3-540-35422-2. Available from: doi:10.1007/3-540-35426-3_4

[18] PETERSILKA, M., U. J. GOSSMANN and E. K. U. GROSS. Excitation Energies from Time-Dependent Density-Functional Theory. Physical Review Letters [online]. 1996, 76(8), 1212-1215 [accessed 2022-09-05]. ISSN 0031-9007. Available from: doi:10.1103/PhysRevLett.76.1212

[19] DREUW, Andreas and Martin HEAD-GORDON. Failure of Time-Dependent Density Functional Theory for Long-Range Charge-Transfer Excited States: The Zincbacteriochlorin−Bacteriochlorin and Bacteriochlorophyll−Spheroidene Complexes. Journal of the American Chemical Society [online]. 2004, 126(12), 4007-4016 [accessed 2022-09-05]. ISSN 0002-7863. Available from: doi:10.1021/ja039556n

[20] MAITRA, Neepa T., Ivo SOUZA and Kieron BURKE. Current-density functional theory of the response of solids. Physical Review B [online]. 2003, 68(4) [accessed 2022-09-05]. ISSN 0163-1829. Available from: doi:10.1103/PhysRevB.68.045109

[21] BOTTI, Silvana, Arno SCHINDLMAYR, Rodolfo Del SOLE and Lucia REINING. Time-dependent density-functional theory for extended systems. Reports on Progress in Physics [online]. 2007, 70(3), 357-407 [accessed 2022-09-05]. ISSN 0034-4885. Available from: doi:10.1088/0034-4885/70/3/R02

[22] GRUNENBERG, Jorg. Computational Spectroscopy: Methods Experiments and Applications. WILEY-VCH Verlag GmbH & Co., 2010. ISBN 978-3-527-32649-5.

[23] ATKINS, Peter a Julio DE PAULA. Physical Chemistry. 8th. Oxford: Oxford University Press, 2006. ISBN 0-7167-8759-8.

[24] WONG, Ming Wah, Michael J. FRISCH and Kenneth B. WIBERG. Solvent effects. 1. The mediation of electrostatic effects by solvents. Journal of the American Chemical Society [online]. 1991, 113(13), 4776-4782 [accessed 2022-03-23]. ISSN 0002-7863. Available from: doi:10.1021/ja00013a010

[25] MIERTUŠ, S., E. SCROCCO and J. TOMASI. Electrostatic interaction of a solute with a continuum. A direct utilizaion of AB initio molecular potentials for the prevision of solvent effects. Chemical Physics [online]. 1981, 55(1), 117-129 [accessed 2022-03-23]. ISSN 03010104. Available from: doi:10.1016/0301-0104(81)85090-2

[26] MANTINA, Manjeera, Adam C. CHAMBERLIN, Rosendo VALERO, Christopher J. CRAMER and Donald G. TRUHLAR. Consistent van der Waals Radii for the Whole Main Group. The Journal of Physical Chemistry A [online]. 2009, 113(19), 7 [accessed 2022-03-24]. ISSN 5806–5812. Available from: doi:10.1021/jp8111556

[27] KAMMEYER, Carl W. and Donald R. WHITMAN. Quantum Mechanical Calculation of Molecular Radii. I. Hydrides of Elements of Periodic Groups IV through VII. The Journal of Chemical Physics [online]. 1972, 56(9), 4 [accessed 2022-03-24]. Available from: doi:10.1063/1.1677883

[28] FORESMAN, Todd A. KEITH, Kenneth B. WIBERG, John SNOONIAN and Michael J. FRISCH. Solvent Effects. 5. Influence of Cavity Shape, Truncation of Electrostatics, and Electron Correlation on ab Initio Reaction Field Calculations. Journal of Physical Chemistry [online]. 1996, 100(40), 7 [accessed. 2022-03-24]. Available from: doi:10.1021/jp960488j

[29] CANCÈS, E., B. MENNUCCI and J. TOMASI. A new integral equation formalism for the polarizable continuum model: Theoretical background and applications to isotropic and anisotropic dielectrics. The Journal of Chemical Physics [online]. 1997, 107(8), 11 [accessed 2022-03-24]. Available from: doi:10.1063/1.474659

[30] DITCHFIELD, R., W. J. HEHRE and J. A. POPLE. Self-Consistent Molecular-Orbital Methods. IX. An Extended Gaussian-Type Basis for Molecular-Orbital Studies of Organic Molecules. The Journal of Chemical Physics [online]. 1971, 54(2), 724-728 [accessed 2022-09-05]. ISSN 0021-9606. Available from: doi:10.1063/1.1674902

[31] MCLEAN, A. D. and G. S. CHANDLER. Contracted Gaussian basis sets for molecular calculations. I. Second row atoms, Z =11–18. The Journal of Chemical Physics [online]. 1980, 72(10), 5639-5648 [accessed 2022-09-05]. ISSN 0021-9606. Available from: doi:10.1063/1.438980

[32] WEIGEND, Florian and Reinhart AHLRICHS. Balanced basis sets of split valence, triple zeta valence and quadruple zeta valence quality for H to Rn: Design and assessment of accuracy. Physical Chemistry

Chemical Physics [online]. 2005, 7(18) [accessed 2022-09-05]. ISSN 1463-9076. Available from: doi:10.1039/b508541a

[33] DUNNING, Thom H. Gaussian basis sets for use in correlated molecular calculations. I. The atoms boron through neon and hydrogen. The Journal of Chemical Physics [online]. 1989, 90(2), 1007-1023 [accessed 2022-09-05]. ISSN 0021-9606. Available from: doi:10.1063/1.456153

[34] LUKEŠ, Vladimír, Viliam LAURINC, Michal ILČIN and Erik KLEIN. Počítačové modelovanie molekúl: Metódy počítačovej chémie. Bratislava: Nakladateľstvo STU, 2011. ISBN 978-80-227-3456-1.

[35] STRANG, Gilbert. Calculus. 2nd ed. Wellesley: Wellesley Cambridge Press, 2010. ISBN 978-0980232745.

[36] SULEIMANOV, Yury V. and William H. GREEN. Automated Discovery of Elementary Chemical Reaction Steps Using Freezing String and Berny Optimization Methods. Journal of Chemical Theory and Computation [online]. 2015, 11(9), 4248-4259 [accessed 2020-04-28]. DOI: 10.1021/acs.jctc.5b00407. ISSN 1549-9618. Available from: https://pubs.acs.org/doi/10.1021/acs.jctc.5b00407

[37] PAWŁOWSKI, Filip, Jeppe OLSEN and Poul JØRGENSEN. Molecular response properties from a Hermitian eigenvalue equation for a time-periodic Hamiltonian. The Journal of Chemical Physics [online]. 2015, 142(11) [accessed 2022-09-05]. ISSN 0021-9606. Available from: doi:10.1063/1.4913364

[38] GAVEZZOTTI, Angelo. Computational Studies of Crystal Structure and Bonding. Advanced X-Ray Crystallography [online]. Berlin, Heidelberg: Springer Berlin Heidelberg, 2012, 2011-4-20, , 1-32 [accessed 2020-04-28]. Topics in Current Chemistry. DOI: 10.1007/128_2011_131. ISBN 978-3-642-27406-0. Available from: http://link.springer.com/10.1007/128_2011_131

[39] KATRITZKY, Alan R., Karl JUG and Daniela C. ONICIU. Quantitative Measures of Aromaticity for Mono-, Bi-, and Tricyclic Penta- and Hexaatomic Heteroaromatic Ring Systems and Their Interrelationships. Chemical Reviews [online]. 2001, 101(5), 1421-1450 [accessed 2020-04-28]. DOI: 10.1021/cr990327m. ISSN 0009-2665. Available from: https://pubs.acs.org/doi/10.1021/cr990327m

[40] FRIZZO, Clarissa P. and Marcos A. P. MARTINS. Aromaticity in heterocycles: new HOMA index parametrization. Structural Chemistry [online]. 2012, 23(2), 375-380 [accessed 2020-04-28]. DOI: 10.1007/s11224-011-9883-z. ISSN 1040-0400. Available from: http://link.springer.com/10.1007/s11224-011-9883-z

[41] SCHLEYER, Paul von Ragué, Christoph MAERKER, Alk DRANSFELD, Haijun JIAO and Nicolaas J. R. VAN EIKEMA HOMMES. Nucleus-Independent Chemical Shifts: A Simple and Efficient Aromaticity Probe. Journal of the American Chemical Society [online]. 1996, 118(26), 6317-6318 [accessed 2022-09-05]. ISSN 0002-7863. Available from: doi:10.1021/ja960582d

[42] STANGER, Amnon. Nucleus-Independent Chemical Shifts (NICS): Distance Dependence and Revised Criteria for Aromaticity and Antiaromaticity. The Journal of Organic Chemistry [online]. 2006, 71(3), 883-893 [accessed 2020-04-28]. DOI: 10.1021/jo051746o. ISSN 0022-3263. Available from: https://pubs.acs.org/doi/10.1021/jo051746o

[43] MERZ, Thomas, Genaro BIERHANCE, Ernst-Christian FLACH, Daniel KATS, Denis USVYAT and Martin SCHÜTZ. Description of excited states in photochemistry with theoretical methods. Physical Sciences Reviews [online]. 2021, 6(3) [accessed 2022-03-28]. ISSN 2365-659X. Available from: doi:10.1515/psr-2017-0178

[44] CASIDA, MARK E. Time-Dependent Density Functional Response Theory for Molecules. In: CHONG, Delano P. Recent Advances in Density Functional Methods [online]. WORLD SCIENTIFIC, 1995, 1995-11-21, s. 155-192 [accessed 2022-09-05]. Recent Advances in Computational Chemistry. ISBN 978-981-02-2442-4. Available from: doi:10.1142/9789812830586_0005

[45] HIRATA, So and Martin HEAD-GORDON. Time-dependent density functional theory within the Tamm–Dancoff approximation. Chemical Physics Letters [online]. 1999, 314(3-4), 291-299 [accessed 2022-09-05]. ISSN 00092614. Available from: doi:10.1016/S0009-2614(99)01149-5

[46] GHOSH, Swapan K. and Asish K. DHARA. Density-functional theory of many-electron systems subjected to time-dependent electric and magnetic fields. Physical Review A [online]. 1988, 38(3), 1149-1158 [accessed 2022-03-29]. ISSN 0556-2791. Available from: doi:10.1103/PhysRevA.38.1149

[47] CASIDA, M.E. and M. HUIX-ROTLLANT. Progress in Time-Dependent Density-Functional Theory. Annual Review of Physical Chemistry [online]. 2012, 63(1), 287-323 [accessed 2022-03-29]. ISSN 0066-426X. Available from: doi:10.1146/annurev-physchem-032511-143803

[48] RAPTA, Peter, LUKEŠ, Vladimír, Viliam LAURINC, Michal ILČIN and Erik KLEIN. Organické materiály pro elektroniku, Optoelektroniku a senzoriku; Aplikace moderných. ISBN 978-80-227-3617-6.

[49] MANAA, M. Riad. Determination of adiabatic ionization potentials and electron affinities of energetic molecules with the Gaussian-4 method. Chemical Physics Letters [online]. 2017, 678, 102-106 [accessed 2022-09-05]. ISSN 00092614. Available from: doi:10.1016/j.cplett.2017.04.038

[50] FELLER, David and Ernest R. DAVIDSON. A theoretical study of the adiabatic and vertical ionization potentials of water. The Journal of Chemical Physics [online]. 2018, 148(23) [accessed 2022-09-05]. ISSN 0021-9606. Available from: doi:10.1063/1.5037346

[51] OTERO, R., A.L. VÁZQUEZ DE PARGA and J.M. GALLEGO. Electronic, structural and chemical effects of charge-transfer at organic/inorganic interfaces. Surface Science Reports [online]. 2017, 72(3), 105-145 [accessed 2022-09-05]. ISSN 01675729. Available from: doi:10.1016/j.surfrep.2017.03.001

[52] PEARSON, Ralph G. Recent advances in the concept of hard and soft acids and bases. Journal of Chemical Education [online]. 1987, 64(7) [accessed 2022-09-05]. ISSN 0021-9584. Available from: doi:10.1021/ed064p561

[53] ZHAN, Chang-Guo, Jeffrey A. NICHOLS and David A. DIXON. Ionization Potential, Electron Affinity, Electronegativity, Hardness, and Electron Excitation Energy: Molecular Properties from Density Functional Theory Orbital Energies. The Journal of Physical Chemistry A [online]. 2003, 107(20), 4184-4195 [accessed 2022-09-05]. ISSN 1089-5639. Available from: doi:10.1021/jp0225774

[54] RICE, Betsy M. and Jennifer J. HARE. A Quantum Mechanical Investigation of the Relation between Impact Sensitivity and the Charge Distribution in Energetic Molecules. The Journal of Physical Chemistry A [online]. 2002, 106(9), 1770-1783 [accessed 2022-09-05]. ISSN 1089-5639. Available from: doi:10.1021/jp012602q

[55] BRÉDAS, Jean-Luc, David BELJONNE, Veaceslav COROPCEANU and Jérôme CORNIL. Charge-Transfer and Energy-Transfer Processes in π-Conjugated Oligomers and Polymers: A Molecular Picture. Chemical Reviews [online]. 2004, 104(11), 4971-5004 [accessed 2022-09-05]. ISSN 0009-2665. Available from: doi:10.1021/cr040084k

[56] PURUSHOTHAM, Uppula and G. Narahari SASTRY. Conjugate acene fused buckybowls: evaluating their suitability for p-type, ambipolar and n-type air stable organic semiconductors. Physical Chemistry Chemical Physics [online]. 2013, 15(14) [accessed 2022-09-05]. ISSN 1463-9076. Available from: doi:10.1039/c3cp44673e

[57] COROPCEANU, Veaceslav, Jérôme CORNIL, Demetrio A. DA SILVA FILHO, Yoann OLIVIER, Robert SILBEY and Jean-Luc BRÉDAS. Charge Transport in Organic Semiconductors. Chemical Reviews [online]. 2007, 107(4), 926-952 [accessed. 2022-09-05]. ISSN 0009-2665. . Available from: doi:10.1021/cr050140x

[58] BLYTHE, Tony and David BLOOR. Electrical properties of polymers. 2nd ed. Cambridge: Cambridge University Press, c2005. ISBN 0521552192.

[59] GARTNER, Thomas E. and Arthi JAYARAMAN. Modeling and Simulations of Polymers: A Roadmap. Macromolecules [online]. 2019, 52(3), 755-786 [accessed. 2022-09-05]. ISSN 0024-9297. Available from: doi:10.1021/acs.macromol.8b01836

[60] BHATTA, Ram S. and Mesfin TSIGE. Chain length and torsional dependence of exciton binding energies in P3HT and PTB7 conjugated polymers: A first-principles study. Polymer [online]. 2014, 55(11), 2667-2672 [accessed. 2022-09-05]. ISSN 00323861. Available from: doi:10.1016/j.polymer.2014.04.022

[61] GIERSCHNER, J., J. CORNIL and H.-J. EGELHAAF. Optical Bandgaps of π-Conjugated Organic Materials at the Polymer Limit: Experiment and Theory. Advanced Materials [online]. 2007, 19(2), 173-191 [accessed 2022-09-05]. ISSN 09359648. Available from: doi:10.1002/adma.200600277

[62] KUHN, Hans. A Quantum-Mechanical Theory of Light Absorption of Organic Dyes and Similar Compounds. The Journal of Chemical Physics [online]. 1949, 17(12), 1198-1212 [accessed 2022-09-05]. ISSN 0021-9606. Available from: doi:10.1063/1.1747143

[63] WYKES, Michael, Begoña MILIÁN-MEDINA and Johannes GIERSCHNER. Computational engineering of low bandgap copolymers. Frontiers in Chemistry [online]. 2013, 1 [accessed 2022-09-05]. ISSN 2296-2646. Available from: doi:10.3389/fchem.2013.00035

[64] MEIER, Herbert. Conjugated Oligomers with Terminal Donor–Acceptor Substitution. Angewandte Chemie International Edition [online]. 2005, 44(17), 2482-2506 [accessed 2022-09-05]. ISSN 1433-7851. Available from: doi:10.1002/anie.200461146

[65] GUEYMARD, Christian A. Solar Radiation Spectrum. In: MEYERS, Robert A., ed. Encyclopedia of Sustainability Science and Technology [online]. New York, NY: Springer New York, 2012, 2012, s. 9705-9730 [accessed 2022-09-05]. ISBN 978-0-387-89469-0. Available from: doi:10.1007/978-1-4419-0851-3_445

[66] PRESIADO, I., Y. EREZ, R. GEPSHTEIN and D. HUPPERT. Excited-State Intermolecular Proton Transfer of Lumazine. The Journal of Physical Chemistry C [online]. 2010, 114(8), 3634-3640 [accessed 2022-02-18]. ISSN 1932-7447. Available from: doi:10.1021/jp907141b

[67] CIBULKA, Radek and Marco W. FRAAIJE, ed. Flavin-Based Catalysis: Principles and Applications. 1. Weinheim: Wiley-VCH, 2021. ISBN 978-3-527-34834-3.

[68] KLEIN, R. and I. TATISCHEFF. TAUTOMERISM AND FLUORESCENCE OF LUMAZINE. Photochemistry and Photobiology [online]. 1987, 45(1), 55-65 [accessed 2022-02-18]. ISSN 0031-8655. Available from: doi:10.1111/j.1751-1097.1987.tb08405.x

[69] MIR, Miquel, Ewa SIKORSKA, Marek SIKORSKI and Francis WILKINSON. Study of the effect of β-cyclodextrin on the photophysics of alloxazines in the solid state. Journal of the Chemical Society, Perkin Transactions 2 [online]. (6), 1095-1098 [accessed 2022-02-18]. ISSN 03009580. Available from: doi:10.1039/a608613f

[70] SIKORSKI, Marek and Ewa SIKORSKA. Applied Photochemistry Lab: Publications. Amu.edu.pl [online]. Poznan: Adam Mickiewicz University, 2008, 2008 [accessed 2022-02-18]. Available from: http://sikorski-photolab.home.amu.edu.pl/publications/excited.html

[71] MUKHERJEE, Arnab and Charles M SCHROEDER. Flavin-based fluorescent proteins: emerging paradigms in biological imaging. Current Opinion in Biotechnology [online]. 2015, 31, 16-23 [accessed 2022-02-21]. ISSN 09581669. Available from: doi:10.1016/j.copbio.2014.07.010

[72] MOHAMMED, Nabeel, Alan A. WILES, Michael BELSLEY, Sara S. M. FERNANDES, Michele CARIELLO, Vincent M. ROTELLO, M. Manuela M. RAPOSO and Graeme COOKE. Synthesis and characterisation of push–pull flavin dyes with efficient second harmonic generation (SHG) properties. RSC Advances [online]. 2017, 7(39), 24462-24469 [accessed 2022-02-21]. ISSN 2046-2069. Available from: doi:10.1039/C7RA03400H

[73] SIKORSKA, Ewa, Igor V. KHMELINSKII, David R. WORRALL, Jacek KOPUT and Marek SIKORSKI. Spectroscopy and Photophysics of Iso- and Alloxazines: Experimental and Theoretical Study. Journal of Fluorescence [online]. 2004, 14(1), 57-64 [accessed 2022-02-21]. ISSN 1053-0509. Available from: doi:10.1023/B:JOFL.0000014660.59105.31

[74] RICHTAR, Jan, Patricie HEINRICHOVA, Dogukan APAYDIN, et al. Novel Riboflavin-Inspired Conjugated Bio-Organic Semiconductors. Molecules [online]. 2018, 23(9) [accessed 2022-02-21]. ISSN 1420-3049 Available from: doi:10.3390/molecules23092271

[75] KIS, Klaus, Rainer VOLK and Adelbert BACHER. Biosynthesis of Riboflavin. Studies on the Reaction Mechanism of 6,7-Dimethyl-8-ribityllumazine Synthase. Biochemistry [online]. 1995, 34(9), 2883-2892 [accessed 2022-09-06]. ISSN 0006-2960. Available from: doi:10.1021/bi00009a019

[76] MAL, Madhushree and Debabrata MANDAL. Solvent and pH-sensitive Fluorescence Response of Alloxazine. Journal of Photochemistry and Photobiology A: Chemistry [online]. 2021, 404 [accessed 2022-02-18]. ISSN 10106030. Available from: doi:10.1016/j.jphotochem.2020.112888

[77] MOYON, N. Shaemningwar and Sivaprasad MITRA. Fluorescence Solvatochromism in Lumichrome and Excited-State Tautomerization: A Combined Experimental and DFT Study. The Journal of Physical Chemistry A [online]. 2011, 115(12), 2456-2464 [accessed 2022-09-07]. ISSN 1089-5639. Available from: doi:10.1021/jp1102687

[78] MOYON, N. Shaemningwar, Pynsakhiat Miki GASHNGA, Smritakshi PHUKAN and Sivaprasad MITRA. Specific solvent effect on lumazine photophysics: A combined fluorescence and intrinsic reaction coordinate analysis. Chemical Physics [online]. 2013, 421, 22-31 [accessed 2022-09-07]. ISSN 03010104. Available from: doi:10.1016/j.chemphys.2013.05.012

[79] DENOFRIO, M. Paula, Andrés H. THOMAS, André M. BRAUN, Esther OLIVEROS and Carolina LORENTE. Photochemical and photophysical properties of lumazine in aqueous solutions. Journal of Photochemistry and Photobiology A: Chemistry [online]. 2008, 200(2-3), 282-286 [accessed 2022-09-07]. ISSN 10106030. Available from: doi:10.1016/j.jphotochem.2008.08.003

[80] PRESIADO, I., Y. EREZ, R. GEPSHTEIN and D. HUPPERT. Excited-State Intermolecular Proton Transfer of Lumazine. The Journal of Physical Chemistry C [online]. 2010, 114(8), 3634-3640 [accessed. 2022-09-07]. ISSN 1932-7447. Available from: doi:10.1021/jp907141b

[81] SIMKOVITCH, Ron and Dan HUPPERT. Photoprotolytic Processes of Lumazine. The Journal of Physical Chemistry B [online]. 2017, 121(1), 129-142 [accessed 2022-09-07]. ISSN 1520-6106. Available from: doi:10.1021/acs.jpcb.6b10828

[82] AFANEH, Akef T. and Georg SCHRECKENBACH. Conformation/Tautomerization effect on the pK a values of lumazine and 6-thienyllumazine. Journal of Physical Organic Chemistry [online]. 2014, 27(8), 690-700 [accessed 2022-09-07]. ISSN 08943230. Available from: doi:10.1002/poc.3320

[83] WÖRNER, Jakob, Jing CHEN, Adelbert BACHER and Stefan WEBER. Non-classical disproportionation revealed by photo-chemically induced dynamic nuclear polarization NMR. Magnetic Resonance [online]. 2021, 2(1), 281-290 [accessed 2022-09-07]. ISSN 2699-0016. Available from: doi:10.5194/mr-2-281-2021

[84] PENZKOFER, Alfons. Absorption and emission spectroscopic investigation of alloxazine in aqueous solutions and comparison with lumichrome. Journal of Photochemistry and Photobiology A: Chemistry [online]. 2016, 314, 114-124 [accessed 2022-02-21]. ISSN 10106030. Available from: doi:10.1016/j.jphotochem.2015.08.011

[85] PRUKAŁA, Dorota, Ewa SIKORSKA, Jacek KOPUT, Igor KHMELINSKII, Jerzy KAROLCZAK, Mateusz GIERSZEWSKI and Marek SIKORSKI. Acid–Base Equilibriums of Lumichrome and its 1-Methyl, 3-Methyl, and 1,3-Dimethyl Derivatives. The Journal of Physical Chemistry A [online]. 2012, 116(28), 7474-7490 [accessed 2022-03-08]. ISSN 1089-5639. Available from: doi:10.1021/jp300522h

[86] NAVARRO, Amparo, Sonia B. JIMÉNEZ-PULIDO, Andrés GARZÓN-RUIZ, Nuria A. ILLÁN-CABEZA, Francisco HUESO-UREÑA, Alfonso ALEJO-ARMIJO and Miguel N. MORENO-CARRETERO. New bioinspired luminescent compounds based on lumazine: A photophysical study in solution and solid state. Dyes and Pigments [online]. 2019, 168, 281-294 [accessed. 2022-09-07]. ISSN 01437208. Available from: doi:10.1016/j.dyepig.2019.04.066

[87] DUTTA CHOUDHURY, Sharmistha and Haridas PAL. Intriguing Tautomerism of Lumichrome in Binary Aqueous Solvent Mixtures: Implications for Probing Microenvironments. The Journal of Physical Chemistry B [online]. 2016, 120(46), 11970-11977 [accessed 2022-09-07]. ISSN 1520-6106. Available from: doi:10.1021/acs.jpcb.6b08777

[88] GHARAT, Poojan Milan, Jiddhu M. CHETHODIL, Amit P. SRIVASTAVA, Praseetha P. K., Haridas PAL and Sharmistha DUTTA CHOUDHURY. An insight into the molecular and surface state photoluminescence of carbon dots revealed through solvent-induced modulations in their excitation wavelength dependent emission properties. Photochemical & Photobiological Sciences [online]. 2019, 18(1), 110-119 [accessed 2022-09-07]. ISSN 1474-905X. Available from: doi:10.1039/C8PP00373D

[89] KHATTAB, Muhammad, Feng WANG and Andrew H. A. CLAYTON. Micro-solvation of tyrosine-kinase inhibitor AG1478 explored with fluorescence spectroscopy and computational chemistry. RSC Advances [online]. 2017, 7(50), 31725-31735 [accessed 2022-09-07]. ISSN 2046-2069. Available from: doi:10.1039/C7RA04435F

[90] CHOSROWJAN, Haik, Seiji TANIGUCHI, Noboru MATAGA, Takeshi NAKANISHI, Yoshihiro HARUYAMA, Shuta SATO, Masaya KITAMURA and Fumio TANAKA. Effects of the Disappearance of One Charge on Ultrafast Fluorescence Dynamics of the FMN Binding Protein. The Journal of Physical Chemistry B [online]. 2010, 114(18), 6175-6182 [accessed 2022-02-28]. ISSN 1520-6106. Available from: doi:10.1021/jp912137s

[91] MURAKAMI, Motonobu, Kei OHKUBO and Shunichi FUKUZUMI. Inter- and Intramolecular Photoinduced Electron Transfer of Flavin Derivatives with Extremely Small Reorganization Energies. Chemistry - A European Journal [online]. 2010, 16(26), 7820-7832 [accessed 2022-02-28]. ISSN 09476539. Available from: doi:10.1002/chem.200903236

[92] LEE, Minah, Jihyun HONG, Dong-Hwa SEO, Dong Heon NAM, Ki Tae NAM, Kisuk KANG and Chan Beum PARK. Redox Cofactor from Biological Energy Transduction as Molecularly Tunable Energy-Storage Compound. Angewandte Chemie International Edition [online]. 2013, 52(32), 8322-8328 [accessed 2022-02-28]. ISSN 14337851. Available from: doi:10.1002/anie.201301850

[93] GOLCZAK, Anna, Małgorzata INSIŃSKA-RAK, Amirali DAVOUDPOUR, et al. Photophysical properties of alloxazine derivatives with extended aromaticity – Potential redox-sensitive fluorescent probe. Spectrochimica Acta Part A: Molecular and Biomolecular Spectroscopy [online]. 2022, 272 [accessed 2022-09-07]. ISSN 13861425. Available from: doi:10.1016/j.saa.2022.120985

[94] YOSHIMOTO, Satoshi, Nana KOHARA, Natsu SATO, Hideya ANDO a Masamitsu ICHIHASHI. Riboflavin Plays a Pivotal Role in the UVA-Induced Cytotoxicity of Fibroblasts as a Key Molecule in the Production of H2O2 by UVA Radiation in Collaboration with Amino Acids and Vitamins. International Journal of Molecular Sciences [online]. 2020, 21(2) [accessed 2022-09-07]. ISSN 1422-0067. Available from: doi:10.3390/ijms21020554

[95] GUO, Huimin, Hongyu XIA, Xiaolin MA, Kepeng CHEN, Can DANG, Jianzhang ZHAO and Bernhard DICK. Efficient Photooxidation of Sulfides with Amidated Alloxazines as Heavy-atom-free Photosensitizers. ACS Omega [online]. 2020, 5(18), 10586-10595 [accessed. 2022-09-07]. ISSN 2470-1343. Available from: doi:10.1021/acsomega.0c01087

[96] ZEN, Yang Hwang and Chong Mou WANG. A novel optical transistor device based on photo-induced proton transfer reactions. Journal of the Chemical Society, Chemical Communications [online]. 1994, (22) [accessed 2022-09-07]. ISSN 0022-4936. Available from: doi:10.1039/c39940002625

[97] WALALAWELA, Niluksha, María Noel URRUTIA, Andrés H. THOMAS, Alexander GREER and Mariana VIGNONI. Alkane Chain-extended Pterin Through a Pendent Carboxylic Acid Acts as Triple Functioning Fluorophore, 1 O 2 Sensitizer and Membrane Binder. Photochemistry and Photobiology [online]. 2019, 95(5), 1160-1168 [accessed 2022-09-07]. ISSN 0031-8655. Available from: doi:10.1111/php.13098

[98] VIGNONI, Mariana, Maria Noel URRUTIA, Helena C. JUNQUEIRA, Alexander GREER, Ana REIS, Mauricio S. BAPTISTA, Rosangela ITRI and Andrés H. THOMAS. Photo-Oxidation of Unilamellar Vesicles by a Lipophilic Pterin: Deciphering Biomembrane Photodamage. Langmuir [online]. 2018, 34(50), 15578-15586 [accessed 2022-09-07]. ISSN 0743-7463. Available from: doi:10.1021/acs.langmuir.8b03302

[99] TOSATO, Maira Gaspar, Patricia SCHILARDI, Mónica Fernández LORENZO DE MELE, Andrés H. THOMAS, Carolina LORENTE and Alejandro MIÑÁN. Synergistic effect of carboxypterin and methylene blue applied to antimicrobial photodynamic therapy against mature biofilm of Klebsiella pneumoniae. Heliyon [online]. 2020, 6(3) [accessed 2022-09-07]. ISSN 24058440. Available from: doi:10.1016/j.heliyon.2020.e03522

[100] CARMONA-MARTÍNEZ, Violeta, Antonio J. RUIZ-ALCARAZ, María VERA, Antonio GUIRADO, María MARTÍNEZ-ESPARZA and Pilar GARCÍA-PEÑARRUBIA. Therapeutic potential of pteridine derivatives: A comprehensive review. Medicinal Research Reviews [online]. 2019, 39(2), 461-516 [accessed 2022-09-07]. ISSN 0198-6325. Available from: doi:10.1002/med.21529

[101] KOVANDOVÁ, Martina. Publications-Department of Organic Chemistry. Department of Organic Chemistry [online]. Praha: VŠCHT, 2022 [accessed 2022-09-07]. Available from: https://uoch.vscht.cz/research-groups/cibulka-en/publications

[102] HARTMAN, Tomáš, Martina REISNEROVÁ, Josef CHUDOBA, Eva SVOBODOVÁ, Nataliya ARCHIPOWA, Roger Jan KUTTA and Radek CIBULKA. Photocatalytic Oxidative [2+2] Cycloelimination Reactions with Flavinium Salts: Mechanistic Study and Influence of the Catalyst Structure. ChemPlusChem [online]. 2021, 86(3), 373-386 [accessed 2022-09-07]. ISSN 2192-6506. Available from: doi:10.1002/cplu.202000767

[103] POKLUDA, Adam, Zubair ANWAR, Veronika BOGUSCHOVÁ, Iwona ANUSIEWICZ, Piotr SKURSKI, Marek SIKORSKI and Radek CIBULKA. Robust Photocatalytic Method Using Ethylene-

Bridged Flavinium Salts for the Aerobic Oxidation of Unactivated Benzylic Substrates. Advanced Synthesis & Catalysis [online]. 2021, 363(18), 4371-4379 [accessed 2022-09-07]. ISSN 1615-4150. Available from: doi:10.1002/adsc.202100024

[104] HASSAN TOLBA, Amal, Martin KRUPIČKA, Josef CHUDOBA and Radek CIBULKA. Amide Bond Formation via Aerobic Photooxidative Coupling of Aldehydes with Amines Catalyzed by a Riboflavin Derivative. Organic Letters [online]. 2021, 23(17), 6825-6830 [accessed 2022-09-07]. ISSN 1523-7060. Available from: doi:10.1021/acs.orglett.1c02391

[105] MATARANGA-POPA, L. N., I. TORJE, T. GHOSH, M. J. LEITL, A. SPÄTH, M. L. NOVIANTI, R. D. WEBSTER and B. KÖNIG. Synthesis and electronic properties of π-extended flavins. Organic & Biomolecular Chemistry [online]. 2015, 13(40), 10198-10204 [accessed 2022-09-07]. ISSN 1477-0520. Available from: doi:10.1039/C5OB01418B

[106] MONDAL, Padmabati, Karno SCHWINN and Miquel HUIX-ROTLLANT. Impact of the redox state of flavin chromophores on the UV–vis spectra, redox and acidity constants and electron affinities. Journal of Photochemistry and Photobiology A: Chemistry [online]. 2020, 387 [accessed 2022-09-07]. ISSN 10106030. Available from: doi:10.1016/j.jphotochem.2019.112164

[107] HE, Run-Xia and Da-Wei ZHA. Cyclic voltammetry and voltabsorptometry studies of redox mechanism of lumazine. Journal of Electroanalytical Chemistry [online]. 2017, 791, 103-108 [accessed 2022-09-07]. ISSN 15726657. Available from: doi:10.1016/j.jelechem.2017.03.026

[108] SALZMANN, Susanne and Christel M. MARIAN. The photophysics of alloxazine: a quantum chemical investigation in vacuum and solution. Photochemical & Photobiological Sciences [online]. 2009, 8(12) [accessed 2022-09-07]. ISSN 1474-905X. Available from: doi:10.1039/b9pp00022d

[109] SIKORSKA, Ewa, Igor V. KHMELINSKII, David R. WORRALL, Jacek KOPUT and Marek SIKORSKI. Spectroscopy and Photophysics of Iso- and Alloxazines: Experimental and Theoretical Study. Journal of Fluorescence [online]. 2004, 14(1), 57-64 [accessed 2022-09-07]. ISSN 1053-0509. Available from: doi:10.1023/B:JOFL.0000014660.59105.31

[110] SIKORSKA, Ewa, Igor V KHMELINSKII, Siân L WILLIAMS, David R WORRALL, Jose R HERANCE, Jose L BOURDELANDE, Jacek KOPUT and Marek SIKORSKI. Spectroscopy and photophysics of 6,7-dimethyl-alloxazine: experimental and theoretical study. Journal of Molecular Structure [online]. 2004, 697(1-3), 199-205 [accessed 2022-09-07]. ISSN 00222860. Available from: doi:10.1016/j.molstruc.2004.04.011

[111] KABIR, Mohammad Pabel, Yoelvis OROZCO-GONZALEZ, Gary HASTINGS and Samer GOZEM. The effect of hydrogen-bonding on flavin's infrared absorption spectrum. Spectrochimica Acta Part A: Molecular and Biomolecular Spectroscopy [online]. 2021, 262 [accessed 2022-09-07]. ISSN 13861425. Available from: doi:10.1016/j.saa.2021.120110

[112] CHANG, Xue-Ping, Xiao-Ying XIE, Shi-Yun LIN and Ganglong CUI. QM/MM Study on Mechanistic Photophysics of Alloxazine Chromophore in Aqueous Solution. The Journal of Physical Chemistry A [online]. 2016, 120(31), 6129-6136 [accessed 2022-09-07]. ISSN 1089-5639. Available from: doi:10.1021/acs.jpca.6b02669

[113] GUO, Huimin, Xiaolin MA, Zhiwen LEI, Yang QIU, Jianzhang ZHAO and Bernhard DICK. Photophysical properties of N -methyl and N -acetyl substituted alloxazines: a theoretical investigation. Physical Chemistry Chemical Physics [online]. 2021, 23(24), 13734-13744 [accessed 2022-09-07]. ISSN 1463-9076. Available from: doi:10.1039/D1CP01201K

[114] SIKORSKI, M, E SIKORSKA, F WILKINSON and R P STEER. Studies of the photophysics and spectroscopy of alloxazine and related compounds in solution and in the solid state. Canadian Journal of Chemistry [online]. 1999, 77(4), 472-480 [accessed 2022-09-07]. ISSN 0008-4042. Available from: doi:10.1139/v99-076

[115] CLIMENT, Teresa, Remedios GONZÁLEZ-LUQUE, Manuela MERCHÁN and Luis SERRANO-ANDRÉS. Theoretical Insight into the Spectroscopy and Photochemistry of Isoalloxazine, the Flavin Core Ring. The Journal of Physical Chemistry A [online]. 2006, 110(50), 13584-13590 [accessed 2022-09-07]. ISSN 1089-5639. Available from: doi:10.1021/jp065772h

[116] KLAUMÜNZER, Bastian, Dominik KRÖNER, Hans LISCHKA and Peter SAALFRANK. Non-adiabatic excited state dynamics of riboflavin after photoexcitation. Physical Chemistry Chemical Physics [online]. 2012, 14(24) [accessed 2022-09-07]. ISSN 1463-9076. Available from: doi:10.1039/c2cp40978j

[117] MAL, Madhushree and Debabrata MANDAL. Phototautomerism of Alloxazine in Acetic acid – Water solvent systems. Journal of Molecular Liquids [online]. 2021, 322 [accessed 2022-09-07]. ISSN 01677322. Available from: doi:10.1016/j.molliq.2020.114928

[118] PENZKOFER, Alfons. Absorption and emission spectroscopic investigation of alloxazine in aqueous solutions and comparison with lumichrome. Journal of Photochemistry and Photobiology A: Chemistry [online]. 2016, 314, 114-124 [accessed 2022-09-07]. ISSN 10106030. Available from: doi:10.1016/j.jphotochem.2015.08.011

[119] NORTH, Michael A., Sudeep BHATTACHARYYA and Donald G. TRUHLAR. Improved Density Functional Description of the Electrochemistry and Structure−Property Descriptors of Substituted Flavins. The Journal of Physical Chemistry B [online]. 2010, 114(46), 14907-14915 [accessed 2022-09-07]. ISSN 1520-6106. Available from: doi:10.1021/jp108024b

[120] KORMÁNYOS, Attila, Mohammad S. HOSSAIN, Ghazaleh GHADIMKHANI, et al. Flavin Derivatives with Tailored Redox Properties: Synthesis, Characterization, and Electrochemical Behavior. Chemistry – A European Journal [online]. 2016, 22(27), 9209-9217 [accessed 2022-09-07]. ISSN 0947-6539. Available from: doi:10.1002/chem.201600207

[121] RICHTAR, Jan, Lucia IVANOVA, Dong Ryeol WHANG, et al. Tunable Properties of Nature-Inspired N,N′-Alkylated Riboflavin Semiconductors. Molecules [online]. 2021, 26(1) [accessed 2022-09-07]. ISSN 1420-3049. Available from: doi:10.3390/molecules26010027

[122] MARIAN, Christel M., Setsuko NAKAGAWA, Vidisha RAI-CONSTAPEL, Bora KARASULU and Walter THIEL. Photophysics of Flavin Derivatives Absorbing in the Blue-Green Region: Thioflavins As Potential Cofactors of Photoswitches. The Journal of Physical Chemistry B [online]. 2014, 118(7), 1743-1753 [accessed 2022-09-07]. ISSN 1520-6106. Available from: doi:10.1021/jp4098233

[123] BRACKER, Mario, Fabian DINKELBACH, Oliver WEINGART and Martin KLEINSCHMIDT. Impact of fluorination on the photophysics of the flavin chromophore: a quantum chemical perspective. Physical Chemistry Chemical Physics [online]. 2019, 21(19), 9912-9923 [accessed 2022-09-07]. ISSN 1463-9076. Available from: doi:10.1039/C9CP00805E

[124] PRUKAŁA, Dorota, Mateusz GIERSZEWSKI, Maciej KUBICKI, Tomasz PĘDZIŃSKI, Ewa SIKORSKA and Marek SIKORSKI. Spectroscopy and photophysics of trimethyl-substituted derivatives of 5-deazaalloxazine. Experimental and theoretical approaches. Journal of Molecular Structure [online]. 2015, 1079, 139-146 [accessed 2022-09-07]. ISSN 00222860. Available from: doi:10.1016/j.molstruc.2014.09.028

[125] INSIŃSKA-RAK, Małgorzata, Ewa SIKORSKA, Jose L. BOURDELANDE, et al. Spectroscopy and photophysics of flavin-related compounds: 5-deaza-riboflavin. Journal of Molecular Structure [online]. 2006, 783(1-3), 184-190 [accessed 2022-09-07]. ISSN 00222860. Available from: doi:10.1016/j.molstruc.2005.09.005

[126] ABBAS, Zina A. A., Najwa M. J. ABU-MEJDAD, Zeenah W. ATWAN and Najim A. AL-MASOUDI. Synthesis and Biological Evaluation of New Dipyridylpteridines, Lumazines, and Related Analogues. Journal of Heterocyclic Chemistry [online]. 2017, 54(2), 895-903 [accessed 2022-09-07]. ISSN 0022152X. Available from: doi:10.1002/jhet.2651

[127] SAKAI, Ken-ichi, Kenta NAGAHARA, Yuuya YOSHII, Norihisa HOSHINO and Tomoyuki AKUTAGAWA. Structural and Spectroscopic Study of 6,7-Dicyano-Substituted Lumazine with High Electron Affinity and Proton Acidity. The Journal of Physical Chemistry A [online]. 2013, 117(17), 3614-3624 [accessed 2022-09-07]. ISSN 1089-5639. Available from: doi:10.1021/jp401528c

[128] CARMONA-MARTÍNEZ, Violeta, Antonio J. RUIZ-ALCARAZ, María VERA, Antonio GUIRADO, María MARTÍNEZ-ESPARZA and Pilar GARCÍA-PEÑARRUBIA. Therapeutic potential of pteridine derivatives: A comprehensive review. Medicinal Research Reviews [online]. 2019, 39(2), 461-516 [accessed 2022-09-07]. ISSN 0198-6325. Available from: doi:10.1002/med.21529

[129] SOSA, María José, María Noel URRUTIA, Patricia L. SCHILARDI, et al. Mono - and Bis -Alkylated Lumazine Sensitizers: Synthetic, Molecular Orbital Theory, Nucleophilic Index and Photochemical

Studies. Photochemistry and Photobiology [online]. 2021, 97(1), 80-90 [accessed 2022-09-07]. ISSN 0031-8655. Available from: doi:10.1111/php.13310

[130] TURKOGLU, Gulsen, M. Emin CINAR and Turan OZTURK. Thiophene-Based Organic Semiconductors. Topics in Current Chemistry [online]. 2017, 375(6) [accessed 2022-09-07]. ISSN 2365-0869. Available from: doi:10.1007/s41061-017-0174-z

[131] DELL, Emma J., Brian CAPOZZI, Jianlong XIA, Latha VENKATARAMAN and Luis M. CAMPOS. Molecular length dictates the nature of charge carriers in single-molecule junctions of oxidized oligothiophenes. Nature Chemistry [online]. 2015, 7(3), 209-214 [accessed 2022-09-07]. ISSN 1755-4330. Available from: doi:10.1038/nchem.2160

[132] PALAMÀ, Ilaria Elena, Gabriele MAIORANO, Francesca DI MARIA, et al. Spontaneous Coassembly of the Protein Terthiophene into Fluorescent Electroactive Microfibers in 2D and 3D Cell Cultures. ACS Omega [online]. 2022, 7(15), 12624-12636 [accessed 2022-09-07]. ISSN 2470-1343. Available from: doi:10.1021/acsomega.1c06677

[133] JIANG, Chuanyu, Ping LIU and Wenji DENG. Synthesis and Photovoltaic Properties of Formyl End-Capped Oligothiophenes. Synthetic Communications [online]. 2009, 39(13), 2360-2369 [accessed 2022-09-07]. ISSN 0039-7911. Available from: doi:10.1080/00397910802654849

[134] KUNUGI, Yoshihito, Kazuo TAKIMIYA, Nobukazu NEGISHI, Tetsuo OTSUBO and Yoshio ASO. An ambipolar organic field-effect transistor using oligothiophene incorporated with two [60]fullerenes. Journal of Materials Chemistry [online]. 2004, 14(19) [accessed 2022-09-07]. ISSN 0959-9428. Available from: doi:10.1039/b412177e

[135] HALIK, Marcus, Hagen KLAUK, Ute ZSCHIESCHANG, Günter SCHMID, Wolfgang RADLIK, Sergei PONOMARENKO, Stephan KIRCHMEYER and Werner WEBER. High-mobility organic thin-film transistors based on α,α′-didecyloligothiophenes. Journal of Applied Physics [online]. 2003, 93(5), 2977-2981 [accessed 2022-09-07]. ISSN 0021-8979. Available from: doi:10.1063/1.1543246

[136] FACCHETTI, Antonio, Melissa MUSHRUSH, Myung-Han YOON, Geoffrey R. HUTCHISON, Mark A. RATNER and Tobin J. MARKS. Building Blocks for n-Type Molecular and Polymeric Electronics. Perfluoroalkyl- versus Alkyl-Functionalized Oligothiophenes (nT; n = 2−6). Systematics of Thin Film Microstructure, Semiconductor Performance, and Modeling of Majority Charge Injection in Field-Effect Transistors. Journal of the American Chemical Society [online]. 2004, 126(42), 13859-13874 [accessed 2022-09-07]. ISSN 0002-7863. Available from: doi:10.1021/ja0489846

[137] MISHRA, Amaresh and Peter BÄUERLE. Small Molecule Organic Semiconductors on the Move: Promises for Future Solar Energy Technology. Angewandte Chemie International Edition [online]. 2012, 51(9), 2020-2067 [accessed 2022-09-07]. ISSN 14337851. Available from: doi:10.1002/anie.201102326

[138] ZHANG, Maojie, Xia GUO, Wei MA, Harald ADE and Jianhui HOU. A Polythiophene Derivative with Superior Properties for Practical Application in Polymer Solar Cells. Advanced Materials [online]. 2014, 26(33), 5880-5885 [accessed 2022-09-07]. ISSN 09359648. Available from: doi:10.1002/adma.201401494

[139] HE, Xin, Tong SHAN, Xiangyang TANG, Yu GAO, Jinyu LI, Bing YANG and Ping LU. Highly efficient organic light emitting diodes based on a D–A–D type dibenzothiophene derivative exhibiting thermally activated delayed fluorescence with small ΔE ST. Journal of Materials Chemistry C [online]. 2016, 4(43), 10205-10208 [accessed 2022-09-07]. ISSN 2050-7526. Available from: doi:10.1039/C6TC03382B

[140] GUO, Xin, Martin BAUMGARTEN and Klaus MÜLLEN. Designing π-conjugated polymers for organic electronics. Progress in Polymer Science [online]. 2013, 38(12), 1832-1908 [accessed 2022-09-07]. ISSN 00796700. Available from: doi:10.1016/j.progpolymsci.2013.09.005

[141] ASHRAF, Raja Shahid, Iain MEAGER, Mark NIKOLKA, et al. Chalcogenophene Comonomer Comparison in Small Band Gap Diketopyrrolopyrrole-Based Conjugated Polymers for High-Performing Field-Effect Transistors and Organic Solar Cells. Journal of the American Chemical Society [online]. 2015, 137(3), 1314-1321 [accessed 2022-09-07]. ISSN 0002-7863. Available from: doi:10.1021/ja511984q

[142] LEE, J. L., E. M. PEARCE and T. K. KWEI. Side-Chain Crystallization in Alkyl-Substituted Semiflexible Polymers. Macromolecules [online]. 1997, 30(22), 6877-6883 [accessed 2022-09-07]. ISSN 0024-9297. Available from: doi:10.1021/ma970404k

[143] CUI, Chaohua and Wai-Yeung WONG. Macromol. Rapid Commun. 4/2016. Macromolecular Rapid Communications [online]. 2016, 37(4), 281-281 [accessed 2022-09-07]. ISSN 10221336. Available from: doi:10.1002/marc.201670015

[144] CAO, Zhiqiang, Luke GALUSKA, Zhiyuan QIAN, et al. The effect of side-chain branch position on the thermal properties of poly(3-alkylthiophenes). Polymer Chemistry [online]. 2020, 11(2), 517-526 [accessed 2022-09-07]. ISSN 1759-9954. Available from: doi:10.1039/C9PY01026B

[145] WANG, Chengliang, Huanli DONG, Wenping HU, Yunqi LIU and Daoben ZHU. Semiconducting π-Conjugated Systems in Field-Effect Transistors: A Material Odyssey of Organic Electronics. Chemical Reviews [online]. 2012, 112(4), 2208-2267 [accessed 2022-09-07]. ISSN 0009-2665. Available from: doi:10.1021/cr100380z

[146] SCHAFFRINNA, Roy and Martina SCHWAGER. Effect of interchain interactions on the optical characteristics of polythiophene derivatives. Materials Research Innovations [online]. 2021, 25(1), 23-28 [accessed 2022-09-07]. ISSN 1432-8917. Available from: doi:10.1080/14328917.2020.1728485

[147] BLASI, Davide, Fabrizio VIOLA, Francesco MODENA, et al. Printed, cost-effective and stable poly(3-hexylthiophene) electrolyte-gated field-effect transistors. Journal of Materials Chemistry C [online]. 2020, 8(43), 15312-15321 [accessed 2022-09-07]. ISSN 2050-7526. Available from: doi:10.1039/D0TC03342A

[148] KLEINSCHMIDT, Andrew T., Samuel E. ROOT and Darren J. LIPOMI. Poly(3-hexylthiophene) (P3HT): fruit fly or outlier in organic solar cell research?. Journal of Materials Chemistry A [online]. 2017, 5(23), 11396-11400 [accessed 2022-09-07]. ISSN 2050-7488. Available from: doi:10.1039/C6TA08317J

[149] NGUYEN, Thanh-Danh, Van-Hai NGUYEN, Jongwoo SONG, Jongdeok AN, Ngoc-Thuan TRUONG, Chi-Hien DANG and Chan IM. Molecular Weight-Dependent Physical and Photovoltaic Properties of Poly(3-alkylthiophene)s with Butyl, Hexyl, and Octyl Side-Chains. Polymers [online]. 2021, 13(19) [accessed 2022-09-07]. ISSN 2073-4360. Available from: doi:10.3390/polym13193440

[150] PARK, Hyeonjung, Moon Jong HAN, Youngkwon KIM, Eun Ji KIM, Hyeong Jun KIM, Dong Ki YOON and Bumjoon J. KIM. Regioregularity-Dependent Crystalline Structures and Thermal Transitions in Poly(3-dodecylthiophene)s. Chemistry of Materials [online]. 2021, 33(9), 3312-3320 [accessed 2022-09-07]. ISSN 0897-4756. Available from: doi:10.1021/acs.chemmater.1c00466

[151] LIN, Po-Shen, Yamato SHOJI, Shakil N. AFRAJ, et al. Controlled Synthesis of Poly[(3-alkylthio)thiophene]s and Their Application to Organic Field-Effect Transistors. ACS Applied Materials & Interfaces [online]. 2021, 13(27), 31898-31909 [accessed 2022-09-07]. ISSN 1944-8244. Available from: doi:10.1021/acsami.1c04404

[152] KRAJČOVIČ, Jozef, Alexander KOVALENKO, Patricie HEINRICHOVÁ, Martin VALA and Martin WEITER. Adamantyl side groups boosting the efficiency and thermal stability of organic solid-state fluorescent dyes. Journal of Luminescence [online]. 2016, 175, 94-99 [accessed 2022-09-07]. ISSN 00222313. Available from: doi:10.1016/j.jlumin.2016.02.019

[153] KOVALENKO, Alexander, Cigdem YUMUSAK, Patricie HEINRICHOVA, et al. Adamantane substitutions: a path to high-performing, soluble, versatile and sustainable organic semiconducting materials. Journal of Materials Chemistry C [online]. 2017, 5(19), 4716-4723 [accessed 2022-09-07]. ISSN 2050-7526. Available from: doi:10.1039/C6TC05076J

[154] LIAO, Mao, Jieming DUAN, Peng'ao PENG, Jingfeng ZHANG and Ming ZHOU. Progress in the synthesis of imide-based N-type polymer semiconductor materials. RSC Advances [online]. 2020, 10(68), 41764-41779 [accessed 2022-09-07]. ISSN 2046-2069. Available from: doi:10.1039/D0RA04972G

[155] KANIBOLOTSKY, Alexander L, Neil J FINDLAY and Peter J SKABARA. Polythiophene and oligothiophene systems modified by TTF electroactive units for organic electronics. Beilstein Journal of Organic Chemistry [online]. 2015, 11, 1749-1766 [accessed 2022-09-07]. ISSN 1860-5397. Available from: doi:10.3762/bjoc.11.191

[156] MARKS, Tobin, Antonio FACCHETTI, Henning SIRRINGHAUS and Richard FRIEND. N-type thiophene semiconductors. US6608323B2.

[157] BARBOZA, Bruno Hori, Orisson Ponce GOMES and Augusto BATAGIN-NETO. Polythiophene derivatives as chemical sensors: a DFT study on the influence of side groups. Journal of Molecular

Modeling [online]. 2021, 27(1) [accessed 2022-09-07]. ISSN 1610-2940. Available from: doi:10.1007/s00894-020-04632-w

[158] MORENO, Margherita, Mosè CASALEGNO, Guido RAOS, Stefano V. MEILLE and Riccardo PO. Molecular Modeling of Crystalline Alkylthiophene Oligomers and Polymers. The Journal of Physical Chemistry B [online]. 2010, 114(4), 1591-1602 [accessed 2022-09-07]. ISSN 1520-6106. Available from: doi:10.1021/jp9106124

[159] MARCON, Valentina and Guido RAOS. Molecular Modeling of Crystalline Oligothiophenes: Testing and Development of Improved Force Fields. The Journal of Physical Chemistry B [online]. 2004, 108(46), 18053-18064 [accessed 2022-09-07]. ISSN 1520-6106. Available from: doi:10.1021/jp047128d

[160] DARLING, Seth B. and Michael STERNBERG. Importance of Side Chains and Backbone Length in Defect Modeling of Poly(3-alkylthiophenes). The Journal of Physical Chemistry B [online]. 2009, 113(18), 6215-6218 [accessed 2022-09-07]. ISSN 1520-6106. Available from: doi:10.1021/jp808045j

[161] WILDMAN, Jack, Peter REPIŠČÁK, Martin J. PATERSON and Ian GALBRAITH. General Force-Field Parametrization Scheme for Molecular Dynamics Simulations of Conjugated Materials in Solution. Journal of Chemical Theory and Computation [online]. 2016, 12(8), 3813-3824 [accessed 2022-09-07]. ISSN 1549-9618. Available from: doi:10.1021/acs.jctc.5b01195

[162] BOUZZINE, Si Mohamed, Saïd BOUZAKRAOUI, Mohammed BOUACHRINE and Mohamed HAMIDI. Density functional theory (B3LYP/6-31G*) study of oligothiophenes in their aromatic and polaronic states. Journal of Molecular Structure: THEOCHEM [online]. 2005, 726(1-3), 271-276 [accessed 2022-09-07]. ISSN 01661280. Available from: doi:10.1016/j.theochem.2005.04.023

[163] HUANG, David M., Roland FALLER, Khanh DO and Adam J. MOULÉ. Coarse-Grained Computer Simulations of Polymer/Fullerene Bulk Heterojunctions for Organic Photovoltaic Applications. Journal of Chemical Theory and Computation [online]. 2010, 6(2), 526-537 [accessed 2022-09-07]. ISSN 1549-9618. Available from: doi:10.1021/ct900496t

[164] SCHILINSKY, Pavel, Udom ASAWAPIROM, Ullrich SCHERF, Markus BIELE and Christoph J. BRABEC. Influence of the Molecular Weight of Poly(3-hexylthiophene) on the Performance of Bulk Heterojunction Solar Cells. Chemistry of Materials [online]. 2005, 17(8), 2175-2180 [accessed 2022-09-07]. ISSN 0897-4756. Available from: doi:10.1021/cm047811c

[165] DUBAY, Kateri H., Michelle Lynn HALL, Thomas F. HUGHES, Chuanjie WU, David R. REICHMAN and Richard A. FRIESNER. Accurate Force Field Development for Modeling Conjugated Polymers. Journal of Chemical Theory and Computation [online]. 2012, 8(11), 4556-4569 [accessed 2022-09-07]. ISSN 1549-9618. Available from: doi:10.1021/ct300175w

[166] SCHERER, C. and D. ANDRIENKO. Comparison of systematic coarse-graining strategies for soluble conjugated polymers. The European Physical Journal Special Topics [online]. 2016, 225(8-9), 1441-1461 [accessed 2022-09-07]. ISSN 1951-6355. Available from: doi:10.1140/epjst/e2016-60154-9

[167] BHATTA, Ram S. and Mesfin TSIGE. Chain length and torsional dependence of exciton binding energies in P3HT and PTB7 conjugated polymers: A first-principles study. Polymer [online]. 2014, 55(11), 2667-2672 [accessed 2022-09-07]. ISSN 00323861. Available from: doi:10.1016/j.polymer.2014.04.022

[168] SIROHI, Ankit, Boddepalli SANTHIBHUSHAN and Anurag SRIVASTAVA. Charge transport in polythiophene molecular device: DFT analysis. Journal of Molecular Modeling [online]. 2021, 27(3) [accessed 2022-09-07]. ISSN 1610-2940. Available from: doi:10.1007/s00894-021-04680-w

[169] LAN, Yi-Kang, Cheng Han YANG and Hsiao-Ching YANG. Theoretical investigations of electronic structure and charge transport properties in polythiophene-based organic field-effect transistors. Polymer International [online]. 2010, 59(1), 16-21 [accessed 2022-09-07]. ISSN 09598103. Available from: doi:10.1002/pi.2683

[170] HOSSAIN, Mohammad S., Cuong Q. LE, Ebenezer JOSEPH, Toan Q. NGUYEN, Kayunta JOHNSON-WINTERS and Frank W. FOSS. Convenient synthesis of deazaflavin cofactor FO and its activity in F 420 -dependent NADP reductase. Organic & Biomolecular Chemistry [online]. 2015, 13(18), 5082-5085 [accessed 2022-09-07]. ISSN 1477-0520. Available from: doi:10.1039/C5OB00365B

[171] LEE, Chengteh, Weitao YANG and Robert G. PARR. Development of the Colle-Salvetti correlation-energy formula into a functional of the electron density. Physical Review B [online]. 1988, 37(2), 785-789 [accessed 2022-09-07]. ISSN 0163-1829. Available from: doi:10.1103/PhysRevB.37.785

[172] BECKE, A. D. Density-functional exchange-energy approximation with correct asymptotic behavior. Physical Review A [online]. 1988, 38(6), 3098-3100 [accessed 2022-09-07]. ISSN 0556-2791. Available from: doi:10.1103/PhysRevA.38.3098

[173] DAIDONE, Isabella, Andrea AMADEI, Massimiliano ASCHI and Laura ZANETTI-POLZI. On the nature of solvatochromic effect: The riboflavin absorption spectrum as a case study. Spectrochimica Acta Part A: Molecular and Biomolecular Spectroscopy [online]. 2018, 192, 451-457 [accessed 2022-09-07]. ISSN 13861425. Available from: doi:10.1016/j.saa.2017.11.031

[174] KLENE, Michael, Michael A. ROBB, Michael J. FRISCH and Paolo CELANI. Parallel implementation of the CI-vector evaluation in full CI/CAS-SCF. The Journal of Chemical Physics [online]. 2000, 113(14), 5653-5665 [accessed 2022-09-07]. ISSN 0021-9606. Available from: doi:10.1063/1.1290014

[175] BARTLETT, Rodney J. and George D. PURVIS. Many-body perturbation theory, coupled-pair many-electron theory, and the importance of quadruple excitations for the correlation problem. International Journal of Quantum Chemistry [online]. 1978, 14(5), 561-581 [accessed 2022-09-07]. ISSN 0020-7608. Available from: doi:10.1002/qua.560140504

[176] ADAMO, Carlo and Vincenzo BARONE. Toward reliable density functional methods without adjustable parameters: The PBE0 model. The Journal of Chemical Physics [online]. 1999, 110(13), 6158-6170 [accessed 2022-09-07]. ISSN 0021-9606. Available from: doi:10.1063/1.478522

[177] FORESMAN, James B. and AEleen FRISCH. Exploring chemistry with electronic structure methods. Third edition. Wallingford, CT: Gaussian, 2015. ISBN 978-1-935522-03-4.

[178] HARIHARAN, P. C. and J. A. POPLE. The influence of polarization functions on molecular orbital hydrogenation energies. Theoretica Chimica Acta [online]. 1973, 28(3), 213-222 [accessed 2022-09-07]. ISSN 0040-5744. Available from: doi:10.1007/BF00533485

[179] INSIŃSKA-RAK, Małgorzata, Ewa SIKORSKA, Jose R. HERANCE, et al. Spectroscopy and photophysics of flavin-related compounds: 3-benzyl-lumiflavin. Photochemical & Photobiological Sciences [online]. 2005, 4(6) [accessed 2022-09-07]. ISSN 1474-905X. Available from: doi:10.1039/b503898g

[180] KRISHNAN, R., J. S. BINKLEY, R. SEEGER and J. A. POPLE. Self-consistent molecular orbital methods. XX. A basis set for correlated wave functions. The Journal of Chemical Physics [online]. 1980, 72(1), 650-654 [accessed 2022-09-07]. ISSN 0021-9606. Available from: doi:10.1063/1.438955

[181] SCHÄFER, Ansgar, Christian HUBER and Reinhart AHLRICHS. Fully optimized contracted Gaussian basis sets of triple zeta valence quality for atoms Li to Kr. The Journal of Chemical Physics [online]. 1994, 100(8), 5829-5835 [accessed 2022-09-07]. ISSN 0021-9606. Available from: doi:10.1063/1.467146

[182] AFANEH, Akef T. and Georg SCHRECKENBACH. Fluorescence Enhancement/Quenching Based on Metal Orbital Control: Computational Studies of a 6-Thienyllumazine-Based Mercury Sensor. The Journal of Physical Chemistry A [online]. 2015, 119(29), 8106-8116 [accessed 2022-09-07]. ISSN 1089-5639. Available from: doi:10.1021/acs.jpca.5b04691

[183] DUNNING, Thom H. Gaussian basis sets for use in correlated molecular calculations. I. The atoms boron through neon and hydrogen. The Journal of Chemical Physics [online]. 1989, 90(2), 1007-1023 [accessed 2022-09-07]. ISSN 0021-9606. Available from: doi:10.1063/1.456153

[184] WEIGEND, Florian and Reinhart AHLRICHS. Balanced basis sets of split valence, triple zeta valence and quadruple zeta valence quality for H to Rn: Design and assessment of accuracy. Physical Chemistry Chemical Physics [online]. 2005, 7(18) [accessed 2022-09-07]. ISSN 1463-9076. Available from: doi:10.1039/b508541a

[185] YANAI, Takeshi, David P TEW and Nicholas C HANDY. A new hybrid exchange–correlation functional using the Coulomb-attenuating method (CAM-B3LYP). Chemical Physics Letters [online]. 2004, 393(1-3), 51-57 [accessed 2022-09-07]. ISSN 00092614. Available from: doi:10.1016/j.cplett.2004.06.011

[186] CARICATO, Marco. Absorption and Emission Spectra of Solvated Molecules with the EOM–CCSD–PCM Method. Journal of Chemical Theory and Computation [online]. 2012, 8(11), 4494-4502 [accessed 2022-09-07]. ISSN 1549-9618. Available from: doi:10.1021/ct3006997

[187] MCCORMICK, Theresa M., Colin R. BRIDGES, Elisa I. CARRERA, Paul M. DICARMINE, Gregory L. GIBSON, Jon HOLLINGER, Lisa M. KOZYCZ and Dwight S. SEFEROS. Conjugated Polymers: Evaluating DFT Methods for More Accurate Orbital Energy Modeling. Macromolecules [online]. 2013, 46(10), 3879-3886 [accessed 2022-09-07]. ISSN 0024-9297. Available from: doi:10.1021/ma4005023

[188] ZHAO, Yan and Donald G. TRUHLAR. Comparative DFT Study of van der Waals Complexes: Rare-Gas Dimers, Alkaline-Earth Dimers, Zinc Dimer, and Zinc-Rare-Gas Dimers. The Journal of Physical Chemistry A [online]. 2006, 110(15), 5121-5129 [accessed 2022-09-07]. ISSN 1089-5639. Available from: doi:10.1021/jp060231d

[189] OLIVEIRA, Eliezer Fernando, Juan Carlos ROLDAO, Begoña MILIÁN-MEDINA, Francisco Carlos LAVARDA and Johannes GIERSCHNER. Calculation of low bandgap homopolymers: Comparison of TD-DFT methods with experimental oligomer series. Chemical Physics Letters [online]. 2016, 645, 169-173 [accessed 2022-09-07]. ISSN 00092614. Available from: doi:10.1016/j.cplett.2015.12.059

[190] OLIVEIRA, Eliezer Fernando and Francisco Carlos LAVARDA. Design of diblock co-oligomers as low bandgap small molecules for organic solar cells. Molecular Simulation [online]. 2017, 43(18), 1496-1501 [accessed 2022-09-07]. ISSN 0892-7022. Available from: doi:10.1080/08927022.2017.1321759

[191] KÖRZDÖRFER, Thomas, John S. SEARS, Christopher SUTTON and Jean-Luc BRÉDAS. Long-range corrected hybrid functionals for π-conjugated systems: Dependence of the range-separation parameter on conjugation length. The Journal of Chemical Physics [online]. 2011, 135(20) [accessed 2022-09-07]. ISSN 0021-9606. Available from: doi:10.1063/1.3663856

[192] WILBRAHAM, Liam, Enrico BERARDO, Lukas TURCANI, Kim E. JELFS and Martijn A. ZWIJNENBURG. High-Throughput Screening Approach for the Optoelectronic Properties of Conjugated Polymers. Journal of Chemical Information and Modeling [online]. 2018, 58(12), 2450-2459 [accessed 2022-09-07]. ISSN 1549-9596. Available from: doi:10.1021/acs.jcim.8b00256

[193] YAO, Ze-Fan, Qi-Yi LI, Hao-Tian WU, Yi-Fan DING, Zi-Yuan WANG, Yang LU, Jie-Yu WANG and Jian PEI. Building crystal structures of conjugated polymers through X-ray diffraction and molecular modeling. SmartMat [online]. 2021, 2(3), 378-387 [accessed 2022-09-07]. ISSN 2688-819X. Available from: doi:10.1002/smm2.1053

[194] ATA, Ibrahim, Sadok Ben DKHIL, Martin PFANNMÖLLER, et al. The influence of branched alkyl side chains in A–D–A oligothiophenes on the photovoltaic performance and morphology of solution-processed bulk-heterojunction solar cells. Organic Chemistry Frontiers [online]. 2017, 4(8), 1561-1573 [accessed 2022-09-07]. ISSN 2052-4129. Available from: doi:10.1039/C7QO00222J

[195] Dimethyl sulfoxide|51779. Honeywell Research Chemicals [online]. Honeywell International, 2022 [accessed 2022-09-07]. Available from: https://lab.honeywell.com/shop/dimethyl-sulfoxide-51779

[196] Dimethyl Sulfoxide. Penta Chemicals [online]. Praha: PENTA, 2020 [cit. 2022-09-09]. Dostupné z: https://www.pentachemicals.eu/en/chemicals/dimethyl-sulfoxide-69

[197] M. J. Frisch, G. W. Trucks, H. B. Schlegel, G. E. Scuseria, M. A. Robb, J. R. Cheeseman, G. Scalmani, V. Barone, G. A. Petersson, H. Nakatsuji, X. Li, M. Caricato, A. V. Marenich, J. Bloino, B. G. Janesko, R. Gomperts, B. Mennucci, H. P. Hratchian, J. V. Ortiz, A. F. Izmaylov, J. L. Sonnenberg, D. Williams-Young, F. Ding, F. Lipparini, F. Egidi, J. Goings, B. Peng, A. Petrone, T. Henderson, D. Ranasinghe, V. G. Zakrzewski, J. Gao, N. Rega, G. Zheng, W. Liang, M. Hada, M. Ehara, K. Toyota, R. Fukuda, J. Hasegawa, M. Ishida, T. Nakajima, Y. Honda, O. Kitao, H. Nakai, T. Vreven, K. Throssell, J. A. Montgomery, Jr., J. E. Peralta, F. Ogliaro, M. J. Bearpark, J. J. Heyd, E. N. Brothers, K. N. Kudin, V. N. Staroverov, T. A. Keith, R. Kobayashi, J. Normand, K. Raghavachari, A. P. Rendell, J. C. Burant, S. S. Iyengar, J. Tomasi, M. Cossi, J. M. Millam, M. Klene, C. Adamo, R. Cammi, J. W. Ochterski, R. L. Martin, K. Morokuma, O. Farkas, J. B. Foresman, and D. J. Fox, Gaussian, Inc., Wallingford CT, 2016.

[198] Analytik Jena GmbH. ASpect UV Software, Jena, Germany, 2020.

[199] Horiba Instruments Incorporated, FluorEssence Software, Minami-ku Kyoto, Japan, 2019.

[200] MetaCentrum [online]. Praha: MetaCentrum, VO, 2022 [accessed 2022-09-07]. Available from: https://metavo.metacentrum.cz/en/index.html

[201] Hanwell, M.; Curtis, D. E.; Lonie, D. C.; Vandermeersch, T.; Zurek, E.; Hutchinson, G. R. Avogadro: An advanced semantic chemical editor, visualization, and analysis platform. J Cheminform 2012 4.

[202] Flukiger P, Luthi HP, Sortmann S, Weber J. Molekel 4.3 (2002), Swiss National Supercomputing Centre, Manno, Switzerland.

[203] Macrae, C. F.; Sovago, I.; Cottrell, S. J.; Galek, P. T. A.; McCabe, P.; Pidcock, E.; Platings, M.; Shields, G. P.; Stevens, J. S.; Towler, M.; Wood, P. A. Mercury 4.0: from visualization to analysis, design and prediction. Journal of Applied Crystallography 2020, 53, 226-235.

[204] HOROWITZ, Gilles, Bernard BACHET, Abderrahim YASSAR, Philippe LANG, Frederic DEMANZE, Jean-Louis FAVE and Francis GARNIER. Growth and Characterization of Sexithiophene Single Crystals. Chemistry of Materials [online]. 1995, 7(7), 1337-1341 [accessed 2022-09-07]. ISSN 0897-4756. Available from: doi:10.1021/cm00055a010

[205] NEUMANN, Marcus A., Consiglia TEDESCO, Silvia DESTRI, Dino R. FERRO and William PORZIO. Bridging the gap – structure determination of the red polymorph of tetrahexylsexithiophene by Monte Carlo simulated annealing, first-principles DFT calculations and Rietveld refinement. Journal of Applied Crystallography [online]. 2002, 35(3), 296-303 [accessed 2022-09-07]. ISSN 0021-8898. Available from: doi:10.1107/S0021889802002844

[206] PROSA, T. J., M. J. WINOKUR, Jeff MOULTON, Paul SMITH and A. J. HEEGER. X-ray structural studies of poly(3-alkylthiophenes): an example of an inverse comb. Macromolecules [online]. 1992, 25(17), 4364-4372 [accessed 2022-09-07]. ISSN 0024-9297. Available from: doi:10.1021/ma00043a019

[207] DAG, Sefa and Lin-Wang WANG. Packing Structure of Poly(3-hexylthiophene) Crystal: Ab Initio and Molecular Dynamics Studies. The Journal of Physical Chemistry B [online]. 2010, 114(18), 5997-6000 [accessed 2022-09-07]. ISSN 1520-6106. Available from: doi:10.1021/jp1008219

10 OVERWIEV OF THE AUTHOR'S PUBLICATIONS

10.1 Publications containing the results presented in this work

[JT1] Spectroscopic behavior of alloxazine-based dyes with extended aromaticity: Theory vs Experiment.

CAGARDOVÁ, Denisa, **TRUKSA, Jan**, MICHALÍK, Martin, RICHTÁR, Jan, WEITER, Martin, KRAJČOVIČ, Jozef, LUKEŠ Vladimír

In this paper, the large conjugated alloxazines were studied, and the theoretically predicted properties were compared to experimental results. The B3LYP and CAM-B3LYP functionals were used, together with the 6-31+G** basis set. While the range-corrected CAM-B3LYP did not give correct predictions, the B3LYP/6-31+G** method proved to be efficient for the spectroscopic properties' predictions. To the author's knowledge, this was the first scientific paper where systematic theoretical investigations of alloxazines with fused benzene rings was published.

The author's personal contribution

The author ran the theoretical calculations, evaluated the resulting data – e.g. the HOMED indices, and the fit of experimental and theoretical data, and co-authored the manuscript.

[JT2] Theoretical modeling of optical spectra of N(1) and N(10) substituted lumichrome derivatives

CAGARDOVÁ, Denisa, **TRUKSA, Jan**, MICHALÍK, Martin, RICHTÁR, Jan, WEITER, Martin, KRAJČOVIČ, Jozef, LUKEŠ Vladimír

In this paper, the influence of substitutions in the N(1) and N(10) positions of alloxazine on the structure and frontier orbital energies was investigated. The bending of the **iAL** molecule was described, as anticipated in previous literature [North 2010].

The author's personal contribution

The author evaluated the data from theoretical calculations and co-authored the manuscript.

[JT3] Novel Adamantane Substituted Polythiophenes as Competitors to Poly(3-Hexylthiophene)

JANČÍK, Jan, POSPÍŠIL, Jan, KRATOCHVÍL, Matouš, TRUKSA, Jan, ALTAMURA, Davide, GIANNINI, Cinza, WEITER, Martin, BLASI, Davide, LUKEŠ, Vladimír, GŁOWACKI, Eric D., KRAJČOVIČ, Jozef

Here, the novel adamantyl-substituted polythiophene chains were introduced, and the synthesis, purification and characterization were described, including the theoretical study of chain conformations, spectroscopic and electrochemical measurements, crystallography and AFM scanning. These materials were found to have comparable properties to P3HT, showing the utility of adamantyl substitutions.

The author's personal contribution

The author performed the conformation analysis of the model oligomers and their theoretical electronic excitations and co-authored this part of the manuscript with prof. Lukeš. Further, the author performed the AFM scans, and authored this part of the manuscript.

10.2 Conference Contributions

TRUKSA, Jan, CAGARDOVÁ, Denisa, MICHALÍK, Martin, RICHTÁR, Jan, WEITER, Martin, KRAJČOVIČ, Jozef, LUKEŠ, Vladimír. Spectroscopic behavior of alloxazine derivates: Theory vs Experiment. DCMS Materials 4.0 Summer School. Book of Abstracts, Dresden 2021 pp.60

TRUKSA, Jan, CAGARDOVÁ, Denisa, MICHALÍK, Martin, RICHTÁR, Jan, WEITER, Martin, KRAJČOVIČ, Jozef, LUKEŠ, Vladimír. Visible-Light Spectroscopy of Alloxazines: Theory and Experiment. 8th Meeting on Chemistry and Life. 2021. Book of abstracts. Brno: Vysoké učení technické v Brně, 2021.

TRUKSA, Jan, CAGARDOVÁ, Denisa, MICHALÍK, Martin, RICHTÁR, Jan, WEITER, Martin, KRAJČOVIČ, Jozef, LUKEŠ, Vladimír. The Effect of Substitution and Aromatic Ring Condensation on the Optical Properties of Alloxazine: a Theoretical Study. CHEMIE JE ŽIVOT 2020 Book of Abstracts. Brno: Vysoké učení technické v Brně, 2020. pp. 225-230. ISBN 978-80-214-5921-2

TRUKSA, Jan, SALYK, Ota. Modelling of Bioelectronic Devices. 7th Meeting on Chemistry and Life 2018. CZECH CHEMICAL SOCIETY SYMPOSIUM SERIES 16 (2018). Asociace Českých Chemických Společností, 2018. p 518-522. ISSN 2336-7210

11 APPENDIX A – THE SUPPLEMENTARY INFORMATION

Table 1S *Selected TD–B3LYP(DMSO)/6–31+G** lowest energy singlet ($S_0 \rightarrow S_n$) transitions and the corresponding oscillator strengths f. The probability of electron orbital transition is in percentage.*

Molecule	*n*	*E* / eV	*λ* / nm	*f*	Dominant transition
AL	1	3.323	373	0.08	HOMO → LUMO: 96 %
	2	3.498	354	0.00	HOMO – 2 → LUMO: 96 %
	3	3.819	325	0.28	HOMO – 1 → LUMO: 91 %
	4	4.058	306	0.00	HOMO – 3 → LUMO: 89 %
	5	4.766	260	0.06	HOMO – 4 → LUMO: 77 %
iAL	1	2.966	418	0.22	HOMO → LUMO: 94 %
	2	3.397	365	0.00	HOMO – 2 → LUMO: 67 %
	3	3.541	350	0.00	HOMO – 3 → LUMO: 67 %
	4	3.613	343	0.23	HOMO – 1 → LUMO: 94 %
	5	4.147	299	0.01	HOMO – 5 → LUMO: 91 %
Ph2	1	2.404	516	0.03	HOMO → LUMO: 99 %
	2	3.316	374	0.00	HOMO – 2 → LUMO: 96 %
	3	3.330	372	0.38	HOMO – 1 → LUMO: 87 %
	4	3.914	317	0.00	HOMO – 4 → LUMO: 90 %
	5	4.155	298	0.53	HOMO → LUMO + 1: 44 %
iPh2	1	2.330	532	0.01	HOMO → LUMO: 99 %
	2	3.029	409	0.63	HOMO – 1 → LUMO: 96 %
	3	3.297	376	0.00	HOMO – 2 → LUMO: 67 %
	4	3.444	360	0.00	HOMO – 3 → LUMO: 66 %
	5	4.029	308	0.03	HOMO – 5 → LUMO: 44 %
Ph3	1	1.790	693	0.03	HOMO → LUMO: 100 %
	2	3.036	408	0.27	HOMO – 1 → LUMO: 79 %
	3	3.206	387	0.00	HOMO – 3 → LUMO: 95 %
	4	3.342	371	0.32	HOMO → LUMO + 1: 83 %
	5	3.414	363	0.01	HOMO – 2 → LUMO: 91 %
iPh3	1	1.754	707	0.03	HOMO → LUMO: 99 %
	2	2.814	441	0.67	HOMO – 1 → LUMO: 93 %
	3	3.235	383	0.00	HOMO – 3 → LUMO: 67 %
	4	3.349	370	0.27	HOMO → LUMO + 1: 88 %
	5	3.381	367	0.00	HOMO – 5 → LUMO: 67 %
PyPh2	1	2.170	571	0.04	HOMO → LUMO: 99 %
	2	2.732	454	0.00	HOMO – 2 → LUMO: 96 %
	3	2.978	416	0.56	HOMO – 1 → LUMO: 91 %
	4	3.046	407	0.00	HOMO – 4 → LUMO: 93 %
	5	3.273	379	0.08	HOMO – 3 → LUMO: 88 %
iPyPh2	1	2.167	572	0.03	HOMO → LUMO: 99 %
	2	2.755	450	0.00	HOMO – 2 → LUMO: 95 %
	3	2.789	445	0.77	HOMO – 1 → LUMO: 94 %
	4	3.091	401	0.00	HOMO – 4 → LUMO: 73 %
	5	3.244	382	0.00	HOMO – 5 → LUMO: 73 %

Table 1S (continued) *Selected TD–B3LYP(DMSO)/6–31+G** lowest energy singlet ($S_0 \rightarrow S_n$) transitions and the corresponding oscillator strengths f. The probability of electron orbital transition is in percentage*

Molecule	*n*	*E* / eV	□ / nm	*f*	Dominant transition
Phe	1	3.086	402	0.09	HOMO → LUMO: 70 %
	2	3.197	388	0.28	HOMO – 1 → LUMO: 70 %
	3	3.591	345	0.00	HOMO – 3 → LUMO: 96 %
	4	3.918	316	0.05	HOMO – 2 → LUMO: 81 %
	5	4.054	306	0.15	HOMO – 1 → LUMO + 1: 55 %
iPhe	1	2.665	465	0.33	HOMO → LUMO: 98 %
	2	2.885	430	0.07	HOMO – 1 → LUMO: 98 %
	3	3.412	363	0.00	HOMO – 2 → LUMO: 63 %
	4	3.566	348	0.00	HOMO – 5 → LUMO: 62 %
	5	3.797	327	0.09	HOMO – 3 → LUMO: 68 %
PhePh	1	2.582	480	0.02	HOMO → LUMO: 99 %
	2	2.925	424	0.43	HOMO – 1 → LUMO: 95 %
	3	3.156	393	0.11	HOMO – 2 → LUMO: 97 %
	4	3.394	365	0.00	HOMO – 3 → LUMO: 96 %
	5	3.926	316	0.13	HOMO – 4 → LUMO: 60 %
iPhePh	1	2.421	512	0.07	HOMO → LUMO: 94 %
	2	2.679	463	0.48	HOMO – 1 → LUMO: 94 %
	3	3.047	407	0.18	HOMO – 2 → LUMO: 97 %
	4	3.334	372	0.00	HOMO – 4 → LUMO: 70 %
	5	3.477	357	0.00	HOMO – 5 → LUMO: 70 %
PhePh2	1	2.011	616	0.02	HOMO → LUMO: 99 %
	2	2.748	451	0.49	HOMO – 1 → LUMO: 93 %
	3	2.864	433	0.07	HOMO – 2 → LUMO: 98 %
	4	3.260	380	0.00	HOMO – 5 → LUMO: 85 %
	5	3.482	356	0.16	HOMO – 3 → LUMO: 53 %
iPhePh2	1	1.951	636	0.01	HOMO → LUMO: 99 %
	2	2.564	484	0.71	HOMO – 1 → LUMO: 96 %
	3	2.755	450	0.10	HOMO – 2 → LUMO: 97 %
	4	3.252	381	0.13	HOMO – 3 → LUMO: 97 %
	5	3.261	380	0.00	HOMO – 5 → LUMO: 70 %

Table 1S (continued) *Selected TD–B3LYP(DMSO)/6–31+G** lowest energy singlet ($S_0 \rightarrow S_n$) transitions and the corresponding oscillator strengths f. The probability of electron orbital transition is in percentage.*

Molecule	*n*	*E* / eV	*λ* / nm	*f*	Dominant transition
Pyr	1	2.675	463	0.19	HOMO → LUMO: 98 %
	2	3.228	384	0.01	HOMO – 1 → LUMO: 93 %
	3	3.586	346	0.36	HOMO → LUMO + 1: 88 %
	4	3.597	345	0.00	HOMO –3 → LUMO: 96 %
	5	3.779	328	0.16	HOMO – 2 → LUMO: 96 %
iPyr	1	2.331	532	0.23	HOMO → LUMO: 99 %
	2	2.989	415	0.00	HOMO – 1 → LUMO: 94 %
	3	3.213	386	0.17	HOMO – 2 → LUMO: 93 %
	4	3.412	363	0.00	HOMO – 3 → LUMO: 65 %
	5	3.525	352	0.47	HOMO → LUMO + 1: 92 %
PyrPh	1	2.414	514	0.23	HOMO → LUMO: 97 %
	2	2.647	468	0.05	HOMO – 1 → LUMO: 97 %
	3	3.332	372	0.04	HOMO – 2 → LUMO: 97 %
	4	3.395	365	0.00	HOMO – 4 → LUMO: 95 %
	5	3.555	349	0.14	HOMO – 3 → LUMO: 74 %
iPyrPh	1	2.191	566	0.26	HOMO → LUMO: 98 %
	2	2.551	486	0.07	HOMO – 1 → LUMO: 98 %
	3	3.042	408	0.26	HOMO – 2 → LUMO: 97 %
	4	3.332	372	0.00	HOMO – 4 → LUMO: 70 %
	5	3.354	370	0.24	HOMO – 3 → LUMO: 96 %
Lum	1	3.757	330	0.00	HOMO – 2 → LUMO: 95 %
	2	4.080	304	0.26	HOMO → LUMO: 98 %
	3	4.348	285	0.00	HOMO – 2 → LUMO: 95 %
	4	4.848	256	0.00	HOMO – 1 → LUMO + 1: 96 %
	5	5.095	243	0.08	HOMO → LUMO + 1: 65 %
iLum	1	3.235	383	0.26	HOMO → LUMO: 99 %
	2	3.466	358	0.00	HOMO – 1 → LUMO: 58 %
	3	3.656	339	0.01	HOMO – 2 → LUMO: 52 %
	4	4.290	289	0.00	HOMO – 4 → LUMO: 95%
	5	4.354	285	0.01	HOMO – 3 → LUMO: 96 %
CNLum	1	3.560	348	0.00	HOMO – 1 → LUMO: 97 %
	2	3.574	347	0.27	HOMO → LUMO: 99 %
	3	4.142	299	0.00	HOMO – 3 → LUMO: 57 %
	4	4.269	290	0.55	HOMO → LUMO + 1: 97 %
	5	4.320	287	0.00	HOMO → LUMO + 2: 95 %

Table 1S (continued) *Selected TD–B3LYP(DMSO)/6–31+G** lowest energy singlet ($S_0 \rightarrow S_n$) transitions and the corresponding oscillator strengths f. The probability of electron orbital transition is in percentage.*

Molecule	*n*	*E* / eV	□ / nm	*f*	Dominant transition
iCNLum	1	2.850	435	0.22	HOMO → LUMO: 99 %
	2	3.118	398	0.00	HOMO – 1 → LUMO: 96 %
	3	3.411	363	0.00	HOMO – 2 → LUMO: 95 %
	4	3.784	328	0.01	HOMO – 3 → LUMO: 96 %
	5	3.859	321	0.00	HOMO – 4 → LUMO: 96 %
FAL	1	3.393	365	0.29	HOMO → LUMO: 98 %
	2	3.453	359	0.01	HOMO – 2 → LUMO: 97 %
	3	3.930	315	0.31	HOMO – 1 → LUMO: 98 %
	4	4.050	306	0.00	HOMO – 3 → LUMO: 96 %
	5	4.728	262	0.03	HOMO – 4 → LUMO: 95 %
iFAL	1	2.923	424	0.41	HOMO → LUMO: 99 %
	2	3.271	379	0.00	HOMO – 1 → LUMO: 90 %
	3	3.463	358	0.00	HOMO – 3 → LUMO: 89 %
	4	3.830	324	0.26	HOMO – 2 → LUMO: 98 %
	5	4.058	306	0.00	HOMO – 5 → LUMO: 97 %
PheLum	1	3.215	386	0.45	HOMO → LUMO: 99 %
	2	3.769	329	0.01	HOMO – 3 → LUMO: 60 %
	3	3.882	319	0.01	HOMO – 1 → LUMO: 95 %
	4	3.979	312	0.30	HOMO → LUMO + 1: 60 %
	5	4.034	307	0.24	HOMO – 2 → LUMO: 61 %
iPheLum	1	2.696	460	0.44	HOMO → LUMO: 99 %
	2	3.470	357	0.00	HOMO – 1 → LUMO: 90 %
	3	3.523	352	0.00	HOMO – 3 → LUMO: 62 %
	4	3.628	342	0.01	HOMO – 4 → LUMO: 62 %
	5	3.724	333	0.05	HOMO – 2 → LUMO: 59 %
ImiLum	1	3.387	366	0.42	HOMO → LUMO: 99 %
	2	3.668	338	0.02	HOMO – 1 → LUMO: 80 %
	3	3.984	311	0.06	HOMO – 2 → LUMO: 70 %
	4	4.037	307	0.06	HOMO – 3 → LUMO: 65 %
	5	4.063	305	0.42	HOMO → LUMO + 1: 90 %
iImiLum	1	2.713	457	0.44	HOMO → LUMO: 99 %
	2	3.433	361	0.01	HOMO – 1 → LUMO: 63 %
	3	3.522	352	0.01	HOMO – 2 → LUMO: 78 %
	4	3.665	338	0.04	HOMO – 5 → LUMO: 59 %
	5	3.769	329	0.63	HOMO → LUMO + 1: 98 %

Table 1S (continued) *Selected TD–B3LYP(DMSO)/6–31+G** lowest energy singlet ($S_0 \rightarrow S_n$) transitions and the corresponding oscillator strengths f. The probability of electron orbital transition is in percentage.*

Molecule	*n*	*E* / eV	□ / nm	*f*	Dominant transition
FurLum	1	2.836	437	0.47	HOMO → LUMO: 99 %
	2	3.488	355	0.31	HOMO – 1 → LUMO: 95 %
	3	3.602	344	0.45	HOMO → LUMO + 1: 96 %
	4	3.817	325	0.03	HOMO – 3 → LUMO: 61 %
	5	4.204	295	0.02	HOMO – 3 → LUMO: 59 %
iFurLum	1	2.368	523	0.42	HOMO → LUMO: 99 %
	2	3.232	383	0.32	HOMO – 1 → LUMO: 98 %
	3	3.467	357	0.00	HOMO – 3 → LUMO: 98 %
	4	3.535	350	0.62	HOMO → LUMO + 1: 98 %
	5	3.605	343	0.11	HOMO – 2 → LUMO: 95 %
ThLum	1	2.745	451	0.42	HOMO → LUMO: 99 %
	2	3.367	368	0.44	HOMO → LUMO + 1: 98 %
	3	3.632	341	0.24	HOMO – 1 → LUMO: 90 %
	4	3.722	333	0.03	HOMO – 3 → LUMO: 78 %
	5	3.799	326	0.02	HOMO – 2 → LUMO: 92 %
iThLum	1	2.308	537	0.36	HOMO → LUMO: 99 %
	2	3.318	373	0.23	HOMO – 1 → LUMO: 80 %
	3	3.356	369	0.20	HOMO – 2 → LUMO: 72 %
	4	3.386	366	0.31	HOMO – 1 → LUMO: 79 %
	5	3.491	355	0.09	HOMO – 3 → LUMO: 75 %
PyLum	1	1.848	670	0.33	HOMO → LUMO: 98 %
	2	1.951	635	0.01	HOMO – 1 → LUMO: 95 %
	3	2.336	530	0.02	HOMO – 2 → LUMO: 98 %
	4	2.454	505	0.05	HOMO – 3 → LUMO: 95 %
	5	2.709	457	0.03	HOMO – 4 → LUMO: 65 %
iPyLum	1	1.929	642	0.26	HOMO → LUMO: 98 %
	2	2.099	590	0.02	HOMO – 1 → LUMO: 98 %
	3	2.377	521	0.01	HOMO – 2 → LUMO: 98 %
	4	2.525	490	0.10	HOMO – 4 → LUMO: 65 %
	5	2.808	441	0.41	HOMO – 4 → LUMO: 65 %

Table 1S (continued) *Selected TD–B3LYP(DMSO)/6–31+G** lowest energy singlet ($S_0 \rightarrow S_n$) transitions and the corresponding oscillator strengths f. The probability of electron orbital transition is in percentage.*

Molecule	***n***	***E* / eV**	□ **/ nm**	***f***	**Dominant transition**
78CH	1	3.274	378	0.19	HOMO → LUMO: 98 %
	2	3.439	360	0.00	HOMO – 2 → LUMO: 97%
	3	3.668	337	0.50	HOMO – 1 → LUMO: 97 %
	4	4.076	304	0.00	HOMO – 3 → LUMO: 95 %
	5	4.765	260	0.66	HOMO → LUMO + 1: 86 %
i78CH	1	2.857	433	0.42	HOMO → LUMO: 99 %
	2	3.316	373	0.00	HOMO – 2 → LUMO: 97%
	3	3.503	353	0.00	HOMO – 3 → LUMO: 85
	4	3.523	351	0.35	HOMO – 1 → LUMO: 97 %
	5	4.123	300	0.00	HOMO – 5 → LUMO: 97 %

Table 2S *Selected TD–CAM–B3LYP(DMSO)/B3LYP(DMSO)/6–31+G** lowest energy singlet ($S_0 \rightarrow S_n$) transitions and the corresponding oscillator strengths f. The probability of electron orbital transition is in percentage.*

Molecule	***n***	***E* / eV**	**□ / nm**	***f***	**Dominant transition**
AL	1	3.711	334	0.19	HOMO → LUMO: 95 %
	2	3.870	320	0.00	HOMO – 2 → LUMO: 86 %
	3	4.140	300	0.24	HOMO – 1 → LUMO: 92 %
	4	4.584	270	0.00	HOMO – 3 → LUMO: 95 %
	5	5.247	236	0.83	HOMO → LUMO + 1: 72 %
iAL	1	3.300	376	0.37	HOMO → LUMO: 98 %
	2	3.794	327	0.00	HOMO – 3 → LUMO: 73 %
	3	4.044	307	0.21	HOMO – 1 → LUMO: 96 %
	4	4.214	294	0.00	HOMO – 2 → LUMO: 56 %
	5	4.903	253	0.15	HOMO → LUMO + 1: 40 %
Ph2	1	2.896	428	0.05	HOMO → LUMO: 97 %
	2	3.607	344	0.43	HOMO – 1 → LUMO: 85 %
	3	3.711	334	0.00	HOMO – 2 → LUMO: 84 %
	4	4.467	278	0.00	HOMO – 4 → LUMO: 62 %
	5	4.564	272	1.48	HOMO → LUMO + 1: 67 %
iPh2	1	2.880	430	0.04	HOMO → LUMO: 96 %
	2	3.338	371	0.80	HOMO – 1 → LUMO: 93 %
	3	3.696	335	0.00	HOMO – 4 → LUMO: 68 %
	4	4.124	301	0.00	HOMO – 2 → LUMO: 53 %
	5	4.492	276	0.45	HOMO → LUMO + 1: 34 %
Ph3	1	2.294	540	0.06	HOMO → LUMO: 98 %
	2	3.349	370	0.32	HOMO – 1 → LUMO: 74 %
	3	3.619	343	0.00	HOMO – 3 → LUMO: 81 %
	4	3.780	328	0.32	HOMO → LUMO + 1: 61 %
	5	4.094	303	1.48	HOMO → LUMO + 2: 35 %
iPh3	1	2.335	531	0.06	HOMO → LUMO: 96 %
	2	3.155	393	0.86	HOMO – 1 → LUMO: 89 %
	3	3.641	340	0.00	HOMO – 5 → LUMO: 64 %
	4	3.771	329	0.47	HOMO → LUMO + 1: 80 %
	5	4.025	308	0.47	HOMO→ LUMO + 2: 45 %
PyPh2	1	2.616	474	0.08	HOMO → LUMO: 98 %
	2	3.217	385	0.00	HOMO – 3 → LUMO: 83 %
	3	3.265	380	0.74	HOMO – 1 → LUMO: 87 %
	4	3.542	350	0.00	HOMO – 4 → LUMO: 72 %
	5	3.771	329	0.14	HOMO – 2 → LUMO: 68 %
iPyPh2	1	2.695	460	0.11	HOMO → LUMO: 95 %
	2	3.128	396	0.96	HOMO – 1 → LUMO: 89 %
	3	3.292	377	0.00	HOMO – 3 → LUMO: 77 %
	4	3.567	348	0.00	HOMO – 6 → LUMO: 57 %
	5	3.814	325	0.30	HOMO – 2 → LUMO: 52 %

Table 2S (continued) *Selected TD–CAM–B3LYP(DMSO)/B3LYP(DMSO)/6–31+G** lowest energy singlet ($S_0 \rightarrow S_n$) transitions and the corresponding oscillator strengths f. The probability of electron orbital transition is in percentage.*

Molecule	*n*	*E* / eV	□ / nm	*f*	Dominant transition
Phe	1	3.528	351	0.43	HOMO → LUMO: 91 %
	2	3.854	322	0.09	HOMO – 1 → LUMO: 88 %
	3	3.982	311	0.00	HOMO – 3 → LUMO: 86 %
	4	4.429	280	0.28	HOMO → LUMO + 1: 57 %
	5	4.523	274	0.11	HOMO – 1 → LUMO + 1: 48 %
iPhe	1	2.983	416	0.49	HOMO → LUMO: 97 %
	2	3.614	343	0.08	HOMO – 1 → LUMO: 91 %
	3	3.837	323	0.00	HOMO – 5 → LUMO: 72 %
	4	4.267	291	0.41	HOMO → LUMO + 1: 68 %
	5	4.294	289	0.00	HOMO – 4 → LUMO: 54 %
PhePh	1	3.164	392	0.08	HOMO → LUMO: 85 %
	2	3.444	360	0.64	HOMO – 1 → LUMO: 81 %
	3	3.791	327	0.00	HOMO – 4 → LUMO: 83 %
	4	4.100	302	0.05	HOMO – 2 → LUMO: 76 %
	5	4.353	285	1.12	HOMO → LUMO + 1: 73 %
iPhePh	1	2.956	419	0.43	HOMO → LUMO: 88 %
	2	3.290	377	0.52	HOMO – 1 → LUMO: 78 %
	3	3.747	331	0.00	HOMO – 5 → LUMO: 71 %
	4	4.006	310	0.05	HOMO – 2 → LUMO: 72 %
	5	4.155	298	0.00	HOMO – 4 → LUMO: 55 %
PhePh2	1	2.558	485	0.04	HOMO → LUMO: 94 %
	2	3.264	380	0.69	HOMO – 1 → LUMO: 75 %
	3	3.669	338	0.00	HOMO – 5 → LUMO: 81 %
	4	3.871	320	0.18	HOMO – 2 → LUMO: 52 %
	5	4.010	309	1.95	HOMO → LUMO + 1: 57 %
iPhePh2	1	2.571	482	0.02	HOMO → LUMO: 91 %
	2	3.060	405	1.16	HOMO – 1 → LUMO: 81 %
	3	3.669	338	0.00	HOMO – 6 → LUMO: 66 %
	4	3.855	322	0.10	HOMO – 2 → LUMO: 57 %
	5	3.971	312	0.86	HOMO → LUMO + 1: 36 %

Table 2S (continued) *Selected TD–CAM–B3LYP(DMSO)/B3LYP(DMSO)/6–31+G** lowest energy singlet ($S_0 \rightarrow S_n$) transitions and the corresponding oscillator strengths f. The probability of electron orbital transition is in percentage.*

Molecule	***n***	***E* / eV**	**□ / nm**	***f***	**Dominant transition**
Pyr	1	3.238	383	0.35	HOMO → LUMO: 91 %
	2	3.819	325	0.09	HOMO – 1 → LUMO: 51 %
	3	3.990	311	0.00	HOMO – 4 → LUMO: 84 %
	4	4.077	304	0.41	HOMO → LUMO + 1: 27 %
	5	4.191	296	0.26	HOMO – 1 → LUMO: 28 % HOMO → LUMO + 1: 25 %
iPyr	1	2.790	444	0.43	HOMO → LUMO: 93 %
	2	3.645	340	0.04	HOMO – 1 → LUMO: 74 %
	3	3.795	327	0.26	HOMO – 2 → LUMO: 71 %
	4	3.845	322	0.00	HOMO – 5 → LUMO: 72 %
	5	4.004	310	0.48	HOMO → LUMO + 1: 67 %
PyrPh	1	3.095	401	0.33	HOMO → LUMO: 68 %
	2	3.293	377	0.26	HOMO – 1 → LUMO: 70 %
	3	3.795	327	0.00	HOMO – 4 → LUMO: 83 %
	4	3.987	311	0.30	HOMO – 2 → LUMO: 24 %
	5	4.068	305	0.53	HOMO → LUMO + 1: 74 %
iPyrPh	1	2.840	437	0.54	HOMO → LUMO: 79 %
	2	3.258	381	0.26	HOMO – 1 → LUMO: 80 %
	3	3.739	332	0.22	HOMO – 2 → LUMO: 68 %
	4	3.747	331	0.00	HOMO – 6 → LUMO: 72 %
	5	4.034	307	0.55	HOMO → LUMO + 1: 81 %

Table 3S (continued) *Selected TD–B3LYP(DMSO)/def2SVP lowest energy singlet ($S_0 \rightarrow S_n$) transitions and the corresponding oscillator strengths f. The probability of electron orbital transition is in percentage.*

Molecule	*n*	*E* / eV	□ / nm	*f*	Dominant transition
AL	1	3.389	365	0.20	HOMO → LUMO: 99 %
	2	3.411	363	0.00	HOMO – 2 → LUMO: 98 %
	3	3.871	320	0.39	HOMO – 1 → LUMO: 98 %
	4	4.043	306	0.00	HOMO – 3 → LUMO: 96 %
	5	4.767	260	0.12	HOMO – 4 → LUMO: 90 %
iAL	1	2.954	419	0.36	HOMO → LUMO: 99 %
	2	3.282	377	0.00	HOMO – 1 → LUMO: 88 %
	3	3.475	356	0.00	HOMO – 3 → LUMO: 76 %
	4	3.711	334	0.29	HOMO – 2 → LUMO: 98 %
	5	4.190	295	0.01	HOMO – 5 → LUMO: 95 %
Ph2	1	2.506	494	0.05	HOMO → LUMO: 99 %
	2	3.206	386	0.00	HOMO – 2 → LUMO: 98 %
	3	3.319	373	0.69	HOMO – 1 → LUMO: 96 %
	4	3.875	319	0.00	HOMO – 3 → LUMO: 92 %
	5	4.110	301	1.29	HOMO → LUMO + 1: 91 %
iPh2	1	2.439	508	0.04	HOMO → LUMO: 99 %
	2	2.989	414	0.93	HOMO – 1 → LUMO: 99 %
	3	3.169	391	0.00	HOMO – 2 → LUMO: 90 %
	4	3.364	368	0.00	HOMO – 3 → LUMO: 72 %
	5	4.191	295	0.00	HOMO – 5 → LUMO: 65 %
Ph3	1	1.875	661	0.06	HOMO → LUMO: 99 %
	2	3.044	407	0.63	HOMO – 1 → LUMO: 97 %
	3	3.082	402	0.00	HOMO – 3 → LUMO: 98 %
	4	3.317	373	0.55	HOMO → LUMO + 1: 98 %
	5	3.510	353	0.01	HOMO → LUMO + 2: 95 %
iPh3	1	1.866	664	0.06	HOMO → LUMO: 99 %
	2	2.778	446	1.09	HOMO – 1 → LUMO: 97 %
	3	3.098	400	0.00	HOMO – 2 → LUMO: 86 %
	4	3.293	376	0.00	HOMO – 4 → LUMO: 78 %
	5	3.318	373	0.39	HOMO → LUMO + 1: 98 %
PyPh2	1	2.201	563	0.08	HOMO → LUMO: 99 %
	2	2.619	473	0.00	HOMO – 2 → LUMO: 98 %
	3	2.910	426	0.00	HOMO – 3 → LUMO: 96 %
	4	2.931	422	1.02	HOMO – 1 → LUMO: 98 %
	5	3.335	371	0.11	HOMO – 4 → LUMO: 98 %

Table 3S (continued) *Selected TD–B3LYP(DMSO)/def2SVP lowest energy singlet ($S_0 \rightarrow S_n$) transitions and the corresponding oscillator strengths f. The probability of electron orbital transition is in percentage.*

Molecule	*n*	*E* / eV	□ / nm	*f*	Dominant transition
iPyPh2	1	2.222	557	0.09	HOMO → LUMO: 99 %
	2	2.661	465	0.00	HOMO – 2 → LUMO: 98 %
	3	2.740	452	1.18	HOMO – 1 → LUMO: 99 %
	4	2.957	419	0.00	HOMO – 3 → LUMO: 79 %
	5	3.149	393	0.00	HOMO – 5 → LUMO: 78 %
Phe	1	3.172	390	0.40	HOMO → LUMO: 98 %
	2	3.314	374	0.19	HOMO – 1 → LUMO: 98 %
	3	3.547	349	0.00	HOMO – 2 → LUMO: 96 %
	4	4.018	308	0.31	HOMO → LUMO + 1: 78 %
	5	4.094	302	0.19	HOMO – 1 → LUMO + 1: 68 %
iPhe	1	2.648	468	0.49	HOMO → LUMO: 98 %
	2	3.053	406	0.09	HOMO – 1 → LUMO: 98 %
	3	3.309	374	0.00	HOMO – 2 → LUMO: 86 %
	4	3.506	353	0.00	HOMO – 3 → LUMO: 78%
	5	3.852	321	0.50	HOMO → LUMO + 1: 95 %
PhePh	1	2.704	458	0.06	HOMO → LUMO: 99 %
	2	2.976	416	0.74	HOMO – 1 → LUMO: 98 %
	3	3.294	376	0.00	HOMO – 3 → LUMO: 97%
	4	3.298	375	0.10	HOMO – 2 → LUMO: 99 %
	5	3.881	319	1.28	HOMO → LUMO + 1: 88 %
iPhePh	1	2.511	493	0.29	HOMO → LUMO: 99 %
	2	2.759	449	0.60	HOMO – 1 → LUMO: 99 %
	3	3.197	387	0.16	HOMO – 2 → LUMO: 99 %
	4	3.211	386	0.00	HOMO – 4 → LUMO: 87%
	5	3.399	364	0.00	HOMO – 5 → LUMO: 87%
PhePh2	1	1.635	758	0.05	HOMO → LUMO: 99 %
	2	2.648	468	0.80	HOMO – 1 → LUMO: 96 %
	3	2.780	445	0.254	HOMO – 2 → LUMO: 97 %
	4	2.852	434	0.321	HOMO → LUMO + 1: 98 %
	5	3.044	407	0.00	HOMO – 5 → LUMO: 99%
iPhePh2	1	1.635	758	0.07	HOMO → LUMO: 99 %
	2	2.501	495	1.21	HOMO – 1 → LUMO: 96 %
	3	2.743	451	0.20	HOMO – 2 → LUMO: 97 %
	4	2.848	435	0.35	HOMO → LUMO + 1: 97 %
	5	3.055	405	0.03	HOMO – 3 → LUMO: 96%

Table 3S (continued) *Selected TD–B3LYP(DMSO)/def2SVP lowest energy singlet ($S_0 \rightarrow S_n$) transitions and the corresponding oscillator strengths f. The probability of electron orbital transition is in percentage.*

Molecule	*n*	*E* / eV	□ / nm	*f*	Dominant transition
Pyr	1	2.785	445	0.33	HOMO → LUMO: 99 %
	2	3.379	366	0.04	HOMO – 1 → LUMO: 95 %
	3	3.530	351	0.73	HOMO → LUMO + 1: 95 %
	4	3.550	349	0.00	HOMO – 3 → LUMO: 98%
	5	3.834	323	0.32	HOMO – 2 → LUMO: 92 %
iPyr	1	2.397	517	0.38	HOMO → LUMO: 99 %
	2	3.146	393	0.00	HOMO – 1 → LUMO: 95 %
	3	3.286	377	0.15	HOMO – 2 → LUMO: 92 %
	4	3.306	374	0.00	HOMO – 3 → LUMO: 78%
	5	3.419	362	0.87	HOMO → LUMO + 1: 95 %
PyrPh	1	2.519	492	0.392	HOMO → LUMO: 99 %
	2	2.778	446	0.08	HOMO – 1 → LUMO: 99 %
	3	3.293	376	0.00	HOMO – 4 → LUMO: 96%
	4	3.44	360	0.15	HOMO – 3 → LUMO: 98%
	5	3.542	349	0.78	HOMO → LUMO + 1: 95 %
iPyrPh	1	2.292	540	0.447	HOMO → LUMO: 99 %
	2	2.699	459	0.09	HOMO – 1 → LUMO: 99 %
	3	3.104	399	0.40	HOMO – 2 → LUMO: 99 %
	4	3.209	386	0.00	HOMO – 4 → LUMO: 78%
	5	3.396	365	0.00	HOMO – 5 → LUMO: 87%
Lum	1	3.757	330	0.00	HOMO – 2 → LUMO: 95 %
	2	4.080	304	0.26	HOMO → LUMO: 98 %
	3	4.348	285	0.00	HOMO – 2 → LUMO: 95 %
	4	4.848	256	0.00	HOMO – 1 → LUMO + 1: 96 %
	5	5.095	243	0.08	HOMO → LUMO + 1: 65 %
iLum	1	3.235	383	0.26	HOMO → LUMO: 99 %
	2	3.466	358	0.00	HOMO – 1 → LUMO: 58 %
	3	3.656	339	0.01	HOMO – 2 → LUMO: 52 %
	4	4.290	289	0.00	HOMO – 4 → LUMO: 95%
	5	4.354	285	0.01	HOMO – 3 → LUMO: 96 %
CNLum	1	3.509	353	0.00	HOMO – 2 → LUMO: 95 %
	2	3.663	338	0.22	HOMO → LUMO: 99 %
	3	4.128	300	0.00	HOMO – 4 → LUMO: 75%
	4	4.228	293	0.00	HOMO – 1 → LUMO + 1: 92 %
	5	4.350	284	0.52	HOMO → LUMO + 1: 95 %

Table 3S (continued) *Selected TD–B3LYP(DMSO)/def2SVP lowest energy singlet ($S_0 \rightarrow S_n$) transitions and the corresponding oscillator strengths f. The probability of electron orbital transition is in percentage.*

Molecule	*n*	*E* / eV	□ / nm	*f*	Dominant transition
iCNLum	1	2.897	427	0.18	HOMO → LUMO: 99 %
	2	3.041	407	0.00	HOMO – 1 → LUMO: 88 %
	3	3.322	373	0.00	HOMO – 2 → LUMO: 88 %
	4	3.785	327	0.01	HOMO – 3 → LUMO: 96 %
	5	3.823	324	0.00	HOMO – 4 → LUMO: 95%
FAL	1	3.393	365	0.29	HOMO → LUMO: 99 %
	2	3.453	359	0.00	HOMO – 2 → LUMO: 96 %
	3	3.930	315	0.30	HOMO – 1 → LUMO: 98 %
	4	4.050	306	0.00	HOMO – 3 → LUMO: 96 %
	5	4.727	262	0.03	HOMO – 4 → LUMO: 93%
iFAL	1	2.922	424	0.40	HOMO → LUMO: 99 %
	2	3.271	379	0.01	HOMO – 1 → LUMO: 91 %
	3	3.463	357	0.00	HOMO – 3 → LUMO: 89 %
	4	3.830	323	0.25	HOMO – 2 → LUMO: 98 %
	5	4.057	305	0.00	HOMO – 5 → LUMO: 96 %
PheLum	1	3.340	371	0.42	HOMO → LUMO: 99 %
	2	3.727	332	0.01	HOMO – 2 → LUMO: 78 %
	3	3.992	310	0.45	HOMO – 1 → LUMO + 1: 97 %
	4	4.081	303	0.06	HOMO – 1 → LUMO: 93 %
	5	4.218	293	0.11	HOMO – 3 → LUMO: 76 %
iPheLum	1	2.774	446	0.39	HOMO → LUMO: 99 %
	2	3.414	363	0.00	HOMO – 2 → LUMO: 88 %
	3	3.607	343	0.00	HOMO – 3 → LUMO: 67 %
	4	3.692	335	0.00	HOMO – 1 → LUMO: 98 %
	5	3.855	321	0.53	HOMO → LUMO + 1: 96 %
ImiLum	1	3.467	357	0.38	HOMO → LUMO: 99 %
	2	3.617	342	0.01	HOMO – 1 → LUMO: 81 %
	3	3.950	313	0.06	HOMO – 2 → LUMO: 78 %
	4	4.017	308	0.47	HOMO → LUMO + 1: 96 %
	5	4.041	306	0.02	HOMO – 3 → LUMO: 67 %
iImiLum	1	2.743	451	0.36	HOMO → LUMO: 99 %
	2	3.333	371	0.00	HOMO – 1 → LUMO: 81 %
	3	3.485	355	0.00	HOMO – 2 → LUMO: 78 %
	4	3.622	342	0.03	HOMO – 3 → LUMO: 86 %
	5	3.678	337	0.68	HOMO → LUMO + 1: 96 %

Table 3S (continued) *Selected TD–B3LYP(DMSO)/def2SVP lowest energy singlet ($S_0 \rightarrow S_n$) transitions and the corresponding oscillator strengths f. The probability of electron orbital transition is in percentage.*

Molecule	*n*	*E* / eV	□ / nm	*f*	Dominant transition
FurLum	1	2.946	420	0.42	HOMO → LUMO: 99 %
	2	3.568	347	0.43	HOMO → LUMO + 1: 94 %
	3	3.680	336	0.18	HOMO – 2 → LUMO: 68 %
	4	3.821	324	0.23	HOMO – 1 → LUMO: 70 %
	5	4.305	287	0.02	HOMO – 4 → LUMO: 80 %
iFurLum	1	2.394	517	0.38	HOMO → LUMO: 99 %
	2	3.362	368	0.01	HOMO – 2 → LUMO: 68 %
	3	3.448	359	0.59	HOMO – 1 → LUMO: 98 %
	4	3.536	350	0.39	HOMO – 1 → LUMO: 70 %
	5	3.574	346	0.02	HOMO – 4 → LUMO: 75 %
ThLum	1	2.878	430	0.39	HOMO → LUMO: 99 %
	2	3.434	361	0.47	HOMO → LUMO + 1: 74 %
	3	3.666	338	0.03	HOMO – 3 → LUMO: 96 %
	4	3.833	323	0.28	HOMO – 1 → LUMO: 95 %
	5	3.944	314	0.03	HOMO – 2 → LUMO: 90 %
iThLum	1	2.416	513	0.32	HOMO → LUMO: 99 %
	2	3.331	372	0.01	HOMO – 2 → LUMO: 85 %
	3	3.356	369	0.57	HOMO → LUMO + 1: 97 %
	4	3.508	353	0.05	HOMO – 1 → LUMO: 75 %
	5	3.670	337	0.13	HOMO – 1 → LUMO: 74 %
PyLum	1	1.883	658	0.30	HOMO → LUMO: 99 %
	2	1.979	626	0.01	HOMO – 1 → LUMO: 97 %
	3	2.339	530	0.02	HOMO – 2 → LUMO: 85 %
	4	2.351	527	0.05	HOMO – 2 → LUMO: 75 %
	5	2.541	487	0.01	HOMO – 4 → LUMO: 90 %
iPyLum	1	1.969	629	0.26	HOMO → LUMO: 99 %
	2	2.150	576	0.01	HOMO – 1 → LUMO: 97 %
	3	2.397	517	0.02	HOMO – 3 → LUMO: 80 %
	4	2.402	516	0.03	HOMO – 2 → LUMO: 59 %
	5	2.714	456	0.02	HOMO – 5 → LUMO: 70 %
N10Rib	1	2.908	426	0.37	HOMO → LUMO: 99 %
	2	3.396	365	0.14	HOMO – 4 → LUMO: 67 %
	3	3.435	360	0.23	HOMO – 1 → LUMO: 65 %
	4	3.468	357	0.04	HOMO – 2 → LUMO: 73%
	5	3.581	346	0.00	HOMO – 5 → LUMO: 67 %

Table 4S *Selected TD–B3LYP(DMSO)/aug-cc-PVDZ lowest energy singlet ($S_0 \rightarrow S_n$) transitions and the corresponding oscillator strengths f. The probability of electron orbital transition is in percentage.*

Molecule	*n*	*E* / eV	□ / nm	*f*	Dominant transition
AL	1	3.227	384	0.18	HOMO → LUMO: 99 %
	2	3.441	360	0.00	HOMO – 2 → LUMO: 96%
	3	3.684	336	0.48	HOMO – 1 → LUMO: 97 %
	4	4.009	309	0.00	HOMO – 3 → LUMO: 95 %
	5	4.691	264	0.27	HOMO – 4 → LUMO: 80 %
iAL	1	2.840	436	0.38	HOMO → LUMO: 99 %
	2	3.360	368	0.00	HOMO – 2 → LUMO: 82%
	3	3.505	353	0.00	HOMO – 3 → LUMO: 85 %
	4	3.522	351	0.33	HOMO – 1 → LUMO: 98 %
	5	4.159	298	0.02	HOMO – 4 → LUMO: 96 %
Ph2	1	2.331	531	0.05	HOMO → LUMO: 99 %
	2	3.189	388	0.80	HOMO – 1 → LUMO: 98 %
	3	3.258	380	0.00	HOMO – 2 → LUMO: 98%
	4	3.862	321	0.00	HOMO – 4 → LUMO: 98 %
	5	4.000	309	1.29	HOMO → LUMO + 1: 93 %
iPh2	1	2.283	542	0.03	HOMO → LUMO: 99 %
	2	2.858	433	1.01	HOMO – 1 → LUMO: 99 %
	3	3.258	380	0.00	HOMO – 2 → LUMO: 90%
	4	3.406	363	0.00	HOMO – 3 → LUMO: 86 %
	5	4.169	297	0.69	HOMO – 4 → LUMO: 80 %
Ph3	1	1.716	722	0.06	HOMO → LUMO: 99 %
	2	2.935	422	0.74	HOMO – 1 → LUMO: 97 %
	3	3.149	393	0.00	HOMO – 3 → LUMO: 98 %
	4	3.209	386	0.61	HOMO → LUMO + 1: 98 %
	5	3.369	368	0.02	HOMO – 2 → LUMO: 98%
iPh3	1	1.707	726	0.06	HOMO → LUMO: 99 %
	2	2.670	464	1.16	HOMO – 1 → LUMO: 97 %
	3	3.196	387	0.00	HOMO – 3 → LUMO: 88 %
	4	3.223	384	0.40	HOMO → LUMO + 1: 98 %
	5	3.344	370	0.00	HOMO – 5 → LUMO: 80%
PyPh2	1	2.071	598	0.06	HOMO → LUMO: 99 %
	2	2.685	461	0.00	HOMO – 2 → LUMO: 97 %
	3	2.987	439	1.13	HOMO – 4 → LUMO: 97 %
	4	3.208	386	0.18	HOMO – 3 → LUMO: 99 %
	6	3.327	372	0.23	HOMO – 5 → LUMO: 97 %

Table 4S (continued) *Selected TD–B3LYP(DMSO)/aug-cc-PVDZ lowest energy singlet ($S_0 \rightarrow S_n$) transitions and the corresponding oscillator strengths f. The probability of electron orbital transition is in percentage.*

Molecule	*n*	*E* / eV	□ / nm	*f*	Dominant transition
iPyPh2	1	2.100	590	0.07	HOMO → LUMO: 99 %
	2	2.624	472	1.28	HOMO – 1 → LUMO: 99 %
	3	2.718	456	0.00	HOMO – 2 → LUMO: 96 %
	4	3.053	406	0.00	HOMO – 4 → LUMO: 97 %
	5	3.205	386	0.00	HOMO – 5 → LUMO: 80 %
Phe	1	3.005	412	0.37	HOMO → LUMO: 98 %
	2	3.119	397	0.25	HOMO – 1 → LUMO: 98 %
	4	3.874	320	0.16	HOMO – 2 → LUMO: 91 %
	5	3.991	310	0.40	HOMO → LUMO + 1: 60 %
	6	4.065	304	0.35	HOMO → LUMO + 1: 60 %
iPhe	1	2.529	490	0.51	HOMO → LUMO: 99 %
	2	2.863	433	0.10	HOMO – 1 → LUMO: 99 %
	3	3.371	367	0.00	HOMO – 2 → LUMO: 88 %
	4	3.527	351	0.00	HOMO – 5 → LUMO: 81 %
	5	3.751	330	0.22	HOMO – 3 → LUMO: 85 %
PhePh	1	2.530	490	0.04	HOMO → LUMO: 99 %
	2	2.817	440	0.81	HOMO – 1 → LUMO: 99 %
	3	3.112	398	0.11	HOMO – 2 → LUMO: 99 %
	4	3.338	371	0.00	HOMO – 3 → LUMO: 95 %
	5	3.812	325	1.25	HOMO → LUMO + 1: 96 %
Pyr	1	2.598	477	0.31	HOMO → LUMO: 99 %
	2	3.202	387	0.01	HOMO – 1 → LUMO: 96 %
	3	3.434	360	0.75	HOMO → LUMO + 1: 96 %
	4	3.537	350	0.00	HOMO – 3 → LUMO: 96 %
	5	3.686	336	0.31	HOMO – 2 → LUMO: 98 %
iPyr	1	2.243	552	0.36	HOMO → LUMO: 99 %
	2	2.971	417	0.01	HOMO – 1 → LUMO: 96 %
	3	3.149	393	0.26	HOMO – 2 → LUMO: 98 %
	4	3.356	369	0.81	HOMO → LUMO + 1: 86 %
	7	3.773	328	0.01	HOMO → LUMO + 2: 86 %

Table 4S (continued) *Selected TD–B3LYP(DMSO)/aug-cc-PVDZ lowest energy singlet ($S_0 \rightarrow S_n$) transitions and the corresponding oscillator strengths f. The probability of electron orbital transition is in percentage.*

Molecule	*n*	*E* / eV	□ / nm	*f*	Dominant transition
Lum	1	3.750	330	0.00	HOMO – 1 → LUMO: 96 %
	2	3.904	317	0.29	HOMO → LUMO: 99 %
	3	4.282	289	0.00	HOMO – 2 → LUMO: 93 %
	4	4.911	252	0.00	HOMO – 1 → LUMO + 1: 96 %
	5	4.979	249	0.08	HOMO → LUMO + 1: 75 %
iLum	1	3.126	396	0.28	HOMO → LUMO: 99 %
	2	3.532	351	0.00	HOMO – 1 → LUMO: 86 %
	3	3.666	338	0.01	HOMO – 2 → LUMO: 83 %
	4	4.298	288	0.00	HOMO – 4 → LUMO: 96 %
	5	4.305	287	0.01	HOMO – 3 → LUMO: 93 %
CNLum	1	3.518	352	0.00	HOMO – 1 → LUMO: 96 %
	2	3.532	351	0.27	HOMO → LUMO: 99 %
	3	4.103	302	0.00	HOMO – 2 → LUMO: 80 %
	4	4.247	291	0.53	HOMO → LUMO + 1: 95 %
	5	4.293	288	0.00	HOMO – 1 → LUMO + 1: 96 %
iCNLum	1	2.831	437	0.21	HOMO → LUMO: 99 %
	2	3.092	400	0.00	HOMO – 1 → LUMO: 96 %
	3	3.384	366	0.00	HOMO – 2 → LUMO: 93 %
	4	3.771	328	0.01	HOMO – 3 → LUMO: 96 %
	5	3.841	322	0.00	HOMO – 4 → LUMO: 93 %
FAL	1	3.271	378	0.29	HOMO → LUMO: 98 %
	2	3.487	355	0.00	HOMO – 2 → LUMO: 96 %
	3	3.778	328	0.37	HOMO – 1 → LUMO: 98 %
	4	4.014	308	0.00	HOMO – 3 → LUMO: 96 %
	5	4.661	265	0.04	HOMO – 4 → LUMO: 90 %
iFAL	1	2.835	437	0.43	HOMO → LUMO: 99 %
	2	3.339	371	0.01	HOMO – 1 → LUMO: 92 %
	3	3.500	354	0.00	HOMO – 3 → LUMO: 93 %
	4	3.682	336	0.28	HOMO – 2 → LUMO: 90 %
	5	4.079	303	0.01	HOMO – 5 → LUMO: 98 %

Table 4S (continued) *Selected TD–B3LYP(DMSO)/aug-cc-PVDZ lowest energy singlet ($S_0 \rightarrow S_n$) transitions and the corresponding oscillator strengths f. The probability of electron orbital transition is in percentage.*

Molecule	*n*	*E* / eV	□ / nm	*f*	Dominant transition
PheLum	1	3.205	386	0.46	HOMO → LUMO: 99 %
	2	3.737	331	0.01	HOMO – 3 → LUMO: 85 %
	4	3.975	311	0.37	HOMO → LUMO + 1: 98 %
	5	4.038	307	0.17	HOMO – 2 → LUMO: 90 %
	8	4.380	283	0.14	HOMO – 5 → LUMO: 83 %
iPheLum	1	2.683	462	0.44	HOMO → LUMO: 99 %
	2	3.474	356	0.00	HOMO – 1 → LUMO: 65 %
	3	3.516	352	0.00	HOMO – 1 → LUMO: 73 %
	4	3.613	343	0.01	HOMO – 2 → LUMO: 76 %
	8	3.989	310	0.15	HOMO – 5 → LUMO: 83 %
ImiLum	1	3.368	368	0.43	HOMO → LUMO: 99 %
	2	3.642	340	0.01	HOMO – 1 → LUMO: 90 %
	3	3.970	312	0.06	HOMO – 2 → LUMO: 89 %
	4	4.018	308	0.05	HOMO – 3 → LUMO: 76 %
	5	4.045	306	0.43	HOMO → LUMO + 1: 94 %
iImiLum	1	2.696	459	0.43	HOMO → LUMO: 99 %
	2	3.411	363	0.01	HOMO – 2 → LUMO: 90 %
	3	3.505	353	0.01	HOMO – 2 → LUMO: 89 %
	4	3.653	339	0.04	HOMO – 1 → LUMO: 76 %
	5	3.748	330	0.63	HOMO → LUMO + 1: 94 %
FurLum	1	2.830	438	0.48	HOMO → LUMO: 99 %
	2	3.468	357	0.31	HOMO – 1 → LUMO: 96 %
	3	3.607	343	0.44	HOMO → LUMO + 1: 97 %
	4	3.783	327	0.04	HOMO – 3 → LUMO: 66 %
	7	4.287	289	0.36	HOMO – 1 → LUMO + 1: 96 %
iFurLum	1	2.371	522	0.43	HOMO → LUMO: 99 %
	2	3.205	386	0.31	HOMO – 1 → LUMO: 96 %
	3	3.438	360	0.00	HOMO – 3 → LUMO: 66 %
	4	3.545	349	0.59	HOMO → LUMO + 1: 97
	5	3.586	345	0.12	HOMO – 2 → LUMO: 96 %
ThLum	1	2.728	454	0.43	HOMO → LUMO: 99 %
	2	3.352	369	0.44	HOMO → LUMO + 1: 97 %
	3	3.614	342	0.22	HOMO – 1 → LUMO: 86 %
	4	3.694	335	0.06	HOMO – 3 → LUMO: 75 %
	6	4.084	303	0.03	HOMO – 2 → LUMO: 90 %

Table 4S (continued) *Selected TD–B3LYP(DMSO)/aug-cc-PVDZ lowest energy singlet ($S_0 \rightarrow S_n$) transitions and the corresponding oscillator strengths f. The probability of electron orbital transition is in percentage.*

Molecule	***n***	***E* / eV**	**□ / nm**	***f***	**Dominant transition**
iThLum	1	2.301	538	0.35	HOMO → LUMO: 99 %
	2	3.301	375	0.40	HOMO → LUMO + 1: 97 %
	4	3.381	366	0.22	HOMO – 1 → LUMO: 75 %
	5	3.487	355	0.10	HOMO – 3 → LUMO: 90 %
	8	3.841	322	0.02	HOMO – 5 → LUMO: 90 %
PyLum	1	1.833	676	0.32	HOMO → LUMO: 99 %
	2	1.954	634	0.01	HOMO – 1 → LUMO: 96 %
	3	2.347	528	0.02	HOMO – 2 → LUMO: 93 %
	4	2.438	508	0.06	HOMO – 3 → LUMO: 96 %
	5	2.706	458	0.04	HOMO – 4 → LUMO: 93 %
iPyLum	1	1.924	644	0.26	HOMO → LUMO: 99 %
	2	2.111	587	0.01	HOMO – 1 → LUMO: 96 %
	3	2.392	518	0.01	HOMO – 2 → LUMO: 93 %
	4	2.516	492	0.10	HOMO – 3 → LUMO: 96 %
	5	2.796	443	0.37	HOMO – 4 → LUMO: 93 %
N10Rib	1	2.817	440	0.40	HOMO → LUMO: 99 %
	2	3.444	360	0.05	HOMO – 4 → LUMO: 87 %
	3	3,512	353	0.29	HOMO – 1 → LUMO: 95 %
	4	3.552	349	0.01	HOMO – 2 → LUMO: 83%
	5	3.690	336	0.00	HOMO – 5 → LUMO: 76 %

Table 5S *The calculated vertical TD–B3LYP(DMSO) and TD–CAM–B3LYP(DMSO) 6-31+G** de–excitation energies and oscillator strengths (f). The wavelength values in nm are written in parentheses.*

Molecule	**Transition**	**Energy / eV (λ / nm)**	***f***	**Energy / eV (λ / nm)**	***f***
		B3LYP		CAM–B3LYP	
AL	$S_1 \rightarrow S_0$	2.823 (439)	0.06	3.211 (386)	0.12
iAL	$S_1 \rightarrow S_0$	2.527 (491)	0.16	2.855 (434)	0.28
Ph2	$S_1 \rightarrow S_0$	1.967 (630)	0.02	2.393 (518)	0.05
iPh2	$S_1 \rightarrow S_0$	1.829 (678)	0.01	2.321 (534)	0.03
Ph3	$S_1 \rightarrow S_0$	1.430 (867)	0.03	1.865 (665)	0.05
iPh3	$S_1 \rightarrow S_0$	1.332 (931)	0.02	1.848 (671)	0.04
PyPh2	$S_1 \rightarrow S_0$	1.792 (692)	0.03	2.161 (574)	0.07
iPyPh2	$S_1 \rightarrow S_0$	1.732 (716)	0.03	2.202 (563)	0.09
Phe	$S_1 \rightarrow S_0$	2.593 (478)	0.03	3.239 (383)	0.15
iPhe	$S_1 \rightarrow S_0$	2.374 (522)	0.29	2.673 (464)	0.43
PhePh	$S_1 \rightarrow S_0$	2.184 (568)	0.02	2.728 (454)	0.04
iPhePh	$S_1 \rightarrow S_0$	2.002 (619)	0.06	2.521 (492)	0.23
PhePh2	$S_1 \rightarrow S_0$	1.652 (750)	0.02	2.128 (583)	0.03
iPhePh2	$S_1 \rightarrow S_0$	1.531 (810)	0.01	2.082 (595)	0.02
Pyr	$S_1 \rightarrow S_0$	2.312 (536)	0.16	2.883 (430)	0.31
iPyr	$S_1 \rightarrow S_0$	2.025 (612)	0.19	2.481 (500)	0.37
PyrPh	$S_1 \rightarrow S_0$	2.102 (590)	0.20	2.788 (445)	0.27
iPyrPh	$S_1 \rightarrow S_0$	1.868 (664)	0.22	2.503 (495)	0.43
Lum	$S_1 \rightarrow S_0$	3.107 (399)	0.01		
iLum	$S_1 \rightarrow S_0$	2.577 (480)	0.15		
CNLum	$S_1 \rightarrow S_0$	2.854 (434)	0.01		
iCNLum	$S_1 \rightarrow S_0$	2.124 (583)	0.13		
FAL	$S_1 \rightarrow S_0$	2.978 (416)	0.21		
iFAL	$S_1 \rightarrow S_0$	2.476 (500)	0.31		
PheLum	$S_1 \rightarrow S_0$	2.622 (472)	0.43		
iPheLum	$S_1 \rightarrow S_0$	2.225 (557)	0.38		
ImiLum	$S_1 \rightarrow S_0$	2.654 (467)	0.01		
iImiLum	$S_1 \rightarrow S_0$	2.211 (560)	0.36		
FurLum	$S_1 \rightarrow S_0$	2.323 (533)	0.35		
iFurLum	$S_1 \rightarrow S_0$	1.925 (643)	0.33		
ThLum	$S_1 \rightarrow S_0$	2.205 (562)	0.36		
iThLum	$S_1 \rightarrow S_0$	1.855 (668)	0.309		
PyLum	$S_1 \rightarrow S_0$	1.503 (824)	0.11		
iPyLum	$S_1 \rightarrow S_0$	1.531 (809)	0.11		
N10Rib	$S_1 \rightarrow S_0$				

Table 6S *The calculated vertical TD–B3LYP(DMSO) def2SVP and aug-cc-PVDZ de–excitation energies and oscillator strengths (f). The wavelength values in nm are written in parentheses.*

Molecule	**Transition**	**Energy / eV (λ / nm)**	***f***	**Energy / eV (λ / nm)**	***f***
		def2SVP		aug-cc-PVDZ	
AL	$S_1 \rightarrow S_0$	2.925 (423)	0.13	2.736 (453)	0.11
iAL	$S_1 \rightarrow S_0$	2.496 (496)	0.27	2.412 (513)	0.28
Ph2	$S_1 \rightarrow S_0$	2.066 (600)	0.06	1.886 (657)	0.04
iPh2	$S_1 \rightarrow S_0$	1.937 (639)	0.03	1.779 (696)	0.02
Ph3	$S_1 \rightarrow S_0$	1.513 (819)	0.06	1.348 (919)	0.05
iPh3	$S_1 \rightarrow S_0$	1.442 (859)	0.03	1.283 (966)	0.03
PyPh2	$S_2 \rightarrow S_0$	2.447 (506)	0.01	2.512 (470)	0.92
iPyPh2	$S_3 \rightarrow S_0$	2.513 (493)	1.10	2.397 (517)	1.15
Phe	$S_1 \rightarrow S_0$	2.793 (443)	0.10	2.858 (433)	0.49
iPhe	$S_1 \rightarrow S_0$	2.332 (531)	0.42	2.242 (552)	0.45
PhePh	$S_1 \rightarrow S_0$	2.317 (535)	0.05		
iPhePh	$S_1 \rightarrow S_0$	2.105 (589)	0.20		
PhePh2	$S_1 \rightarrow S_0$	1.324 (936)	0.05		
iPhePh2	$S_1 \rightarrow S_0$	1.269 (976)	0.05		
Pyr	$S_1 \rightarrow S_0$	2.438 (508)	0.28	2.598 (477)	0.31
iPyr	$S_1 \rightarrow S_0$	2.099 (590)	0.34	2.016 (614)	0.33
PyrPh	$S_1 \rightarrow S_0$	2.220 (558)	0.33		
iPyrPh	$S_1 \rightarrow S_0$	1.967 (630)	0.38		
Lum	$S_1 \rightarrow S_0$	3.107 (399)	0.01	3.113 (398)	0.01
iLum	$S_1 \rightarrow S_0$	2.577 (480)	0.15	2.578 (480)	0.18
CNLum	$S_2 \rightarrow S_0$	3.365 (368)	0.23	3.234 (383)	0.27
iCNLum	$S_1 \rightarrow S_0$	2.094 (591)	0.11	2.118 (585)	0.13
FAL	$S_1 \rightarrow S_0$	2.978 (416)	0.21	2.825 (438)	0.20
iFAL	$S_1 \rightarrow S_0$	2.476 (500)	0.31	2.411 (514)	0.32
PheLum	$S_1 \rightarrow S_0$	2.635 (470)	0.39	2.683 (462)	0.40
iPheLum	$S_1 \rightarrow S_0$	2.236 (554)	0.34	2.536 (488)	0.44
ImiLum	$S_1 \rightarrow S_0$	2.017 (614)	0.01	2.620 (473)	0.31
iImiLum	$S_1 \rightarrow S_0$	2.173 (570)	0.29	2.696 (459)	0.43
FurLum	$S_1 \rightarrow S_0$	2.482 (499)	0.35	2.312 (536)	0.36
iFurLum	$S_1 \rightarrow S_0$	2.016 (614)	0.31	1.913 (647)	0.33
ThLum	$S_1 \rightarrow S_0$	2.278 (544)	0.33	2.190 (566)	0.36
iThLum	$S_1 \rightarrow S_0$	1.890 (655)	0.27	1.835 (675)	0.31
PyLum	$S_2 \rightarrow S_0$	1.526 (812)	0.11	1.508 (821)	0.15
iPyLum	$S_1 \rightarrow S_0$	1.593 (778)	0.15	1.327 (934)	0.15
N10Rib	$S_1 \rightarrow S_0$	2.517 (492)	0.25		

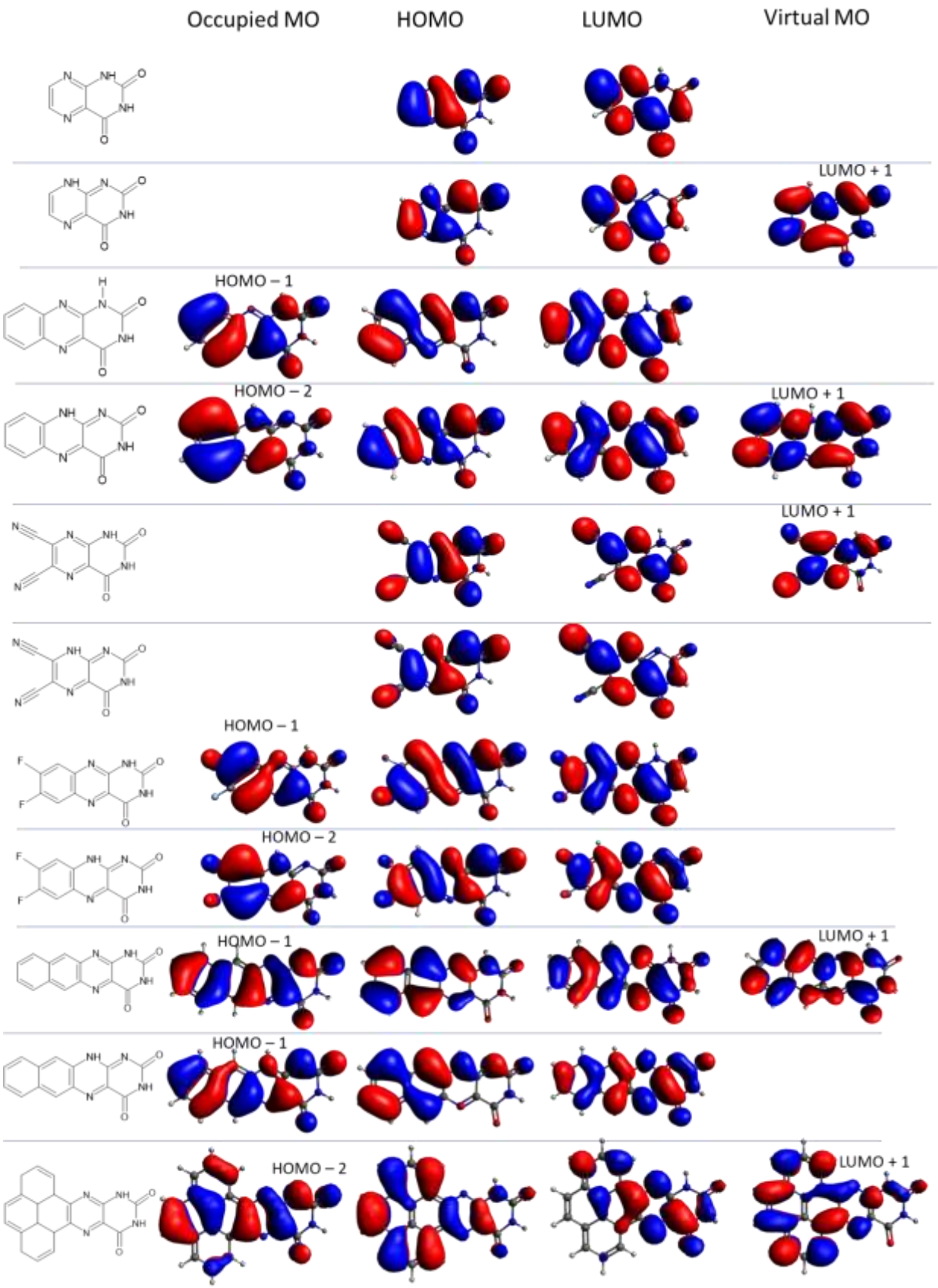

Fig. 1S *The selected molecular orbitals of both alloxo-form and iso-form molecules*

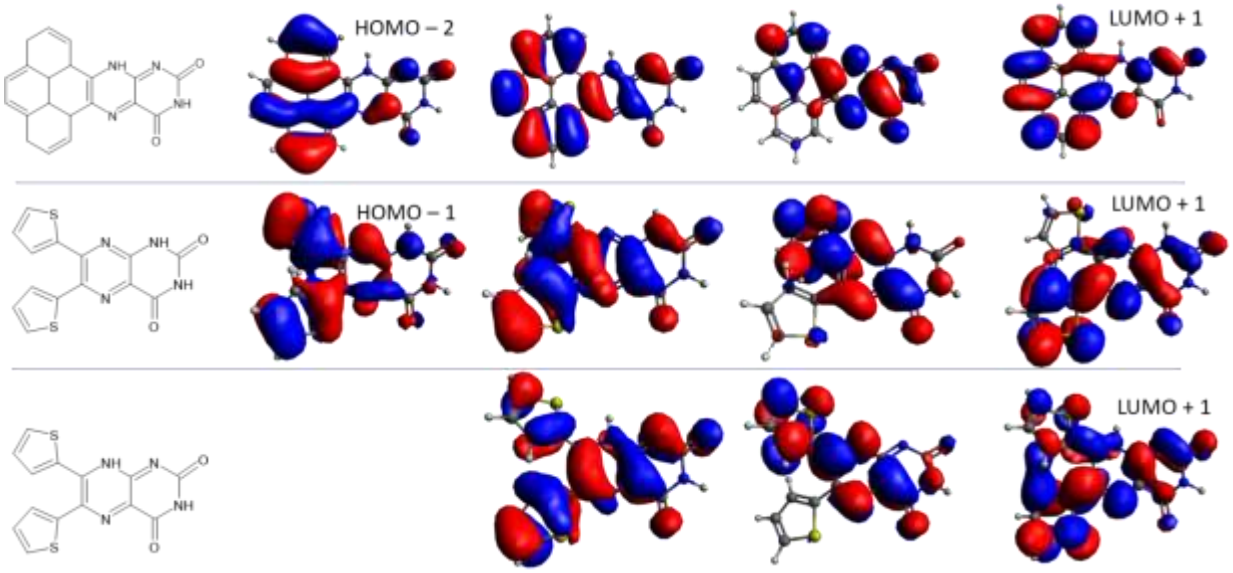

Fig. 1S (Continued) *The selected molecular orbitals of both alloxo-form and iso-form molecules*

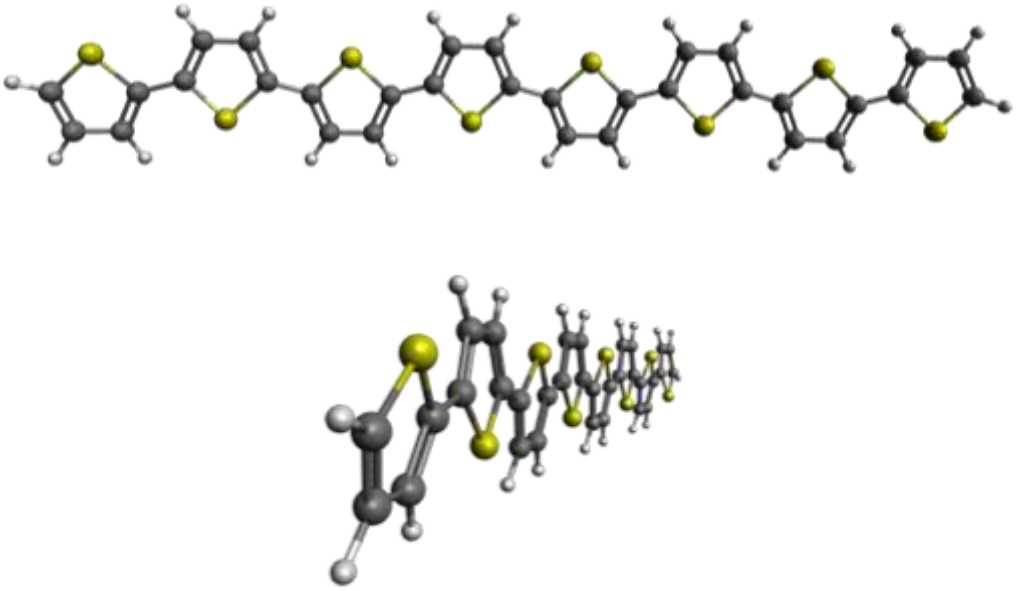

T-s (–4413.979663 hartree)

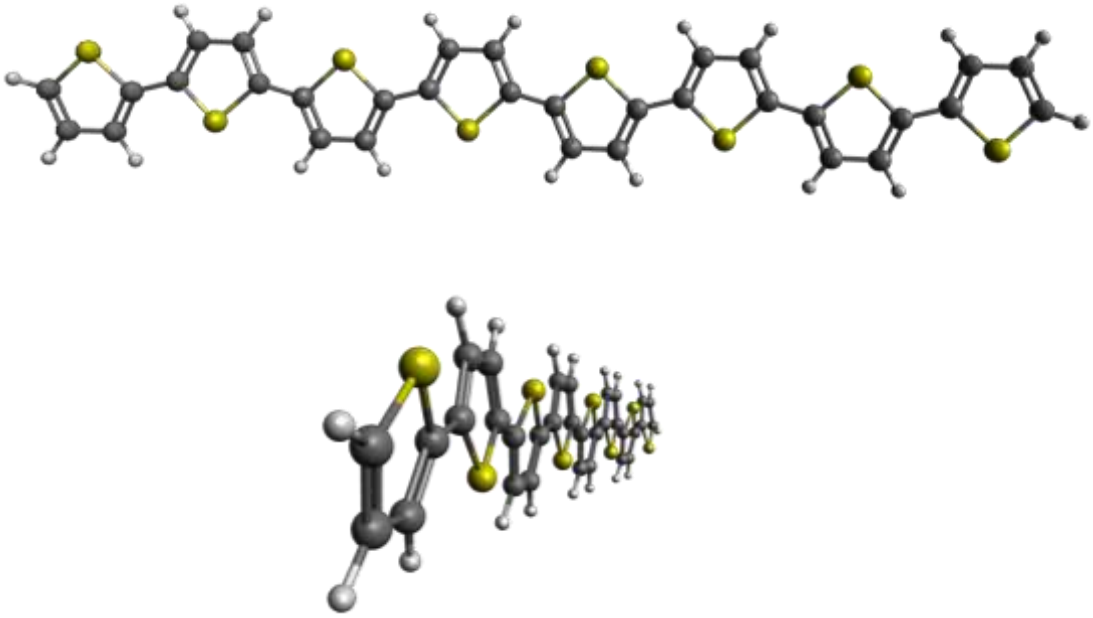

T-a (–4413.979325 hartree)

Fig. 2S *The optimal B3LYP gas-phase geometries of studied model oligomers in all-trans arrangements for syn- and anti-orientation. The electronic energies are in parentheses.*

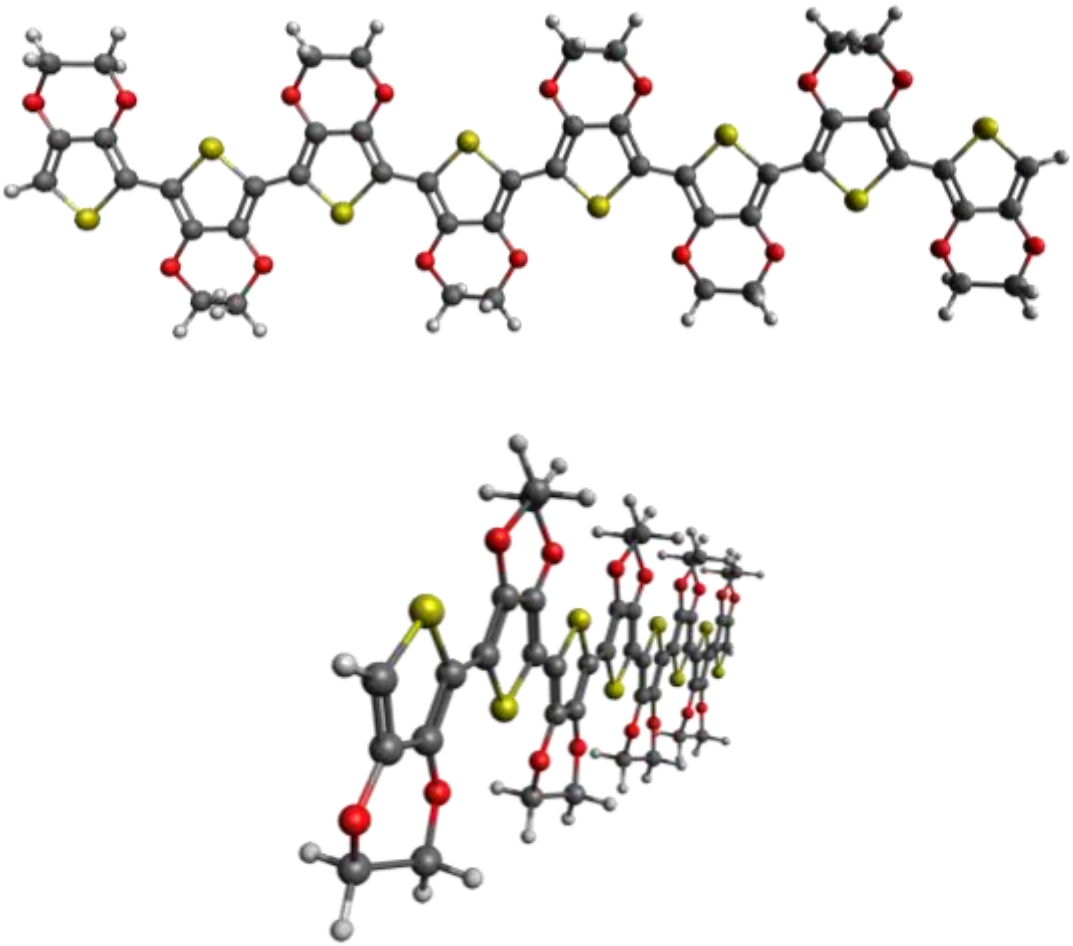

EDOT (–6235.3453069 hartree)

Fig. 2S (continued) *The optimal B3LYP gas-phase geometries of studied model oligomers in all-trans arrangements for syn- and anti-orientation. The electronic energies are in parentheses.*

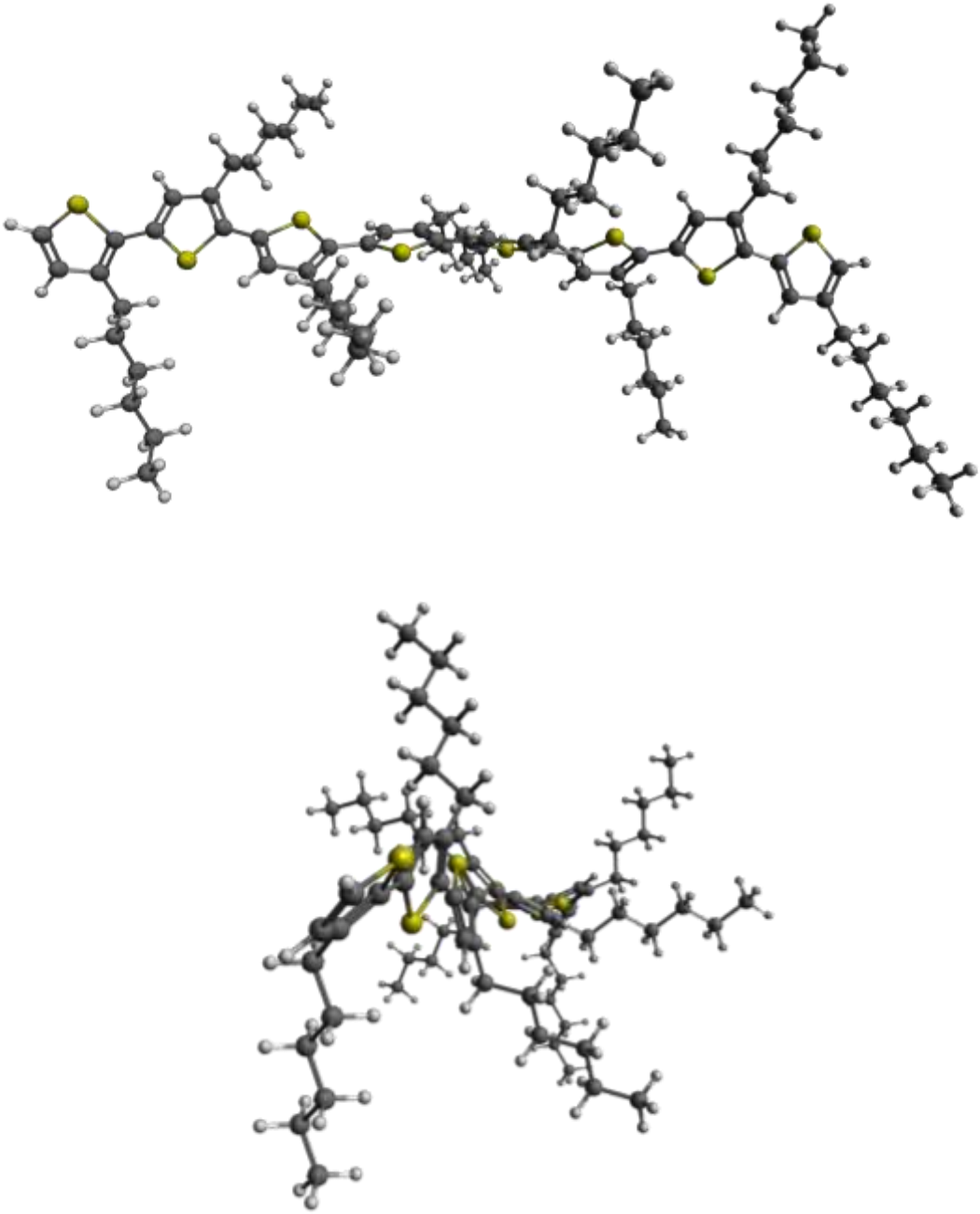

HT-s (–6299.690592 hartree)

Fig. 2S (continued) *The optimal B3LYP gas-phase geometries of studied model oligomers in all-trans arrangements for syn- and anti-orientation. The electronic energies are in parentheses.*

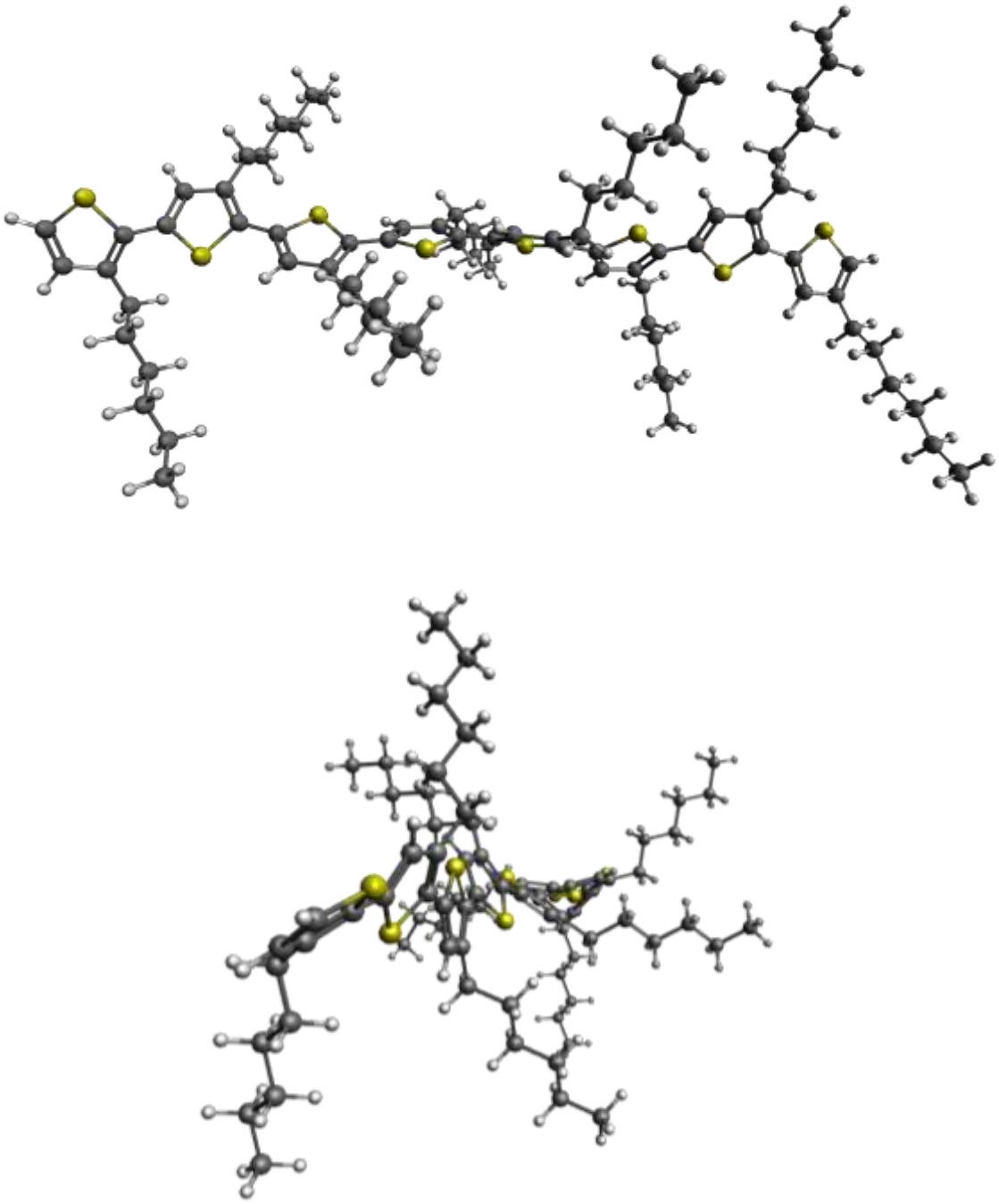

HT-a (–6299.696394 hartree)

Fig. 2S (continued) *The optimal B3LYP gas-phase geometries of studied model oligomers in all-trans arrangements for syn- and anti-orientation. The electronic energies are in parentheses.*

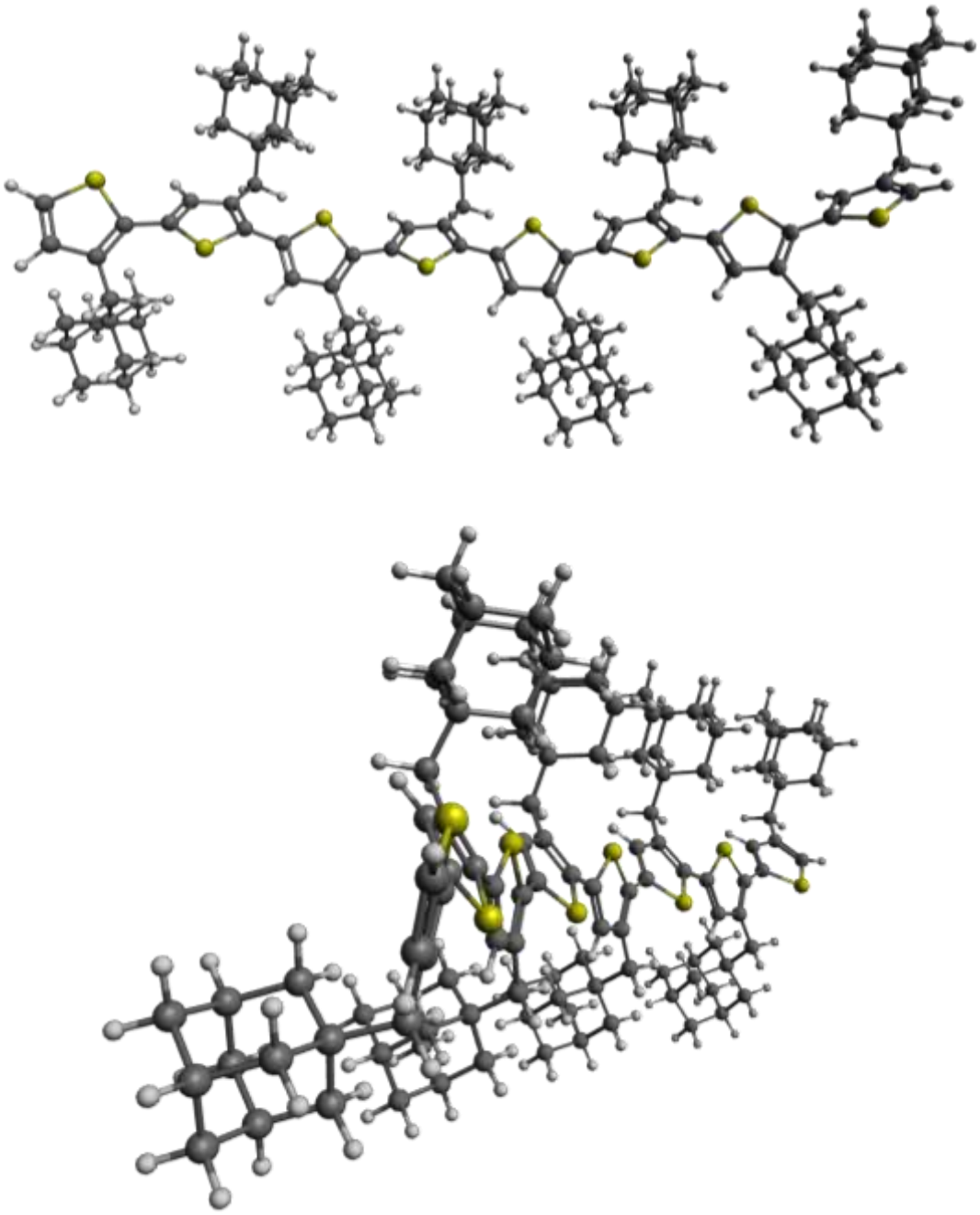

21 **MAT-s** (–7842.236228 hartree)

Fig. 2S (continued) *The optimal B3LYP gas-phase geometries of studied model oligomers in all-trans arrangements for syn- and anti-orientation. The electronic energies are in parentheses.*

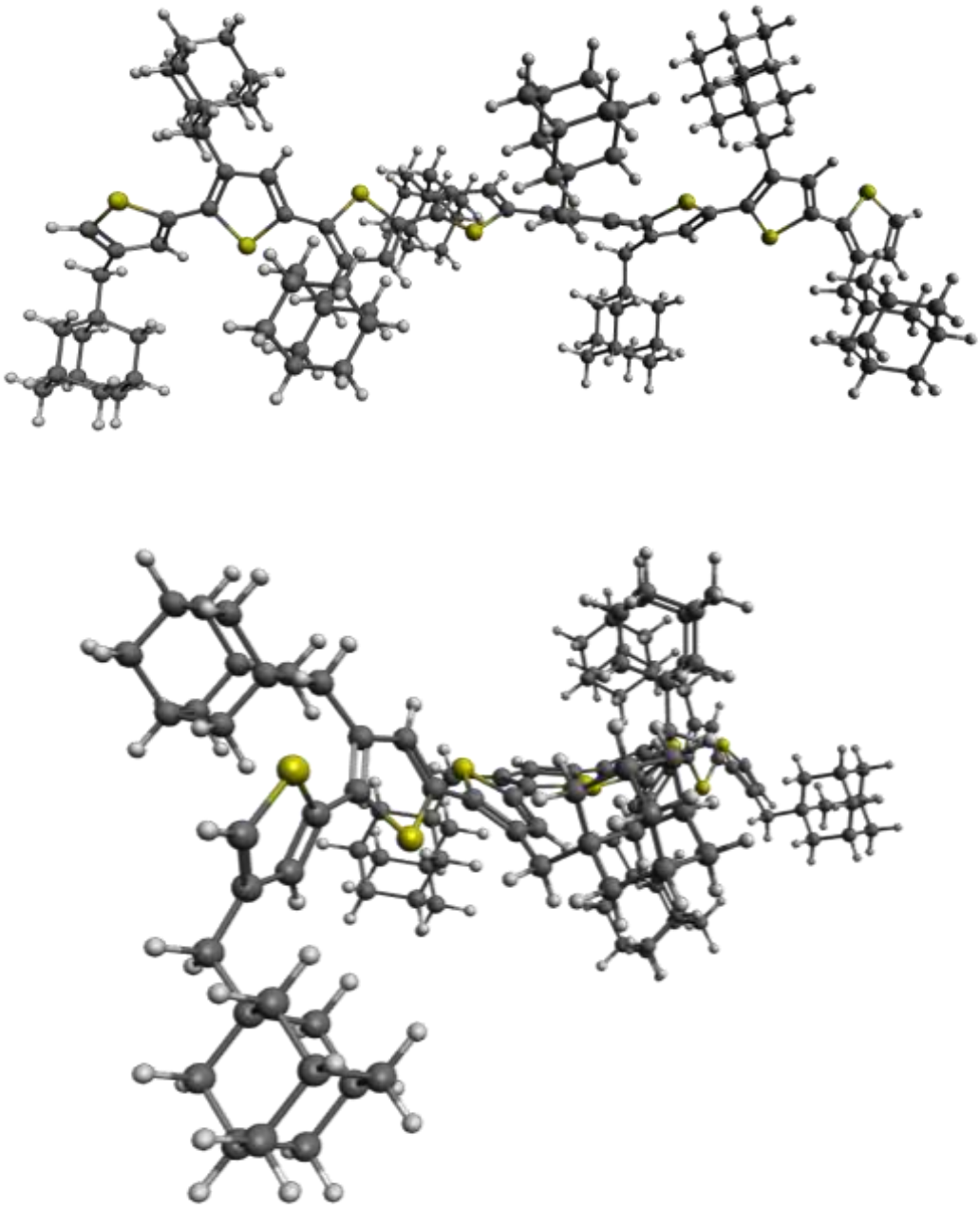

MAT-a (–7842.238678 hartree)

Fig. 2S (continued) *The optimal B3LYP gas-phase geometries of studied model oligomers in all-trans arrangements for syn- and anti-orientation. The electronic energies are in parentheses.*

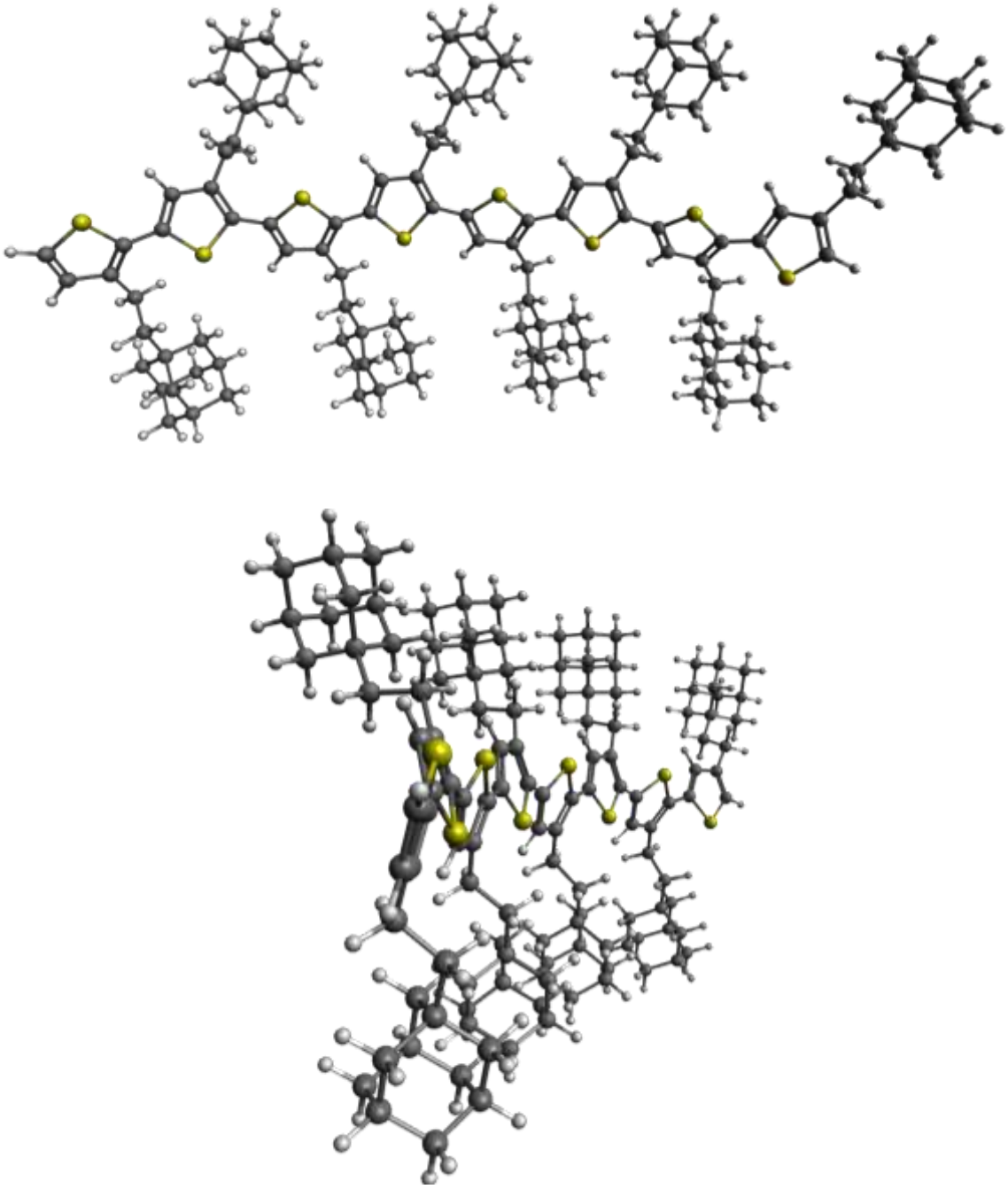

EAT-s (–8156.522533 hartree)

Fig. 2S (continued) *The optimal B3LYP gas-phase geometries of studied model oligomers in all-trans arrangements for syn- and anti-orientation. The electronic energies are in parentheses.*

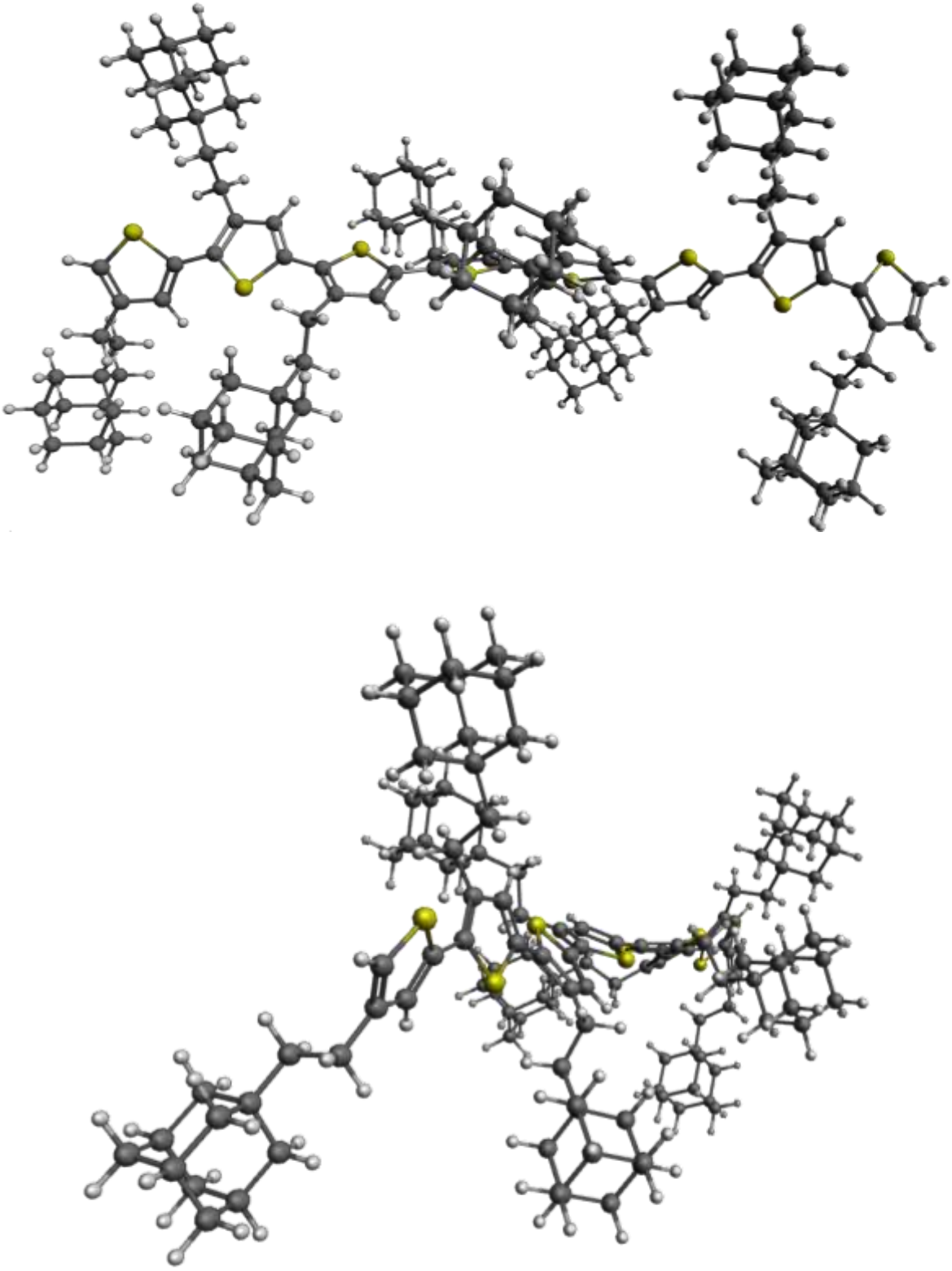

EAT-a (–8156.523925 hartree)

Fig. 2S (continued) *The optimal B3LYP gas-phase geometries of studied model oligomers in all-trans arrangements for syn- and anti-orientation. The electronic energies are in parentheses.*

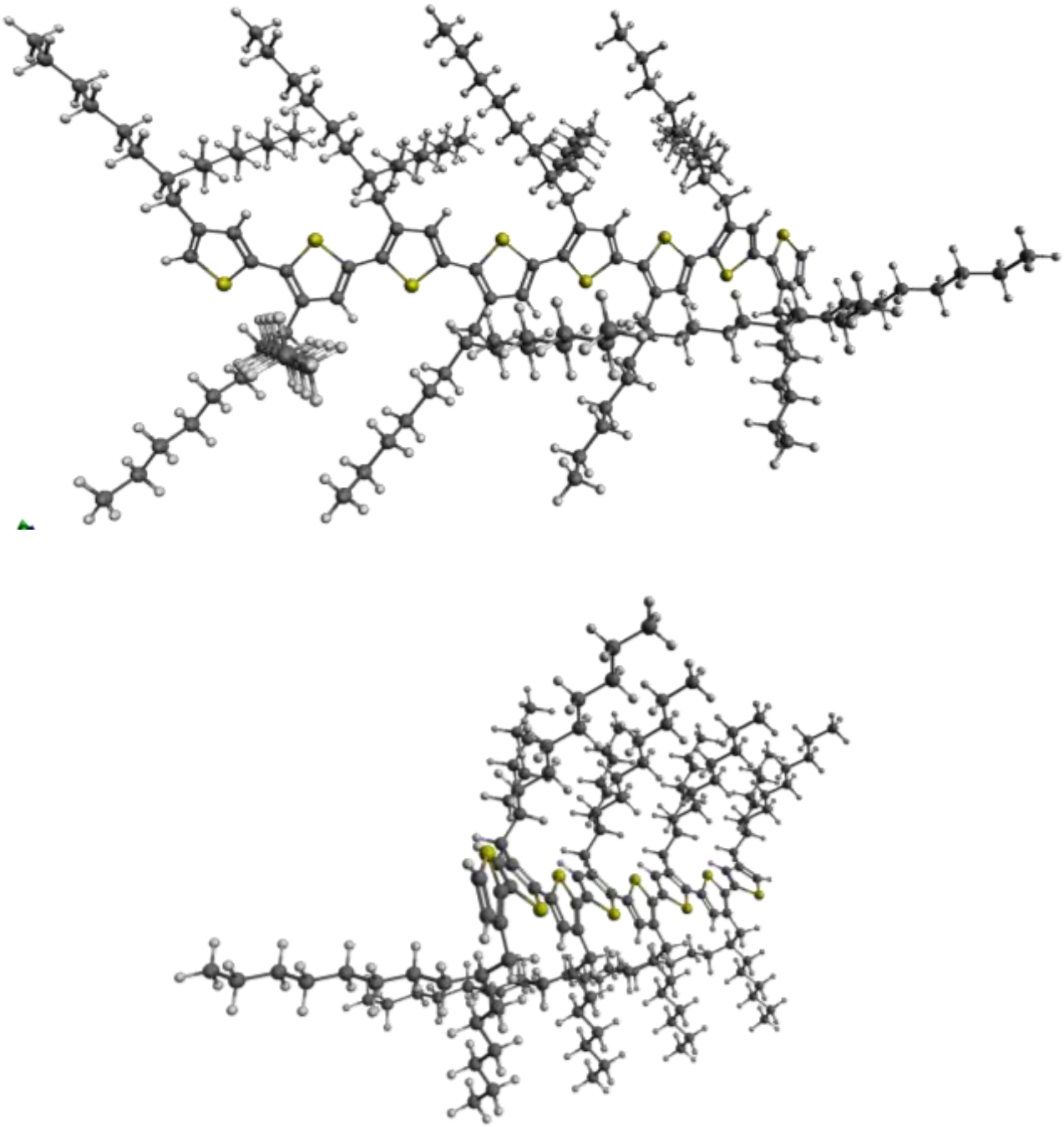

MPT-s (–8775.292733 hartree)

Fig. 2S (continued) *The optimal B3LYP gas-phase geometries of studied model oligomers in all-trans arrangements for syn- and anti-orientation. The electronic energies are in parentheses.*

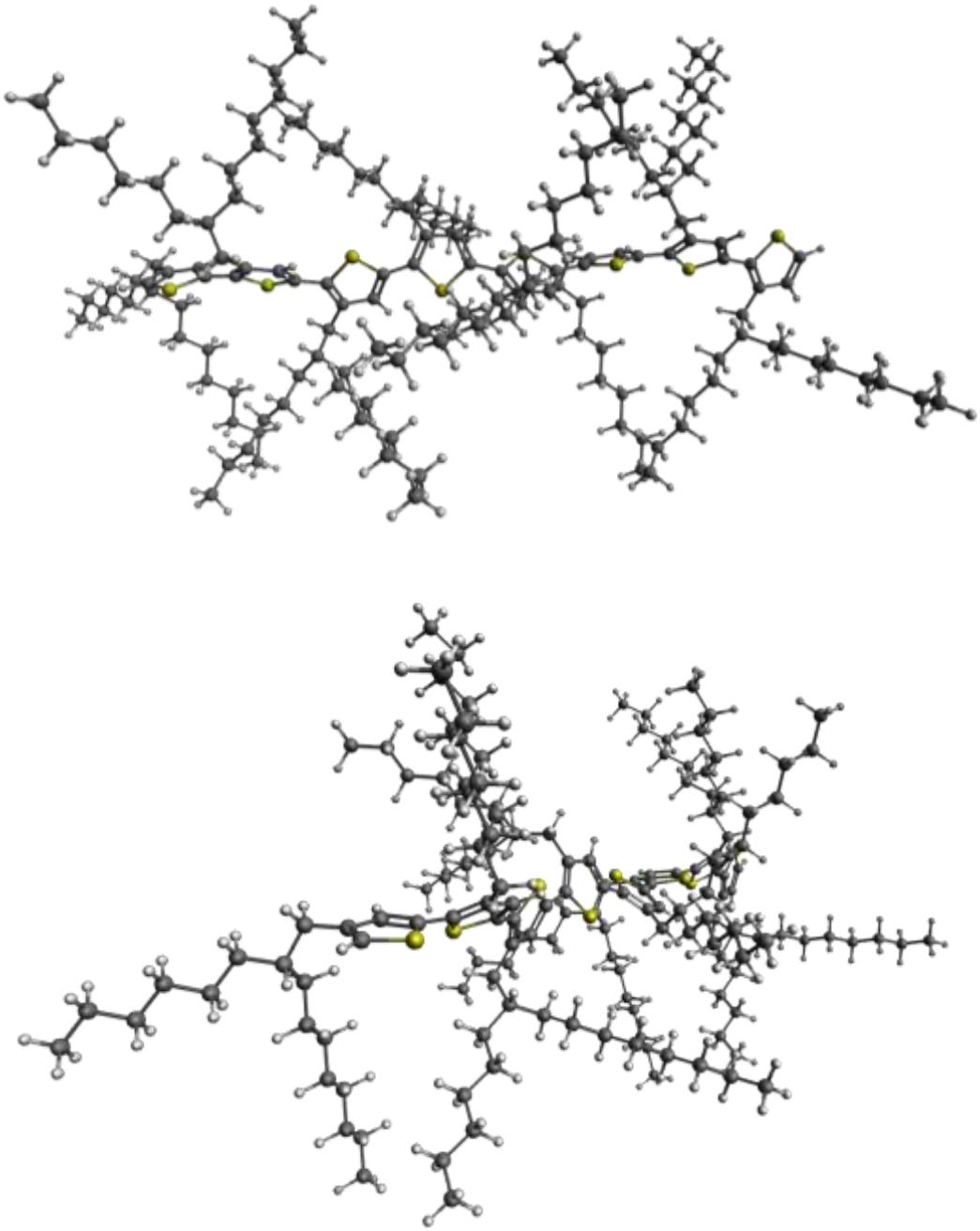

MPT-a (–8775.2938141 hartree)

Fig. 2S (continued) *The optimal B3LYP gas-phase geometries of studied model oligomers in all-trans arrangements for syn- and anti-orientation. The electronic energies are in parentheses.*

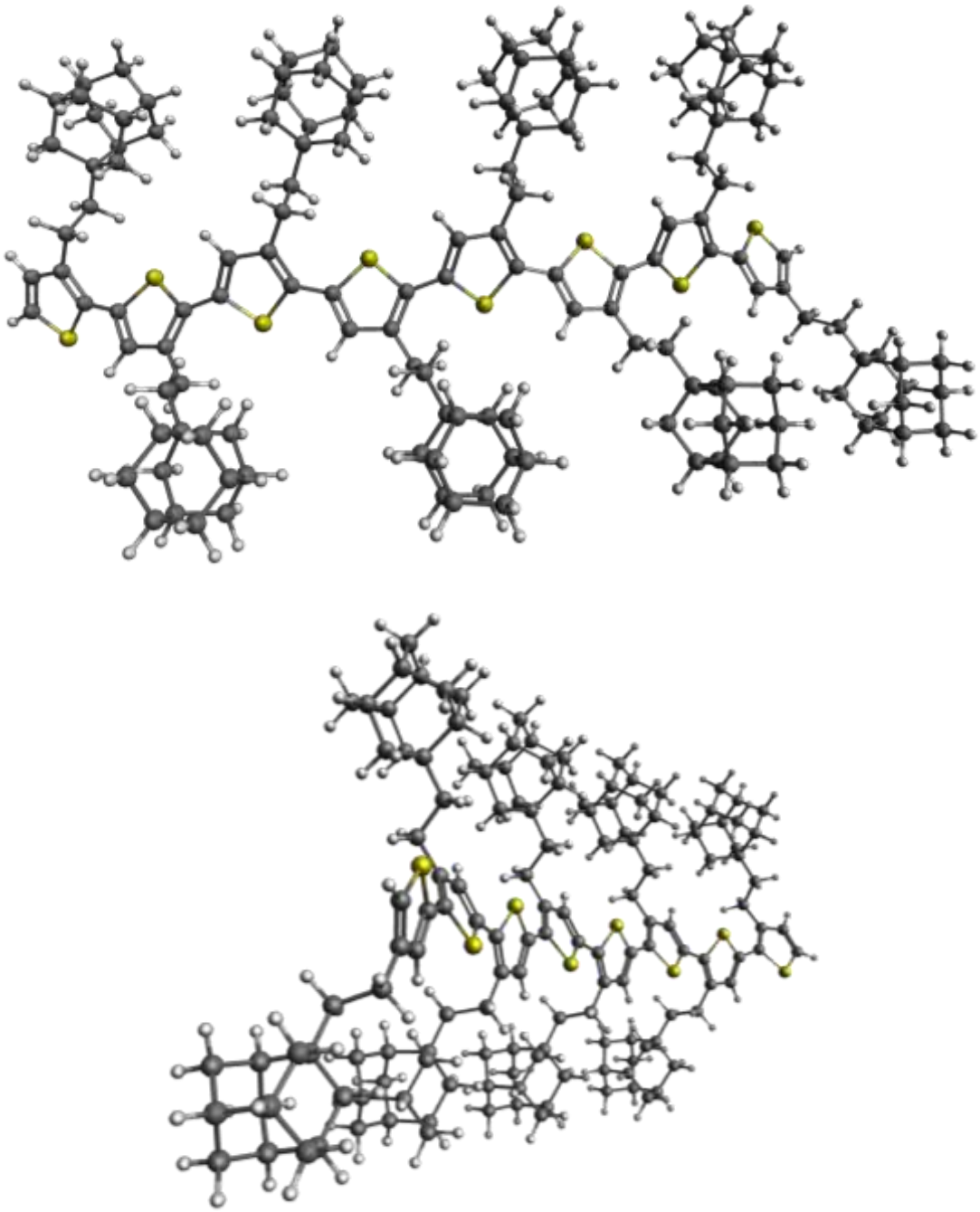

ETT-s (–9442.4759305 hartree)

Fig. 2S (continued) *The optimal B3LYP gas-phase geometries of studied model oligomers in all-trans arrangements for syn- and anti-orientation. The electronic energies are in parentheses.*

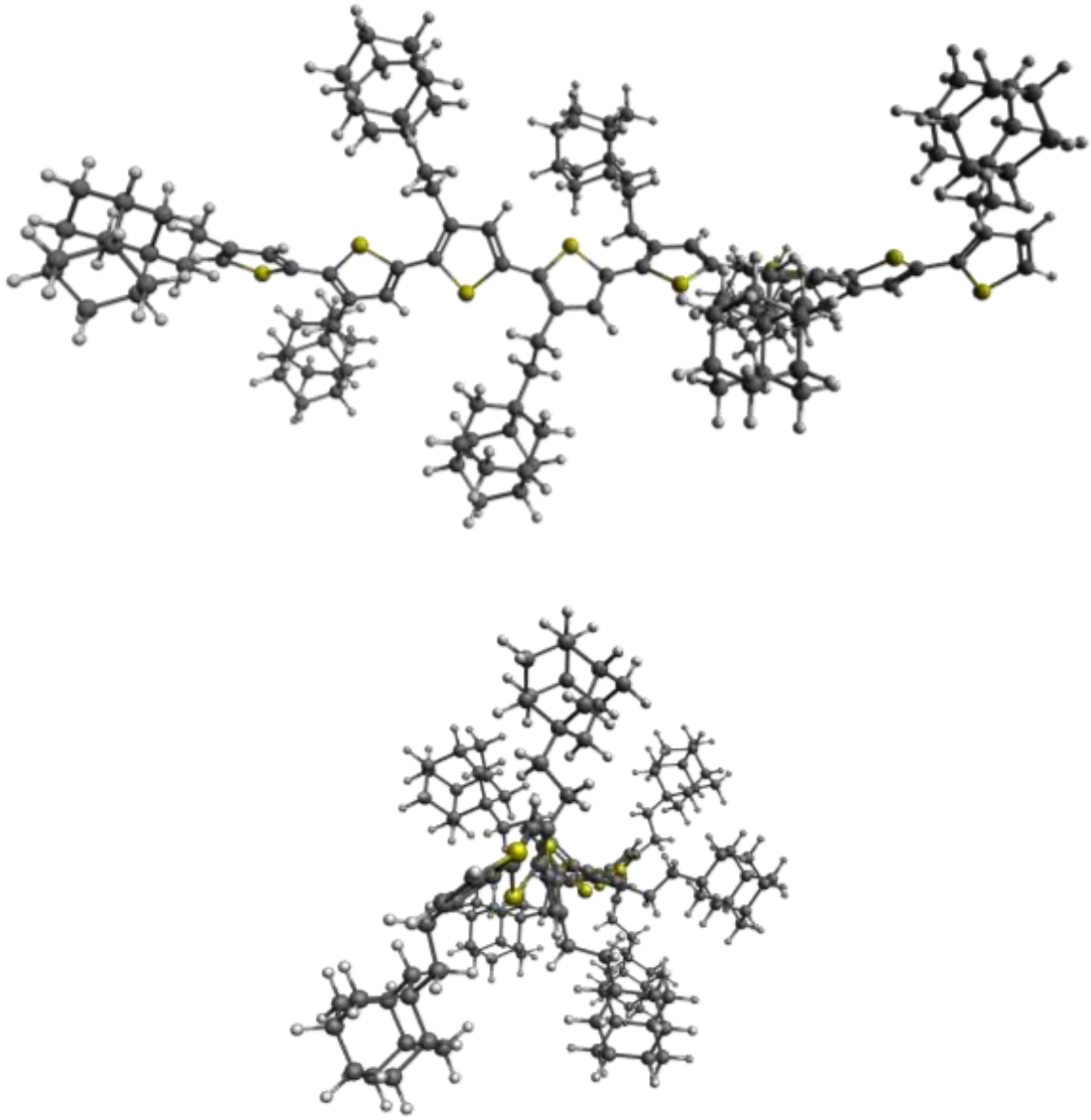

ETT-a (–9442.4732152 hartree)

Fig. 2S (continued) The optimal B3LYP gas-phase geometries of studied model oligomers in *all-trans* arrangements for *syn*- and *anti*-orientation. The electronic energies are in parentheses.

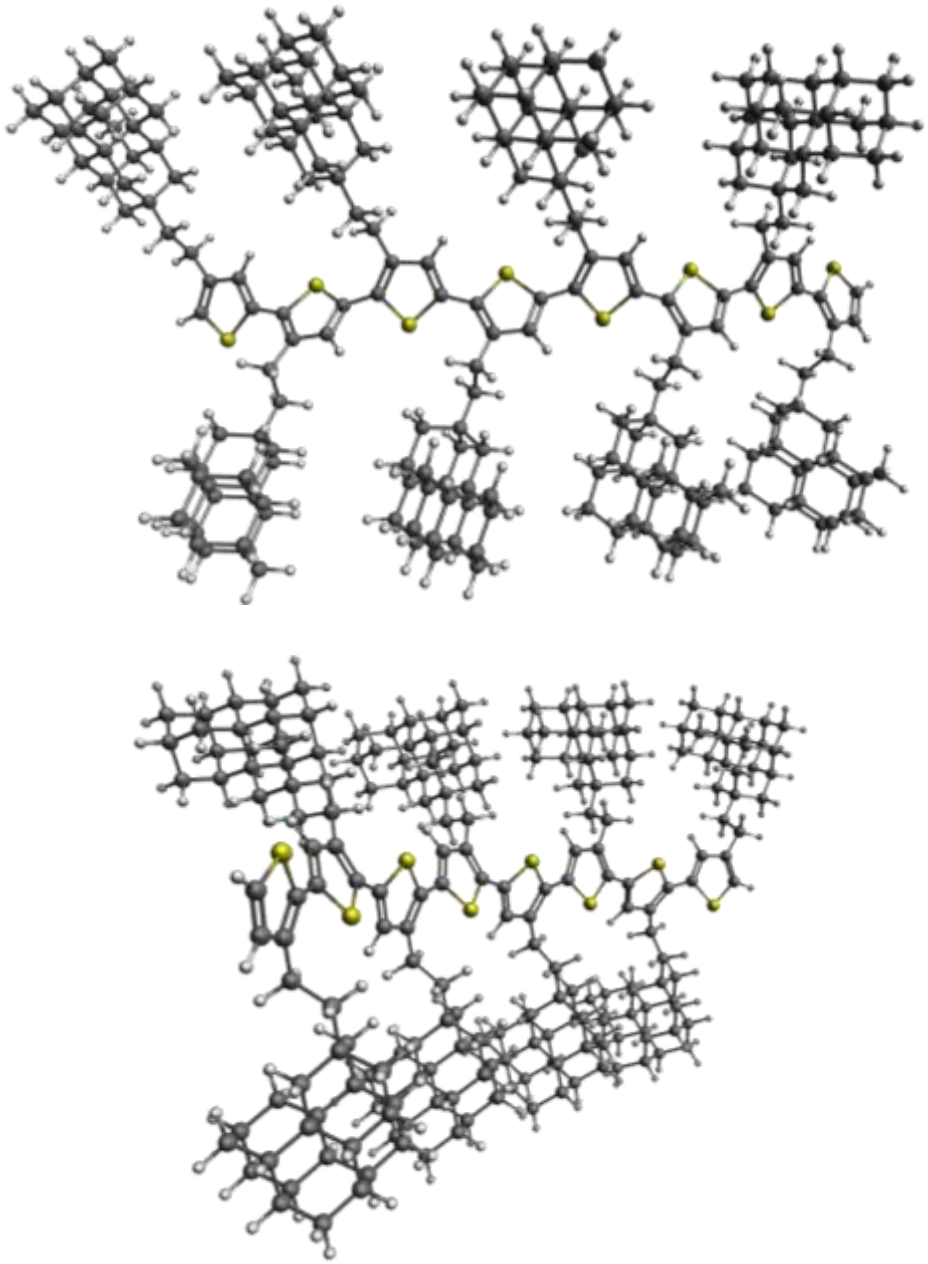

ETAT-s (–11870.2409565 hartree)

Fig. 2S (continued) *The optimal B3LYP gas-phase geometries of studied model oligomers in all-trans arrangements for syn- and anti-orientation. The electronic energies are in parentheses.*

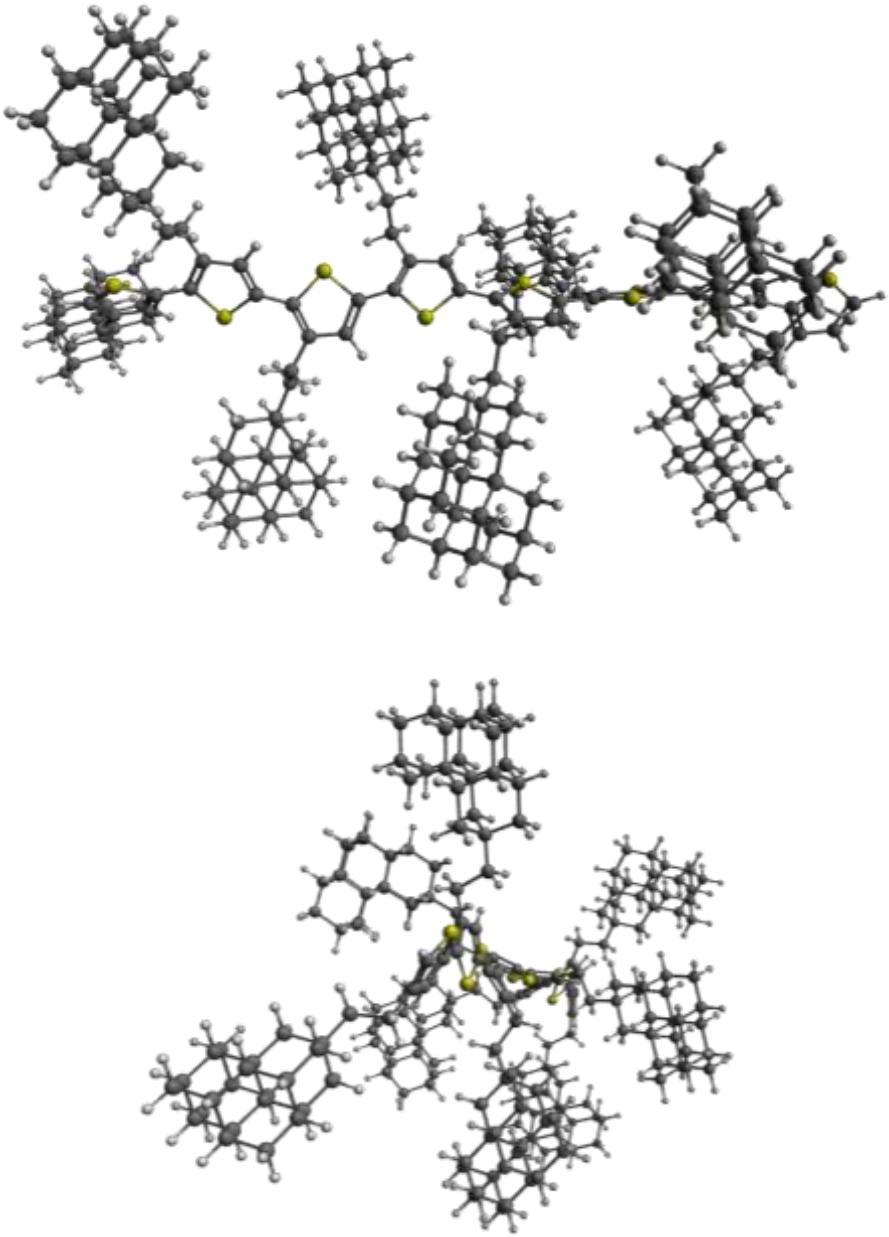

ETAT-a (–11870.2421222 hartree)

Fig. 2S (continued) *The optimal B3LYP gas-phase geometries of studied model oligomers in all-trans arrangements for syn- and anti-orientation. The electronic energies are in parentheses.*

Tab. 7S *the gas-phase B3LYP/def2SVP dihedral angles α (in degrees) between the aromatic rings (from left to right) for S_0 geometry, and the corresponding electronic energies. The anti- conformer is denoted by -a, and the syn- conformer by the -s suffix.*

Molecule	α_1	α_2	α_3	α_4	α_5	α_6	α_7	Energy (Hartree)
$(PT)_8$-s	167	171	173	173	173	171	167	-4413.20798663
$(PT)_8$-a	167	–171	173	–173	173	–171	167	-4413.20798634
$(EDOT)_8$	179	180	180	180	180	180	179	-6233.92438491
$(3HT)_8$-s	147	151	151	151	150	149	145	-6297.73088378
$(3HT)_8$-a	147	–151	151	–151	150	–149	145	-6297.73088387
$(3MAT)_8$-s	139	142	144	142	142	144	136	-7839.49228647
$(3MAT)_8$-a	136	–151	142	–149	143	–153	136	-7839.49504983
$(3EAT)_8$-s	145	151	150	149	149	147	144	-8153.57686244
$(3EAT)_8$-a	145	–148	153	–148	152	–144	143	-8153.57840300
$(3MPT)_8$-s	150	–164	158	–159	154	–155	146	-9438.52120683
$(3MPT)_8$-a	139	137	138	137	138	138	140	-9438.52166682
$(3ETT)_8$-s	146	145	147	146	146	146	144	-8772.02039610
$(3ETT)_8$-a	147	–148	151	–151	152	–149	146	-8772.02165524
$(3ETAT)_8$-s	146	147	149	148	146	147	144	-11865.3342430
$(3ETAT)_8$-a	150	–145	151	–144	158	–146	146	-11865.3344850

12 APPENDIX B – THE SELECTED RESEARCHED PAPERS

Below, the publications described in section 10.1 may be found. Since [JT3] was accepted shortly before this thesis was submitted, only the preprint is included.

Optical Materials 117 (2021) 111205

Contents lists available at ScienceDirect

Optical Materials

journal homepage: www.elsevier.com/locate/optmat

Research Article

Spectroscopic behavior of alloxazine-based dyes with extended aromaticity: Theory vs Experiment

Denisa Cagardová [a,*], Jan Truksa [a,b], Martin Michalík [a], Jan Richtár [b], Martin Weiter [b], Jozef Krajčovič [b], Vladimír Lukeš [a]

[a] Institute of Physical Chemistry and Chemical Physics, Slovak University of Technology in Bratislava, Radlinského 9, SK-812 37 Bratislava, Slovakia
[b] Faculty of Chemistry, Brno University of Technology, Purkyňova 118, CZ-612 00 Brno, Czech Republic

ARTICLE INFO

Keywords:
Alloxazine
Flavins
Aromaticity index
Vertical excited states
Fluorescence
Dyes

ABSTRACT

The chemical and electronic structure of parent (iso)alloxazine and their eight aromatic derivatives as possible candidates for dyes usage were systematically investigated by the Density Functional Theory. The effect of condensation by various (mostly benzene-like) aromatic moieties to the initial benzo[g]pteridine moiety on the energies of frontier molecular orbitals and spectroscopic properties - absorption, and emission characterization, was discussed. The spectroscopic behavior experimentally measured in alkaline dimethylsulfoxide for parent alloxazine, and its four available derivatives were compared with the theoretical predictions. In this context, the optical properties of iso-tautomers and deprotonated species were also theoretically quantified. Impact of chain modification relating to several linear and two-dimensional structure variations on electron structure and optical properties was analyzed. The correlations between theoretical estimation and experiment were proposed and could be helpful for future synthesis of novel molecules in optoelectronics or biosensing technology.

1. Introduction

Organic compounds derived from the tricyclic isoalloxazine and alloxazine have been subjects of several studies in photophysics and electrochemistry [1–4], revealing them as efficient luminescent chromophores. Substituted flavins, i.e., isoalloxazines, are widely spread in animals and plants as a part of flavoproteins and coenzymes. For example, riboflavin, also known as vitamin B2, supports the integrity of mucous membranes, skin, eyes, and the nervous system. Various molecules containing benzo[g]pteridine moiety were, therefore, proved to be suitable candidates for future application in bioorganic molecular sensors and semiconductor technology [5,6].

Although the alloxazine (**AL**) and its tautomer, isoalloxazine (**iAL**), are closely related compounds (see Fig. 1) differing only by the shift of hydrogen atom from N(1) to N(10) position, their spectroscopic and photophysical properties are quite dissimilar. In particular, the absorption spectra of alloxazine sample in aqueous solution differ from those of isoalloxazine by a hypsochromic shift of both long-wavelength maxima from about 440 nm to 340 nm to about 380 nm and 330 nm, respectively [7]. The shape of absorption spectrum is determined by the equilibrium concentration of both tautomers. In aqueous solutions, the equilibrium can be changed by solvent acidity and temperature. At pH = 4 and room temperature, alloxazine in aqueous solution is expected to be free of a tautomeric isoalloxazine contribution, while at pH = 10, a partial presence of isoalloxazine (9%) is estimated [8].

The isoalloxazine exhibits one order of magnitude larger fluorescence quantum yields and correspondingly longer fluorescence lifetimes than alloxazine [9]. The fluorescence wavelength maximum of 456 nm was detected at pH = 4 for excitation wavelength λ_{exc} = 330 nm. At pH = 10, the emission maximum at 530 nm is observed following the excitation wavelength of 440 nm. The solvent acidity in aqueous solutions or in different solvents combined with the photoexcitation also supports the formation of the isoalloxazine tautomer [10–12]. This proton transfer from N(1) to N(10) atom was experimentally also observed for other flavin derivatives in water or pyridine solutions, e.g. lumichrome [13] or 6,7-dicyano-lumazine [14]. The possible role of tautomerization process and deprotonated specie for different pH in water and BDHC micelles was discussed by Choudhury et al. and Prukała et al. [15,16].

Recently, Richtar et al. [17,18] suggested and applied two efficient approaches to the synthesis of various novel alloxazine derivatives. Most prepared compounds exhibit high thermal stability and versatile

* Corresponding author.
E-mail address: denisa.cagardova@stuba.sk (D. Cagardová).

https://doi.org/10.1016/j.optmat.2021.111205
Received 16 April 2021; Accepted 11 May 2021
Available online 28 May 2021

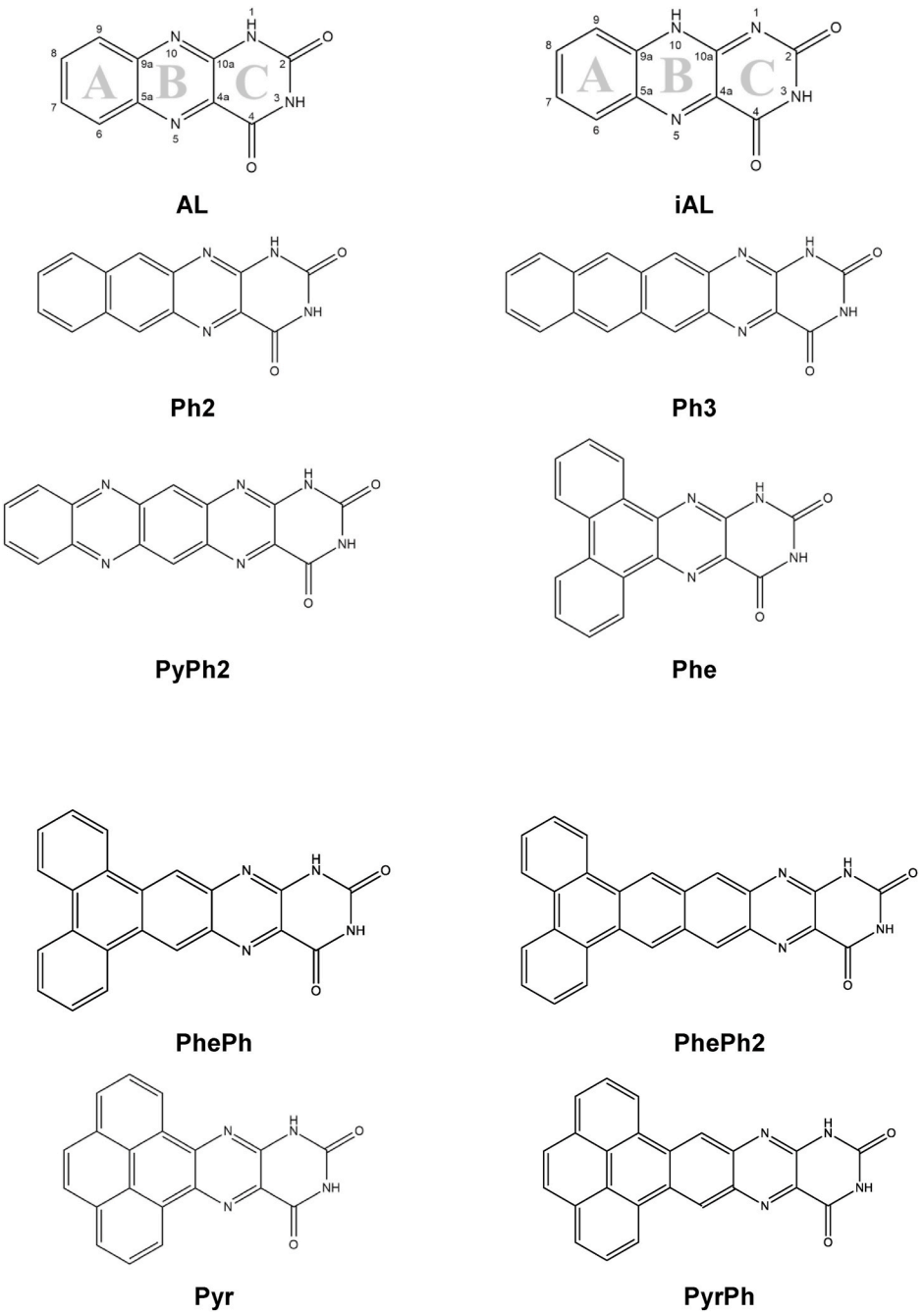

Fig. 1. Schematic structures of studied molecules. In case of iso-tautomers, the hydrogen atom is bonded to N(10), see **iAL**.

chemical use. The fluorescence spectra of certain compounds in aqueous and aprotic solvents (DMSO, $CHCl_3$) consist of more than one emission band with different intensities. The authors assumed that this multi-chromophoric behavior results dominantly from an intramolecular proton transfer [17].

Although this study has demonstrated that the optical properties are changed by the modification of initial alloxazine core, the variation effect of the terminal part in molecular structure on the chemical and electronic structure was not systematically analyzed. In this context, we decided to perform a quantum chemical analysis of (iso)alloxazine and their eight derivatives where the aromatic chromophore is fused to the smaller benzo[g]pteridine moiety (see Fig. 1). The partial aims of this study are: (1) to calculate the optimal geometries of molecules in the electronic ground-state and lowest excited-state in the gas-phase and in alkaline dimethylsulfoxide environment (DMSO); (2) to evaluate the gas-phase energies of frontier molecular orbitals (MOs) and (3) to calculate the TD-B3LYP and TD-CAM-B3LYP electron transitions contributing to absorption and fluorescence spectra. The obtained theoretical results are compared with the experimental absorption and fluorescence spectra measured for available samples in alkaline DMSO. In this context, the possible contribution of deprotonated anionic species or iso-tautomers to the experimental spectra in DMSO is also discussed.

2. Methodology

2.1. Computational details

The Gaussian 16 program package was used for performing the quantum chemical calculations [19]. Optimal geometries of the studied molecules were calculated by the Density Functional Theory (DFT) with

Table 1
Selected gas-phase B3LYP HOMED indices for A, B and C rings of benzo[g]pteridine moiety related to the reference **AL** and **iAL**, and dipole moments (μ) of the studied molecules. The HOMED values for reference **AL** and **iAL** are in parentheses.

Molecule	A	B	C	μ / D	Molecule	A	B	C	μ / D
AL	0.00	0.00	0.00	4.78	**iAL**	0.00	0.00	0.00	8.38
	(0.94)	(0.93)	(0.83)			(0.98)	(0.87)	(0.68)	
Ph2	–0.02	–0.05	–0.01	5.38	**iPh2**	–0.04	–0.03	0.00	9.02
Ph3	–0.04	–0.09	–0.02	5.93	**iPh3**	–0.08	–0.05	0.00	9.73
PyPh2	–0.04	–0.09	–0.02	5.18	**iPyPh2**	–0.08	–0.06	–0.02	8.58
Phe	–0.14	0.05	0.04	5.54	**iPhe**	–0.13	0.06	0.05	9.93
PhePh	0.00	–0.01	0.00	6.15	**iPhePh**	–0.01	0.00	0.00	10.10
PhePh2	–0.02	–0.07	–0.02	6.55	**iPhePh2**	–0.05	–0.04	0.00	10.51
Pyr	–0.10	0.05	0.04	5.60	**iPyr**	–0.10	0.06	0.05	10.03
PyrPh	0.00	–0.01	0.00	6.20	**iPyrPh**	–0.02	0.00	0.00	10.18

the B3LYP functional [20,21] without any constraints (energy cut-off of 10^{-5} kJ × mol^{-1}, final RMS energy gradient under 0.01 kJ × mol^{-1} × A^{-1}). The 6-31 + G** basis set of atomic orbitals was applied [22,23]. In pursuance of optimized B3LYP geometries, the vertical singlet transition energies and oscillator strengths between the initial and final electronic states were computed by time-dependent TD-DFT method [24] using the B3LYP and CAM-B3LYP [25] functionals. TD-DFT calculations of excited state geometries of organic heterocycles including flavins can lead to saddle points at the potential energy surface [26], but the theoretical analysis of selected de-excitation energies can offer a certain view on the fluorescence properties. The conformation with the lowest gas-phase electron energy was used as the starting geometry for implicit solvent model calculations. The influence of the solvent was approximated by Solvation Model based on Density (SMD) [27]. In case of geometry optimization within SMD, the Grimme's dispersion corrections were included (keyword GD3BJ) [28].

The true minima on the potential energy surface were confirmed by an inspection of the frequencies (no imaginary frequencies). The molecules, shapes of molecular orbitals and dipole moment vectors were visualized using the Molekel [29] and Avogadro [30] program packages. The chemical structure of selected aromatic rings was quantified using the Harmonic Oscillator Model of Electron Delocalization (HOMED) [31–34]. The expressions used for the calculations of these parameters are collected in the Supplementary material.

2.2. Spectral measurements

The optical measurements were performed for five selected compounds previously synthetized by Richtar et al. [17]. The absorption spectra were measured using a Varian Cary Probe 50 UV–Vis spectrophotometer (Agilent Technology, Santa Clara, CA, USA). The spectra were corrected to a baseline, which was determined by measurement of absorption spectra of alkaline dimethylsulfoxide solvent. Emission spectra of solution were measured using a Horiba Fluorolog (Horiba Jobin Yvon, Kyoto, Japan). Measurements have been performed in Hellma QS quartz cuvette with an optical path of 1 cm at ambient temperature. The recorded absorption spectra were processed using the CaryWinUV software [35] and for the fluorescence measurement the FluorEssence software [36] was used. Solution concentrations of sublimed materials for optical measurements were adjusted to a level of light absorption less than 1. The concentration of all compounds/samples was 10 μmol L^{-1}. DMSO (HPLC grade) was purchased from Aldrich, Germany. Deionized water with conductivity 0.06 μS/cm was used.

3. Results and discussion

3.1. Chemical structure

Compounds in this study are based on the N(1)H-alloxazine core and its N(10)H iso-tautomeric form with various aromatic rings condensed to one end. Despite their differences, the local aromaticity of three rings common for all the derivatives (denoted A, B, and C in Fig. 1) can be compared utilizing the HOMED index (see Supplementary material). The effect of chemical structure modification on the aromaticity can be deduced from this comparison [31–34]. In the parent alloxazine (**AL**), both HOMED(A) and HOMED(B) indices above 0.9 indicate extensive electron delocalization while HOMED(C) of 0.83 confirms perturbed aromaticity of C ring containing two nitrogen atoms (see Table 1). In general, it was observed that the condensation of aromatic rings leads to decreased aromaticity within the analyzed rings. Generally, the B and C rings of derivatives fused with phenanthrene (**i)Phe** and pyrene (**i)Pyr** experienced the biggest increase. The biggest decrease of HOMED(A) relative to **AL** by 0.14 was also found for **Phe** in favor of the other rings. Within the studied group of molecules, the A ring aromaticity is remarkably higher for the iso-tautomer, e.g., 0.85 for **iPhe** and 0.88 for **iPyr** compared to 0.80 for **Phe** and 0.84 for **Pyr**, respectively. Aromaticity changes caused by the deprotonation are observable mostly for B and C rings (see Table 1S).

The chemical structure also causes an uneven charge distribution resulting in a permanent dipole moment μ. Typical dipole moments for most organic molecules range between 0 D and 12 D, but there are some compounds, such as polymethine dyes, which have dipole moments of 20 D or higher [37]. The static dipole moments of molecules can affect the solubility in solvents as well as the mutual orientation of interacting molecules in real samples.

The calculated gas-phase dipole moment of alloxazine is 4.78 D and a larger value of 8.38 D is predicted for **iAL**. The consecutive ring condensation increases the dipole moment values. For N(1)H-tautomers, the values range from 5.18 D (**PyPh2**) to 6.55 D (**PhePh2**). The dipole moments of iso-tautomers are between 8.58 D (**iPyPh2**) to 10.51 D (**iPhePh2**). As shown in Table 1, acenic elongation of the backbone chain increases dipole moment, e.g., 5.38 D for **Ph2** and 5.93 for **Ph3**. However, the presence of pyrazine significantly lowers μ, e.g., one pyrazine ring in a 5-membered chain of (**i)PyPh** causes a decrease of μ by 12% in comparison with a 5-membered chain with acene-type end in (**i)Ph3**. The dipole moment vector is diagonally oriented from C to A rings (see a graphical depiction of the dipole moment vector in Fig. 1S).

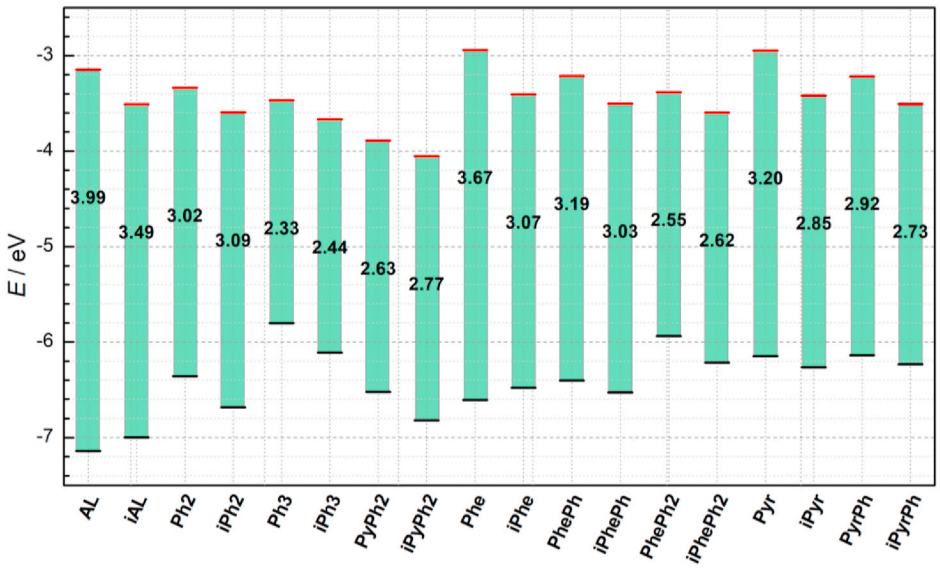

Fig. 2. Energy diagram of gas-phase B3LYP frontier molecular orbitals for the electroneutral state of studied molecules. Values written within green bars are energy gaps in eV.

3.2. Frontier molecular orbitals

Electronic structure and electrochemical properties of the investigated molecules can be estimated from the energy levels of frontier molecular orbitals (MOs) depicted in Fig. 2 and from the analysis of their shapes. The gas-phase B3LYP HOMO and LUMO energies for the reference alloxazine **AL** are −7.14 eV and −3.15 eV, respectively. Particularly high HOMO levels are predicted for **PhePh2** (−5.94 eV), **Ph3** (−5.80 eV) and conversely, the highest LUMOs of −2.94 eV and −2.95 eV correspond to **Phe** and **Pyr**, respectively.

The HOMO and LUMO energy levels of iso-tautomers are generally lowered by the value of 0.08–0.45 eV, apart from the **(i)AL** and **(i)Phe** derivatives (HOMO is raised by 0.13 eV). Within the tautomer couples, in case of **(i)AL** and its bigger non-linear condensed derivatives **(i)Phe, (i)PhePh, (i)Pyr**, **(i)PyrPh**, the HOMO−LUMO gaps are smaller in iso-tautomers than in their N(1)H-counterparts.

Comparing to the **AL**, the derivatives containing additional condensed aromatic rings exhibit larger electron delocalization of HOMO electrons, which are uniformly delocalized over the longest axial direction in the center of the molecule (Fig. 2S). This is evident for linear fused derivatives, i.e., acene-type **Ph2**, **Ph3**, and linear pyrazine-containing **PyPh2**. The addition of a larger pyrene moiety to a lumazine backbone (**Pyr** and **PyrPh**) results in a decreased electron delocalization over the N(10) and negligible electron delocalization over the N(5) which is in contrast with other derivatives. On the other hand, the lobes of LUMO are mostly delocalized over the benzo[g]pteridine moiety for all derivatives. Hydrogen at N(10) has minimal influence on the shape of HOMOs and LUMOs of linear acene-type derivatives. The LUMO electron delocalization occurs above the N(1) and C(2)O. In most studied molecules, HOMO appears above the modified end of the backbone chain and LUMO is mostly delocalized above two lumazine B and C rings resulting in a prediction of good charge transfer from HOMO to LUMO (see Fig. 2S).

3.3. Optical properties

We measured absorption spectrum of alloxazine sample with the concentration of 10^{-5} M freshly dissolved in pure DMSO without exposure to air, sunlight or water to prevent of iso-tautomer formation (see Fig. 3S). According to the previously published spectroscopic studies of alloxazine in different environments, the absorption band in pure DMSO at 3.23 eV (383 nm) with absorbance $A = 0.09$ corresponds to the alloxazine specie (Fig. 3S). The extinction coefficient for this absorption maximum is 7326 M^{-1} cm^{-1}. Simpler shape of the spectrum occurs, i.e., significant peak under 3 eV was not observed, thus it does not correspond to isoalloxazine. A nice band at 3.85 eV (322 nm) appears, its shape is clearer. The calculated TD-B3LYP excitation energy of the first excited vertical singlet state (S_1) over the electronic ground state for **AL** is 3.32 eV (373 nm) and it corresponds to the HOMO to LUMO transition (see also Table 2S). The significant absorption probability of 91% and oscillator strength of 0.28 is indicated for the third (HOMO–1 → LUMO) vertical transition. The corresponding theoretical excitation energy is 3.82 eV (325 nm). The HOMO–1 orbital has also a π-type character (Fig. 2S). Based on this comparison, we can assign two experimental absorption peaks at 3.85 eV and 3.23 eV to alloxazine.

The experimental absorption spectra of alloxazine and its four derivatives in alkaline DMSO exhibit two or three relatively broad bands with differently resolved structure (see Fig. 3). In the experimental spectrum of alloxazine sample (Fig. 3a), we can thereby confirm the presence of alloxazine and determine its excitation energies. However, the more significant (in comparison to Fig. 3S) additional absorption band with energy range smaller than 3.0 eV (or larger than 410 nm) occurs. The increase of the corresponding longer-wavelength absorption band was reported previously also in alkaline aqueous solution [38]. This additional small energy broad band can be attributed to isoalloxazine, the tautomeric form of alloxazine. The TD-B3LYP excitation energy of this optical transition of **iAL** is 2.97 eV (418 nm) with $a^1(\pi\pi^*)$ character and oscillator strength of 0.22. The value is close to the $S_0 \rightarrow S_1$ excitation energy of 2.86 eV (434 nm) predicted for deprotonated alloxazine anion located in DMSO cavity (see Table 2S). Based on this consideration, the deprotonated specie can also contribute to the formation of additional absorption peak.

The experimental absorption spectra of **Ph2** and **PyPh2** samples in alkaline DMSO depicted in Fig. 3b,c exhibit very broad bands at 2.75 eV (451 nm) and 2.38 eV (520 nm), respectively. These agree well with their theoretical $S_0 \rightarrow S_1$ excitation energies of 2.40 eV (516 nm) and 2.17 eV (571 nm), respectively. However, the oscillator strengths are smaller than 0.05. On the other hand, the calculations predict the significant oscillator strengths of $S_0 \rightarrow S_3$ transitions. The transition energies are 3.33 eV (372 nm, $f = 0.38$) for **Ph2** and 2.98 eV (416 nm, $f = 0.56$) for **PyPh2**. These values correspond to another observed experimental absorption band with resolved vibronic structure at 3.18 eV (387 nm)

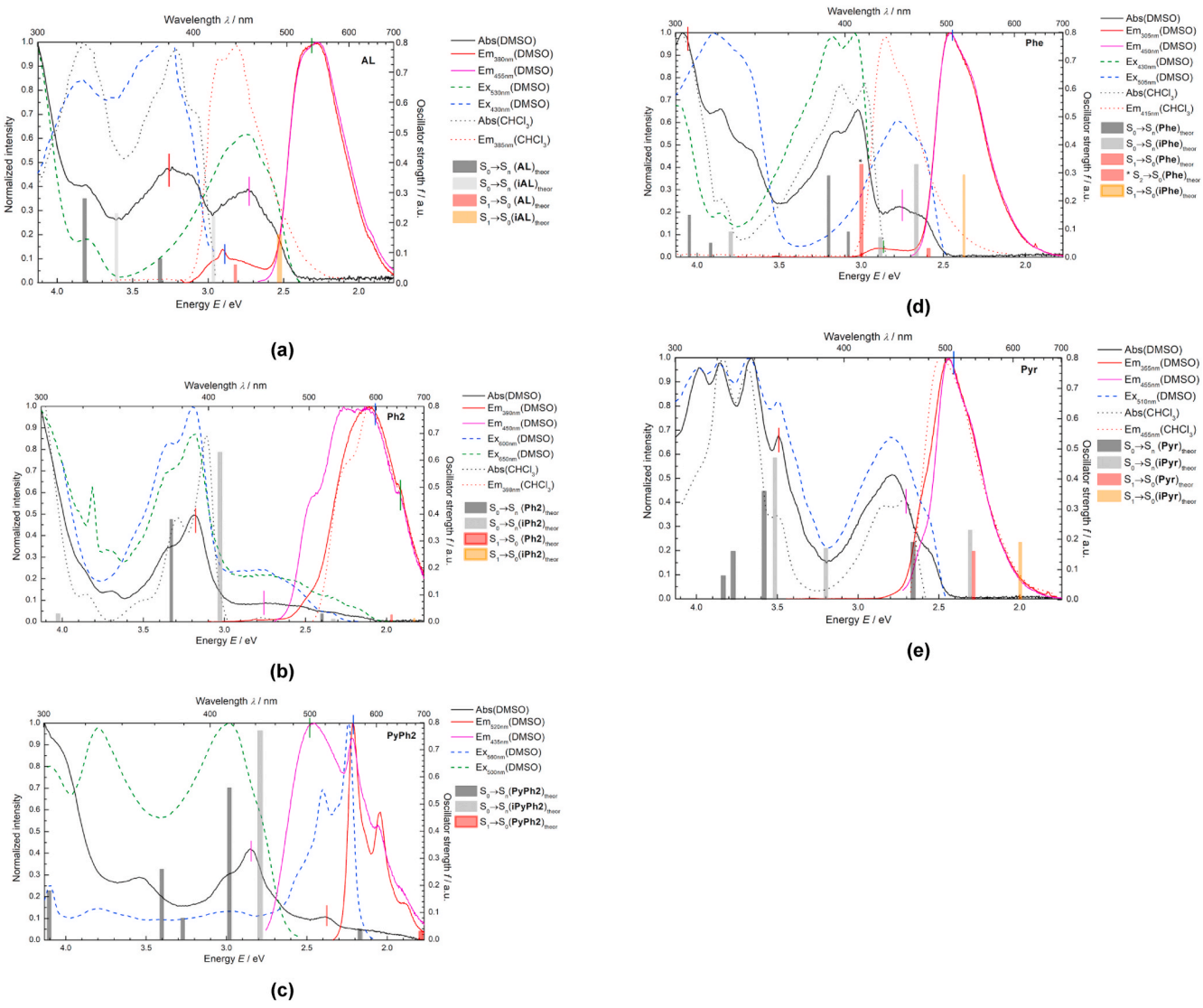

Fig. 3. Normalized experimental absorption (Abs), excitation (Ex) and emission (Em) spectra of **AL** (a), **Ph2** (b), **PyPh2** (c), **Phe** (d) and **Pyr** (e) samples in alkaline DMSO. The dotted lines represent the absorption and emission spectra measured for the corresponding N(1),N(3)-dibutyl substituted flavins in $CHCl_3$ [18]. The oscillator strengths (right *y* axis) correspond to theoretical TD-B3LYP(DMSO) vertical transitions within absorption or emission of the molecules and anions and are noted by bars.

with absorbance of 0.315 and extinction coefficient of 31535 M^{-1} cm^{-1} for **Ph2**; and 2.85 eV (435 nm) with absorbance of 0.367 and extinction coefficient of 36742 M^{-1} cm^{-1} for **PyPh2**. Furthermore, there are strong theoretically predicted transitions for the **iPh2** molecule at 3.03 eV (409 nm), and at 3.10 eV (400 nm) for the anionic form. These transitions may be contributing to the structure of the absorption band – the main peak at 387 nm being the iso- and anionic form transition, and the shoulder of the peak, at 370 nm, corresponding to the **Ph2** transition mentioned above. Similarly, in the case of the **PyPh2** derivative, the **iPyPh2** transition at 2.79 eV (445 nm) and the anion transition at 2.75 eV (451 nm) may contribute to the 435 nm absorption band.

The shape of experimental absorption spectrum of **Phe** in alkaline DMSO is similar to that of the alloxazine sample. The significant band with vibronic structure was found at 3.02 eV (411 nm) with absorbance of 0.181 and the corresponding extinction coefficient of 18057 M^{-1} cm^{-1}. According to the (iso)alloxazine pattern, the smaller and broad absorption band with maximum at 2.75 eV (450 nm) can be related to the optical properties of **iPhe** and its deprotonated specie. The theoretically calculated $S_0 \rightarrow S_1$ excitation energies for **iPhe** and its anion specie are 2.67 eV (465 nm) and 2.86 eV (434 nm) with significant oscillator strengths *f*, respectively.

The experimental long wavelength absorption band of pyrene derivative **Pyr** exhibits a maximum at 2.78 eV (446 nm) with small side band at 2.57 eV (482 nm). The molar extinction coefficient of the maximum is 22190 M^{-1} cm^{-1}. The calculated $S_0 \rightarrow S_1$ excitation energy for **Pyr** is slightly lower, i.e., 2.68 eV (463 nm). In case of **iPyr** and its anionic form, the first transition has energy of 2.33 eV (532 nm) and 2.75 eV (451 nm), respectively, with sufficiently high *f*. There are also quite strong transitions in the 350–370 nm range for **iPyr** and the **Pyr** anion at 3.53 eV (352 nm) and 3.40 eV (365 nm), respectively, which correspond to the experimental peak at 355 nm. Since all the experimentally studied molecules exhibit absorption bands that may be related to the presence of an N(1)H-tautomers, and since absorption bands of the iso- and anionic forms generally occur together, it seems reasonable to say that the anionic form is involved in the isomerization process.

Our hypothesis of iso-tautomer and/or anion formation is supported by the experimental absorption spectra of corresponding flavins with blocked N(1),N(3)-positions. The usage of alkyl substitution improves the molecular solubility; it has minimal influence on the electronic structure and ensures the only presence of the alloxazine form. As it was

reported by Richtar et al. [18], the additional low energy spectroscopic band with significant absorbance is not observed for **AL** and **Phe** butyl substituted derivatives solvated in chloroform (see black dotted lines in Fig. 3). For butyl derivatives of **Ph2** and **Pyr**, the lowest energy absorption bands (around 2.75 eV and 2.7 eV, respectively) are well resolved and narrower. The TD-B3LYP theoretical excitation energies analysis of (iso)tautomers is in Fig. 3 indicated by bars.

Analysis of the frontier B3LYP molecular orbitals for the linear dyes (**Ph2**, **Ph3**) showed the charge-transfer probability between two sides of these molecules. It should be noted that a global hybrid such as B3LYP is not adapted for simulating such strong charge transfer transitions and a range separated hybrid could be more suitable. For this reason, we have performed the TD-CAM-B3LYP(DMSO)//TD-B3LYP(DMSO) calculations of optical transitions. The data collected in Table 3S indicate that the excitation energies for CAM-B3LYP functional are energetically more overestimated comparing with the B3LYP ones and experimental data.

The computational accuracy of theoretical transition energies can be estimated from the comparison of TD-B3LYP calculated excitation energies ($\Delta E_{\mathrm{exc,B3LYP}}$) with the corresponding experimental energies $\Delta E_{\mathrm{Abs\text{-}exp}}$ identified for alloxazine-type N(1)H- tautomers. The obtained linear dependence is shown in Fig. 4Sa and it is expressed by the equation

$$\Delta E_{\mathrm{Abs-exp}} \,/\, \mathrm{eV} \;=\; 0.440 \;+\; 0.868 \times \Delta E_{\mathrm{exc,B3LYP}} \qquad (1)$$

The correlation coefficient R for the dependence is 0.97. Although the calculated TD-B3LYP vertical excitation energies for larger molecules are red shifted with respect to the experiment, the linear dependence presented in Eq. (1) can be used for the evaluation of experimentally relevant values in solvent.

We used this model dependence to predict experimental absorption energies reversely for the studied molecules by putting the theoretical computed excitation and de-excitation energies into the equation. Fig. 4 offers graphical illustration of predicted experimental absorption wavelengths (by equation (1)) in visible spectrum with original theoretical oscillator strengths. For instance, the lowest vertical excitation energy predicted for **Ph3** is 1.99 eV (622 nm). The series of **Phe**, **PhePh** and **PhePh2** exhibit small oscillator strengths of the lowest $S_0 \rightarrow S_1$ vertical excitations. For **Pyr** molecule, the oscillator strength of $S_0 \rightarrow S_1$ transition is ca two-times larger than for parent **AL**. The addition of benzene ring (**PyrPh**) increases slightly the oscillator strength to 0.23. The **PyPh2** compound has its HOMO to LUMO excitation wavelength at 2.32 eV (534 nm), which is in the visible green light range i.e., 500–565 nm.

The theoretical TD-B3LYP and TD-CAM-B3LYP excitation energies of remaining studied molecules in DMSO are collected in Tables 2S and 3S, respectively. For the previously mentioned reason of energy overestimation of CAM-B3LYP, we discuss only B3LYP results. To conclude, the lowest energy transition is always connected with the vertical excitation from HOMO to LUMO. In case of $S_0 \rightarrow S_2$ and $S_0 \rightarrow S_3$ transitions, the electron is dominantly excited from HOMO–1/2/3 to LUMO. The significant oscillator strength relates to the transitions from HOMO–1 to LUMO. The shape of HOMO–1 for selected molecules is depicted in Fig. 2S. In contrast to HOMO shape, HOMO–1 lobe is delocalized along the whole molecular chain; thus, we could not predict charge-transfer in this transition. One exception represents **Pyr** molecule where the $S_0 \rightarrow S_3$ transition comes from HOMO to LUMO+1 excitation.

The electronic structure of molecules in real samples affects the resulting luminescence properties. The fluorescence of alloxazine sample in alkaline DMSO initiated with excitation energy belonging to the absorption maximum of **AL** molecule (3.26 eV/380 nm) leads to two emission bands (see Fig. 3a). The smaller band reaches maximum at 2.88 eV (430 nm) and the lead one at 2.34 eV (530 nm). If the sample is excited by 455 nm (2.72 eV), only one fluorescence band occurs at 2.34 eV. On the other hand, the N(1),N(3)-dibutyl substituted alloxazine dissolved in chloroform has only one significant fluorescence band at 440 nm (2.82 eV) upon excitation by 385 nm (3.22 eV), see red dotted line in Fig. 3a [18]. It seems that the double fluorescence band of alloxazine dissolved in the DMSO results from the reabsorption of photons by the anion. Additionally, this initiates the proton transfer processes leading to increasing concentration of isoalloxazine. The presence of different chromophoric species in alkaline DMSO is confirmed by the measurement of excitation spectra. The absorption spectrum of alloxazine sample is well fitted by the superposition of excitations bands measured at 2.34 eV/530 nm and 2.88 eV/430 nm (see dashed lines in Fig. 3a). The TD-B3LYP LUMO to HOMO de-excitation energy calculated for alloxazine is 2.82 eV (439 nm), for **iAL** 2.53 eV (491 nm) and 2.42 eV (512 nm) for anion.

The experimental fluorescence spectrum of **Ph2** sample (see Fig. 3b) measured by initiation with excitation wavelength of 450 nm exhibits very broad band with two maxima at 2.11 eV (588 nm) and 2.29 eV (542 nm). It seems that this band is superposed by equivalent contributions from both chromophoric species.

In the case of the **PyPh2** sample (Fig. 3c), the excitation wavelength of 520 nm (2.38 eV) leads to a structured fluorescence band with the main peak at 2.21 eV (560 nm) and two vibronic peaks at 2.04 eV (608 nm) and 1.88 eV (659 nm). In the case of excitation wavelength of 435 nm (2.85 eV), broad emission band at 500 nm occurs together with the reabsorption. Correspondingly with experimental measurements, the TD-B3LYP theoretical calculations predicted the LUMO→HOMO de-excitation energy for **PyPh2** of 1.79 eV (692 nm). The de-excitation energy of **iPyPh2** is slightly shifted (1.73 eV or 716 nm, see orange bar).

As it is clear from Fig. 3d, two well-separated fluorescence bands are observed for the **Phe** sample excited at 4.07 eV (305 nm). The fluorescence wavelength maximum at 2.90 eV (428 nm) corresponds to the **Phe** molecule while the second maximum is detected at 2.46 eV (504 nm). The dibutyl substituted molecule dissolved in chloroform has only one significant fluorescence band at 2.83 eV (438 nm) caused by excitation of 415 nm (2.99 eV), see red dotted line [18]. If the sample in alkaline DMSO is excited at 450 nm (2.75 eV), only one dominant fluorescent band is occurred at 504 nm. As it is depicted in Fig. 3d by bars, corresponding TD-B3LYP $S_1 \rightarrow S_0$ de-excitation energy is 2.59 eV (478 nm) and the oscillator strength is very small (0.03). On the other hand, the de-excitation energy from the second electronic excited state $S_2 \rightarrow S_0$ is 3.00 eV (414 nm) and it agrees well with the experimental fluorescence maximum of 2.90 eV (428 nm). The predicted TD-B3LYP $S_1 \rightarrow S_0$ energy for **iPhe** is 2.37 eV (522 nm). Based on the comparison of experimental and theoretical data, we can suppose that the observed fluorescence double band is generated after the photon reabsorption processes.

Finally, as shown in Fig. 3e, the intensive experimental emission band of **Pyr** sample is located at 2.44 eV (508 nm) upon both excitation wavelength of 355 nm and 455 nm. The shape of this band agrees well with the dibutyl substituted derivative in chloroform (see red dotted line [18]). The theoretical TD-B3LYP $S_1 \rightarrow S_0$ de-excitation energy of **Pyr** is slightly lower, i.e., 2.31 eV (536 nm). The predicted de-excitation for iso-tautomer **iPyr** is 2.03 eV (612 nm). Derivatives of pyrene are often used in various biological imaging applications, where fluorescence properties are changed upon incorporation into DNA fragments or peptides [39,40].

Despite nontrivial identification of experimental fluorescence energies ($\Delta E_{\mathrm{FL\text{-}exp}}$), their correlation with the theoretically calculated TD-B3YP de-excitation energies ($E_{\mathrm{de\text{-}exc,\ B3LYP}}$) leads to a statistically relevant linear dependence (Fig. 4Sb)

$$\Delta E_{\mathrm{FL-exp}} \,/\, \mathrm{eV} = 0.731 + 0.741 \times \Delta E_{\mathrm{de-exc,\ B3LYP}} \qquad (2)$$

Despite only a few points, the correlation coefficient is 0.97. Analogously to the vertical excitation energies, Eq. (2) can be used for the estimation of experimentally relevant fluorescence energies for non-synthesized dyes. We used the model for the studied molecules as well to correlate experimental energies. These correlated lowest de-excitation LUMO to HOMO transition energies are depicted as

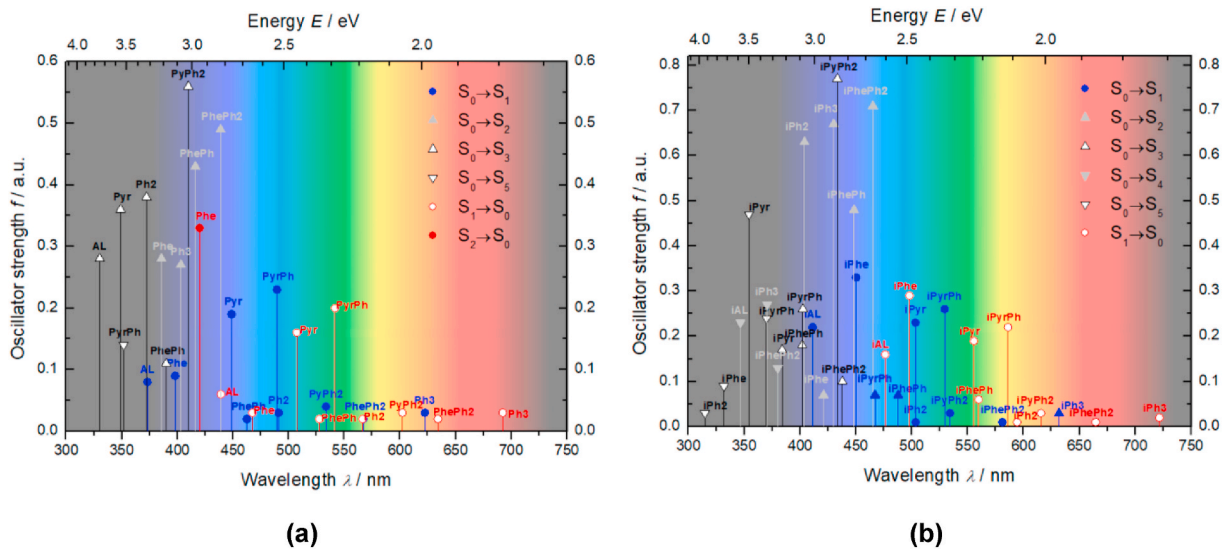

Fig. 4. The selected theoretical TD-B3LYP(DMSO) excitation and de-excitation lowest energy transitions calculated for studied alloxazine-type N(1)H-tautomers(a) and iso-N(10)H-tautomers (b).

illustration with colorful visible spectrum in Fig. 4a. Corresponding iso-tautomers are collected in Fig. 4b. Small oscillator strengths were found for the compounds with linearly condensed aromatic rings. On the other hand, molecules with a two-dimensional π-conjugated pyrene moiety fused to the central core exhibit high oscillator strengths up to 0.29 for **iPhe** (see also Table 4S).

4. Conclusions

The optimal geometries and electronic structure of (iso)alloxazine and eight condensed alloxazine derivatives were investigated using the Density Functional Theory. The local aromaticity of benzo[g]pteridine core was described using the HOMED aromaticity indices and the influence of chemical structure on the static dipole moment was discussed. We have shown that the consecutive addition of aromatic rings could lead to an increase of static dipole moments by about 2 D with respect to the parent **AL**. On the other hand, the aromaticity of the A, B, and C rings is changed minimally. The TD-B3LYP calculations of optical transitions predicted that many of the studied derivatives can absorb and emit light in the visible spectral range. Although the theoretical absorption and emission energies are shifted with respect to the experiment, the obtained linear correlations for B3LYP functional can be used for the prediction of experimentally relevant values for molecules in DMSO before synthesis.

Analysis of the results provides a decreasing oscillator strength caused by linear elongation of the molecular structure. Opposite to that is two-dimensional enlargement of the chain (variation with pyrene or phenanthrene moiety) which has more significant oscillator strengths for both absorption and emission transitions; thus, well defined vertical excitation energies and fluorescence maxima. In the case of the longest chains with 2D-end, **(i)PyrPh** and **(i)PhePh2**, the effect of benzo[g] pteridine moiety is suppressed and the influence of pyrene or phenanthrene unit is more pronounced. However, additional rings in 2D structure would have negligible effect to optical properties improvement. The theoretical calculations indicated that the **(i)Phe** and **Pyr** have properly separated lowest excited state energy and the corresponding π-π* transition has a significant oscillator strength; thus, they were considered to be the most potential for the practical application. The experimental fluorescence wavelengths maxima are at 428, 504 for **(i)Phe** and 508 nm for **Pyr**. To conclude, based on experimental spectra we proved, that alkaline DMSO causes iso-tautomer signal increasing. The biological origin of the benzo[g]pteridine moiety may support its incorporation into other biomolecules. Obtained theoretical results might be helpful for experimentalists to prepare potentially suitable organic molecules for novel bio-inspired materials applicable in biology or molecular sensor construction.

Declaration of competing interest

The authors declare that they have no known competing financial interests or personal relationships that could have appeared to influence the work reported in this paper.

Acknowledgment

The work has been supported by Slovak Research and Development Agency (APVV-19-0024) and VEGA 1/0461/21. V.L. thanks to Ministry of Education, Science, Research and Sport of the Slovak Republic for funding within the scheme “Excellent research teams”. We are grateful to the HPC center at the Slovak University of Technology in Bratislava, which is a part of the Slovak Infrastructure of High Performance Computing (SIVVP project, ITMS code 26230120002, funded by the European region development funds, ERDF) for the computational time and resources made available. The research was supported by Czech Science Foundation project 17–24707 S. J.T. thanks to the internal grant FCH–S-20-6340 of the Brno University of Technology. Computational resources were supplied by the project “e-Infrastruktura CZ” (e-INFRA LM2018140) provided within the program Projects of Large Research, Development and Innovations Infrastructures. D.C. would like to thank for support from the STU Grant scheme for Support of Young Researchers (1848).

Appendix A. Supplementary data

Supplementary data to this article can be found online at https://doi.org/10.1016/j.optmat.2021.111205.

Author agreement statement

All authors declare that this manuscript is original, has not been published before and is not currently being considered for publication elsewhere. We confirm that the manuscript has been read and approved by all named authors and that there are no other persons who satisfied the criteria for authorship but are not listed. We further confirm that the

order of authors listed in the manuscript has been approved by all of us. We understand that the Corresponding Author is the sole contact for the Editorial process. She is responsible for communicating with the other authors about progress, submissions of revisions and final approval of proofs.

References

[1] P. Mondal, K. Schwinn, M. Huix-Rotllant, Impact of the redox state of flavin chromophores on the UV-vis spectra, redox and acidity constants and electron affinities, J. Photochem. Photobiol., A 387 (2019) 112164, https://doi.org/10.1016/j.jphotochem.2019.112164.

[2] C.M. Marian, S. Nakagawa, V. Rai-Constapel, B. Karasulu, W. Thei, Photophysics of flavin drivatives absorbing in the blue-green region: thioflavins as potential cofactors of photoswitches, J. Phys. Chem. B 118 (2014) 1743–1753, https://doi.org/10.1021/jp4098233.

[3] A. Kormányos, M.S. Hossain, G. Ghadimkhani, J.J. Johnson, C. Janáky C, N.R. de Tacconi, F.W. Foss, Y. Paz, K. Rajeshwar, Flavin derivatives with tailored redox properties: synthesis, characterization, and electrochemical behavior, Chem. Eur J. 22 (2016) 9209–9217, https://doi.org/10.1002/chem.201600207.

[4] M. Bracker, F. Dinkelbach, O. Weingart, M. Kleinschmidt, Impact of fluorination on the photophysics of the flavin chromophore: a quantum chemical perspective, Phys. Chem. Chem. Phys. 21 (2019) 9912–9923, https://doi.org/10.1039/C9CP00805E.

[5] M. Irimia-Vladu, A.T. Pavel, M. Reisinger, L. Shmygleva, Y. Kanbur, G. Schwabegger, M. Bodea, R. Schwodiauer, A. Mumyatov, J.W. Fergus, V. F. Razumov, H. Sitter, N.S. Sariciftci, S. Bauer, Biocompatible and biodegradable materials for organic field-effect transistors, Adv. Funct. Mater. 20 (2010) 4069–4076, https://doi.org/10.1002/adfm.201001031.

[6] K. Lin, R. Gómez-Bombarell, E.S. Beh, L. Tong, Q. Chen, A. Valle, A. Aspuru-Guzik, M.J. Gaziz, R.G. Gordon, A redox-flow battery with an alloxazine-based organic electrolyte, Nat. Energy. 1 (2016) 16102, https://doi.org/10.1038/NENERGY.2016.102.

[7] E. Sikorska, I.V. Khmelinskii, D.R. Worrall, J. Koput, M. Sikorski, Spectroscopy and photophysics of iso- and alloxazines: experimental and theoretical study, J. Fluoresc. 14 (2004) 57–64, https://doi.org/10.1023/b:jofl.0000014660.59105.31.

[8] A. Penzkofer, Absorption and emission spectroscopic investigation of alloxazine in aqueous solutions and comparison with lumichrome, J. Photochem. Photobiol., A 314 (2016) 114–124, https://doi.org/10.1016/j.jphotochem.2015.08.011.

[9] M. Mal, D. Mandal, Solvent and pH-sensitive fluorescence response of alloxazine, J. Photochem. Photobiol., A 404 (2021) 112888, https://doi.org/10.1016/j.jphotochem.2020.112888.

[10] P.S. Song, M. Sun, A. Koziolowa, J. Koziol, Photo tautomerism of lumichromes and alloxazines, J. Am. Chem. Soc. 96 (1974) 4319–4323, https://doi.org/10.1021/ja00820a045.

[11] A. Koziolowa, Solvent and methyl substituent effect on phototautomerism and ionization of alloxazines, Photochem. Photobiol. 29 (1978) 459–471, https://doi.org/10.1111/j.1751-1097.1979.tb07076.x.

[12] S.D. Choudhury, H. Pal, Intriguing tautomerism of lumichrome in binary aqueous solvent mixtures: implications for probing microenvironments, J. Phys. Chem. 120 (2016) 11970, https://doi.org/10.1021/acs.jpcb.6b08777.

[13] A. Tyagi, A. Penzkofer, Absorption and emission spectroscopic characterization of lumichrome in aqueous solutions, Photochem. Photobiol. 87 (2010) 524–533, https://doi.org/10.1111/j.1751-1097.2010.00836.x.

[14] K. Sakai, K. Nagahara, Y. Yoshii, N. Hoshino, T. Akutagawa, Structural and spectroscopic study of 6,7-dicyano-substituted lumazine with high electron affinity and proton acidity, J. Phys. Chem. 117 (2013) 3614–3624, https://doi.org/10.1021/jp401528c.

[15] S.D. Choudhury, P. Vir, J. Mohanty, A.C. Bhasikuttan, H. Pal, Selective prototropism of lumichrome in cationic micelles and reverse micelles: a photophysical perspective, RSC Adv. 6 (2016) 6111–6124, https://doi.org/10.1039/C5RA23562F.

[16] D. Prukała, E. Sikorska, J. Koput, I. Khmelinskii, J. Karolzcak, M. Gierszewski, M. Sikorski, Acid−Base equilibriums of lumichrome and its 1-methyl, 3-methyl, and 1,3-dimethyl derivatives, J. Phys. Chem. 116 (2012) 7474–7490, https://doi.org/10.1021/jp300522h.

[17] J. Richtar, P. Heinrichova, D.H. Apaydin, V. Schmiedova, C. Yumusak, A. Kovalenko, M. Weiter, N.S. Sariciftci, J. Krajcovic, Novel riboflavin-inspired conjugated bio-organic semiconductors, Molecules 23 (2018) 2271, https://doi.org/10.3390/molecules23092271.

[18] J. Richtar, L. Ivanova, D.R. Whang, C. Yumusak, D. Wielend, M. Weiter, M. C. Scharber, A. Kovalenko, N.S. Sariciftci, J. Krajcovic, Tunable properties of nature-inspired N,N′-Alkylated riboflavin semiconductors, Molecules 26 (2021) 27, https://doi.org/10.3390/molecules26010027.

[19] M.J. Frisch, G.W. Trucks, H.B. Schlegel, G.E. Scuseria, M.A. Robb, J.R. Cheeseman, G. Scalmani, V. Barone, G.A. Petersson, H. Nakatsuji, X. Li, M. Caricato, A. V. Marenich, J. Bloino, B.G. Janesko, R. Gomperts, B. Mennucci, H.P. Hratchian, J. V. Ortiz, A.F. Izmaylov, J.L. Sonnenberg, D. Williams-Young, F. Ding, F. Lipparini, F. Egidi, J. Goings, B. Peng, A. Petrone, T. Henderson, D. Ranasinghe, V. G. Zakrzewski, J. Gao, N. Rega, G. Zheng, W. Liang, M. Hada, M. Ehara, K. Toyota, R. Fukuda, J. Hasegawa, M. Ishida, T. Nakajima, Y. Honda, O. Kitao, H. Nakai, T. Vreven, K. Throssell, J.A. Montgomery Jr., J.E. Peralta, F. Ogliaro, M. J. Bearpark, J.J. Heyd, E.N. Brothers, K.N. Kudin, V.N. Staroverov, T.A. Keith, R. Kobayashi, J. Normand, K. Raghavachari, A.P. Rendell, J.C. Burant, S.S. Iyengar, J. Tomasi, M. Cossi, J.M. Millam, M. Klene, C. Adamo, R. Cammi, J.W. Ochterski, R.L. Martin, K. Morokuma, O. Farkas, J.B. Foresman, D.J. Fox, Gaussian, Inc., Wallingford CT, 2016.

[20] C. Lee, W. Yang, R.G. Parr, Development of the Colle-Salvetti correlation-energy formula into a functional of the electron density, Phys. Rev. B 37 (1988) 785–789, https://doi.org/10.1103/PhysRevB.37.785.

[21] A.D. Becke, Density-functional exchange-energy approximation with correct asymptotic behaviour, Phys. Rev. A 38 (1998) 3098–3100, https://doi.org/10.1103/10.1103/PhysRevA.38.3098.

[22] P.C. Hariharan, J.A. Pople, The influence of polarization functions on molecular orbital hydrogenation energies, Theor. Chim. Acta 28 (1973) 213–222, https://doi.org/10.1007/BF00533485.

[23] V.A. Rassolov, J.A. Pople, M.A. Ratner, T.L. Windus, 6-31G*basis set for atoms K through Zn, J. Chem. Phys. 109 (1998) 1223–1229, https://doi.org/10.1063/1.476673.

[24] F. Furche, R. Ahlrichs, Adiabatic time-dependent density functional methods for excited state properties, J. Chem. Phys. 117 (2002) 7433, https://doi.org/10.1063/1.1508368.

[25] T. Yanai, D. Tew, N. Handy, A new hybrid exchange-correlation functional using the Coulomb-attenuating method (CAM-B3LYP), Chem. Phys. Lett. 393 (2004) 51–57, https://doi.org/10.1016/j.cplett.2004.06.011.

[26] S. Salzmann, M.C. Marian, The photophysics of alloxazine: a quantum chemical investigation in vacuum and solution, Photochem. Photobiol. Sci. 8 (2009) 1655–1666, https://doi.org/10.1039/b9pp00022d.

[27] A.V. Marenich, C.J. Cramer, D.G. Truhlar, Universal solvation model based on solute electron density and a continuum model of the solvent defined by the bulk dielectric constant and atomic surface tensions, J. Phys. Chem. B 113 (2009) 6378–6396, https://doi.org/10.1021/jp810292n.

[28] S. Grimme, S. Ehrlich, L. Goerigk, Effect of damping function in dispersion corrected density functional theory, J. Comput. Chem. 32 (2011) 1456–1465, https://doi.org/10.1002/jcc.21759.

[29] P. Flukiger, H.P. Luthi, S. Sortmann, J. Weber, Molekel 4.3, Swiss National Supercomputing Centre, Manno, Switzerland, 2002.

[30] M.D. Hanwell, D.E. Curtis, D.C. Lonie, T. Vandermeersch, E. Zurek, G.R. Hutchison, " Avogadro, An advanced semantic chemical editor, visualization, and analysis platform, J. Cheminf. 4 (2012), https://doi.org/10.1186/1758-2946-4-17.

[31] M.K. Cyrański, T.M. Krygowski, A.R. Katritzky, P. von R. Schleyer, To what extent can aromaticity Be defined uniquely? J. Org. Chem. 67 (2002) 1333–1338, https://doi.org/10.1021/jo016255s.

[32] C.P. Frizzo, M.A. P Martins, Aromaticity in heterocycles: new HOMA index parametrization, Struct. Chem. 23 (2012) 375–380, https://doi.org/10.1007/s11224-011-9883-z.

[33] B. Ośmiałowski, E.D. Raczyńska, T.M. Krygowski, Tautomeric equilibria and pi electron delocalization for some monohydroxyarenes – quantum chemical studies, J. Org. Chem. 71 (2006) 3727–3736, https://doi.org/10.1021/jo052615q.

[34] F.H. Allen, O. Kennard, D.G. Watson, L. Brammer, A.G. Orpen, R. Taylor, Tables of bond lengths determined by X-ray and neutron diffraction. Part 1. Bond lengths in organic compounds, J. Chem. Soc. Perkin Trans. 2 (1987) 12, https://doi.org/10.1039/p298700000s1. S1–S19.

[35] Agilent Technologies, Inc. CaryWinUV Software, Santa Clara, California, USA, 2020.

[36] Horiba Instruments Incorporated, FluorEssence Software, Minami-ku Kyoto, Japan, 2019.

[37] C. Párkányi, J.J. Aaron, Dipole moments of aromatic heterocycles, Theoretical and Computational Chemistry 5 (1998) 233–254, https://doi.org/10.1016/S1380-7323(98)80011-3.

[38] A. Penzkofer, Absorption spectroscopic determination of solubility of alloxazine in aqueous solutions, J. Anal. Sci. Methods Instrum. 5 (2015) 13–21, https://doi.org/10.4236/jasmi.2015.52002.

[39] B.A. Anderson, J.J. Onley, P.J. Hrdlicka, Recognition of double-stranded DNA using energetically activated duplexes modified with N2'-pyrene-, perylene-, or coronene-functionalized 2'-N-Methyl-2'-amino-DNA monomers, J. Org. Chem. 80 (2015) 5395–5406, https://doi.org/10.1021/acs.joc.5b00742.

[40] G. Bains, A.B. Patel, V. Narayanaswami, Pyrene: a Probe to study protein conformation and conformational changes, Molecules 16 (2011) 7909–7935, https://doi.org/10.3390/molecules16097909.

sciendo

Theoretical modeling of optical spectra of N(1) and N(10) substituted lumichrome derivatives

Denisa Cagardová[1], Jan Truksa[2], Martin Michalík[1], Jan Richtár[2], Jozef Krajčovič[2], Martin Weiter[2], Vladimír Lukeš[1]

[1]Institute of Physical Chemistry and Chemical Physics, Slovak University of Technology in Bratislava, Radlinského 9, SK-812 37 Bratislava, Slovakia
[2]Faculty of Chemistry, Brno University of Technology, Purkyňova 118, CZ-612 00 Brno, Czech Republic
denisa.cagardova@stuba.sk

Abstract: A systematic study of (7,8-dimethylated) alloxazine, isoalloxazine, and their derivatives with substituted N(1) and N(10) positions was conducted using the density functional theory. The main aim of this work was the direct investigation of substituent effect on the molecular structure. Furthermore, HOMED aromaticity indices were calculated to describe the scope of the geometry changes. Frontier molecular orbitals of reference alloxazine, isoalloxazine and lumichrome derivatives were discussed by means of changes in their shape and energy levels. Photophysical properties were analyzed by determination of optical transition energies using the TD-DFT method. Obtained results were compared with previously published experimental data.

Keywords: Aromaticity index; vertical excited transitions; excited states; fluorescence; lumichrome; alloxazine

Introduction

Photochemical and photophysical properties of alloxazine and its derivatives have been studied since 1966 (Kozioł, 1966). Methyl-substituted alloxazines, mainly riboflavin and lumichrome are present in many foods and they play a key role in many enzymatic reactions and processes such as phototropism and phototaxis (Ai et al., 2010). Although the parent alloxazine and isoalloxazine are closely related compounds (see Fig. 1), the shift of a hydrogen atom from position N(1) to N(10) causes

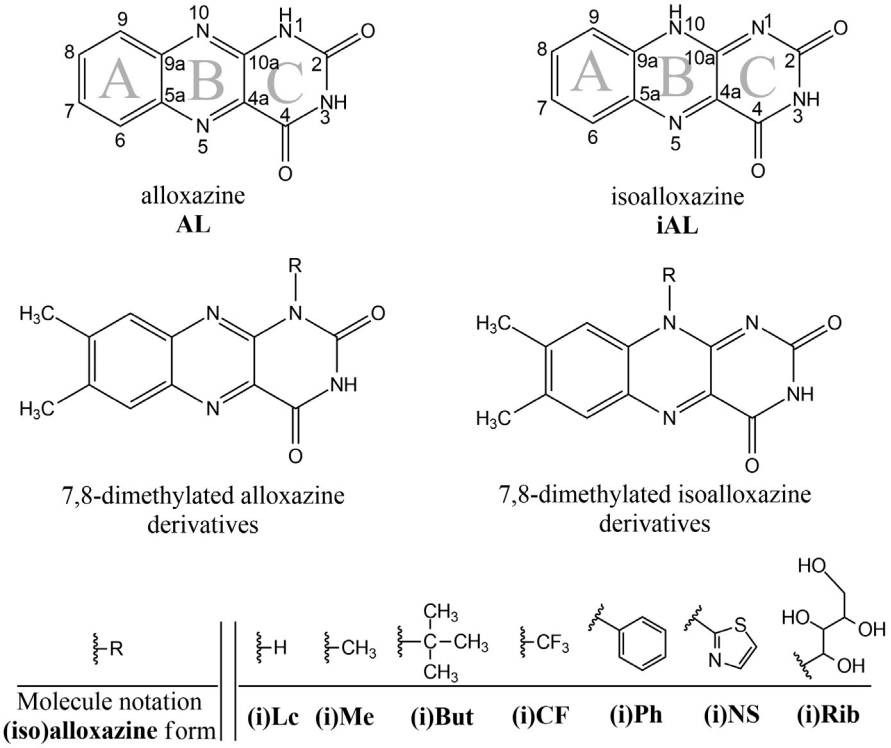

Fig. 1. Schematic structure of studied molecules: ring and atom notation of the benzo[g]pteridine moiety applied for all derivatives.

significant changes in their spectroscopic and photophysical properties.

Alloxazine exhibits absorption spectra differing from those of isoalloxazine by a hypsochromic shift of both long-wavelength maxima from about 440 nm and 340 nm to about 380 nm and 330 nm (Sikorska et al., 2004a). Moreover, isoalloxazine exhibits one order of magnitude larger fluorescence quantum yields and correspondingly longer fluorescence lifetimes than alloxazine. At pH = 10, the presence of isoalloxazine (9 %) is expected while at pH = 4, the solution does not contain the tautomeric isoalloxazine form (Penzkofer, 2016). The fluorescence wavelength maximum of an alloxazine sample in an aqueous solution at pH = 4 for fluorescence excitation wavelength λ_{exc} = 330 nm is 456 nm. At pH = 10, the emission wavelength of 530 nm is observed for the fluorescence excitation wavelength λ_{exc} = 440 nm. The first absorption bands of alloxazine and lumichrome show minimal environmental dependence. A significant effect of polarity and proticity of the solvent was observed for their second absorption band (Salzmann and Marian, 2009). Surprising differences between these two molecules were found in the absorption strength, fluorescence lifetime, fluorescence quantum yield, and thermal ground-state tautomeric content at pH = 10. The absorption spectrum of riboflavin and iso-(6,7)-riboflavin in methanol shows two characteristic bands at longer wavelengths, with the maxima at approximately 360 nm and 444 nm for riboflavin; and at 343 nm and 447 nm for iso-(6,7)-riboflavin, which indicates the effect of the methyl group position on the shorter-wavelength maximum. The effect of methyl group on the positions of absorption maxima was examined by Sikorska et al. using both experiment and theory with a broad range of (iso)alloxazine derivatives (Sikorska et al., 2004b; Sikorska et al., 2004c).

Available information about the chemical and electronic structure of (iso)7,8-dimethyl-alloxazine substituted in position N(1) or N(10) is incomplete. Previous experimental and theoretical studies of these compounds were focused on two substituents — methyl and 2,3,4,5-tetrahydroxypentyl groups (Gross et al., 1996; Sikorska et al., 2005; Zanetti-Polzi et al., 2017). Therefore, theoretical analysis of 14 derivatives based on the modification of the initial benzo[g]pteridine moiety in (iso) alloxazine by 7,8-dimethylation and substitution in N(1) or N(10) positions (Fig. 1) is presented here. In laboratory practice, the selected functional groups can be synthetically added to the benzo[g]pteridine moiety into selected positions. Partial aims of this study are: (1) to calculate optimal geometries of the electroneutral molecules and selected lowest energy excited electronic states; (2) to evaluate the energies of frontier molecular orbitals (MOs) and (3) to calculate optical transitions contributing to the lowest energy in absorption and fluorescence spectra.

Computational details

The Gaussian 09 program package (Frisch et al., 2013) was applied for all quantum chemical calculations by means of the density functional theory. In these calculations, the B3LYP hybrid functional (Lee et al., 1988; Becke, 1988) without any constraints (energy cut-off of 10^{-5} kJ · mol^{-1}, final RMS energy gradient under 0.01 kJ · mol^{-1} · A^{-1}) was used. A sufficiently large basis set of atomic orbitals 6-311++G** was applied (Hariharan and Pople, 1973; Rassolov et al., 1998). In search of optimized B3LYP geometries, the time dependent TD-DFT method was used. As a result, vertical singlet and triplet transition energies and the corresponding oscillator strengths between the initial and final electronic states were determined (Furche and Ahlrichs, 2002). The molecules and their frontier molecular orbitals were visualized using the Molekel (Flukiger et al., 2002) and Avogadro (Hanwell et al., 2012) program packages.

Aromaticity of molecules gives significant information about their chemical structure. One way to describe aromaticity is the structure-based Harmonic Oscillator Model of Electron Delocalization (HOMED) index (Cyrañski et al., 2002; Frizzo and Martins, 2012), which describes the bond length changes in molecules of interest with respect to the reference aromatic molecules. The index can be calculated by the equation:

$$\mathrm{HOMED} = 1 - \frac{1}{m}\left\{\alpha_{XY}\sum_{i=1}^{m}\left(R(XY)_{ref} - R(XY)_i\right)^2\right\} \qquad (1)$$

where m stands for the number of bonds considered in the investigated aromatic ring, $R(XY)_{ref}$ is the reference bond length, α_{XY} is a normalization constant (see below) and $R(XY)_i$ is the actual bond length between X and Y atoms.

In case of the studied derivatives, C—C, C—N and C—N(H) aromatic bond lengths were determined. Suitable reference quantities, R_{ref}, used in Eq(1) were obtained from the B3LYP/6-311++G** optimized structures of benzene, 1,3,5-triazine and pyrrole molecules for CC, CN and CN(H) bonds, respectively. The proposed R_{ref} values for the basis set are: 1.3943 Å ($R(CC)_{ref}$), 1.3344 Å ($R(CN)_{ref}$) and 1.3749 Å ($R(CN(H))_{ref}$). Normalization constants α_{XY} were calculated as follows (Ośmiałowski et al., 2006):

$$\alpha(XY) = \qquad (2)$$
$$= 2\left\{\left(R(XY)_{ref} - R(XY)_{sin}\right)^2 + \left(R(XY)_{ref} - R(XY)_{doub}\right)^2\right\}^{-1}$$

where the reference single R_{sin} and double R_{doub} bond lengths were taken from the optimized structures of ethane and ethene (CC bonds), N—$(CH_3)_3$ and H_2C=N—CH_3 (CN bonds), $(H_3C)_2$—NH and H_2C=NH (CN(H) bonds) molecules, respectively (Allen et al., 1987). The calculated B3LYP R_{sin} bond lengths are: 1.5317 Å (C—C), 1.4554 Å (C—N) and 1.4574 Å for the C—N(H) bond. Moreover, the double bond lengths R_{doub} of 1.3289 Å (C=C), 1.2631 Å (C=N) and 1.2672 Å (C=N(H)) were used to determine α_{XY} from Eq(2). The corresponding normalization constants are: α(CC) = 86.40 Å^{-2}, α(CN) = 101.41 Å^{-2} and α(CN(H)) = 108.66 Å^{-2}. The maximal HOMED value of one was assigned to the benzene molecule by convention.

Results and Discussion

Although isobutyl, methyl, trifluoromethyl, thiazole, and 2,3,4,5-tetrahydroxypenthyl substituents show many conformations, chemical structure of the benzo[g]pteridine core is not affected significantly. As seen in Tab. 1, HOMED(A) indices of the isoalloxazine form are consistently by ca. 0.04 higher than those of the alloxazine counterparts. Moreover, dimethylation in C(7) and C(8) positions causes a decrease in the A ring aromaticity (see **Lc**/**iLc**), while additional substitutions slightly increase the HOMED(A).

With respect to the parent **AL** and **iAL** molecules, the HOMED(C) index is much lower for the isoalloxazine derivatives than for the alloxazine forms, with exception of (**i**)**NS**, (**i**)**CF** and (**i**)**But** tautomer couples. This effect is the most significant for **CF** and **But**, possibly because CF_3 is a strongly electron-withdrawing group and tert-butyl group is relatively bulky and electron-donating group with much higher positive inductive effect than the methyl group in **Me**. They cause the most significant decrease in the aromaticity possibly because of the distortion due to steric repulsion and strong inductive effect. **NS** contains larger atoms than carbon, so some steric distortion is expected, but it is smaller due to the two-dimensional nature of the ring. Moreover, in case of substituted rings, the comparison is complicated by the fact that the substituents in tautomers are present on different rings. Therefore, it makes more sense to compare the substitution effect of the C ring in the alloxazine form to the B ring in isoalloxazine form and vice versa (see Fig. 1). Two methyl groups attached to the A ring in **Lc** and **iLc** cause an increase of HOMED for both B and C rings. Additional substitution to the B (C) ring of **iLc** (**Lc**) significantly decreases the aromaticity of the substituted ring. Relative changes correspond to the differences between HOMED of the studied molecule and the reference alloxazine/isoalloxazine molecule divided by the HOMED of reference. Relevant changes of HOMED indices in comparison to alloxazine and isoalloxazine molecules are shown in Fig. 2. Note that all studied derivatives, apart from two methyl groups at C(7) and C(8) atoms such as lumichrome **Lc,** have also another additional substituent. Thus, the B and/or C ring substitution effect is cumulative with respect to the two methyl groups. These side methyl groups bonded to the A ring increase the aromaticity by up to 2 % for both (un)substituted rings in tautomers.

In case of the HOMED index of substituted rings, i.e. C ring of alloxazine derivative and B ring of iso-form, all studied additional substituents decrease their aromaticity (see Tab. 1 and Fig. 2a). The bond length changes caused by the presence of a double bond in the C ring of the iso-form also affect HOMED(C), which is more likely to be visible in molecules with smaller or linear substituents. A similar case may be argued for the HOMED(B) index of isoalloxazine derivatives where the ring lacks a double bond and is influenced by the substituent which leads to a significant distortion of geometry. The largest decrease of around 30 % has been found for the **CF**/**iCF** derivatives while butyl group brings the HOMED indices down by 18 %. It occurs mainly by exceptional ring distortion due to CF_3 because of the above-mentioned strong electron-withdrawing

Tab. 1. HOMED indices of A, B and C rings of studied molecules.

Molecule	A	B	C	Molecule	A	B	C
AL	0.942	0.924	0.814	**iAL**	0.983	0.867	0.664
Lc	0.930	0.934	0.821	**iLc**	0.975	0.880	0.678
Me	0.934	0.933	0.724	**iMe**	0.975	0.798	0.690
But	0.938	0.928	0.668	**iBut**	0.975	0.735	0.680
CF	0.932	0.938	0.585	**iCF**	0.982	0.668	0.645
Ph	0.933	0.934	0.696	**iPh**	0.975	0.784	0.683
NS	0.932	0.935	0.671	**iNS**	0.977	0.763	0.677
Rib	0.936	0.933	0.723	**iRib**	0.974	0.794	0.695

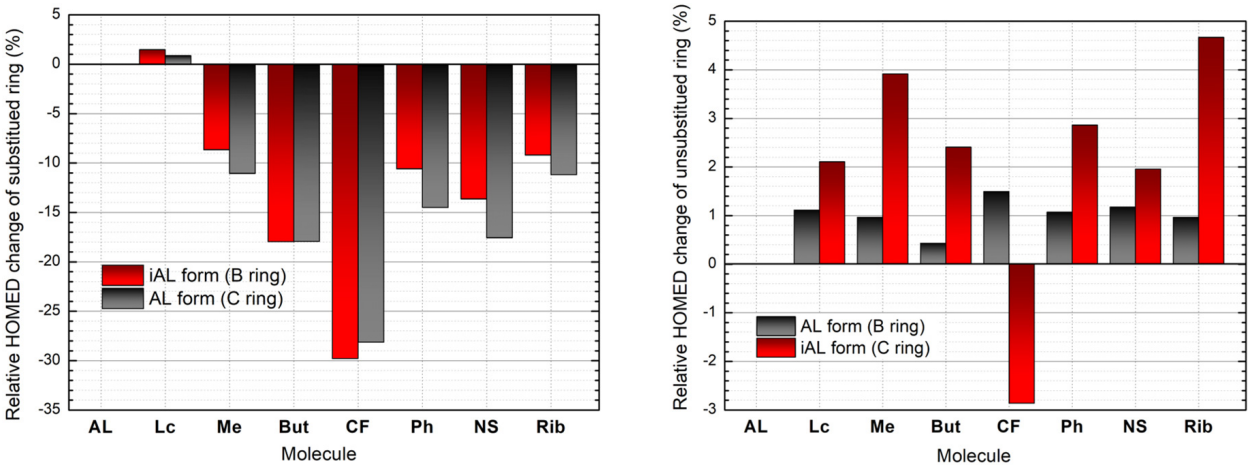

Fig. 2. Relative changes of HOMED indices of a) substituted C/B ring and b) unsubstituted B/C ring of alloxazine/isoalloxazine derivatives.

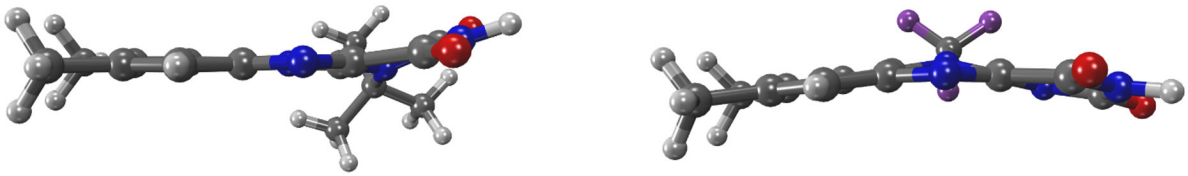

But iCF

Fig. 3. Distortion of rings observable in optimal geometry of **But** and **iCF**.

effect of the group and bulky tert-butyl substituent (e.g. see **But** and **iCF** ring distortion in Fig. 3).

Based on Fig. 2a, the smallest changes of aromaticity in the substituted rings in comparison to their parent (iso)alloxazine molecules are caused by the methyl group in **(i)Me**. Large 2,3,4,5-tetrahydroxypentyl substituent in **(i)Rib** had minimal influence on the HOMED indices. These comparatively small relative changes in HOMED indicate less significant substituent influence (up to 12 %) than the remaining additional substituents, which supports the above-mentioned steric effect hypothesis and small inductive effect.

In heterocyclic rings without a substituent (see Fig. 2b), i.e. B ring of alloxazine and C ring of isoalloxazine, small substituent-induced HOMED increase of up to 5 %, with exception for **iCF,** can be seen. Interestingly, isoalloxazine forms are much more affected; however, it is still considered to be negligible in comparison to HOMED changes of substituted ring. Based on these results, the **iCF** derivative is the least stable within the studied group as the trifluoromethyl group consistently decreases the aromaticity, as evaluated by HOMED indices.

Energy levels of frontier molecular orbitals and their shape allow estimating the electronic structure. Fig. 4 shows energy levels of the highest occupied (HOMOs) and lowest unoccupied (LUMOs) molecular orbitals. The B3LYP HOMO and LUMO energies for alloxazine **AL**/isoalloxazine **iAL** are: –7.18 eV/–7.04 eV and –3.17 eV/–3.53 eV, respectively. In case of two methyl groups addition to C(7) and C(8) in **Lc/iLc**, a slight increase of both HOMO (–6.91 eV/–6.76 eV) and LUMO (–2.97 eV/–3.34 eV) energies can be seen, so the constriction of energy gap occurs. The substitution group variation alters the orbital energies in different ways.

Methyl (**Me/iMe**), butyl (**But/iBut**), phenyl (**Ph/iPh**), and 2,3,4,5-tetrahydroxypentyl (**Rib/iRib**) functional groups have comparable influence on the energies of frontier MOs. Differences are found only between the alloxazine and isoalloxazine forms. Isoalloxazine forms generally have smaller HOMO to LUMO energy difference. Minimal LUMO energy of –3.66 eV was found for the **iCF** derivative. The highest B3LYP HOMO energy is predicted for **iRib** (–6.33 eV) while the **CF** molecule exhibited the lowest one of –7.23 eV.

As it is depicted in Fig. 5, frontier MOs are delocalized over the whole molecule in all cases indicating an effective π-conjugation in the central fused systems. HOMO and LUMO orbitals of the studied molecules have a π-electron character, but the electron clouds are not as uniformly delocalized as in the parent alloxazine and isoalloxa-

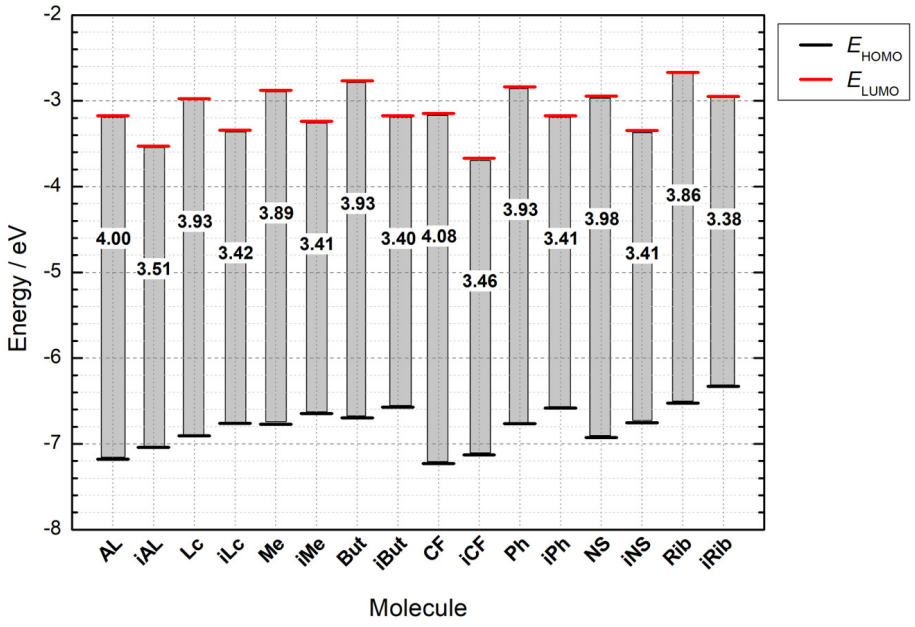

Fig. 4. Energy diagram of B3LYP frontier molecular orbitals for the neutral state of studied molecules. Energy differences between the frontier molecular orbital levels are depicted by grey rectangles and the value corresponds to the energy gap in eV.

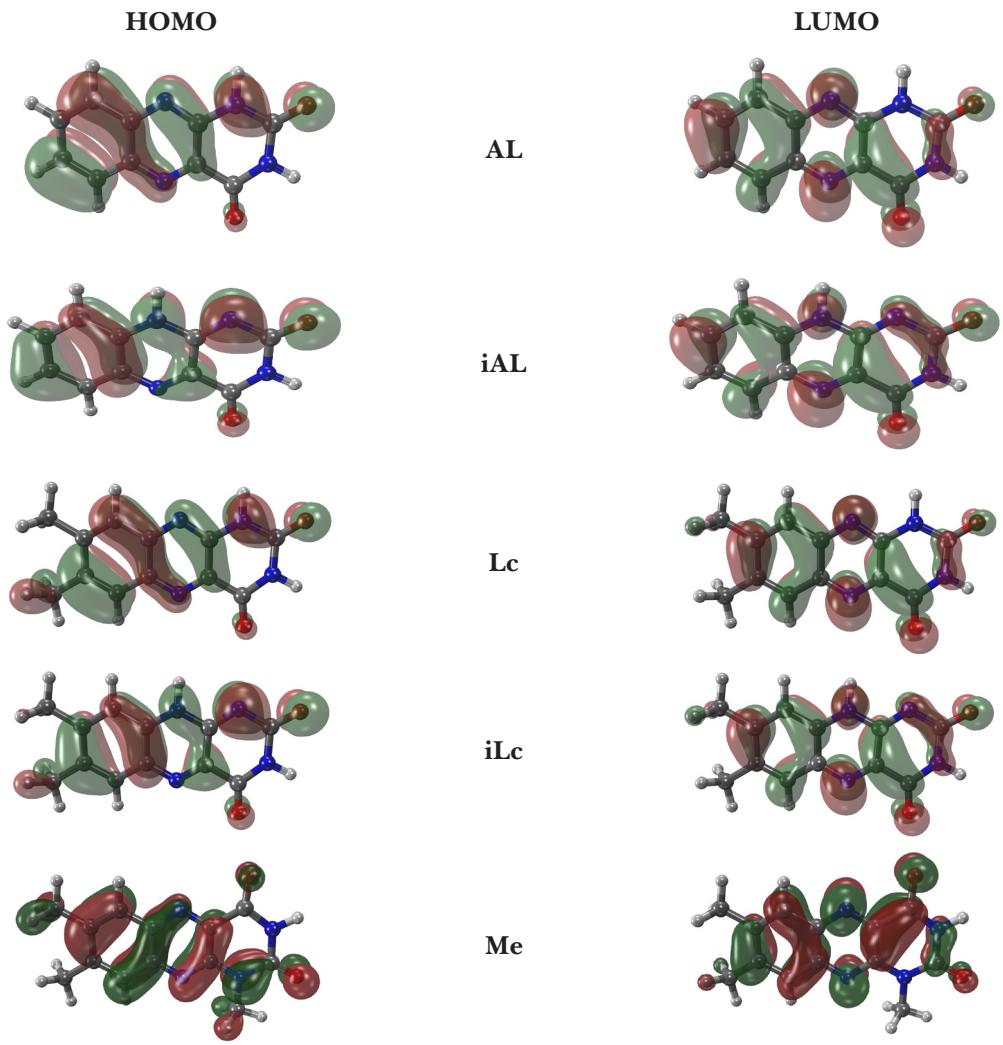

Fig. 5. Shapes of frontier molecular orbitals of studied molecules. Iso-surface value is 0.025.

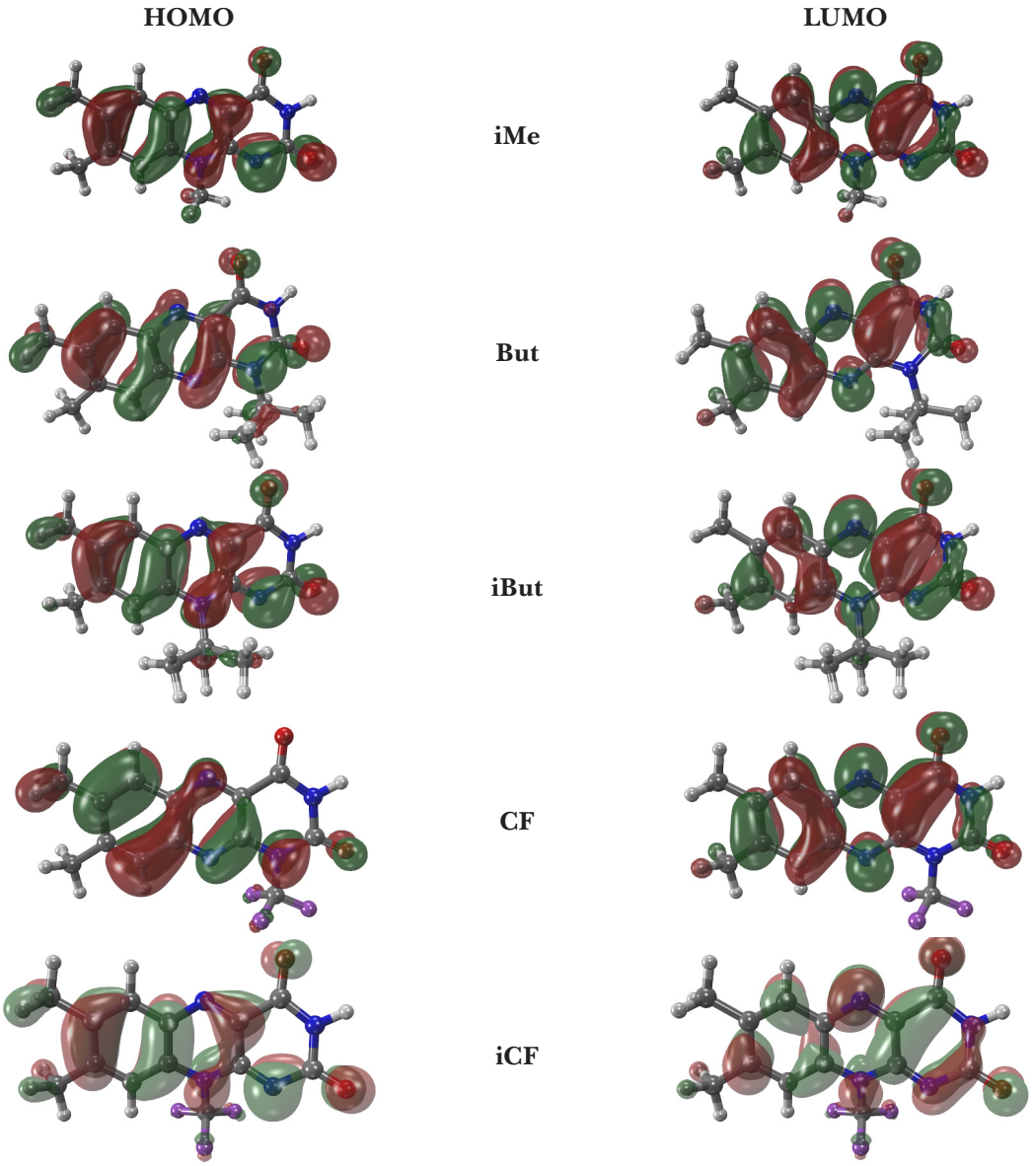

Fig. 5. (continued) Shapes of frontier molecular orbitals of studied molecules. Iso-surface value is 0.025.

zine molecules. Shapes of the orbitals are modulated by the bonding of methyl groups in C(7) and C(8) positions and by the additional studied substitution. Nevertheless, for all studied molecules, the lobes of HOMOs are absent over the C(2) atom and they are present over the methyl group in the vicinity of the C(7) atom. Interestingly, very small electronic clouds were found over the fluorine atoms in (**i**)**CF** and hydrogen atoms in additional methyl group in (**i**)**Me** derivatives. The electron withdrawing CF_3 group also causes an electron cloud formation over the hydrogens of the CH_3-C(7) group and another cloud above CH_3-C(8) occurs in its iso-tautomer. In case of LUMO lobes, distribution of isoalloxazine derivatives, clouds are mostly delocalized over the whole benzo[g]pteridine moiety. On the other hand, molecules in the alloxazine form show lower delocalization over the N(1) nitrogen which is attached to the substituted functional group.

Parent (iso)alloxazine molecules and their alkyl substituted derivatives exhibit experimental absorption spectra with several major bands in the ultraviolet-visible region. For example, the first experimental band maxima of **AL** (Sikorska et al., 2004a) and **Lc** (Sikorski et al., 1998) in aqueous solution are found at 3.27 eV (379 nm) and 3.22 eV (385 nm), respectively. The second absorption band is located at 3.87 eV (320 nm) for alloxazine and at 3.71 eV (334 nm) for lumichrome (**Lc**). Comparison of the lowest vertical gas-phase TD-B3LYP energies for the singlet states is provided in Fig. 6. For alloxazine, energy of the first excited vertical singlet state (S_1) over the electronic ground state is 3.38 eV (367 nm). The corresponding oscillator strength is negligible. This forbidden excitation comes from

an n-type molecular orbital to π*-type HOMO–2 to LUMO transition. The second excited singlet state, related to the HOMO to LUMO transition, is merely 0.06 eV above the S_1 state with $^1(\pi\pi^*)$ character. According to the previously published results, the third excited singlet state (S_3) has $^1(n\pi^*)$ character. The vertical excitation energy of this $S_0 \rightarrow S_3$ transition is 3.93 eV (315 nm) and the oscillator strength is negligible. The fourth vertical optical transition has a significant oscillator strength of 0.16 and the corresponding excitation energy is 3.97 eV (313 nm). For lumichrome **Lc**, first absorption band occurs at 3.39 eV (366 nm), which is insignificantly shifted compared to alloxazine **AL**, thus the two methyl groups bonded to the A ring have negligible effect on the absorption band maxima. Interestingly, oscillator strength increases to 0.06 and this first absorption band matches the HOMO→LUMO transition. The same situation can be observed in iso-tautomers **iAL** and **iLc**. $S_0 \rightarrow S_1$ energies of 3.09 eV (400 nm) with $^1(n\pi^*)$ character for **iAL** and 3.02 eV (411 nm) with $^1(\pi\pi^*)$ character for **iLc** show that dimethylation to C(7) and C(8) slightly decreases the transition energy. However, HOMO→LUMO transition occurs in **Lc** with the corresponding oscillator strength of 0.20, while in **iAL,** HOMO–1 to LUMO transition occurs with negligible oscillator strength. The second excitation of **iAL** (transition from HOMO to LUMO) exhibits the $^1(\pi\pi^*)$ character with oscillator strength of 0.17. Changes in electron distribution and aromaticity of the iso-form within tautomer couples lead to the bathochromic shifts of the lowest energy transitions compared to the alloxazine forms. In case of additional substitution of methyl to the B or C ring for (**i**)**Me**, the calculated TD-B3LYP excitation energies are red shifted in comparison to (**i**)**Lc**, i.e. 3.37 eV (368 nm), 3.40 eV (364 nm) for the first two excitation energies for **Me**. Slightly higher vertical excitation energies (3.41 eV, 3.47 eV, 3.86 eV, 4.02 eV for **AL** and 3.44 eV, 3.41 eV, 3.89 eV, 3.91 eV for **Me**) were obtained using a combination of the density functional and multi-reference configuration interaction method (DFT/MRCI) (Grimme and Waletzke, 1999).

TD-B3LYP predicts zero oscillator strengths for vertical triplet excitations. For **AL**, **Lc** and their substituted derivatives, the lowest energy triplet excitation $S_0 \rightarrow T_1$ ranges between 2.50 eV and 2.65 eV while the iso-forms of tautomer couples show the energy slightly above 2 eV. According to the previously published works (Sikorska et al., 2004d), the $S_0 \rightarrow T_1$ transition has $^3(\pi\pi^*)$ character.

Experimental fluorescence emission spectra of the studied molecules show a single band where the exact position of the maximum depends on the environment and tautomeric forms. For example, maxima of the fluorescence emission measured in acetonitrile are 2.79 eV (444 nm) for alloxazine (**AL**) and 2.84 eV (436 nm) for lumichrome (**Lc**). The fluorescence emission spectrum of lumiflavin (**iMe**) and riboflavin (**iRib**) in methanol (Sikorska et al., 2005) show a band with the maxima at 2.37 eV (526 nm) and 2.33 eV (532 nm), respectively. Isoalloxazine exhibits one order of magnitude higher fluorescence quantum yields and cor-

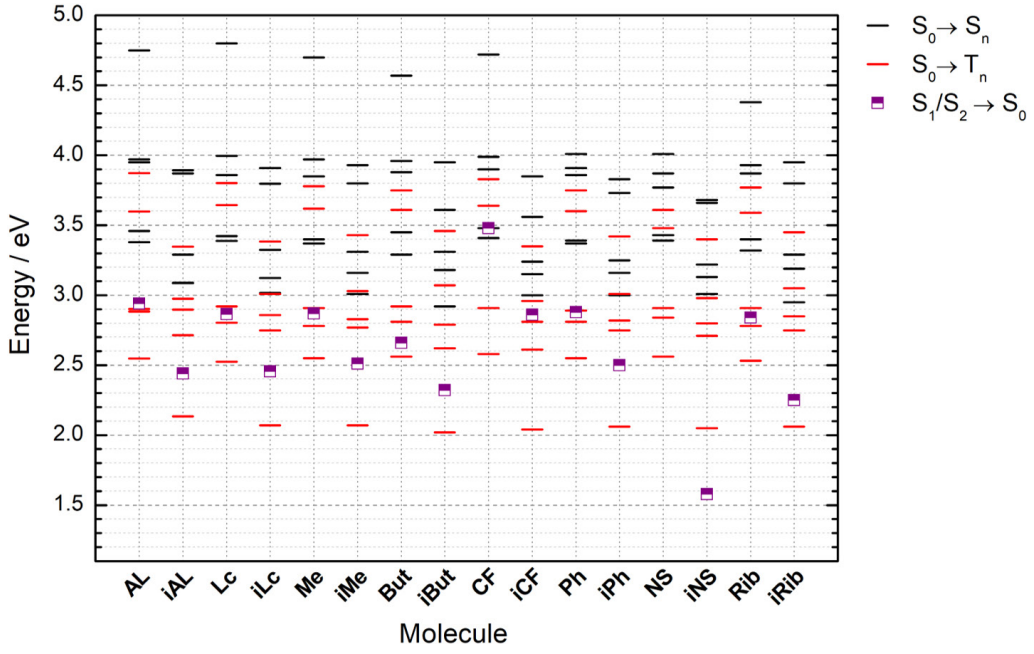

Fig. 6. Energy diagram of selected lowest energy vertical TD-B3LYP singlet ($S_0 \rightarrow S_n$) and triplet ($S_0 \rightarrow T_n$) excitation energies for optimal electronic-ground state geometries and $S_1/S_2 \rightarrow S_0$ deexcitation energies.

respondingly longer fluorescence lifetimes than alloxazine. At the level of time dependent DFT, many optimal geometries of the excited singlet and triplet states of alloxazine derivatives represent a saddle point. As it was reported by Salzmann et al. (2009), one imaginary frequency is obtained for out-of-plane deformation. Nevertheless, TD-DFT deexcitation energies agree with the DFT/MRCI results for the alloxazine and isoalloxazine derivatives.

As it was proved by Sikorska et. al. (2005) for riboflavin (**iRib**), the $^1(\pi\pi^*)$ to $^3(\pi\pi^*)$ intersystem crossing increases the quantum yield of triplet oxygen formation and decreases the quantum yields of singlet oxygen formation with a suitable energy levels difference to influence the $^1O_2$ to $^3O_2$ conversion (Min and Boff, 2006). Since riboflavin (**iRib**) is already in use as a photo-antimicrobial agent with the excitation wavelength of 450 nm (Min and Boff, 2006), a derivative with similar singlet and triplet energy levels has possible future application in medicine. Our theoretical calculations show that the singlet to triplet energy difference of the HOMO→LUMO transition is clearly modulated by tautomerization.

Conclusions

Optimal geometries and electronic structure of (iso)alloxazine, lumichrome, and its model substituted tautomeric derivatives were investigated using the density functional theory. Changes in molecular geometry and local aromaticity of the benzo[g]pteridine core were described using the local HOMED aromaticity indices. The only substituent, which consistently decreases the aromaticity of all rings was —CF_3 bonded to the N(10) atom possibly because of very inductive electron-withdrawing character of the group. The **iCF** derivative is thus the least stable within the studied group. Generally, the smallest changes of the HOMED index were found in the benzene-like A ring mostly due to dimethyl substitution on this ring (0.01). HOMED changes of the heterocyclic B and C rings were larger by one to two tenths depending on the position of the substituent. The substitution using methyl, butyl, phenyl, and 2,3,4,5-tetrahydroxypentyl had minimal effect on the energies of frontier molecular orbitals. Due to the heterocyclic ring substitution, the HOMO–LUMO band gaps were lowered for all cases except for **CF**. TD-B3LYP calculations of optical transitions predicted that the large number of studied derivatives can absorb and emit light in the visible spectral region. Obtained theoretical results can be helpful in the preparation of materials applicable in optoelectronics or medicine in the future.

Acknowledgement

The work has been supported by the Slovak Research and Development Agency (APVV-15-0053) and VEGA 1/0504/20. We are grateful to the HPC center at the Slovak University of Technology in Bratislava, which is a part of the Slovak Infrastructure of High Performance Computing (SIVVP project, ITMS code 26230120002, funded by the European region development funds, ERDF) for the computational time and resources made available.

D.C. would like to thank for the financial support from the STU Grant scheme for Support of Young Researchers (1848).

J.T. thanks the internal grant FCH-S-20-6340 of the Brno University of Technology.

References

Ai Y, Zhang F, Chen S, Luo Y, Fang W (2010) J. Phys. Chem. Lett. 1: 743—747.

Allen FH, Kennard O, Watson DG, Brammer L, Orpen AG, Taylor R (1987) J. Chem. Soc. Perkin Trans. 2.: S1—S19.

Becke AD (1988) Phys. Rev. A 38: 3098—3100.

Cyrañski MK, Krygowski TM, Katritzky AR, Schleyer PvR (2002) J. Org. Chem. 67: 1333—1338.

Flukiger P, Luthi HP, Sortmann S, Weber J (2002) Molekel 4.3, Swiss National Supercomputing Centre, Manno, Switzerland.

Frisch MJ, Trucks GW, Schlegel HB, Scuseria GE, Robb MA, Cheeseman JR, Scalmani G, Barone V, Menucci B, Petersson GA, Nakatsuji H, Caricato M, Li X, Hratchian HP, Izmaylov AF, Bloino J, Zheng G, Sonnenberg JL, Hada M, Ehara M, Toyota K, Fukuda R, Hasegawa J, Ishida M, Nakajima T, Honda Y, Kitao O, Nakai H, Vreven T, Montgomerry JA Jr., Peralta JE, Ogliaro F, Bearpark MJ, Heyd JJ, Brothers EN, Kudin KN, Staroverov VN, Keith TA, Kobayashi R, Normand J, Raghavachari K, Rendell AP, Burant JC, Iyengar SS, Tomasi J, Cossi M, Rega N, Millam JM, Klene M, Knox JE, Cross JB, Bakken V, Adamo C, Jaramillo J, Gomperts R, Stratmann RE, Yazyev O, Austin AJ, Cammi R, Pomelli C, Ochterski JW, Martin RL, Morokuma K, Zakrzewski VG, Voth GA, Salvador P, Dannenberg JJ, Dapprich S, Daniels AD, Farkas O, Foresman JB, Ortiz JV, Cioslowski J, Fox DJ (2013) Gaussian 09, Revision D.01, Gaussian, Inc., Wallingford CT.

Frizzo CP, Martins MAP (2012) Struct Chem 23: 375—380.

Furche F, Ahlrichs R (2002) J. Chem. Phys. 117: 7433.

Grimme S, Waletzke M (1999) J. Chem. Phys. 111(13): 5645—5655.

Gross E, Dobson J, Petersilka M (1996) Top. Curr. Chem. 181: 81.

Hanwell MD, Curtis DE, Lonie DC, Vandermeersch T, Zurek E, Hutchison GR (2012) J. Cheminformatics 4: 17.

Hariharan PC, Pople JA (1973) Theor. Chim. Acta 28: 213—222.

Kozioł J (1966) Photochem. Photobiol. 5: 41.

Lee C, Yang W, Parr RG (1988) Phys. Rev. B 37: 785—789.

Min DB, Boff JM (2006) Comp Rev Food Sci Food Saf. 1(2): 58—72.
Ośmiałowski B, Raczyńska ED, Krygowski TM (2006) J Org Chem 71(10): 3727—3736.
Penzkofer A (2016) J. Photochem. Photobiol. A 314: 114—124.
Rassolov V, Pople JA, Ratner M, Windus TL (1998) J. Chem. Phys. 109: 1223—1229.
Salzmann S, Marian CM (2009) Photochem. Photobiol. Sci. 8: 1655—1666.
Sikorska E, Khmelinskii IV, Bourdelande JL, Bednarek A, Williams SL, Patel M, Worrall DR, Koput J, Sikorski M (2004d) Chem Phys. 301(1): 95—103.
Sikorska E, Khmelinskii IV, Komasa A, Koput J, Ferreira LFV, Herance JR, Bourdelande JL, Williams SL, Worrall DR, Insińska-Rakc M, Sikorski M (2005) Chemical Physics 314: 239—247.
Sikorska E, Khmelinskii IV, Koput J, Sikorski M (2004c) J. Mol. Struct. (Theochem) 676: 155.
Sikorska E, Khmelinskii IV, Prukala W, Williams SL, Patel M, Worrall DR, Bourdelande JL, Koput J, Sikorski M (2004b) J. Phys. Chem. A 108: 1501.
Sikorska E, Khmelinskii IV, Worrall DR, Koput J, Sikorski M (2004a) J Fluoresc. 14(1): 57—64.
Sikorski M, Sikorska E, Worrall DR, Wilkinson D (1998) J. Chem. Soc. 94, 2347—2353.
Zanetti-Polzi L, Aschi M, Daidone I, Amadei A (2017) Chem. Phys. Lett. 669: 119—124.

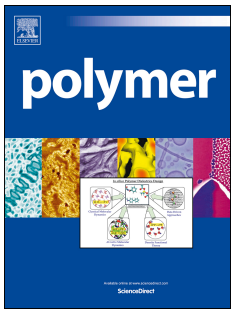

Novel adamantane substituted polythiophenes as competitors to Poly(3-Hexylthiophene)

Jan Jancik, Jan Pospíšil, Matous Kratochvil, Jan Truksa, Davide Altamura, Cinza Giannini, Martin Weiter, Davide Blasi, Vladimír Lukeš, Eric D. Głowacki, Jozef Krajcovic

PII: S0032-3861(22)00762-5

DOI: https://doi.org/10.1016/j.polymer.2022.125274

Reference: JPOL 125274

To appear in: *Polymer*

Received Date: 16 February 2022

Revised Date: 29 July 2022

Accepted Date: 23 August 2022

Please cite this article as: Jancik J, Pospíšil J, Kratochvil M, Truksa J, Altamura D, Giannini C, Weiter M, Blasi D, Lukeš Vladimí, Głowacki ED, Krajcovic J, Novel adamantane substituted polythiophenes as competitors to Poly(3-Hexylthiophene), *Polymer* (2022), doi: https://doi.org/10.1016/j.polymer.2022.125274.

Novel Adamantane Substituted Polythiophenes as Competitors to Poly(3-Hexylthiophene)

Credit author statement:

Jan Jancik: Synthesis, NMR and GPC characterisation, Writing, ***Jan Pospíšil***: Methodology, Electrical properties characterisation, ***Matous Kratochvil***: Optical absorption and emission measurements, Interpretation, ***Jan Truksa***: Computations, Data curation, Writing and editing, ***Davide Altamura*** and ***Cinzia Giannini***: GIWAXS measurements and interpretation, ***Martin Weiter***: Conceptualization, Methodology, ***Davide Blasi***: DSC Measurements, Editing, ***Vladimír Lukeš***: Computations, Writing and editing, ***Eric D. Głowacki***: Cyclic Voltammetry measurement and interpretation, **Jozef Krajcovic**: Conception, Supervision, Writing and Editing

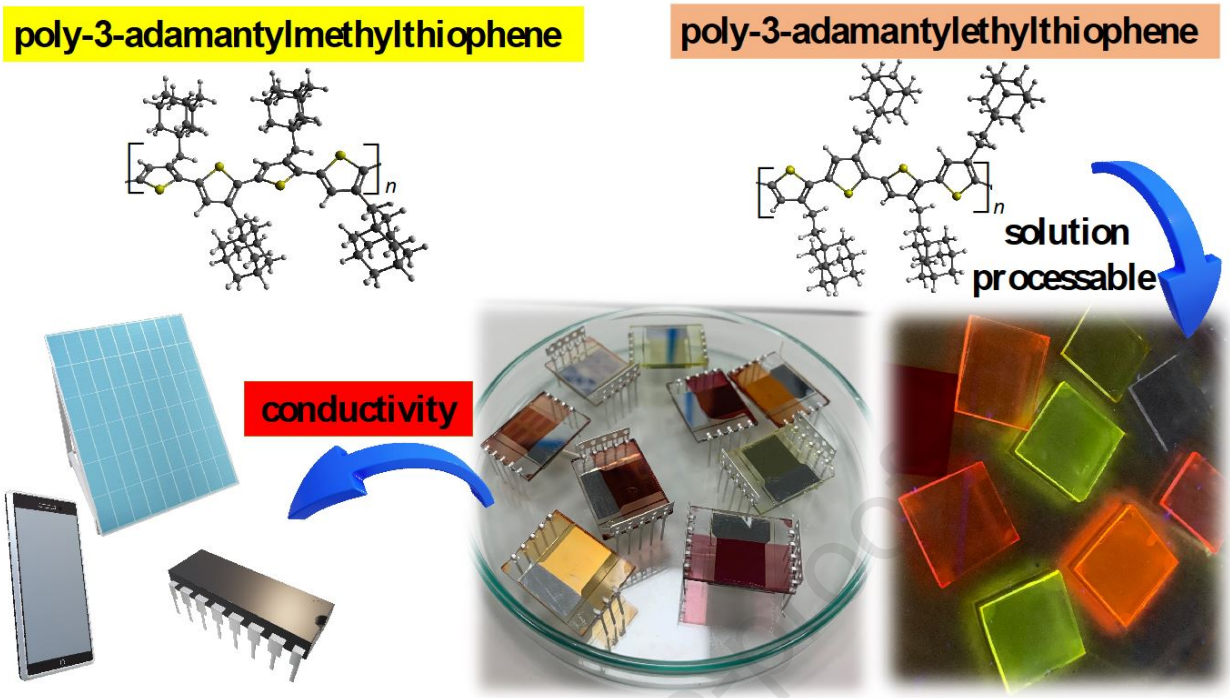

Novel Adamantane Substituted Polythiophenes as Competitors to Poly(3-Hexylthiophene)

*Jan Jancik[a], Jan Pospíšil[a], Matous Kratochvil[a], Jan Truksa[a], Davide Altamura[d], Cinza Giannini[d], Martin Weiter[a], Davide Blasi[e], Vladimír Lukeš[b], Eric D. Głowacki[c] and Jozef Krajcovic[a, e]**

[a] Brno University of Technology, Faculty of Chemistry, Materials Research Centre, Purkyňova 118, 612 00 Brno, Czech Republic.

[b] Institute of Physical Chemistry and Chemical Physics, Faculty of Chemical and Food Technology, Slovak University of Technology in Bratislava, Radlinského 9, SK-812 37 Bratislava, Slovakia

[c] CEITEC Brno University of Technology, Purkyňova 656/123, 612 00 Brno, Czech Republic

[d] Istituto di Cristallografia (CNR-IC), Via Amendola 122/O, 70126-Bari, Italy.

[e] Dipartimento di Chimica, Università degli Studi di Bari Aldo Moro, via Orabona, 4-70125 Bari, Italy

*corresponding author: krajcovic@fch.vut.cz

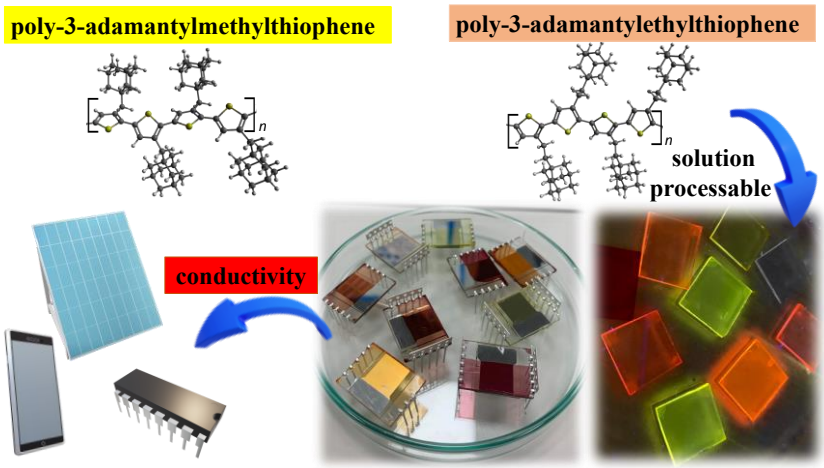

for Table of Contents use only

Abstract

The investigation of poly(3-alkylthiophenes) **(P3ATs)** has gained great attention in the last decades. Here, we present the synthesis, experimental and theoretical study of the novel regioregular poly(3-adamantylmethylthiophene) **(PMAT)** and poly(3-adamantylethylthiophene) **(PEAT)**, characterised by a bulky adamantane side group. The prepared compounds are solution-processable in common organic solvents, possess excellent thermal stability up to 491 °C and have unique chemical endurance. The molecular ordering of the polymers was investigated by the GIWAXS technique, and **PMAT** was found to have the higher content of crystalline phase. The experimental absorption and fluorescence spectra of investigated polymers indicate a higher rigidity of the adamantane side group with respect to torsional rotation in solutions and in thin layers. Electrical measurements exhibit charge carrier mobilities comparable to poly(3-hexylthiophene) **(P3HT)**. In contrast to **P3HT**, adamantyl-substituted polymers show quasi-reversible reduction alongside the expected quasi-reversible oxidation, which in theory supports the ability to transport both types of electric charges. The newly synthetized regioregular adamantane substituted polythiophenes are serious competitors for a wide range of applications in electronics and optoelectronics.

Keywords

Material research; side substituents; DFT; optical spectra; charge-carrier mobilities; GIWAXS; solution-processable polythiophenes

1. Introduction

Organic electronic materials have received much attention over the past decades as promising alternatives to their inorganic counterparts.[1,2] The importance and interest in this field of materials have grown exponentially, and a huge amount of conjugated polymers **(CPs)**, suitable for electronics, have been discovered.[3] These polymers have been widely used in a variety of organic electronic devices, including organic transistors,[4,5,6] light-emitting diodes,[7,8,9] solar cells,[10,11] and sensors.[12,13] Significant advantages of **CPs** are mild synthetic conditions, excellent processability, chemical and structural diversity, structural flexibility, and high-precision molecular design, enabling tunable optical and electrical properties at the molecular level.[14] The key parameters affecting the optical, electrical and electrochemical properties of these materials are the effective conjugation length and the chemical structure, including the intra- and interchain interactions and crystallinity.[15] The oligothiophenes and polythiophenes represent typical commercial organic semiconducting materials used in the fabrication of various optoelectronic devices. However, the unsubstituted aromatic backbone is semiflexible, which results in a strong aggregation of oligomeric or polymeric chains leading to insolubility. This causes a processability problem with respect to layer incorporation.[16,17]

The alkyl side chain substitution of the polymer chain causes several important changes that are closely related to properties and directly to further use of **CPs**. The main aim of the side chain substitutions is to improve the solubility and overall processability and the formation of non-bonding interactions between alkyl side chains, leading directly to the formation of highly organised polymeric structures with self-assembly abilities. This creates space for a targeted study of the effect of alkyl side chains on electronic and optoelectronic properties, mechanical properties, and oxidative and thermal stability. The density and efficiency of the alkyl group overlaps, the molecular distance of the polymer blocks, and the torsion angles between the aromatic units in the polymer chain are the most important factors involved in side-chain engineering.[18]

The **P3AT**s can be considered as one of the most studied and characterised conductive polymers with a wide range of structural variability obtained by side-chain engineering. The intensity of research focused on **P3AT** is evident from the number of recently published works. However, it is

mainly a study of linear and branched alkyl derivatives or their associated alternatives. The study of thermomechanical properties of selected **P3AT**s with branched or linear side chains by Cao *et al.* [19] has brought the first in-depth description of the influence of the side chain branching position, with respect to the polymer backbone, on the application in stretchable and wearable electronics. Another systematic study of cost-effective electrolyte-gated organic field-effect transistors (EGOFETs) based on the benchmark **P3HT** has been performed by Blasi *et al*.[20], demonstrating how the **P3HT** ink-jet printed films creates high-quality crystals in terms of π-π stacking. The printed devices displayed high environmental, mechanical and electrical stability for application in the field of bioelectronics.

The poly(3-dodecylthiophene)s (**P3DDTs**) and their regioregularity control (RR) play a key role in temperature-dependent liquid crystalline phases. Park *et a*l.[21] investigated the impact of the RR of **P3DDT**s on the strengths of their interactions. The **P3DDT**s with lower RR (60%) exhibited significant decreases in the transition temperatures between the phases. Results obtained in this work will serve as a good background for the fine control of **P3DDT**s self-assembly and optoelectronic properties.

Recently published work of Nguyen *et al.* [22] reported the effect of the molecular weight of selected **P3ATs** on the physical and photovoltaic properties of the polymers. A series of well-defined-molecular-weight polymers with different alkyl chain lengths was synthesised. Polymers with a longer side chain exhibited a red shift in the solution absorption and photoluminescence spectra, which might be strong evidence for the extended effective conjugation occurring in polymers with higher chain lengths.

Lin *et al.* [23] adopted a completely new approach for **P3AT** modification by introducing alkylthio side chains poly-[(3-alkylthio)thiophene]s (**P3ATTs**) to the backbone. A direct comparison to respective p3ATs has shown that the presence of a sulfur atom in the polymer side chain influences the aggregation/self-assembly behaviour and frontier energy levels. Moreover, precise control on the conformation of regioregular polythiophenes can be achieved *via* noncovalent S–S and S–π interactions. This could undoubtedly be a method for optimising the solid-state structural organisation and effective charge carrier transport applicable in OFET devices.

All the works discussed above deal with linear or branched alkyl side chains. No paper has described the implementation of a bulky alkyl substituent to regioregular **P3AT** until now.

These bulky groups may effectively increase separation distances between individual polymer chains to bring the optical properties of polymer films closer to those in solution. As a result, we expected the photoluminescent properties of these modified compounds to be independent on the state of matter. However, a very large intermolecular separation is known to be responsible for a big drop or even complete loss of semiconducting electrical properties. The use of the adamantane moiety in this type of chemical modification may represent a promising strategy to enhance the photoluminescence efficiency while preserving a good semiconductivity. In fact, adamantane, being the smallest diamondoid, is the most stable saturated hydrocarbon compound with a relatively small molecular weight and a high melting point. This molecule exhibits large optical transparency, biocompatibility, ability to self-organise into crystals, as well as mechanical and chemical stability.[24]

In this paper, we report the synthesis, experimental and theoretical study of novel adamantane-bearing polythiophenes (**Fig. 1**). The partial aims of this study are: (1) to present the effective synthetic route of studied molecules; (2) to characterise the molecular ordering of the prepared polymer samples by the Grazing Incidence Wide Angle X-Ray Scattering (GIWAXS) technique; (3) to theoretically characterise the chemical and electronic structure for model oligomers; (4) to experimentally determine the optical properties in solution and thin film; (5) to measure the drift mobilities and redox behaviour of prepared solid samples at room temperature ($T \approx 298.15$ K). Finally, the obtained experimental and theoretical results have been compared with the reference polythiophene (**PT**), poly(3-hexylthiophene) (**P3HT**) and poly(3,4-ethylenedioxythiophene) (**PEDOT**) and corresponding model oligomers.

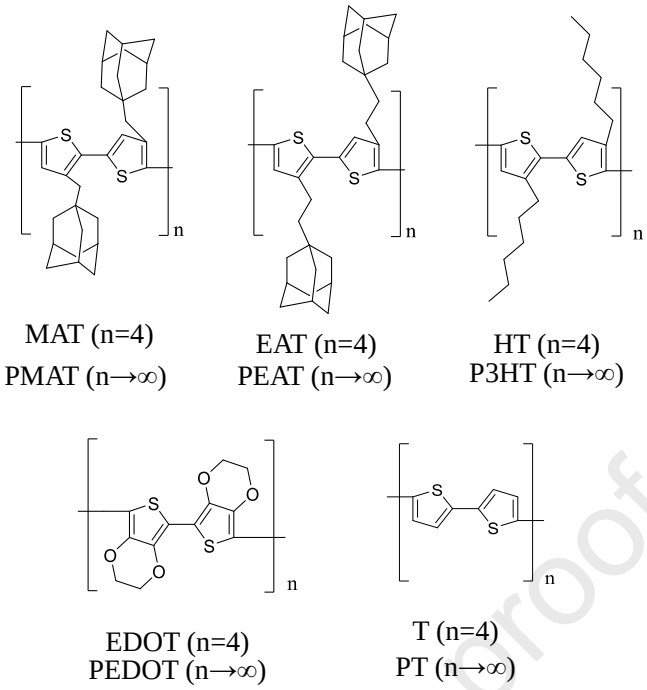

Figure 1. Notations for the studied model oligomers and their corresponding polymers

2. Experimental Section

2.1 Materials and Equipment

All solvents and reagents were obtained commercially and used as received unless stated otherwise. All moisture-sensitive reactions were performed in dry flasks fitted with glass stoppers or rubber septa under a positive pressure of argon. Solvents used for the purposes of purification were obtained from Penta Chemicals (Czech Republic) in p.a. grade. The **P3HT** was purchased from Sigma Aldrich with a declared regioregularity of > 90 %, the molar mass of 50 - 100 kg·mol^{-1} and PDI of < 2.5.

Flash column chromatography was performed using 220 to 440 mesh silica gel. Thin-layer chromatography was conducted on Supelco 60 TLC plates (Sigma Aldrich, St. Louis, MO, USA) with a 254 nm fluorescent indicator. Spots were observed under ultra-violet irradiation (254 nm or 354 nm). The ^{1}H NMR spectra were recorded in $CDCl_3$ using an Avance III 300 MHz spectrometer (Bruker, Billerica, MA, USA) with working frequencies of 300 MHz at 30 °C. Chemical shifts are expressed in parts per million (δ scale) downfield from tetramethylsilane and are referenced to

residual protons in the NMR solvent ($CHCl_3$: δ = 7.25 ppm). Coupling constants (J) are given in Hz with coupling expressed as s-singlet, bs-broad singlet, d-doublet, dd-doublet of a doublet, t-triplet, tdd-doublet of a triplet of doublets, ddd-doublet of doublet of doublets, m-multiplet. Thermogravimetric analysis was performed using TGA Q50 instrument (TA Instruments, New Castle, DE, USA) with nitrogen as the carrier gas. The molecular weight of prepared polymers was measured using GPC Agilent with $CHCl_3$ as eluent. The Agilent PLgel 5 µm MIXED-C column was used with the flow of 1 mL·min^{-1}. The detection was performed using the standard refractometric detector and 10 points calibrations on polystyrene standard.

The morphologies of the thin layers were characterised with AFM (Digital Instruments Multimode) operated in tapping mode with a silicon cantilever. The samples for AFM measurements were prepared as described for the sample fabrication.

2.2 Synthesis of monomers

The adamantylmethyl- and adamantylethylthiophene monomers **(3,4)** were prepared by the Kumada coupling reaction[24] from adamantylalkylbromide and 3-bromothiophene (see **Scheme 1**).

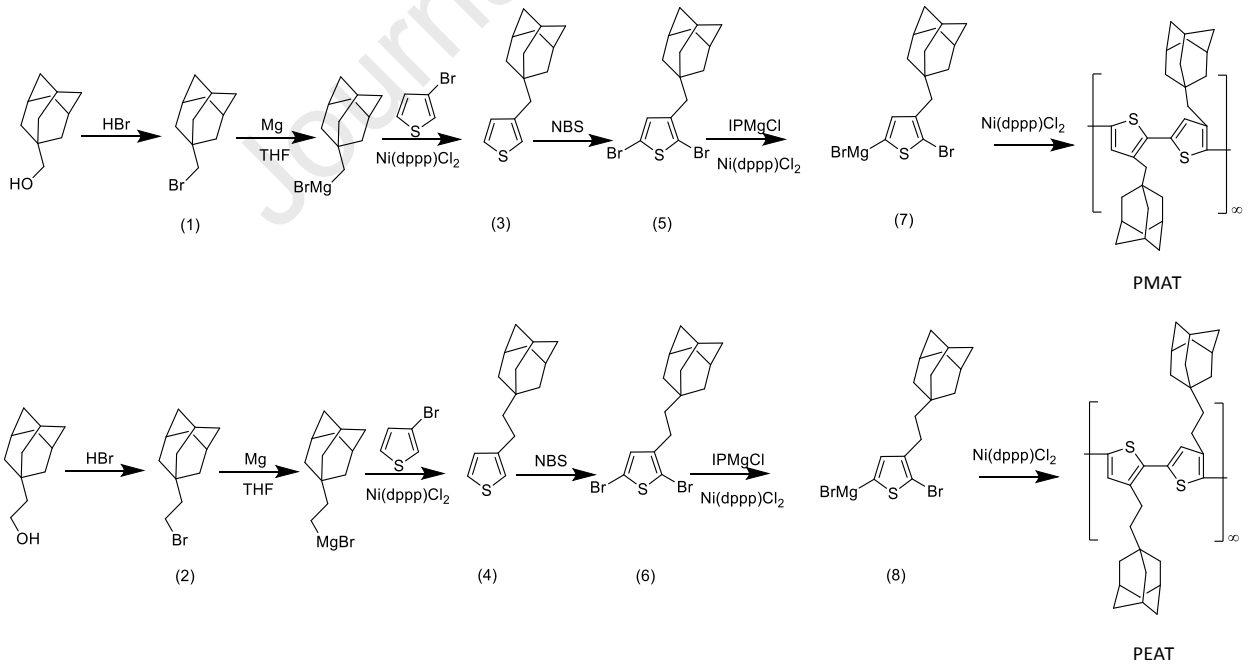

Scheme 1. Synthesis of adamantylmethyl- and adamantylethylthiophene monomers and their polymerisation

Synthesis of dibrominated monomers (5,6)

N-Bromosuccinimide (NBS) (1.5 g, 8.5 mmol for **5** or 1.6 g, 9.0 mmol for **6**) was dissolved in dry DMF (20 mL) in the absence of light and the mixture was added dropwise to a solution of alkylated thiophene derivatives **3** (1.0 g, 4.1 mmol) or **4** (1.0 g, 4.3 mmol) dissolved in DMF (15 mL) and left stirred 24 hours at 50 °C. After 24 hours, the reaction mixture was poured onto ice water and extracted with 3×20 mL of diethylether, then the organic phases were dried over sodium sulphate, and the solvent was evaporated by rotary evaporator. The product was used for polymerisation without further purification.

Monomer unit 5: yield 1.3 g, 77.3 %;

Monomer unit 6: yield 1.5 g, 86.1 %;

2.3 Synthesis of polymers and morphology of prepared samples

Monomer **5** (1.3 g, 3.22 mmol) or **6** (1.5 g, 3.71 mmol) in dry THF (7 mL) was stirred at −5°C and 2M isopropylmagnesiumchloride solution (1.61 mL, 3.22 mmol for **5** or 1.86 mL, 3.71 mmol for **6**) was dropwise added into the reaction mixture at −5°C. The reaction mixture was stirred for 1 hour to selectively prepare the Grignard reagent (**7**,**8**) for polymerisation. Its temperature was maintained at −5°C followed by the addition of catalyst Ni(dppp)Cl_2 (0.84 g, 1.54 mmol for **5** or 0.97 g, 1.78 mmol for **6**) and allowed to spontaneously warm to room temperature. In 20 minutes, the reaction mixture has turned dark red, and after 1 hour, the reaction was quenched by adding 1 mL of 1M HCl and precipitated in a large amount of methanol. The suspension was filtered over the paper, and the solid part was purified.

Purification of PMAT products

The solid part was washed with toluene until the majority of solid material dissolved (after evaporation 0.36 g fraction **PMAT2**), and only yellow-brown metallic material remained on the filtration paper. It was dissolved in chloroform and evaporated to yield 0.23 g (fraction **PMAT1**). The **PMAT1** fraction was dissolved in a small amount of chloroform to get a yellow solution and precipitated in 50 mL of methanol to get a brown suspension. This suspension was centrifugated

at 6000 revolutions per minute (RPM) for 15 minutes, liquid phase poured to waste, and 10 mL of methanol was added to the solid precipitate and centrifugated again to get the product. Finally, to remove all residues and low molecular weight compounds, the product was purified thermally by heating to 370 °C, then dissolved in chloroform, decomposed solid parts were filtered, and the solvent was evaporated by rotary evaporator. Fraction **PMAT1** yield: 0.20 g, 20 %; **PMAT2**: 0.36 g, 40 %). Melting point > 330 °C. ^{1}H NMR ($CDCl_3$, TMS): δ=6.92 (br s, 1H), 2.65 (br s, 2H), 2.38 (br s, 1H), 1.88(s, 4H), 1.58–1.11 (m, 19H) (**Fig. 16S**).

Purification of PEAT products

The solid part was washed with toluene, and most of the solid material dissolved (after evaporation provided 0.41 g – **PEAT2),** and only black waxy plastic material remained on the filtration paper rest. It was dissolved in chloroform and evaporated to yield 0.13 g (fraction **PEAT1**).

The **PEAT1** fraction was dissolved in a small amount of chloroform to get a black solution and precipitated in 50 mL of methanol to get a purple suspension. The suspension was centrifugated at 6000 RPM for 15 minutes, liquid phase poured to waste, and 10 mL of methanol was added to the solid precipitate and centrifugated again to get the final product. Finally, to remove all residues and low molecular weight compounds, the product was purified thermally by heating to 370 °C, then dissolved in chloroform, decomposed solid parts were filtered, and the solvent was evaporated by rotary evaporator. Fraction **PEAT1** yield: 0.1 g, 11 %; **PEAT2**: 0.4 g, 44 %). Melting point > 330 °C. ^{1}H NMR ($CDCl_3$, TMS): δ=6.95 (br s, 1H), 2.72 (br s, 1H), 2.00 (br s, 3H), 1.73–0.86 (m, 19H) (**Fig. 17S**).

The average molar masses of the higher fractions of polymers (**Fig. 18S and 19S**). are around 15 kDa with a polydispersity around 6, which is in accordance with the standard polydispersity range (1.5 – 20) for polymers prepared by chemical chain reaction polymerisation. The lower fractions were in the range from 5 kDa to 8 kDa with a similar polydispersity which is in correspondence with optical and electrochemical measurements where lower fractions exhibit worse results.

The thermal properties of prepared polymers with the highest molar mass (higher fraction) were investigated by thermogravimetric and DSC analysis. The thermogravimetric analysis of **PMAT** shows stability up to 250 °C with only an insignificant weight loss of 3 %, which can be explained

by presence of humidity or volatile substances from synthesis (see **Figure 12S)**. From 250 °C up to 400 °C is recognisable very slow weight loss around 14 %, and after 400 °C is faster weight loss present indicating the degradation of material in two steps, first at 484 °C and second at 556°C. The extreme weight loss by pyrolysis at 700 °C was 96 %. The analysis of **PEAT** (see **Figure 13S)** shows the similar stability up to 250 °C with only insignificant weight loss around 7.5 %, which can be explained like in the case of previous sample. From 250 °C up to 400 °C is present slow weight loss around 11 %, continuing to faster weight loss indicating the degradation of material in two steps, first at 417 °C and second at 553°C. The extreme weight loss by pyrolysis at 700 °C was 94 %. Comparing with the reference **P3HT** or **PEDOT** polymers, the adamantyl based polymers exhibit similar thermal stability, which is essential for application in the field of organic electronics. According to the literature the decomposition of **P3HT** with a much higher molecular weight than our polymers, around 65 kDa, starts at 400 °C, and maximum decomposition is reached at 476 °C.[25] In the case of **PEDOT-PSS**, the decomposition starts at temperatures around 250 °C due to the loss of polystyrene sulfonate in the host **PEDOT-PSS**. The next weight loss at 350 °C is due to disruption of the polymer backbone chain in **PEDOT-PSS**.[26]

The DSC analysis of **PMAT** and **PEAT** (see **Figure 14S, 15S)** sample shows extremely high thermophysical stability up to 300 °C. The samples exhibit no phase changes in the measured range from -90 °C – 300 °C. In case of the **PMAT** there is a visible endotherm around 200 °C, which is too small to prove the melting of the samples, likely it is caused by slow irreversible structural movements.

Furthermore, one of the most exceptional properties of adamantane is the ability to self-organise into crystals.[24] The morphologies of the thin layers were visualised using non-contact atomic force microscopy (AFM). **Figure 2a** shows the typical topography of **P3HT** with some noticeable clusters, which are likely impurities or defects from the layer deposition. In the case of **PMAT**, there is very little variation in height in the scanned area, and several clusters are observed, significantly higher than most of the surface (**Fig. 2b**). On the other hand, the AFM image of **PEAT** (**Fig. 2c**) exhibits clusters around twice as high, as in the case of **PMAT**. These could be impurities from the synthesis and layer fabrication, or crystalline clusters of the polymer itself. Apart from these vertical clusters, the surface of **PMAT** and **PEAT** seems to have visible domains a few nanometers higher than the

rest. We consider these to be crystalline clusters of the polymer, embedded in an amorphous matrix. In **PEAT**, these domains are significantly larger than in **PMAT**. On the other hand, on **Fig. 2a**, no such crystalline grains are discernible. Finally, the large number of small crystal domains in the **PMAT** sample, is determined by a higher content of light orange domains vs. dark orange domains in **Fig. 2b**.

Table 1: Decomposition temperatures of prepared polymers

	PMAT	PEAT
Decomposition temperature	484/556 °C	417/553 °C

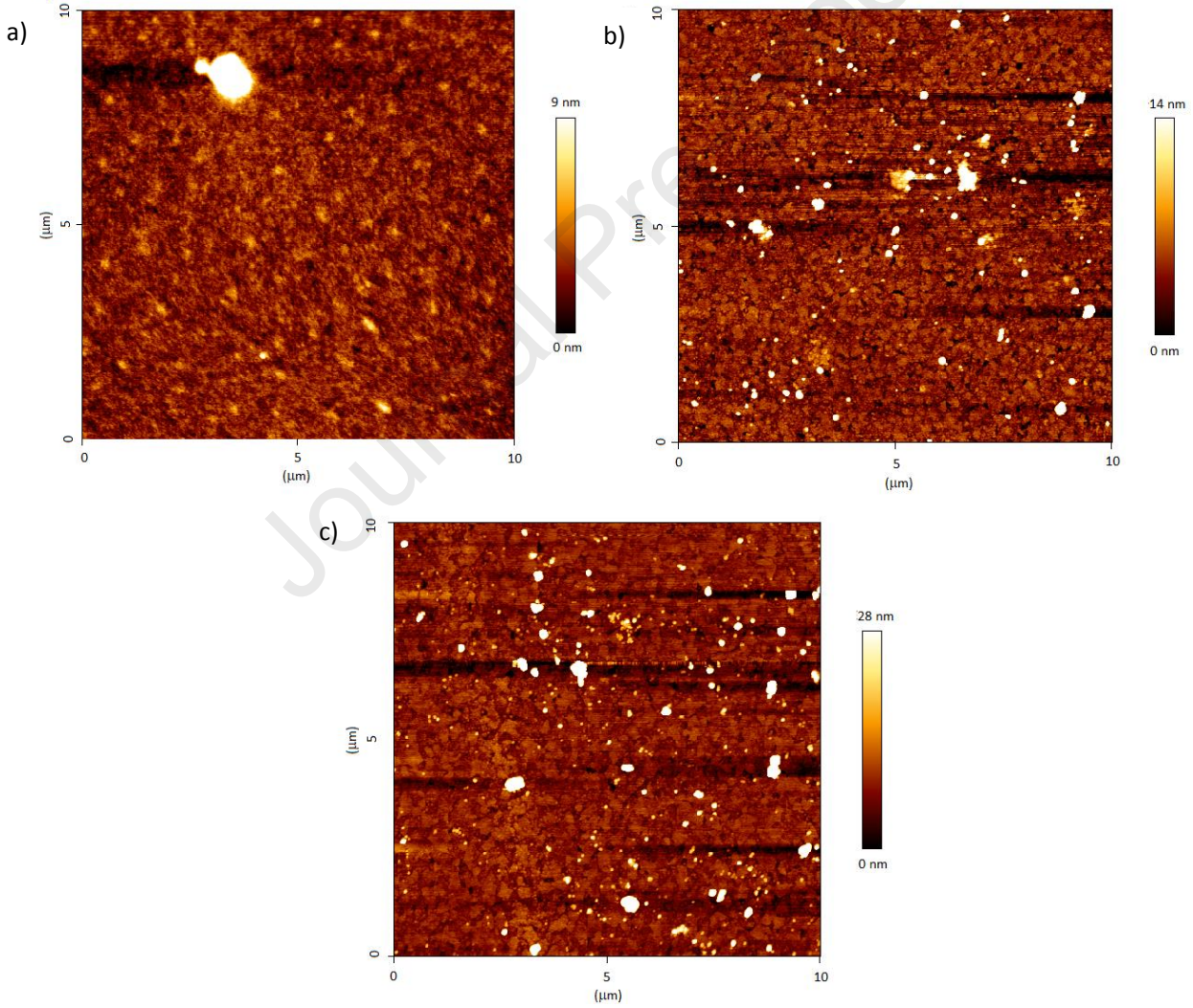

Figure 2. The AFM images of investigated polymer thin layers: (a) **P3HT**; (b) **PMAT,** and (c) **PEAT**

2.3 Molecular Ordering Measurements

The GIWAXS measurements were performed at the XMI-Lab[27], equipped with a Fr-E+ Superbright X-ray micro-source (Rigaku) coupled to a SMAX3000 SAXS/WAXS camera through a focusing optics and a three-pinhole beam shaping system. A Fuji Image Plate was used as detector, placed at 20 cm downstream the sample and off-line read by a Raxia scanner. Data were calibrated by using Ag Behenate powder standard and corrected for flat detector geometry by the program SUNBIM[28]. A high precision goniometer with piezoelectric motors was used for sample alignment. The incidence angle was set to 0.18° for all measurements, so as to avoid scattering contribution from the glass substrate. Samples were kept at about 0.5 mbar vacuum pressure during measurements.

2.4 Optical measurements

Absorption spectra were measured using a U-3900H (Hitachi) Lambda UV-VIS spectrometer. Steady-state fluorescence was measured using the Fluorolog (Horiba JY) fluorimeter. The emission spectra were recorded at excitation wavelength matching the absorption maximum wavelength of samples. The excitation spectra were measured for the wavelength corresponding to the emission maximum. Measurements were performed using a quartz cuvette with a path length of 10.00 mm, at room temperature. All spectra are corrected for equipment response. Photoluminescence quantum efficiency was measured by an absolute method, using an Integrating sphere (Quanta-Phi). The absolute method does not require photoluminiscencence quantum yield standards. Solution measurements were carried out in room-temperature chloroform at concentrations of 4×10^{-5} mol·L^{-1}. Thin layer samples were prepared by spin coating the 10 mg·L^{-1} chloroform solution at 1500 RPM for 1 minute onto plasma-treated glass. Film thickness was around 80 nm.

2.5 Electrochemical and Electrical Measurements

Space-charge-limited current (SCLC) spectroscopy as well as electrochemical experiments were carried out at 298 K. Dark current-voltage (I–V) measurements were performed in a sandwich configuration of ITO electrode / organic compound / Al electrode using electrometer Keithley model 6517B. The **P3HT** layer was used as the reference. The current density *j*, in the framework of the Mott-Gurney law, can be generally expressed by the following equation[29]

$$j = \frac{9}{8}\mu\varepsilon_0\varepsilon_r\frac{V^2}{L^3} \quad (1)$$

where μ is the microscopic electric mobility, ε_0 is the permittivity of vacuum, ε_r is the relative permittivity (for organic compounds $\varepsilon_r \approx 3$), and V is the voltage. The sample thickness (L) was measured by the mechanical profilometer Bruker Dektak XT.

The experimental concentration of trapped charge carriers n_t was evaluated by the equation

$$n_t = \frac{2\varepsilon_0\varepsilon_r V_{TFL}}{eL^2}, \quad (2)$$

where V_{TFL} is the trap-filled limit voltage and e is the elementary electric charge.[30]

Electrochemical measurements were performed in a three electrode system with platinum as the counter electrode and an Ag/AgCl wire in 1M KCl as the reference electrode, using an Ivium PocketSTAT2 potentiostat. Polymer layers on fluorine-doped tin oxide (FTO) glass substrates functioned as the working electrode. This arrangement is typically used for the electrochemical measurements of poly-3-hexylthiophene, see e.g., Wei et. al. [31] Polymer layers were deposited by drop casting 10 mg·mL^{-1} solution from chlorobenzene. Nitrogen-purged 0.1 M of tetrabutylammonium phosphorus hexafluoride ($TBAPF_6$) in anhydrous acetonitrile (CH_3CN) solution was used as the electrolyte.

2.6 Quantum Chemical Calculations

All the calculations were performed by using Gaussian 16 program package.[32] The density functional theory (DFT) with 3-parametric hybrid B3LYP functional[33] and def2svp basis set was used as implemented in the Gaussian package[32]. This hybrid DFT functional is standardly used for the calculations of many aromatic organic molecules.[34] The optimisation process was performed by tight optimisation criteria and a large DFT integration grid. True minima on potential energy surface were confirmed for small model molecules through vibrational analysis by no imaginary frequencies check. Based on optimised B3LYP geometries, the vertical transition energies and oscillator strengths between the initial and final electronic states were computed by the time-dependent (TD)-DFT method.[35] These optical properties were calculated using the CAM-B3LYP (Coulomb-Attenuating Method Applied to B3LYP) functional[36], where the correction on the charge transfer is included. The Avogadro[37] and Mercury[38] program packages were used for the visualisation of molecular geometries, molecular orbitals and crystallographic information in the supplement. The density transition analysis was performed using the Multiwfn program package.[39] The impact of side chain rotation on the molecular energy was determined by performing a scan of energy over the torsional angles between the thiophene unit and the substituent. To further our understanding of the substituents' sterical influence on the molecular geometry and optical properties, we extended the theoretical calculations to the octamers of ethyl-tetraasterane (**ETT**), comparable to **EAT**, and the extremely bulky ethyl-triamantane (**ETAT**), as well as the branched methyl-9-pentadecane (**MPT**), see **Fig. 3S**. Additional discussion of the computed results is given in the supporting information.

3. Results and Discussion

3.1 Molecular geometry of model oligomers

The presence of single bonds connecting the planar thiophene rings enables the formation of a huge number of different conformation states. The dihedral angle bounded by two adjacent thiophenes can be defined between two sulphur atoms and connecting carbon atoms (S–C–C–S).

The *trans* conformers have the sulphur atoms in opposite directions compared to the *cis* conformers. The quantum chemical calculations performed for unsubstituted and substituted gas-phase oligothiophenes showed a distorted backbone. The conformation analysis performed in the past for terthiophene at the *ab initio* Hartree-Fock level of theory using 6-31G(d,p) basis set showed that the average value of distances between two connected thiophenes is 1.465 Å.[40] This value represents a typical single C–C bond character. The inter-ring dihedral angles published for *cis* conformations are between 43° and 44°, and for *trans* conformations are ca 149°. This angular distortion between connecting thiophene-planes perturbs the formation of delocalised π-orbitals. However, the *cis* conformers for unsubstituted and simply substituted oligothiophenes are energetically less preferred due to the larger sterical repulsion of the side chains.[41,42,43] For instance, in the case of regio-regular **P3HT**, the calculated Gibbs free energy per one thiophene pair is higher by 2.5 to 5.0 kJ·mol^{-1}. [44]

To understand the intrinsic conformational preferences, the DFT study was done for model octamers in two ideal *all-trans* arrangements distinguished. In the first case, the alternation of signs of S–C–C–S dihedral angles leads to the bow-shaped backbone (see **Fig. 1S** to **3S**). The individual building blocks consisting of three thiophenes have the spatial *syn* orientation of lateral rings. The spatial *anti* orientation of building blocks represents the second alternative. In the case of the spatial *syn* orientation of the three-thiophene block, both S-C-C-S dihedral angles have a positive value, *e.g.* 150 and 160°, while in the *anti*-orientation, one of the angles has a negative value, *e.g.* 150 and – 160°. The syn rotamer is spiral-shaped because the dihedral angles are always positive. The optimal dihedral angles for the electronic ground and excited states are collected in **Tab. 1S.** The dihedral angles for symmetric unsubstituted thiophene oligomers (C_S symmetry point) are changed between 167 to 173°, and the *syn* orientation is energetically preferred. Interestingly, the experimental crystal structure of sexithiophene shows the fully planar *all-trans* conformation (see **Fig. 2S**).[45] The geometry optimisation of symmetric **EDOT** octamer starting from *syn* and *anti*-orientations of terthiophene units leads to a practically planar geometry. In the case of side substituted oligothiophenes, the anti-orientation is energetically preferred (see **Fig. 1S)**. For our purely theoretical polymers, we note that in the case of **MPT** and **ETAT**, the *anti*- conformation is energetically preferred, which is less suitable for creating a regular morphology (see **Fig. 3S**).

Furthermore, in the *syn*- conformation, **MPT** and **ETAT** have a larger variance of dihedral angles between individual thiophenes with respect to **HT-s** and **EAT-s** respectively, which points to a less regular structure overall (see **Tab. 1S** and the discussion in the supporting information). On the other hand, the geometry of **ETT** is comparable to **EAT**. From this, we conclude that large, branched substituents and extremely bulky substituents create a strain on the main polymer chain, which may result in an undesirable macrostructure. The optimised chain length of elongated hexyl groups is found to be 7.32 Å. This gas-phase value is slightly shorter compared with the experimental X-ray diffraction result of 7.7 Å.[46] Probably, this elongation of alkyl chains in crystals indicates the interaction between neighbouring molecules leading to the planarisation of thiophenes. A detailed discussion of the conformations of thiophene trimer building blocks with different substituents can be found in the supplementary information. In the case of bulky adamantylmethyl groups, only one energetically preferred orientation was found. Therefore, we conclude that the side chains of 3-adamantylmethyl thiophene will be restricted in rotation, while the 3-adamantylethyl thiophene chain will possess rigid adamantylethyl groups, which relatively freely rotate with respect to the thiophene moiety.

These results are in agreement with molecular dynamics simulations performed for various model crystal structures of **P3HT**,[47] and available crystal structures of partially hexylsubstituted sexithiophene, which indicate the presence of both orientations of alky-chains (see **Fig. 2S**).[48,49,50] The experimental X-ray structure measured for the simple adamantyl derivatives supports this theoretical prediction.[24] The electronic excitation leads to the planarisation of the thiophene backbone. The planarisation of oligomers with adamantyl groups are restricted (**Tab. 1S**). The theoretical calculations of model octamers reveal that the minimal hydrogen-hydrogen atom distance between neighbouring substituents is dependent on the size. In the case of **EAT-s** the minimal distance was found to be 3.03 Å. On the largest **ETAT**, this distance is 2.76 Å, similarly, on **MPT**, this distance is 2.68 Å (see discussion in the supporting information). This indicates, that the adamantyl substituents can form sufficient space for the incorporation of substituents from a second molecule and thus improve the intermolecular interaction. This arrangement can support the semiconducting properties of organic molecules.

3.2 Structure and Morphology of Prepared Polymers

Structural information about the molecular packing in the **PMAT** and **PEAT** samples was gained by GIWAXS measurements in the medium angular range (**Fig. 3**), including both the atomic (wide angle side) and nano (small angle side) scale information. GIWAXS patterns are shown in **Fig. 3**, as a function of the scattering vector modulus:

$$Q=(4\pi/\lambda)\sin\theta \quad (3)$$

where λ is the X-ray wavelength and θ is half the scattering angle. Full patterns in the left column show that both samples feature sharp diffraction rings at the opposite sides ($Q \leq 0.6$ Å^{-1}), ($Q \geq 1.5$ Å^{-1}) of the accessed Q-range, and two broad rings in between ($0.6 \leq Q \leq 1.5$ Å^{-1}). This indicates the coexistence of highly crystalline and amorphous moieties.

At large Q-values ($Q \geq 0.6$ Å^{-1}) samples show similar diffraction peaks, marked by asterisks in **Fig. 4**, *i.e.,* the same intramolecular distances, but the **PMAT** sample features higher diffracted intensity allowing to recognize doublets, whereas lower intensity is detected in the case of the **PEAT** sample. Peaks can be identified at Q = 1.52, 1.55, 1.70, 1.72 Å^{-1}, corresponding to the intramolecular spacings d = 4.13, 4.10, 3.71, 3.66 Å.

The presented experiments reveal the presence of intermolecular packing features with edge-on orientation in both **PMAT** and **PEAT** samples, with a similar (out-of-plane) stacking periodicity of 3.5–3.7 nm, which is about twice compared with the **P3HT** *a* lattice parameter (1.6 nm)[51,52]. On the other hand, both the prepared samples feature a (in-plane) d-spacing of 3.7 Å. This value is comparable to the published *b* lattice parameter of **P3HT** (3.8 Å)[51,52], hence ascribed to the intramolecular periodicity along the backbone. The third detected periodicity (4.1 Å) is thus ascribed to the lattice parameter perpendicular to the backbones and parallel to the film plane. As a result, even though a structure solution from single crystal diffraction is not available, an orthorhombic unit cell can be proposed as a first approximation for the **PMAT** and **PEAT** crystals. In particular, in the case of the **PMAT** sample, the higher preferred orientation of the diffracted intensity at small Q (out of plane direction in **Fig. 3b**) is accompanied by a preferred orientation of the diffracted intensity at large Q (in plane direction in **Fig. 3a**). This supports the hypothesis of an orthorhombic lattice

structure with *a* = 37 (or 42) Å, *b* = 3.7 Å, *c* = 4.1 Å. The coexistence of domains differing by the *a* lattice parameter (*a* = 37 or 42 Å) could explain the observed doublets in the GIWAXS patterns. Further details can be found in the supporting information. According to the results presented here and in the SI, the **PMAT** sample exhibits a more ordered structure, which agrees with the larger number of crystallites observed in AFM.

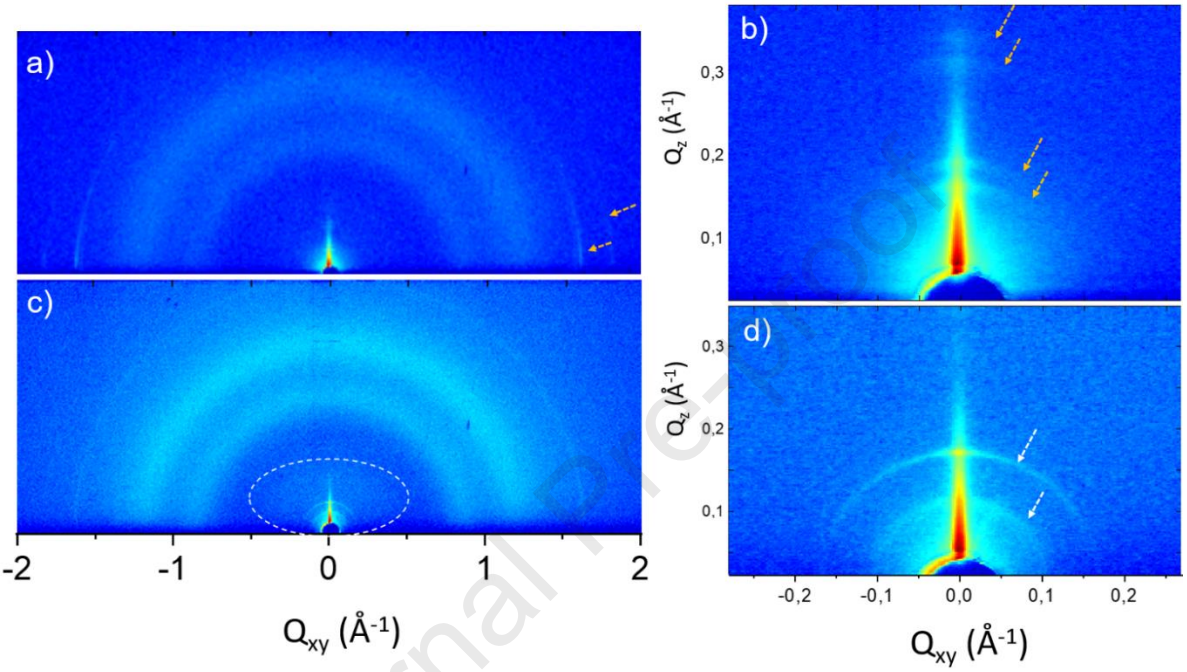

Figure 3. Two-dimensional GIWAXS patterns collected from the **PMAT** (a, b) and **PEAT** (c, d) samples: a, c: full patterns; b, d: zoom in the small angle range. Orange arrows indicate preferred orientation at large (panel a) and small (panel b) *Q* values.

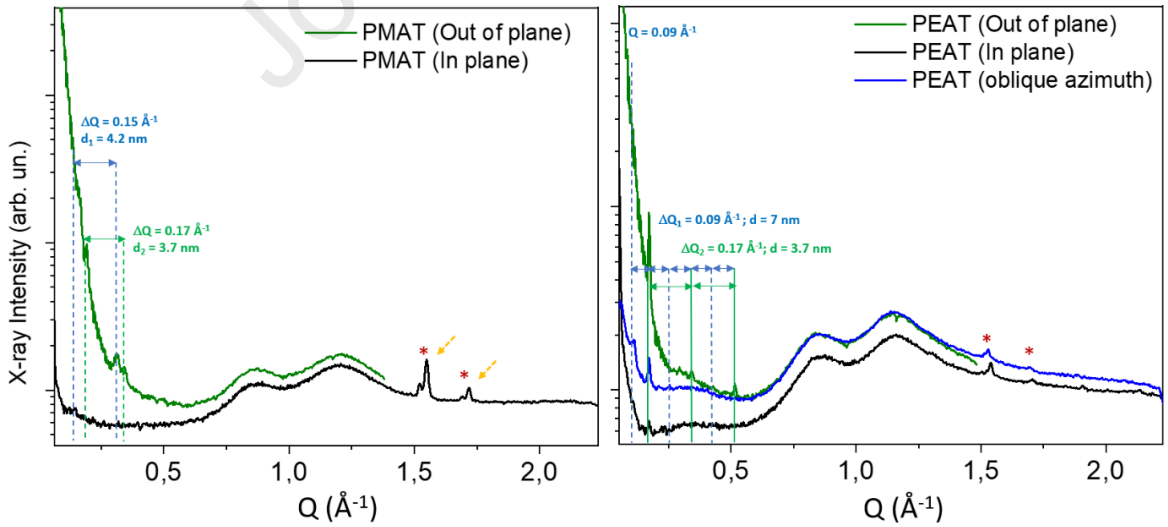

Figure 4. One-dimensional linear cuts folded from GIWAXS patterns of **Fig. 3**. In and out of plane cuts are compared. A further cut is reported for the **PEAT** sample, taken along an intermediate azimuthal direction (angular sector 120°÷150°), to get rid of the reflectivity background and better visualize the peak at Q = 0.09 Å-1. Peaks at large *Q* values related to preferred orientation are indicated by orange arrows in panel a (as in **Fig. 3a**).

3.3 Electronic structure and optical properties

The theoretical concept of molecular orbitals can help us to estimate the basic electrochemical and optical properties of the studied molecules. It is well known that these properties for thiophene oligomers and their derivatives are affected by the Highest Occupied (HOMO) and Lowest Unoccupied (LUMO) Molecular Orbitals. The calculated B3LYP energies of model parent **HT-s** molecule are −4.92 and −2.43 eV. The occupation of beta carbons on thiophene rings using 3,4-ethylenedioxy-groups shifts HOMO to –3.94 eV and LUMO to –1.69 eV. The orientation of the hexyl-groups with respect to the thiophene rings has a direct influence on the HOMO energies. As it is illustrated in **Fig. 5S**, the electron-donating effect of the alkyl group and the highest planarisation of thiophene backbone shifts the HOMO energy from –4.98 eV to –4.55 eV. A significant influence on the HOMO energy is also predicted for the **MAT-a** and **EAT-a** molecules. Maximum energy differences between HOMO and LUMO energies were found for adamantyl derivatives with the highest thiophene distortion. The modification of terminal units has a negligible effect on the shapes of frontier molecular orbitals. As it is shown in **Fig. 6S**, the lobes of LUMO are mostly delocalised over the longest axial direction in the centre of the molecule. The lobes of HOMO electrons are perpendicularly oriented. A small electron delocalisation is indicated for the terminal five-membered heterocyclic moieties.

Table 2. The theoretical TD-CAM-B3LYP//B3LYP lowest energy vertical optical transitions.

	Absorption		
	***E* / eV**	**λ / nm**	Oscillator strength
T-s	2.65	468	2.97
T-a	2.66	466	2.96
EDOT	2.44	509	3.18
HT-s	2.96	419	2.56
HT-a	3.05	406	2.61
HT*	2.53	490	2.94

Table 2 (continued). The theoretical TD-CAM-B3LYP//B3LYP lowest energy vertical optical transitions.

	Absorption		
	***E* / eV**	**λ / nm**	Oscillator strength
MAT-s	3.03	410	2.48
MAT-a	3.22	386	2.36
EAT-s	2.93	423	2.46
EAT-a	3.09	401	2.49
MPT-s	2.72	455	2.54
MPT-a	3.32	374	2.31
ETT-s	2.91	426	2.48
ETT-a	3.18	390	2.48
ETAT-s	2.93	423	2.42
ETAT-a	3.13	396	2.43

The theoretical analysis of the lowest vertical energy optical transitions of model compounds helps us to estimate the optical HOMO/LUMO gap of polymeric compounds. The TD-CAM-B3LYP excitation energies collected in **Table 2** are varied between 2.44 eV (509 nm) for **EDOT** to 3.22 eV (386 nm) for **MAT-a**. All lowest energy $S_0 \rightarrow S_1$ transitions come mainly from the HOMO to LUMO excitation, and the corresponding oscillator strength is larger than 2.0. The orientation of the hexyl group has a direct influence on the excitation energies. The influence of the tetraasterane (see **Fig. 3S**) substitution is predicted to be comparable to ethyladamantyl, which is also the case for the larger theoretical substituents, showing that the size or shape of the substituent influences the spectroscopy of an isolated chain. In contrast to adamantyl derivatives, a larger variability of optical properties between *syn*- and *anti*- conformations is predicted.

The two-dimensional real-space analysis of the transition densities provides an alternative to the traditional molecular orbital-based quantum-chemical analysis of photoexcitation processes. The spatial span and primary sites of the electronic transitions can be visualised using the two-

dimensional representation of the TD-DFT electron transition density matrix. The diagonal size of the transition density matrix corresponds to the number of non-hydrogen atoms over which the optical excitation is spread. The off-diagonal terms signify electron-hole coherence between the corresponding atoms. The shape of the lowest-energy transition density matrix is illustrated in **Figure 5***.* It is modulated by the added groups. The octathiophene oligomer contains 40 non-hydrogen atoms, and the intramolecular charge delocalisation is evident in the central part between four thiophene rings. The side substitution slightly increases the charge delocalisation, and the occurrence of the off-diagonal elements between the terminal and central thiophene moieties indicates coherence. All visualised transition densities are almost symmetric with respect to the diagonal elements. This reflects the absence of electron-hole separation for the lack of preferable direction of motion for electrons (or holes). The electron-hole pair created upon optical excitation becomes primarily localised in the middle of the molecule and away from the edges. The magnitude of the off-diagonal elements represents electronic coherence between different atoms. The comparison of results for **HT-a** and **HT*** indicates a higher coherence for the planar arrangement of thiophene backbones and alkyl chains. In the case of **MAT-a** and **EAT-a** molecules, the smaller distance between the bulky adamanthyl group and the aromatic chain supports effective coherence.

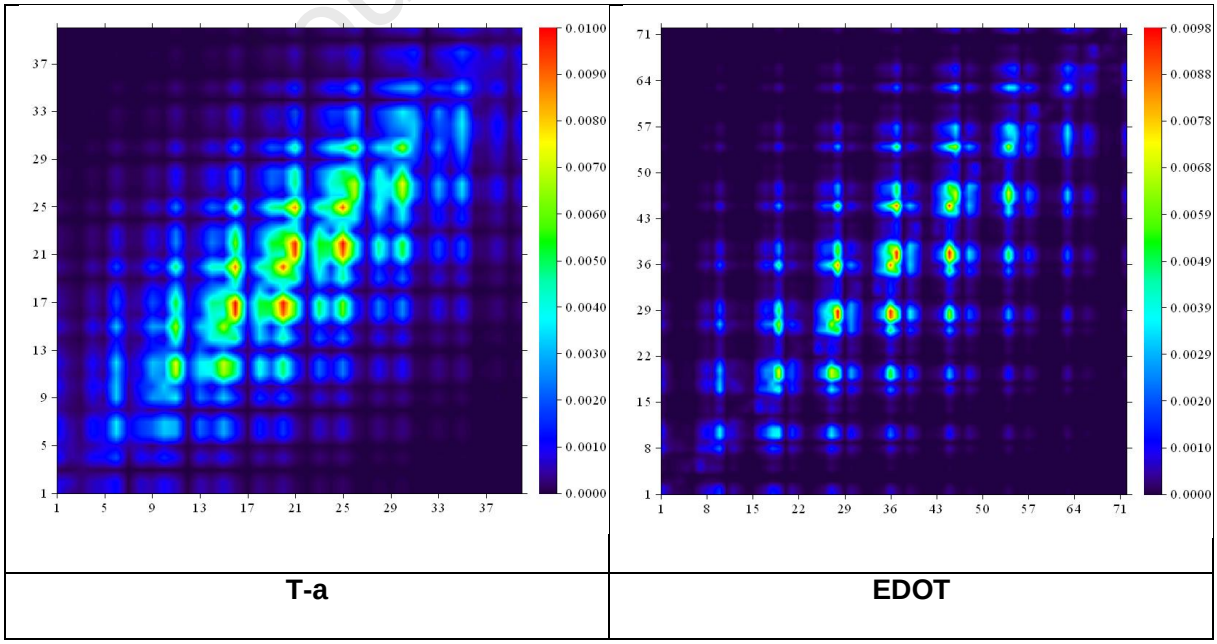

Figure 5 The two-dimensional 2D site representation of transition density matrix in atomic units for vertical S_1 excited state of selected model oligomers. The colour bars are shown at the right

of each figure. (For interpretation of the references to colour in this figure legend, the reader is referred to the web version of this article.)

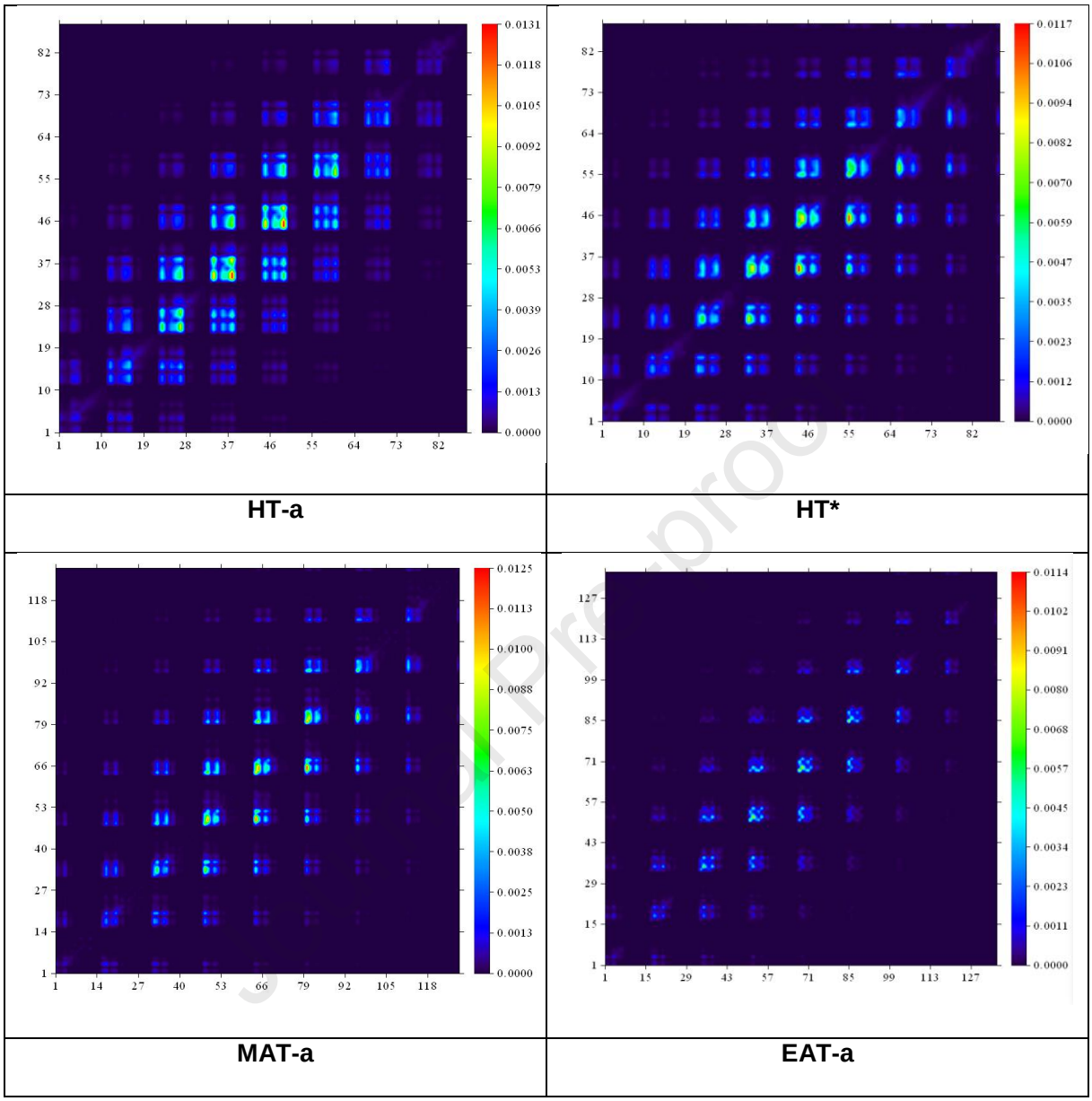

Figure 5 (continued) The two-dimensional 2D site representation of transition density matrix in atomic units for vertical S_1 excited state of selected model oligomers. The colour bars are shown at the right of each figure. (For interpretation of the references to colour in this figure legend, the reader is referred to the web version of this article.)

The experimental absorption spectra of studied polymers in solution and thin film are depicted in **Figure 6**. The significant red shift between solution absorption 2.76 eV (maximum at 450 nm) and thin layer 2.44 eV (maximum 508 nm) is observed for reference **P3HT**. Although the excitation energies calculated for **HT-a** and **HT*** oligomers are slightly lower compared with polymer samples,

the planarisation effect in polymer film is theoretically deduced. It seems that the effective polymer length is probably higher. The literature supposed ca 12 repeating units for solutions.[53]

In accordance with the predicted torsional deformation rigidity of methyladamanthyl group, no significant difference in absorption maxima for **PMAT1** polymer was found. The data collected in **Table 3** show that the measured value for the higher fraction in solution is 3.18 eV (390 nm) and for its thin layer almost the same 3.20 eV (387 nm). Slightly perceptible red-shift is noticeable in the case of **PEAT1** polymer, i.e. 2.70 eV (458 nm) in solution and 2.60 eV (475 nm) in a thin layer. The lower fractions exhibit the same behaviour as higher fractions. That means no red shift for **PMAT2** 3.18 eV (390 nm) in solution and thin layer and a small red shift for the **PEAT2** polymer 2.88 eV (430 nm) in solution and 2.79 eV (444 nm) in a thin layer. The difference in absorption maxima between lower and higher fractions is noticeable in the case of the **PEAT2** polymer. The absorption maximum for polymer from the higher fraction was higher by 30 nm, meaning a longer effective conjugation for the **PEAT1** polymer, which should provide better electric properties. Both fractions of **PMAT** exhibit identical absorption maxima. Therefore, the effective conjugation should be on the same level.

Generally, the difference of absorption spectra in solution and thin layer for **P3HT** is noticeable as a change in the absorption maxima, shape, and width of the peak. On the other hand, in the case of studied polymers, there is almost no significant change between solution and thin-layer samples, which hints towards the presence of similar adamantane side group interactions in solutions and in thin layers. Optical HOMO/LUMO gaps for all polymers were established according to the Tauc plot.[54] In accordance with the published work for **P3HT**,[55] the HOMO/LUMO gap in solution is 2.42 eV and in thin layer 2.00 eV. The HOMO/LUMO gap in solution of the prepared novel polymers was 2.67 eV for **PMAT** and 2.22 eV for **PEAT**. The values of the gap in thin layers were 2.61 eV and 2.13 eV for **PMAT** and **PEAT**, respectively.

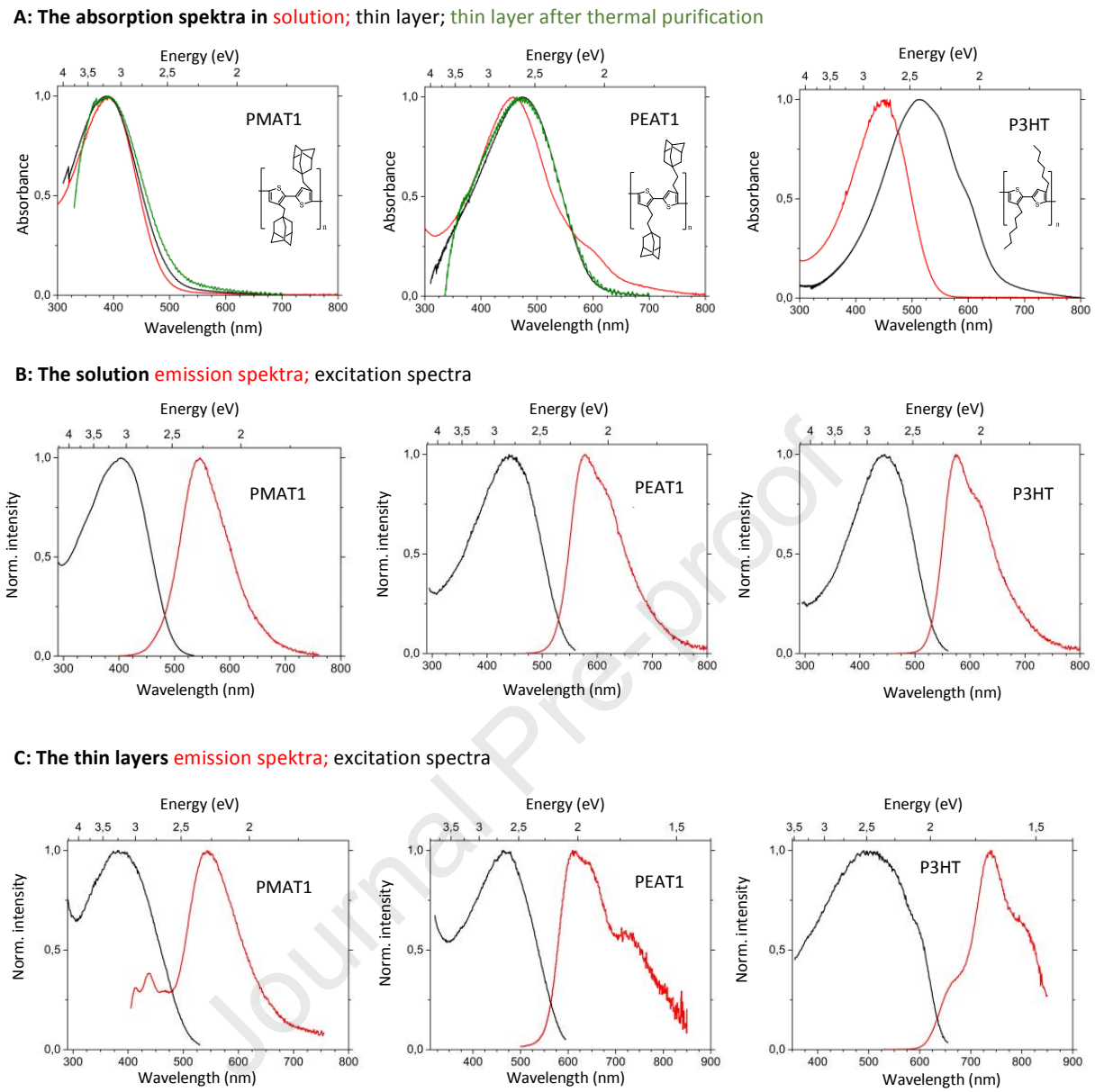

Figure 6. The absorption (a), excitation and emission spectra of investigated polymers measured in chloroform (b) and a thin layer (c)

The emission and excitation spectra of the studied polymers in solution are broad with a single emission peak at 2.27 eV (546 nm) for **PMAT** and 2.14 eV (577 nm) for **PEAT** (**Fig. 6**). The emission maximum of the investigated sample of **P3HT** was found at 2.16 eV (576 nm). The **P3HT** solution emission spectrum shows a shoulder at 2.00 eV (617 nm) and the **PEAT** polymer at 2.00 eV (615 nm). The difference in energy between the peak and shoulder emission is 0.16 eV in the case of **P3HT** and 0.14 eV for **PEAT**. The difference in energy might be ascribed to a C=C bond

stretching frequency in the polymer. Solution excitation spectra closely follow the shape of the absorption profile. The observed Stokes shift for all polymers was in the range from 0.6 to 0.9 eV (**Tab. 2**).

Table 3. Wavelength maxima (in nm) of absorption, excitation, emission optical spectra, Stokes shifts (in eV) and quantum yield (%) measured in solvated samples and thin layers.

Sample	Environment	Absorption	Excitation	Emission	Stokes shift	φ
P3HT	Chloroform	450	445	576	0.60	33 %[51]
	Thin layer	508	509	741	0.77	2 %[51]
PMAT1	Chloroform	390	403	546	0.91	11 %
	Thin layer	387	388	546	0.93	<1 %
PMAT2	Chloroform	390	402	546	0.91	-
	Thin layer	390	388	546	0.91	-
PEAT1	Chloroform	458	446	577	0.56	19 %
	Thin layer	475	472	609	0.57	<1 %
PEAT2	Chloroform	430	431	572	0.72	-
	Thin layer	444	442	603	0.74	-

The excitation and emission spectra of all polymers in thin films prepared by spin coating from a chloroform solution are given in **Fig 6**. In comparison with solution spectra, the thin-film **P3HT** spectrum is red-shifted with a lower-intensity maximum at 1.67 eV (741 nm) and shoulder at 1.56 eV (795 nm). The solid-state emission spectra of **PMAT** polymers exhibit no red-shift with a maximum comparable to the solution. On the other hand, the energy of the photoluminescence maximum for the higher fraction of **PEAT1** is 2.03 eV (609 nm) and 2.05 eV (603 nm) for the lower fraction (see **Fig. 8S**), representing a small red shift with respect to emission in solution. The emission spectra of both fractions show a shoulder at 1.72 eV (720 nm). The fluorescence yield of both polymer fractions in chloroform solution was measured, and the fluorescence quantum yield in solution was found to be 19 % for **PEAT1** and 11 % for **PMAT1** samples. The published quantum yield of **P3HT** in solution is ca 40 %, which is in good accord with literature values for similar polythiophene polymers.[55]

3.4 Electrical and electrochemical properties

The microscopic mobility and concentration of trapped charge carriers of investigated samples were evaluated from SCLC measurements (see **Fig. 9S**). The obtained results are summarised in **Table 4**. The reference **P3HT** sample exhibits the highest charge carrier mobility, with the value of 4.25×10^{-5} $cm^2\ V^{-1}\ s^{-1}$. The other samples have slightly lower mobilities: **PEAT-HT** (2.73×10^{-5} $cm^2\ V^{-1}\ s^{-1}$)), **PMAT-HT** (2.37×10^{-5} $cm^2\ V^{-1}\ s^{-1}$) and **PEAT1** (1.38×10^{-5} $cm^2\ V^{-1}\ s^{-1}$). For the rest of the samples, the mobilities are approximately an order of magnitude lower.

The lowest concentration of trapped carriers is observed for the **P3HT** reference sample, *i.e.*, 4.27×10^{-22} m^{-3}. For **PEAT-HT**, the ohmic region is immediately a trap-free SCLC region. The current is dominated by charge carriers injected from the contacts, and it is proportional to the square of the voltage (see **Fig. 9S**). Therefore, it was not possible to determine the concentration of trapped charge carriers. In the case of the other samples, the trap concentrations are approximately five times larger than for the **P3HT** reference sample (see **Tab. 4**).

Table 4. The thickness (L), trap-filled limit voltage (V_{TEL}), trap concentration (n_t) and microscopic electric mobility (μ) of measured thin layer samples.

Sample		L / nm	V_{TFL} / V	n_t / $10^{23} \times m^{-3}$	μ / $10^{-9} \times m^2\ V^{-1}\ s^{-1}$
P3HT		70	0.63	0.43	4.25
PMAT1		95	3.16	1.19	0.58
PMAT2		90	3.31	1.36	0.63
PMAT1-HT		86	3.16	1.42	2.37
PEAT1		42	3.55	6.67	1.38
PEAT2		70	3.02	1.99	0.44
PEAT1-HT		70	–	–	2.73

To estimate the frontier molecular energy levels, we conducted cyclic voltammetry measurements according to established techniques. Thin films of the polymers deposited on fluorine-doped tin oxide substrates served as the working electrode. The cyclic voltammograms for the three polymers are plotted in **Figure 11S**. All materials were found to have quasi-reversible oxidation. The oxidation potential of the adamantyl-containing polymers was markedly higher than that of **P3HT**. The HOMO level of **P3HT** sample has been estimated by electrochemical techniques frequently used in the literature.[56] Based on these results, we have determined an average HOMO value of –5.13 eV, with a standard deviation of ±0.13 eV. This value of **P3HT** HOMO level was used as a reference value with respect to which we calculate the frontier orbital level of the investigated novel materials (**Table 5**). On the reduction side, likewise, the reduction potential of the adamantyl polymers was more negative than that of **P3HT**, leading to an overall larger electrochemical band-gap in the case of the adamantyl polymers. This corresponds well with the observation of a larger optical HOMO/LUMO gap for these materials. The reversibility of reduction was not very clear, despite efforts to try different scanning rates. The **PEAT** sample showed a resolvable quasi-reversible reduction. Therefore, it can be said that all three polymers can be reversibly oxidised, which is consistent with what is accepted for polythiophenes. However, it is interesting to note that the adamantyl polymers do appear to support quasi-reversible reduction. In the last column of **Table 5,** the optical band gaps are collected, which are slightly larger than the electrochemical ones.

Table 5. Experimental electrochemical values for polymers measured for reference Ag/AgCl electrode, and optical bandgaps of thin films.

	Cyclic voltammetry results					
	E_{ox}^{onset}/V	HOMO /eV	E_{red}^{onset} /V	LUMO /eV	Eg /eV	Optical Eg /eV
PMAT1	0.85	–5.50	–1.46	–3.19	2.31	2.61
PEAT1	0.62	–5.27	–1.49	–3.16	2.11	2.13
P3HT	0.48	–5.13	–0.97	–3.68	1.45	2.00

4. Conclusion

In this study, we present the synthesis and the optical and electrical properties of two novel thermodynamically stable regioregular poly-3-adamantylmethylthiophene and poly-3-adamantylethylthiophene polymers. Up to the present day, there are no reports on the synthesis and investigation of the organic materials based on polythiophene backbones modified by adamantyl groups. The prepared samples are easily processable in common organic solvents like chloroform, toluene, chlorobenzene or dichloromethane and convenient for upscaling and industrial processing. The prepared adamantane polythiophenes possess excellent thermal and chemical stability, which are important properties to produce stable and long-life devices. The quantum chemical torsional analysis for model oligomers showed that the hexyl chain is more flexible with respect to the rotation than the adamantly-methyl/ethyl groups. The bulky adamantyl groups prefer the perpendicular orientation toward the polymer backbone. Compared to the reference poly-3-hexylthiophene, the experimental absorption and emission spectra of two new polymers exhibit no significant change between solution and thin-layer samples. This supports the theoretical results predicting the higher rigidity of the adamantane side group and its effectiveness in creating a well-ordered structure, while larger substituents would create a less spacious structure than adamantane, which presents a reasonable compromise between single chain ordering and

allowing intermolecular interactions. Furthermore, our AFM scans show a clearly discernible granular structure of the **PMAT** and **PEAT** layers, which is not present in our **P3HT** sample. The performed GIWAXS experiment confirmed the presence of both crystalline and amorphous phases, with **PMAT** featuring higher crystallinity and preferred orientation. Both **PMAT** and **PEAT** were found to prefer the edge-on orientation of intermolecular packing.

The fluorescence quantum yields are dramatically decreased in thin layers compared to those in solution, as is the case in reference, indicating the presence of some stronger competing mechanisms induced by intermolecular interaction. The examined electron-hole transition density matrices calculated for the lowest excited vertical energy show that the electron-hole pair created upon optical excitation becomes primarily localised in the middle of the molecule and away from the edges. However, no preferred direction of motion for electrons (or holes) was theoretically predicted. The experimental charge carrier mobility in films is comparable with the reference **P3HT** sample. The electrochemical measurements showed that the investigated novel polymers do appear to be electrochemically reducible, at least with some degree of reversibility. It seems that the newly prepared class of molecules is a promising alternative organic material to the reference **P3HT**.

Acknowledgement

The authors thank for financial support of this investigation by the Czech Science Foundation (project No. 21-01057S). J.K. thanks the project CZ.02.2.69/0.0/0.0/18_053/0016962 of the Ministry of Education Youth and Sports of the Czech Republic. The authors thank the financial support by the Slovak Research and Development Agency (APVV-19-0024) and Slovak Grant Agency (VEGA 1/0461/21). V.L. thanks to the Ministry of Education, Science, Research and Sport of the Slovak Republic for funding within the scheme “Excellent research teams". J.P and J.J. thanks to GACR project 20-29499Y funded by Czech Science Foundation. The authors thank prof. Jiří Kučerík for TGA and DSC measurements. J.T., J.J. and M.K. thank the Brno University of Technology for support through project FCH-S-21-7553. Computational resources were supplied by the project "e-Infrastruktura CZ" (e-INFRA CZ LM2018140) supported by the Ministry of Education, Youth and Sports of the Czech Republic.

References

(1) Huang, J.; Yu, G. Structural Engineering in Polymer Semiconductors with Aromatic N-Heterocycles. *Chemistry of Materials* **2021,** *33*, 1513-1539.

(2) Liu, K.; Liu, B. Recent Advances in Biodegradable Conducting Polymers and Their Biomedical Applications. *Biomacromolecules* **2018,** *19*, 1783-1803.

(3) Gopalan, A-I.; Komathi, S.; Muthuchamy, N.; Lee, K-P.; Whitcombe, M. J.; Dhana, L.; Sai-Anand, G.; Functionalized conjugated polymers for sensing and molecular imprinting applications. *Progress in Polymer Science* **2019** *88*, 1-129.

(4) Zhang, G.; Lee, S.; Gutiérrez-Meza, E.; Buckley, C.; McBride, M.; Valverde-Chávez, D. A.; Kwon, Y. H.; Savikhin, V.; Xiong, H.; Dunn, T. J.; Toney, M. F.; Yuan, Z.; Silva, C.; Reichmanis, E. Robust and Stretchable Polymer Semiconducting Networks: From Film Microstructure to Macroscopic Device Performance. *Chem. Mater.* **2019** *31,* 6530−6539.

(5) Khau, B. V.; Scholz, A. D.; Reichmanis, E. Advances and Opportunities in Development of Deformable Organic

(6) Tsumura, A.; Koezuka, H.; Ando, T. Macromolecular Electronic Device: Field-effect Transistor with A Polythiophene Thin Film. *Appl. Phys. Lett.* **1986** *49,* 1210−1212.

(7) Li, Ch.; Ren, Z.; Sun, X.; Li, H.; Yan, S. Deep-Blue Thermally Activated Delayed Fluorescence Polymers for Nondoped Solution-Processed Organic Light-Emitting Diodes. *Macromolecules* ***2019*** *52*, 2296-2303.

(8) Lee, P-I.; Hsu, L-Ch. S.; Lin, P. White-Light-Emitting Diodes from Single Polymer Systems Based on Polyfluorene Copolymers with Quinoxaline Derivatives. *Macromolecules* ***2010*** *43,* 8051-8057.

(9) Sun, N.; Han, Y.; Sun, L.; Xu, M.; Wang, K.; Lin, J.; Sun, Ch.; An, J.; Wang, S.; Wei, Q.; Zheng, Y.; Zhuo, Z.; Bai, L.; Xie, L.; Yin, Ch.; Zhang, X.; Huang, W. Diarylfluorene Flexible Pendant Functionalization of Polystyrene for Efficient and Stable Deep-Blue Polymer Light-Emitting Diodes. *Macromolecules* ***2021*** *54,* 6525-6533.

(10) Sariciftci, N. S.; Smilowitz, L.; Heeger, A. J.; Wudl, F. Photoinduced Electron Transfer from A Conducting Polymer to Buckminster-fullerene. *Science* **1992** *258,* 1474−1476.

(11) Chen, J.; Chen, Y.; Feng, L.-W.; Gu, C.; Li, G.; Su, N.; Wang, G.; Swick, S. M.; Huang, W.; Guo, X.; Facchetti, A.; Marks, T. J. Hole (Donor) and Electron (Acceptor) Transporting Organic Semi- conductors for Bulk-heterojunction Solar Cells. *EnergyChem* **2020** *2,* 100042.

(12) Someya, T.; Bao, Z.; Malliaras, G. G. The Rise of Plastic Bioelectronics. *Nature* **2016,** *540,* 379–385.

(13) Lee, G.-H.; Moon, H.; Kim, H.; Lee, G. H.; Kwon, W.; Yoo, S.; Myung, D.; Yun, S. H.; Bao, Z.; Hahn, S. K. Multifunctional Materials for Implantable and Wearable Photonic Healthcare Devices. *Nat. Rev. Mater.* **2020***, 5,* 149–165.

(14) Kurioka, T.; Shida, N.; Tomita, I.; Inagi, S. Post-Functionalization of Aromatic C–H Bonds at the Main Chains of π-Conjugated Polymers via Anodic Chlorination Facilitated by Lewis Acids. *Macromolecules* **2021** *54,* 1539-1547.

(15) Michaels, W.; Zhao, Y.; Qin, J. Atomistic Modeling of PEDOT:PSS Complexes I: DFT Benchmarking. *Macromolecules* **2021** *54,* 3634-3646.

(16) Neusser, D.; Malacrida, C.; Kern, M.; Gross, M. Y.; Slageren, J.; Ludwig, S. High Conductivities of Disordered P3HT Films by an Electrochemical Doping Strategy. *Chemistry of Materials* **2020** *32,* 6003-6013.

(17) Jaymand, M.; Hatamzadeh, M.; Omidi, Y. Modification of polythiophene by the incorporation of processable polymeric chains: Recent progress in synthesis and applications. *Progress in Polymer Science* **2015** *47,* 26-29.

(18) Lee, J. L.; Pearce, E. M.; Kwei, T. K. Side-Chain Crystallization in Alkyl-Substituted Semiflexible Polymers. *Macromolecules* **1997** *30,* 6877-6883.

(19) Cao, Z.; Galuska, L.; Quian, Z.; Thang, S.; Huang, L.; Prine, N.; Li, T.; He, Y.; Hong, K. The effect of side-chain branch position on the thermal properties of poly(3-alkylthiophenes). *Polym. Chem.* **2020** *11,* 517-526.

(20) Blasi, D.; Viola, F.; Modena, F.; Luukkonen, A.; Macchia, E.; Picca, A. R.; Gounani, Z.; Tewari, A.; Osterbacka, R.; Caironi, M.; Vajna, Z. M. K. ; Scamarcio, G.; Torricelli, F.; Torsi, L. Printed, cost-effective and stable poly(3-hexylthiophene) electrolyte-gated field-effect transistors. *J. Mater. Chem. C,* **2020,** *8,* 15868-15868.

(21) Park, H.; Han, M. J.; Kim, Y.; Kim, E. J.; Kim, H. J.; Kim, H.J.; Yoon, D. K.; Kim, B. J. Regioregularity-Dependent Crystalline Structures and Thermal Transitions in Poly(3-dodecylthiophene)s. *Chemistry of Materials **2021** 33,* 3312-3320.

(22) Nguyen, T-D.; Nguyen, V-H.; Song, J.; An, J.; Truong, N-T.; Dang, Ch-H.; Im, Ch. Molecular Weight-Dependent Physical and Photovoltaic Properties of Poly(3-alkylthiophene)s with Butyl, Hexyl, and Octyl Side-Chains. *Chemistry of Polymers* **2021***, 13,* 3440.

(23) Lin, P.-S.; Shoji, Y.; Afraj, S. N.; Ueda, M.; Lin, Ch-H.; Inagaki, S.; Endo, T.; Tung, S-H.; Cheng, M-Ch.; Liu, Ch-L.; Higashihara, T. Controlled Synthesis of Poly[(3-alkylthio)thiophene]s and Their Application to Organic Field-Effect Transistors. *ACS Applied Materials & Interfaces* **2021** *13,* 31898-31909.

(24) Krajčovič, J.; Kovalenko, J.; Heinrichová, P.; Vala, M.; Weiter, M. Adamantyl side groups boosting the efficiency and thermal stability of organic solid-state fluorescent dyes. *Journal of Luminescence* **2016** *175,* 94-99.

(25) Rodrigues, A.; Castro, M. C. R.; Farinha, A. S. F.; Oliveira, M.; Tome, J. P. C.; Machado, A. V.; Raposo, M. M. M..; Hilliou, L.; Bernardo, G. Thermal stability of P3HT and P3HT:PCBM blends in the molten state. *Polymer Testing* **2013** *7,* 1192-1201.

(26) Khasim, S.; Pasha, A.; Badi, N.; Lakshmi, M.; Al-Ghamdi, S. A.; Al-Aoh, H. A. PVA Treated PEDOT-PSS: TiO_2 Nanocomposite Based High-Performance Sensors Towards Detection of Relative Humidity and Soil Moisture Content for Agricultural Applications. *Journal of Polymer and the Environment* **2021** *29,* 612-623.

(27) ALTAMURA, D.; LASSANDRO R.; VITTORIA F. A.; DE CARO L.; SILIQI D.; LADISA M; GIANNINI C.. X-ray microimaging laboratory (XMI-LAB). *Journal of Applied Crystallography* **2012** 45, 869-873.

(28) SILIQI, D.; DE CARO L.; LADISA M.; SCATTARELLA, F.; MAZZONE, A.; ALTAMURA, D.; SIBILLANO, T.; GIANNINI, C. SUNBIM: a package for X-ray imaging of nano- and biomaterials using SAXS, WAXS, GISAXS and GIWAXS techniques. *Journal of Applied Crystallography* **2016** 49, 1107-1114.

(29) Nešpůrek, S.; Zmeškal, O.; Sworakowski, J. Space-charge-limited currents in organic films: Some open problems. *Thin Solid Films***, 2008** *516,* 8949-8962.

(30) Pospisil, J.; Zmeškal, O.; Nespurek, S. Sp Density of bulk trap states of hybrid lead halide perovskite single crystals: temperature modulated space-charge-limited-currents. *Sci Rep* **2019** *9,* 3332.

(31) WEI, R.; GRYSZEL, M.; MIGLIACCIO, L.; GŁOWACKI E., D. Tuning photoelectrochemical performance of poly(3-hexylthiophene) electrodes via surface structuring. *Journal of Materials Chemistry C* . 2020 8, 10897-10906

(32) Frisch, M. J.; Trucks, G. W.; Schlegel, H. B.; et Al. *Gaussian 16, Rev. B.01, Gaussian, Inc., Wallingford*, CT. **2016**.

(33) Lee, C.; Yang, W.; Parr, R. G. Development of the Colle-Salvetti correlation-energy formula into a functional of the electron density. *Phys. Rev. B.* **1988** *37,* 785.

(34) McCormick, T. M.; Bridges, C. R.; Carrera, E. I.; DiCarmine, P. M.; Gibson, G-L.; Hollinger, J.; Kozycz, L. M.; Seferos, D. S. Conjugated Polymers: Evaluating DFT Methods for More Accurate Orbital Energy Modeling. *Macromolecules* **2013** *46,* 3879-3886.

(35) Furche, F.; Ahlrich, R. Adiabatic time-dependent density functional methods for excited state properties*. J. Chem. Phys.* **2002** *117***,** 7433–7447.

(36) Yanai, T.; Tew, D. P.; Handy, N. C. A new hybrid exchange–correlation functional using the Coulomb-attenuating method (CAM-B3LYP)*. Chem. Phys. Lett.* **2004** *393,* 51–56.

(37) Hanwell, M.; Curtis, D. E.; Lonie, D. C.; Vandermeersch, T.; Zurek, E.; Hutchinson, G. R. Avogadro: An advanced semantic chemical editor, visualization, and analysis platform. *J Cheminform* **2012** *4.*

(38) Macrae, C. F.; Sovago, I.; Cottrell, S. J.; Galek, P. T. A.; McCabe, P.; Pidcock, E.; Platings, M.; Shields, G. P.; Stevens, J. S.; Towler, M.; Wood, P. A. Mercury 4.0: from visualization to analysis, design and prediction. *Journal of Applied Crystallography* **2020,** *53,* 226-235.

(39) Lu, T.; Chen, F. Multiwfn: A Multifunctional Wavefunction Analyzer. *J. Comput. Chem.* **2012** *33,* 580-592.

(40) Liua, F.; Zuoc, P.; Mengb, L.; Zheng, S. J. On the optical properties of thiophene oligomers: configuration interaction study on their ground (S0) and first singlet excited (S1) states. *J. Mol. Struct. (Theochem)* **2005** *726,* 161–169*.*

(41) Bouzzine, S. M..; Bouzakraoui, S.; Bouachrine, M.; Hamidi, M. Density functional theory (B3LYP/6-31G*) study of oligothiophenes. *J. Mol. Struct. (Theochem)* **3005** *726,* 271-276.

(42) Beenken, W. J. D. Multiwfn: Torsional broadening in absorbtion and emission spectra of bithiophene as calculated by time-dependent density functional theory. *Chem. Phys.* **2008** *349,* 250-255*.*

(43) SAmdal, S.; Samuelsen, E. J.; Volden, H. V. Molecular conformation of 2,2'-bithiophene determined by gas phase electron diffraction and ab initio calculations. *Synth. Met.* **1993** *59*.

(44) Blaskovits, J. T.; Bura, T.; Beaupré, S.; Lopez, S. A.; Roy, C.; Soares, J. G.; Oh, A.; Quinn, J.; Li, Y.; Aspuru-Guzik, A.; Leclerc, M. A. Study of the Degree of Fluorination in Regioregular Poly(3-hexylthiophene). *Macromolecules* **2017** *50,* 162-174.

(45) Ohno, S.; Tanaka, H.; Tanaka, K.; Takahashi, K.; Tanaka, M. Electronic structure of α-sexithiophene ultrathin films grown on $\underline{\mathbf{Si(111)-\sqrt{3}\times\sqrt{3}-Ag}}$. *Phys. Chem. Chem. Phys.* **2018** *20,* 1114-1126.

(46) Prosa, T. J.; Winokur, M. J. X-ray Structural Studies of Poly(3-alkylthiophenes): An Example of an Inverse Comb. *Macromolecules* **1992** *25,* 4364-4372

(47) Dag, S.; Wang, L-W. Packing structure of poly(3-hexylthiophene) crystal: ab initio and molecular dynamics studies. *J Phys Chem B*. **2010** *114*, 5997-6000.

(48) Horowitz, G.; Bachet, B.; Yassar, A.; Lang, P.; Demanze, F.; Fave, J-L.; Garnier, F. Growth and Characterization of Sexithiophene Single Crystals. *Chemistry of Materials* **1995** *7,* 1337-1341

(49) Destri, S.; Ferro, D. R.; Khotina, I. A.; Farina, A. Tetrahexylsexithiophene: crystal structure and molecular mechanics calculations. *Macromolecular Chemistry and Physics,* **1998,** *199.*

(50) Neumann, M. A..; Tedesco, C.; Destri, S.; Ferro, D. R.; Porzio, W. CCDC 214226: Experimental Crystal Structure Determination. *University of Groningen* **2003.**

(51) YANG, H.; ZHANG, R.; WANG, L.; et al. Face-On and Edge-On Orientation Transition and Self-Epitaxial Crystallization of All-Conjugated Diblock Copolymer. *Macromolecules* **2015** 48, 7557-7566

(52) MELE, E.; LEZZI, F.; POLINI, A.; ALTAMURA, D.; GIANNINI, C.; PISIGNANO, D. Enhanced charge-carrier mobility in polymer nanofibers realized by solvent-resistant soft nanolithography. *Journal of Materials Chemistry* **2012** 22

(53) Huang, D. M.; Faller, R.; Do, K.; Moule, A. J. Coarse-Grained Computer Simulations of Polymer/Fullerene Bulk Heterojunctions for Organic Photovoltaic Applications. *Journal of Chemical Theory and Computation* **2010,** *6,* 526-537.

(54) Makula, P.; Pacia, M.; Macyk, W. How To Correctly Determine the Band Gap Energy of Modified Semiconductor Photocatalysts Based on UV–Vis Spectra. *The Journal of Physical Chemistry Letters* **2018** *9,* 6814-6817.

(55) Cook, S.; Furube, A.; Katoh, R. Analysis of the excited states of regioregular polythiophene P3HT. *Energy Environ. Sci.* **2008** *1,* 294-299.

(56) Acevedo-Pena, P.; Baray-Calderón, A.; Hu, H.; Golzalez, I.; Ugalde-Saldivar, V. Measurements of HOMO-LUMO levels of poly(3-hexylthiophene) thin films by a simple electrochemical method. *J. Solid State Electrochem*. **2017** *21*, 2407-2414.

Novel Adamantane Substituted Polythiophenes as Competitors to Poly(3-Hexylthiophene)

Highlights:

- Novel derivates of polythiophene, featuring the bulky adamantyl groups were synthesized
- These materials exhibit high thermal stability as well as electrical conductivity comparable to poly(3-hexylthiophene).
- Furthermore, the materials absorb visible light in the 400 – 500 nm wavelength range, making them serious candidates for use in optoelectronics

Declaration of interests

☒The authors declare that they have no known competing financial interests or personal relationships that could have appeared to influence the work reported in this paper.

☐The authors declare the following financial interests/personal relationships which may be considered as potential competing interests: